THE UNIVERSITY OF QUEENSLAND

AUSTRALIA

Molecular modelling of carbon/ionic liquid interfaces for electric double – layer capacitors

Ryan Murray Burt

Bachelor of Chemical and Process Engineering (Honours)

A thesis submitted for the degree of Doctor of Philosophy at

The University of Queensland in 2017

School of Chemical Engineering

Abstract

Electric double-layer capacitors (EDLCs) are important energy storage devices that have high potential for use in existing and emerging markets such as electric vehicles, portable electronic devices, and smart grid management. This is due to their high power density and long lifetime, which are a result of their simple ion adsorption mechanism for charge storage. A significant and ongoing effort is being made to improve the energy density of ELDCs, so that they financially compete with batteries. EDLC improvement has mainly been facilitated through the investigation and discovery of novel solid and liquid materials.

This topic was studied with the motivation of investigating charge storage mechanisms in EDLCs with configurations where traditional models are not appropriate to describe the phenomena observed in the literature. Significantly, in small pores anomalous results challenged the traditional beliefs of the electric double layer (EDL) and the accessibility of ions to sub-nanometre micropores. Highly dense RTIL electrolyte, which are non-dilute, and can also be solvent free, also can't be described by traditional models and display complex phenomena such as charge over-screening.

This thesis evaluates molecular and charge storage mechanisms at solid-liquid interfaces of room temperature ionic-liquid (RTIL) electrolytes and porous carbon electrodes. Changes in charge storage mechanisms with the addition of an aprotic solvent, acetonitrile (ACN,) to the RTIL, was also investigated in simple slit-pores, and complex carbon electrode structures. The contact angle of RTIL drops was also investigated under a variety of conditions.

The methodology of molecular dynamics (MD) simulation was chosen for this thesis as it offers unique benefits to approach the problem of understanding molecular phenomena in ELDCs. MD simulation was selected as it is possible to systematically control variables of interest to a high level of accuracy. In this way, theoretical structures, or models derived from real materials, can be analysed. Significantly, analysis of charge storage mechanisms occurring within small pores, or with dense electrolytes, can be completed with relative ease, unlike with experiments which require difficult or expensive *in situ* experimental techniques.

The analysis began with studying simple slit-pore electrodes to provide a framework for comparison with more complex electrode materials. The charge storage mechanism was tested under a variety of conditions. Most interestingly, capacitance was found to have a moderate dependence on the amount of ACN in the electrolyte, which contrasts with previously noted behaviour at flat walls. Additionally, solid-like behaviour was observed for the bulk electrolyte in certain systems.

We present the first results for a MD simulation of the RTIL $EMIMBF_4$ in model CDC electrodes at a potential of 1 V, with systematic addition of ACN to the electrolyte. Our simulations showed that the mechanism of charge storage is different between the positive and negative electrode, but converges when highly solvated in ACN. This is consistent with recent NMR results. Capacitance was found to not be sensitive to the concentration of ions over the range tested, and ACN did not significantly alter the ionic structure at the internal surface of the electrodes. Upon higher electric potential, the capacitance of pure $EMIMBF_4$ was found to decrease moderately. To examine the adsorbed structure and orientation of an RTIL inside a disordered CDC-pore, a simulation of EMIMTFSI in a single uncharged pore was performed, as well as simulations of bulk EMIMTFSI. Pair distribution functions (PDF) were then calculated for the empty pores, the bulk RTIL, and the RTIL adsorbed inside the pores. Analysing the structure revealed that porous CDC models used are under-graphitised, and may not capture the behaviour of the most highly confining sites in the pores to the fullest extent.

Interaction between $EMIMBF_4$ and graphitic surfaces was studied in terms of wettability and electrowetting of nanodrops. This has indirect applications for EDLCs (as the liquid is not a bulk) as well as other technologies. Measuring the contact angle at the solid-liquid-gas interface is a standard technique for determining the wettability of a liquid to a surface. Here we present the first MD simulation results of the contact angle of $EMIMBF_4$ (and mixtures with ACN) drops on carbon surfaces of varying interaction potentials. The results showed that a weakly interacting surface had non-linear dependence on ACN mass fraction, but no dependence on drop size. For a strongly interacting sheet, the contact angle became more dependent on drop size, but several non-uniform wetting structures were observed, contrasting with other comparable results in the literature. This highlights that IL behaviour very strongly depends on the pair interactions. Electrowetting under various electrode potentials elicited a negligible change in the contact angle, over the range of potentials simulated (– 5 V to + 5 V). The lack of change was partially explained through the use of charge histograms, and highlighted that constant electrode charge simulations are not appropriate for these types of electrowetting systems. The drop structures were analysed at the surface of both negative and positive electrodes, and were found to be less ordered at the negative electrode due to ion size effects.

Declaration by author

This thesis is composed of my original work, and contains no material previously published or written by another person except where due reference has been made in the text. I have clearly stated the contribution by others to jointly-authored works that I have included in my thesis.

I have clearly stated the contribution of others to my thesis as a whole, including statistical assistance, survey design, data analysis, significant technical procedures, professional editorial advice, and any other original research work used or reported in my thesis. The content of my thesis is the result of work I have carried out since the commencement of my research higher degree candidature and does not include a substantial part of work that has been submitted to qualify for the award of any other degree or diploma in any university or other tertiary institution. I have clearly stated which parts of my thesis, if any, have been submitted to qualify for another award.

I acknowledge that an electronic copy of my thesis must be lodged with the University Library and, subject to the policy and procedures of The University of Queensland, the thesis be made available for research and study in accordance with the Copyright Act 1968 unless a period of embargo has been approved by the Dean of the Graduate School.

I acknowledge that copyright of all material contained in my thesis resides with the copyright holder(s) of that material. Where appropriate I have obtained copyright permission from the copyright holder to reproduce material in this thesis.

Publications during candidature

Burt, R.; Birkett, G.; Zhao, X. S., A Review of Molecular Modelling of Electric Double Layer Capacitors. *PCCP* **2014**, *16*, 6519-6538.

Zhang, L.; Xiong, Z.; Li, L.; Burt, R.; Zhao, X. S., Uptake and Degradation of Orange Ii by Zinc Aluminum Layered Double Oxides. *J. Colloid Interface Sci.* **2016**, *469*, 224-230.

Burt, R.; Breitsprecher, K.; Daffos, B.; Taberna, P.-L.; Simon, P.; Birkett, G.; Zhao, X. S.; Holm, C.; Salanne, M., Capacitance of Nanoporous Carbon-Based Supercapacitors Is a Trade-Off between the Concentration and the Separability of the Ions. *J. Phys. Chem. Lett.* **2016**, *7*, 4015-4021.

Burt, R.; Birkett, G.; Salanne, M.; Zhao, X. S., Molecular Dynamics Simulations of the Influence of Drop Size and Surface Potential on the Contact Angle of Ionic-Liquid Drops. *J. Phys. Chem. C* **2016**, *120*, 15244-15250.

Publications included in this thesis

Burt, R.; Breitsprecher, K.; Daffos, B.; Taberna, P.-L.; Simon, P.; Birkett, G.; Zhao, X. S.; Holm, C.; Salanne, M., Capacitance of Nanoporous Carbon-Based Supercapacitors Is a Trade-Off between the Concentration and the Separability of the Ions. *J. Phys. Chem. Lett.* **2016**, *7*, 4015-4021. – incorporated into Chapter 5

Contributor	Statement of contribution
Author Ryan Burt (Candidate)	Program and conducted simulations (60%) Analysis and interpretation of data (50 %) Wrote the paper (70%)
Author Konrad Breitsprecher	Program and conducted simulations (40%) Analysis and interpretation of data (50 %)
Author Barbara Daffos	Performed experiments (80%)
Author Pierre-Louis Taberna	Performed experiments (20%)
Author Patrice Simon	Edited and reviewed the paper revisions (33%)
Author Greg Birkett	Wrote and edited paper (15%)

Author George Zhao	Edited and reviewed the paper revisions (33%)
Author Christian Holm	Edited and reviewed the paper revisions (33%)
Author Mathieu Salanne	Wrote the paper (30%)

Burt, R.; Birkett, G.; Zhao, X. S., A Review of Molecular Modelling of Electric Double Layer Capacitors. *PCCP* **2014**, *16*, 6519-6538. – incorporated as Chapter 2.

Contributor	Statement of contribution
Author Ryan Burt (Candidate)	Reviewed the literature (100%) Wrote the paper (70%)
Author Greg Birkett	Wrote the paper (15%)
Author George Zhao	Wrote the paper (15%)

Burt, R.; Birkett, G.; Salanne, M.; Zhao, X. S., Molecular Dynamics Simulations of the Influence of Drop Size and Surface Potential on the Contact Angle of Ionic-Liquid Drops. *J. Phys. Chem. C* **2016**, *120*, 15244-15250. – incorporated as Chapter 6

Contributor	Statement of contribution
Author Ryan Burt (Candidate)	Program and conducted simulations (100%) Analysis and interpretation of data (100 %) Wrote the paper (70%)
Author Greg Birkett	Wrote the paper (10%)
Author Mathieu Salanne	Wrote the paper (10%)
Author George Zhao	Wrote the paper (10%)

Contributions by others to the thesis

Contributions were made by Dr Greg Birkett, Prof X. S. Zhao, and Prof Mathieu Salanne in concept, analysis, interpretation, drafting, and writing in the advisory capacity.

Statement of parts of the thesis submitted to qualify for the award of another degree

None

Acknowledgements

I would like to firstly acknowledge my advisors at UQ, Dr Greg Birkett and Prof X. S. Zhao, for giving me the opportunity to work on this project with you, and for all the time and support you have given me. Without the encouragement and direction you provided I would not have made it very far, you both have my deepest gratitude.

I would also like to pay special thanks to my French advisor Prof Mathieu Salanne for hosting me so graciously in France in 2015. The attention and care you provided me during my visit was outstanding, France has a special place in my heart now.

I would like to thank my good friend Konrad Breitsprecher for the great researcher that we did together. I hope to see you again soon. I would also like to acknowledge Dr Boris Dyatkin and his colleagues for the collaborative PDF project and the interesting experimental data you generously provided.

Finally, I want to thank my friends and family for never doubting me.

Keywords

Electric double layer capacitors, room temperature ionic liquids, acetonitrile, electrolytes, carbon interfaces, nanoporous confinement, molecular dynamics, contact angle, electrowetting

Australian and New Zealand Standard Research Classifications (ANZSRC)

ANZSRC code: 030603, Colloid and Surface Chemistry, 40%

ANZSRC code: 030604, Electrochemistry, 40%

ANZSRC code: 030699, Physical Chemistry not elsewhere classified, 20%

Fields of Research (FoR) Classification

FoR code: 0904, Chemical Engineering, 100%

Table of Contents

Abstract ..... **ii**

Declaration by author ..... **iv**

Publications during candidature ..... **v**

Publications included in this thesis ..... **v**

Contributions by others to the thesis ..... **vii**

Statement of parts of the thesis submitted to qualify for the award of another degree ..... **vii**

Acknowledgements ..... **viii**

Keywords ..... **ix**

Australian and New Zealand Standard Research Classifications (ANZSRC) ..... **ix**

Fields of Research (FoR) Classification ..... **ix**

Table of Contents ..... **x**

List of Figures ..... **xiv**

List of Tables ..... **xxii**

List of Abbreviations used in this thesis ..... **xxiii**

1. Introduction **1**

1.1. Background 1

1.1.1. EDLC applications and significance 1

1.1.2. Configurations of EDLCs 1

1.1.3. EDL modelling 2

1.2. Scope and Objectives 4

1.3. Thesis structure and development 5

1.4. References 7

2. Literature Review **10**

2.1. Modelling techniques 10

2.2. Molecular simulations of the EDL 12

2.2.1. RTILs 13

2.2.1.1. Planar electrodes *13*

2.2.1.2. Porous electrodes *19*

2.2.1.3. Exohedral curvature electrodes *27*

2.2.1.4. Dynamics *28*

2.2.1.5. Non-electrostatic forces *30*

2.2.2. Organic solvent based electrolytes 31

2.2.2.1. $[TEA]^+[BF_4]^-$ in ACN and PC *31*

2.2.2.2. RTIL - ACN mixtures *33*

2.2.3. Aqueous electrolytes 37

2.3. Recent insights of significance 40

2.4. Conclusions and gaps in the literature 41

2.5. References 43

3. Methodology 52

3.1. Molecular dynamics principles 52

3.2. Relevant limitations of MD 53

3.3. Details of programs used 54

3.3.1. Gromacs 54

3.3.2. Metalwalls 55

3.4. Details of models used 56

3.4.1. Electrolyte 56

3.4.2. Electrode 57

3.5. Validations and simple analysis 58

3.5.1. Bulk simulations 58

3.5.2. Flat wall EDLC 62

Appendix A3 ..... *65*

3.6. References 67

4. Structure and capacitance of ionic-liquid and acetonitrile mixtures inside slit-pore carbon electrodes 71

4.1. Introduction 72

4.2. Methodology 73

4.2.1. Three-dimensional ensemble with constant charge electrodes 74

4.2.2. Two-dimensional ensemble constant potential 76
4.3. Discussion 77
4.3.1. Constant charge slit-pores 78
4.3.2. Constant potential slit-pores 83
4.4. Conclusions 88
Appendix A4 ..... *90*
4.5. References 91
5. Molecular structure and capacitance properties of imidazolium ionic liquid and acetonitrile mixtures inside disordered porous carbon electrodes 95
5.1. Introduction 96
5.2. Methodology 99
5.2.1. Electrochemistry experiments - $EMIMBF_4$ and ACN mixtures in CDC 800 electrodes 99
5.2.2. Molecular dynamics simulations - $EMIMBF_4$ and ACN mixtures in CDC 800 electrodes 100
5.2.3. PDF analysis- EMIMTFSI in uncharged Ti-CDC 800 and Si-CDC 800 pores 101
5.2.3.1. Experiments *101*
5.2.3.2. MD simulations *101*
5.3. Results and discussion 103
5.3.1. $EMIMBF_4$ and ACN mixtures inside CDC electrodes 103
5.3.1.1. Capacitance *103*
5.3.1.2. Electrolyte compositions and charging mechanism of pores *105*
5.3.1.3. Structure and mobility *108*
5.3.2. $EMIMBF_4$ inside CDC 800 electrodes at 3 V total potential 111
5.3.3. EMIMTFSI structure in disordered pores by PDF analysis 113
5.4. Conclusions 116
Appendix A5 ..... *118*
Appendix B5 ..... *120*
5.5. References 122
6. Influence of Drop Size and Surface Potential on the Contact Angle of Ionic-Liquid Drops 128

6.1. Introduction 129
6.2. Methodology 131
6.3. Results and Discussion 132
6.3.1. Ionic liquid drop size on low-potential graphene sheet 133
6.3.2. Higher sheet interaction potentials 134
6.4. Conclusions 140
Appendix A6 ..... *141*
6.5. References 144
7. Impact of applied potential on the electrowetting of carbon surfaces by highly concentrated electrolytes 149
7.1. Introduction 150
7.2. Methodology 152
7.3. Discussion 154
7.3.1. Drops with ACN solvent on an uncharged surface 154
7.3.2. Electrowetting of pure IL 156
7.3.3. Electrowetting of IL/ACN mixtures 160
7.4. Conclusions 161
Appendix A7 ..... *162*
7.5. References 166
8. Conclusions and Perspectives 170
8.1. Conclusions 170
8.2. Perspectives 172
8.2.1. Potential continuations 172
8.2.2. Future perspectives 172
8.3. References 174

List of Figures

Figure 1-1. Schematic representations of EDL structures according to the (a) Helmholtz model, (b) Gouy-Chapman model, and (c) Gouy-Chapman-Stern model. *H* is the double layer distance described by the Helmholtz model. ψ_s is the potential across the EDL. Reproduced with permission from[26]. Copyright 2011 American Chemical Society. 3

Figure 2-1. All-atom models (top) and coarse-grained equivalents (bottom) for (a) $[BMIM]^+$, (b) $[EMIM]^+$, and (c) $[BF_4]^-$. Reproduced with permission from9. Copyright 2012 American Chemical Society. 11

Figure 2-2. Ion density profiles of RTIL $[BMIM]^+[PF_6]^-$ exhibiting charge overscreening near a planar graphitic electrode with a surface charge density of – 0.112 C m^{-2}. Reproduced from[14] with permission from PCCP Owner Societies. 14

Figure 2-3. (a) Volumetric charge density profiles of counter ions near both negative and positive electrodes along the *z*-direction. (b) Charge densities per unit surface area calculated for 0.1 nm thick slices along the *z*-direction. All charge densities were scaled to the corresponding absolute values of the electrode surface charge density. The arrows indicate the integrals over the first peaks and valleys at each electrode. Reproduced with permission from[36]. Copyright 2008 American Chemical Society. 15

Figure 2-4. Differential capacitance obtained from simulations. The black solid curve is the experimental data for [hmim][Cl] from[37]. Reproduced with permission from[40]. Copyright Elsevier 2010. 16

Figure 2-5. Integral capacitance as a function of electrode potential with varying precision of electrode surface tuning. Reproduced with permission from[51]. Copyright 2012 American Chemical Society. 19

Figure 2-6. Anomalous capacitance behaviour. (a): Differential capacitance per unit surface area as a function of voltage for a few values of pore width (L). (b): Differential capacitance as a function of the pore width for zero electrode polarisation, compared with experimental data from[29] and MFT from.[44] Reproduced from[54] with permission from PCCP Owner Societies. 21

Figure 2-7. Differing ionic composition inside pores as a function of voltage and correlating integral capacitance. Blue circles depict counter-ions, and red circles depict co-ions. Reproduced with permission from[33]. Copyright 2012 American Chemical Society. 22

Figure 2-8. Simulated ion distribution of RTIL $[BMIM]^+[PF_6]^-$ inside electrified pores of a TiCDC-1200 electrode. Blue = C–C bonds, red = $[BMIM]^+$, and green = $[PF_6]^-$. a: Local ion distribution near a positive surface (+ 0.5 V), b: A single anion in a nanotube-like pore positively polarised (+ 0.5 V). c: Local structure near a negative surface (- 0.5 V). Reprinted by permission from Macmillan Publishers Ltd: Nature Materials,[31] copyright 2012. 26

Figure 2-9. Molecular model of a spherical onion-like carbon. Reproduced with permission from[34]. Copyright 2013 American Chemical Society. 28

Figure 2-10. Effect of dispersion forces on differential capacitance as a function surface potential. Reproduced with permission from[80]. Copyright 2010 American Chemical Society. 31

Figure 2-11. Illustration of the filled nanotube forest with periodic boundary conditions. (a): The nanotube model. (b): Cross-sectional configuration perpendicular to the nanotubes, the blue balls depict the $[TEA]^+$ cations, the green balls represent the $[BF_4]^-$ anions, and the stick figures show the PC molecules. Reproduced with permission from[83]. Copyright 2009 American Chemical Society. 33

Figure 2-12. Descriptions of an EDL structure using the CGS framework. (a) Distribution of ions (top panel) and the corresponding space charges (bottom panel) inside an EDL near an electrode with a surface charge density of *q*. An EDL is divided into N layers: the zeroth layer balances the electrode charge, and all other layers consist of a counter-ion sub-layer and a co-ion sub-layer. All EDL layers except the zeroth layer carry zero net charge and are thus considered as "generalised solvents." (b) A description of the effective space charge layers inside an EDL focusing on the change of space charge as the surface charge density of the electrode changes from zero to *q*. Reproduced from[85]. with permission from PCCP Owner Societies. 34

Figure 2-13. Two-dimensional schematic of simulation box with yellow Na^+ ions, green Cl^- ions, red and white water molecules, black neutral carbons, blue positively charged carbons, and purple negatively charged carbons. Reproduced with permission from[99]. Copyright 2013 American Chemical Society. 39

Figure 3-1:All-atom and coarse-grained equivalent of $EMIM^+$ (a) and BF_4^- (b). 57

Figure 3-2: Empty electrode models used for Ti-CDC 800 (a) and Si-CDC 800 (b). 58

Figure 3-3: Bulk density of $EMIMBF_4$ and ACN mixtures at 340 K and 1 bar. The experimental data is at 323 K and atmospheric pressure. 59

Figure 3-4: a: Mean square displacements for diffusion calculations, solid lines are the BF_4^- anions dashed lines are the $EMIM^+$ cations. b: Self-diffusion coefficients for the two ionic species. 60

Figure 3-5:RDFs of ionic species. BF_4-BF_4 (a), EMIM-EMIM (b), BF_4-EMIM (c). 61

Figure 3-6:RDFs of ion-ACN. BF_4-ACN (a), EMIM-ACN (b). 62

Figure 3-7: Snapshot of the planar electrode simulation, the positive and negative electrodes were set to ± 0.10 C m^{-2}. Colour scheme: purple molecules are BF_4^- anions; blue molecules are $BMIM^+$ cations; the red sheet is the positive electrode; the black sheet is the negative electrode; green sheets have neutral charge. 62

Figure 3-8: Potential profiles for varying surface charges from integration of Equation (3-5). 63

Figure 3-9: Electrode charge (a) and integral capacitance (b) across the range of calculated potentials from Equation (3-5). 65

Figure 3-10: Ionic conductivity of the coarse grained $EMIMBF_4$ model used, compared with the all-atom model from ref 39. 66

Figure 3-11: Liquid vapour surface tension at 298 K 67

Figure 4-1: Snapshot of three-dimensional periodic system. Electrolyte is 40 % ACN, blue molecules are $BMIM^+$ cations, purple are BF_4^- anions, bright green are ACN. Red molecules are the positive electrode, black are the negative, and pale green are uncharged sheets. 74

Figure 4-2: Snapshot of two-dimensional periodic system. Electrolyte is 40 % ACN, blue molecules are $EMIM^+$ cations, purple are BF_4^- anions, bright green are ACN. Pale green molecules are the uncharged electrodes with positive on the left and negative on the right. The gold molecules are uncharged wall molecules that keep the bulk electrolyte within the simulation bounds. 76

Figure 4-3: Temperature influence on electrode composition. Pure $BMIMBF_4$ is shown in the positive (a) electrode and negative electrode (b), 50 % mass ACN mixture is shown in the positive electrode (c) and negative electrode (d). 79

Figure 4-4: Counter-ion number density profile for Pure $BMIMBF_4$, positive electrode (a) and negative electrode (b). 40 % mass ACN mixture positive electrode (c) and negative electrode (d). 80

Figure 4-5: Influence of ACN on the ionic composition inside the positive electrode (a) and negative electrode (b) at 298 K for the range of carbon charges simulated. Solid lines indicate counter-ions and dashed lines indicate co-ions. 81

Figure 4-6: Influence of constant electrode charge on the ionic composition inside the positive electrode (a) and negative electrode (b) at 298 K. Solid lines indicate counter-ions and dashed lines indicate co-ions. 81

Figure 4-7: Electrode charge storage efficiency via the difference between number of counter-ions and co-ions. Solid lines indicate counter-ions and dashed lines indicate co-ions. Non-zero PZC charge as the neutral pore favours the anion slightly. 82

Figure 4-8: Positive electrode charging curve at 1 V (a) and 3 V (b). The y-axes are shown on different scales to improve readability. 83

Figure 4-9: Integral areal capacitance calculated from the positive electrode charge. 84

Figure 4-10: (a) Ionic layering occurring in the bulk adjacent to the entrance of the electrodes, for pure $EMIMBF_4$ at 1 V potential. (b) Comparison of the $EMIMBF_4$ layering profiles in the bulk for the different systems simulated. 1 V wall refers to the simulation where the wall atoms facing the surface of the bulk were also included as electrode atoms. 85

Figure 4-11: Ionic layering occurring in the bulk adjacent to the entrance of the electrodes for systems with 15 % mass ACN (a) and 40 % mass ACN (b). 86

Figure 4-12: Number of ions inside the left (a) and right (b) electrode at 1 V total potential, with the equivalent 3 V total potential results given in c and d. The number of ion pairs at zero potential is given as the solid green line, and the difference between counter- and co-ions, which indicates the maximum amount of charge that can be accumulated in the electrode, is shown as the dotted black line. 87

Figure 4-13: Charging mechanism parameter for 1 V (a) and 3 V (b) total system potential. 88

Figure A4-14: Two dimensional number density heat-maps of the centre of mass atoms for the anion (a) and cation (b). The heat maps were produced in Python 2.7.10, using the MDAnalysis toolkit.[29-30] The bin size in the x and z dimensions were set to 0.05 nm. The system shown is pure $BMIMBF_4$ at 323 K where the electrodes were held at ± 0.10 C m^{-2}. 90

Figure A4-15: Positive electrode charging curve at 1 V for the pure $EMIMBF_4$ simulations. Uncharged walls refers to the original 323 K simulation, the 600 K simulation is also with uncharged walls, and the charged walls simulation is at 323 K. 91

Figure 5-1: Simulation cell of an $EMIMBF_4$ and 67 % mass ACN electrolyte mixture wetting uncharged disordered porous Ti-CDC800 electrodes. Colour scheme; blue: 3-site $EMIM^+$ molecules, purple: single-site BF_4^- molecules, green: 3-site ACN molecules, silver: carbon electrode atoms. Gold molecules cap the cell in the z-dimension, as this is non-periodic. 99

Figure 5-2: Cyclic voltammograms of supercapacitor cells assembled with two electrodes based on 0.77 nm average pore size carbide-derived carbons (CDC), in electrolytes composed of $EMIMBF_4$ mixed with ACN at several mass fractions. The potential scan rate is 5 mV s^{-1}. 103

Figure 5-3: Electrolyte composition inside the electrodes. Light green: uncharged CDC electrodes; Orange/Blue: electrodes held at a constant potential difference of 1 V. Dark green: difference between the counter-ions and the co-ions numbers for the 1 V simulation. 105

Figure 5-4: Variation of the charging mechanism parameter with the ACN mass fraction for the positive and negative electrodes. 107

Figure 5-5: Counter-ion distance from the internal surface of the electrodes 108

Figure 5-6: Co-ion distance from the internal surface of the electrodes 109

Figure 5-7: Mean squared displacement of BF_4^- counter-ions inside the positive electrode (a), and diffusion coefficients of all molecular species inside both electrodes (b). 110

Figure 5-8: Electrode charging rate of 1.5 mol L^{-1} $EMIMBF_4$ in ACN at 1 V 111

Figure 5-9: Distance from the internal surface of the electrodes for counter- and co-ions, 1 V counter-ion result also included 113

Figure 5-10: (a): PDF of bulk EMIMTFSI at room temperature from experiment and MD simulation. (b): PDF of empty Si-CDC 800 from experiment and empty Ti-CDC 800 from simulation. (c): PDF of empty Si-CDC 800 from experiment and empty Si-CDC 800 from simulation. 115

Figure 5-11: (a): PDF of EMIMTFSI inside Si-CDC 800 from experiment and Ti-CDC 800 from simulation. (b): PDF of EMIMTFSI inside Si-CDC 800 from experiment and Si-CDC 800 from simulation. 116

Figure A5-12: Electrode charging rate at 3 V. Here two fitting functions have been provided, a mono- and bi-exponential fit. 118

Figure A5-13: Temperature rise due to the Joule effect at application of 3 V total potential. 119

Figure B5-14: Simulation snapshot during equilibration before pore filling. Empty CDC is displayed on the left, and pressurised EMIM-TFSI on the right. The simulation was capped by immobile wall atoms in the non-periodic dimension. 120

Figure B5-15 3D periodic filled CDC pore used for MD production runs. 120

Figure B5-16: (a): Isolated PDF for the pure IL in bulk and Ti-CDC 800 confined-simulations. (b-d): Partial RDFs from MD simulation (multiplied by r^3) for atomic pairs in bulk RTIL, Ti-CDC 800 pores, and Si-CDC 800 pores. (b) H-H pairs for cation-cation interaction. (c) F-F pairs for anion-anion interaction. (d) F-H pairs for anion-cation interaction. 121

Figure 6-1: Two dimensional number (a) and atomic (b) density contours of a drop consisting of 100 EMIM-BF_4 pairs on a surface with low a low interaction potential. The outer layer is fitted with a polynomial, to calculate the contact angle at z_θ^* = 1. Here the coordinates are reduced by 0.34 nm.....131

Figure 6-2: Fractional number density profiles for drop size of 500 IL pairs. Symbols correspond to EMIM cations, and lines to BF_4 anions. A bin depth 0.01 nm was used in the z dimension.....133

Figure 6-3: Solid-fluid interaction energy per IL pair to show the time required to reach equilibrium for increasing carbon interaction potential with drops of 200 pairs (a) and 500 pairs (b). Solid lines depict EMIM cations and broken lines BF_4 anions.....134

Figure 6-4: Contact angle as a function of time at a sheet interaction potential of 0.15 kJ mol^{-1}. ..135

Figure 6-5: Contact angle at various interaction potentials for drops of 100, 200, and 500 IL pairs. The circled systems were considered to be fully wetting, with the filled symbols representing uniform adsorbed structures and unfilled symbols representing non-uniform adsorbed structures.136

Figure 6-6: a: side view of uniform wetting state for the 100 IL pair simulation with an interaction energy of ε = 0.10 kJ mol^{-1}. b: top view of non-uniform wetting state for the 500 IL pair simulation with an interaction energy of ε = 0.23 kJ mol^{-1}. EMIM cations are represented as the blue beads, and BF_4 anions as the purple beads.....137

Figure 6-7: a: 200 IL pairs simulated at 400 K on a sheet with ε = 0.23 kJ mol^{-1}. b and c: Single adsorbed layer film of 200 IL pairs on a large sheet with ε = 0.23 (b) and 0.05 kJ mol^{-1} (c). Top panes show the initial simulation configurations and bottom the final.....139

Figure A6-8: Fractional number density profiles for drops of increasing sizes. Symbols correspond to $EMIM^+$ cations, and lines to BF_4^- anions.....142

Figure A6-9: Contact angle as a function of time at a sheet interaction potential of 0.23 kJ mol^{-1}.143

Figure A6-10: Left: top view snapshot of the 0.60x standard simulation, blue = EMIM cations, purple = BF_4 anions. Centre: corresponding number density contours. Right: corresponding atomic density contours. 143

Figure 7-1: Simulation snapshot of an EMIM-BF_4 and ACN drop (20 % mass ACN) on the surface of the positive electrode. Green molecules are BF_4^- anions, red molecules are $EMIM^+$ cations, and blue molecules are ACN solvent. The IL and electrode atoms are shown with a colour scale (right) where positive charges are red and negative charges are green. It can be seen that the electrode

accumulates charge directly beneath the drop, and the remaining atoms have close to neutral charges. A section of the negative electrode is also shown for perspective. 152

Figure 7-2: Contact angle with increasing ACN fraction in the drops. Zero percent refers to pure $EMIMBF_4$. The Blue diamonds are the contact angles as measured at z_θ^* = 1, where the coordinates are reduced by 0.34 nm. The red squares are the predicted contact angles for the mixtures by mass weighted averages of the pure systems' contact angles. Uncertainties are one standard deviation of the mean, this is repeated in the subsequent figures. 155

Figure 7-3: Electrowetting contact angle of pure IL drop measured at z_θ^* = 1. The potential on the x-axis refers to total cell voltage, for positive (negative) values the drop is adsorbed to the surface of the positive (negative) electrode. The blue squares indicate simulations performed under constant electrode potential, and the red stars are the result for equivalent constant-charge simulations at that voltage.....156

Figure 7-4: Electrode charge histogram of the final nanosecond of simulation for drops adsorbed onto the positive electrode (a) and negative electrode (b). The histograms have been plotted on a log scale, in this way the number of carbons contributing to balancing the drop charge can be more easily seen. The electrode atom charges were sampled every 2 ps.....157

Figure 7-5: Fractional number density profiles for a pure IL drop adsorbed onto the positive (blue) and negative (red) electrode. (a) ± 2 V, (b) ± 3 V, (c) ± 4 V, (d) ± 5 V. Solid lines depict the counter-ions, and dotted lines the co-ions. Densities were calculated from the final nanosecond of production runs using the centre of mass of the ions and a bin depth of 0.023 nm.....159

Figure 7-6: (a) Electrowetting contact angle on the positive electrode (total potential is 4 V, zero charge contact angles from Figure 7-2 are given as the red diamonds for reference). Zero percent refers to pure $EMIMBF_4$. The blue squares are the contact angles measured at z_θ^* = 1. (b) Charge density profile of 4 V drops, 20 % mass ACN omitted for brevity. 160

Figure A7-7: Fractional number density profiles of the molecule type in the drop. Solid lines are $EMIM^+$ cations, dotted lines are BF_4^- anions, and triangles are ACN molecules.....162

Figure A7-8: Fractional number density profiles of the ion type in the drop, with ACN excluded. Solid lines are $EMIM^+$ cations, dotted lines are BF_4^- anions.....162

Figure A7-9: Contact angle with increasing ACN fraction in the drops. Zero percent refers to pure $EMIMBF_4$. The Blue diamonds are the contact angles as measured at the sheet surface. The red squares are the predicted contact angles for the mixtures by mass weighted averages of the pure systems' contact angles.....163

Figure A7-10: Electrowetting contact angle of pure IL drop. The blue squares are the contact angles measured at the sheet surface, and the red diamonds are at z_θ^* = 2. 163

Figure A7-11: Finite size of simulation indicates the maximum applied potential (or electric field strength) which can be used in our systems. The charge on each electrode is shown, (a) positive and (b) negative. 164

Figure A7-12: Electrode charge curve. The black line gives the average charge of the electrode atoms over the voltage range simulated. Constant charge values simulated are also included to indicate the equivalent constant potential voltage. 164

Figure A7-13: Electrode charge histogram of the final ns for the ± 2 V total simulations (a), ± 3 V total simulations (b), ± 4 V total simulations (c), and ± 5 V total simulations (d), with the pure IL drop adsorbed onto the positive and negative electrode. The simulations with the drops adsorbed onto the negative electrodes have been mirrored on the x-axis so that the charges can be compared. 165

Figure A7-14: Electrowetting contact angle on the positive electrode (total potential is 4 V). Zero percent refers to pure $EMIMBF_4$. The blue squares are the contact angles measured at the sheet surface, and the red diamonds at z_θ^* = 2.....166

List of Tables

Table 3-1: Number of RTIL and ACN molecules for each bulk system studied. 59

Table 3-2: Electrode and total potentials calculated from Equation (3-5). 64

Table 4-1: Molecular composition of $BMIMBF_4$ and ACN mixtures. 75

Table 4-2: Constant charge values used for the electrodes. 75

Table 4-3: Molecular composition of $EMIMBF_4$ and ACN mixtures 77

Table A4-4: Ionic composition inside the electrodes, and the charging mechanism parameters, for the additional pure $EMIMBF_4$ 1V simulations 91

Table 5-1: Electrolyte compositions 100

Table 5-2: Summary of the experimental and simulated capacitances. The experimental data is obtained from CV by integration of the electric current during the discharge of the cell at a scan rate of 5 mV s^{-1}. The MD simulation data is extracted from the charge accumulated at the surface of the electrodes for an applied voltage of 1 V. 103

Table 5-3: Electrolyte composition inside the pores and charge storage properties 112

Table 6-1: Contact angle as function of drop size at the sheet surface ($z_\theta^* = 0$) and a height above the sheet of ($z_\theta^* = 1$). Uncertainties are from splitting the 5 ns simulation into 1 ns blocks. 134

Table A6-2: Number of ion pairs, sheet dimensions and number of carbon atoms for all simulation systems. 141

Table 7-1. Number of IL pairs and solvent molecules, with the IL concentration 153

List of Abbreviations used in this thesis

Cl^- = Chloride

$[NO_3]^-$ = nitrate

$[BF_4]^-$ = tetrafluoroborate

$[PF_6]^-$ = hexafluorophosphate

$[FSI]^-$ = bis(fluorosulfonyl)imide

$[TFSI]^-$/$TFSI^-$/TFSI = bis(trifluoromethane)sulfonyl imide

Na^+ = Sodium

Li^+ = Lithium

Ca^{2+} = Calcium

K^+ = Potassium

Cs^+ = Caesium

$[TEA]^+$ = Tetraethylammonium

$[DMIM]^+$ = 1,3-dimethylimidazolium

$[EMIM]^+$/$EMIM^+$/EMIM = 1-ethyl-3-methylimidazolium

$[BMIM]^+$/$BMIM^+$/BMIM = 1-butyl-3-methylimidazolium

$[OMIM]^+$ = 1-octyl-3-methylimidazolium

$[C_nmim]^+$ = 1-alkyl-3-methyimidazolium

$[pyr_{13}]^+$ = N-methyl-N-propylpyrrolidinium

ACN = Acetonitrile

CDC = Carbide-derived carbon

CGS = Counter-charge layer in generalised solvents

CNT = Carbon nanotube

c-DFT = Classical density functional theory

q-DFT = Quantum density functional theory

EDL = Electric double-layer

EDLC = Electric double-layer capacitor

EDCC = Electric double-cylinder capacitor

EMLC = Electric multiple charge-layer capacitor

EWCC = Electric wire-in-cylinder capacitor

ESR = Equivalent series resistance

MC = Monte Carlo

MD = Molecular dynamics

MFT = Mean field theory

MILO = Multiple ion layers with overscreening

OLC = Onion-like carbon

PC = Propylene carbonate

RTIL = Room temperature ionic liquid

PSD = Pore size distribution

PZC = Point of zero charge

RMC = Reverse Monte Carlo

Ti = Titanium

Si = Silicon

1BM = One-bead model

2BM = Two-bead model

wt =Weight

pbc = periodic boundary conditions

YLE = Young-Lippmann Equation

IC = Integral capacitance

DC = Differential capacitance

1. Introduction

1.1. Background

1.1.1. EDLC applications and significance

Electric double-layer capacitors (EDLCs), are energy storage devices that store energy due to charge accumulation in the electric double layer (EDL).[1] Recently, the development of EDLCs has been moving rapidly in response to the increasing demand for energy storage technologies for new applications, such as renewable energy,[2] electrical and hybrid vehicles,[3] and smart grid management.[4-5]

The most prominent feature of EDLCs is their power density, in the order of 15 kW/kg, which is significantly higher than that of batteries, in the order of 1 kW/kg.[1] EDLCs also have a long cycle life, in the order of millions of cycles, compared to batteries which have a lifetime of only several thousand cycles.[1] Another advantage of EDLCs is a wide range of operating temperatures.[6] However, the energy densities of EDLCs are significantly lower than batteries, resulting in much higher costs per unit of energy stored. Improving the costs per unit of energy stored of EDLCs is the primary motivation for the recent increase in research of EDLCs and their materials.

EDLCs are currently used in high power demand applications for power buffering, power saving, and energy recovery.[5, 7-9] One of the main future applications of EDLCs is in the transport industry, for use in personal vehicles, trucks,[3] buses,[10] and trains;[11] to start engines, deliver energy quickly for acceleration,[3] provide energy for electrical power steering,[3] and to store energy from regenerative braking.[11] Further areas where EDLCs can also play an important role are in portable and flexible electronic devices,[12] memory backup,[6] and energy harvesting.[6, 8]

1.1.2. Configurations of EDLCs

An EDLC consists of two electrodes, an electrolyte, a separator that prevents the two electrodes from forming a short circuit, and two current collectors connected to the electrodes. The electrodes are porous with a high specific surface area for maximising the charge density in the EDL. A good electrode material should maximise the specific energy density whilst maintaining high power density, be cost-effective, safe to handle, and easy to produce. The most commonly used electrode in industry is activated carbon.

The electrolytes that are used for EDLCs can be aqueous solutions, electrolytes in organic solvents, or room temperature ionic liquids (RTILs). The aqueous electrolyte solution has a relatively low

equivalent series resistance (ESR) and a high relative permittivity. The main limitation of aqueous electrolytes solutions is low operating voltage of around 1 V, beyond which electrolysis of water occurs. This low operating voltage significantly limits the energy density of the EDLC. Organic solvent based electrolytes can be operated at voltages much higher than aqueous solutions, commonly around 2.5 V, thus offering higher electrocapacitive performance. Most organic solvent based electrolyte EDLCs use fluorinated salts solubilised in acetonitrile (ACN) or propylene carbonate (PC) solvent.[6] RTILs are being considered as a promising electrolyte due to their even wider operating voltage window[13] than the organic solvent based electrolyte, leading to a very high energy density.[5, 14-15] RTILs also have low toxicity,[16] as well as high thermal stability[17] and low volatility,[18-19] which both contribute to a wide operating temperature window. However RTILs have poor conductivity and viscosity, often they are only efficient at low current densities, but this can be improved by mixing with ACN.[20-21]

1.1.3. EDL modelling

With a positively charged electrode as an example, Figure 1-1 schematically shows model EDL structures. Helmholtz first proposed the EDL structure as illustrated in Figure 1-1(a).[22] Helmholtz stated that two layers of opposite charge formed at the electrode/electrolyte interface and were separated by small distance, *H*. The structure of the Helmholtz model is analogous to that of conventional dielectric capacitors where two planar parallel electrodes are separated by a dielectric. The Helmholtz model was respectively modified by Gouy in 1910[23] and Chapman in 1913[24] to account for the fact that ions are mobile in the electrolyte solvent. As illustrated in Figure 1-1(b), instead of closely packed ions near the electrode surface, the ions with an opposite sign to that of the electrode are distributed in a region of thickness much larger than *H*. In 1924, Stern[25] combined the Helmholtz model with the Gouy-Chapman model to explicitly account for the two different regions of charge – namely the Stern layer and the diffuse layer, as shown in Figure 1-1(c). This Gouy-Chapman-Stern EDL theory has been widely adopted in the modelling of EDLCs.

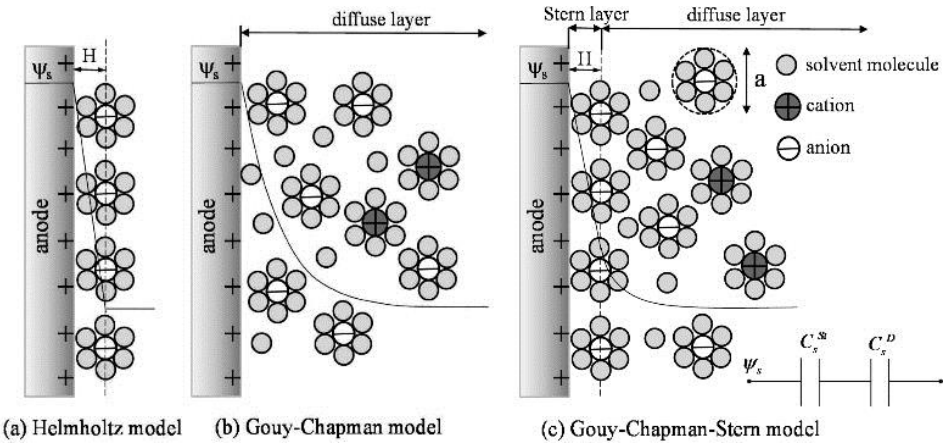

Figure 1-1. Schematic representations of EDL structures according to the (a) Helmholtz model, (b) Gouy-Chapman model, and (c) Gouy-Chapman-Stern model. *H* is the double layer distance described by the Helmholtz model. ψ_s is the potential across the EDL. Reproduced with permission from[26]. Copyright 2011 American Chemical Society.

There are two important parameters characterising the performance of an EDLC cell, namely energy density, *E* (in Watt hours per unit mass or volume), and power density, *P* (in Watts per unit mass or volume), which are respectively defined as,

$$E = \frac{1}{2} C_T V^2 \tag{1-1}$$

$$P = \frac{V^2}{4R} \tag{1-2}$$

where *V* (in Volt) is the operating voltage, C_T (in F) is the total capacitance of the cell, and *R* (in Ω) is the equivalent series resistance (ESR). It therefore follows that to increase the energy density of the EDLC, one can increase C_T and/or *V*. The former is determined by the electrode and electrolyte combination while the latter is limited by only the electrolyte. ESR is determined by a number of things, including the electrical conductivity of the electrolyte, electrode, binder, and current collector; as well as the separator.

EDLCs have a relatively high power density because the mechanism of energy storage and release involves merely charge adsorption and desorption, which leads to low ESR.[1] However, EDLCs have a relatively low energy density. As *V* is given for an electrolyte, the only option left to increase *E* is to increase C_T. In the search for maximising C_T, the configurations of devices (and their storage mechanisms) have become increasingly complicated. Modern EDLCs contain disordered electrodes with high curvature; and dense electrolyte solutions, this deviates significantly from GCS stern theory, which is no longer directly applicable for modelling.

Furthermore, there are still significant areas where various EDL phenomena are not well understood. Examples include the influence of specific adsorption of ions to the electrode surface,[27-30] and the electrokinetic and transport phenomena involving solvated ions in nanopores of varying geometries and sizes.[14, 31] Chmiola *et al.*[31] conducted an experiment using carbide-derived carbon (CDC) electrodes with a narrow pore size distribution (PSD) and pore diameters less than 1 nm, and a $[TEA]^+[BF_4]^-$ electrolyte in AN. The experiment produced very high capacitance for an electrode with a pore diameter of about 0.7 nm, with volumetric energy twice as high as those of activated carbon electrodes. The observed anomalous capacitance behaviour was also observed in a follow up experiment using RTILs as the electrolyte[14] and challenged the long held belief that small pores were inaccessible to solvated ions. This has stimulated a lot of interest in electrodes with pore sizes of less than 1 nm.

Atomistic modelling methods such as molecular dynamics (MD) simulations can be employed to understand the behaviour of EDLCs with complex nanoporous electrodes or dense electrolytes with solvation effects. Molecular investigation is critical, as understanding both the key mechanisms that occur within EDLCs, and the influence of different parametrisation, is crucial in detangling confusing or contradictory results. It is clear that molecular modelling has a key role to play to support effective predictive theories can be made for modern EDLCs and consistent gains in device optimisations can be made.

1.2. Scope and Objectives

In this thesis we use MD simulation to study charge storage mechanisms and ionic structure for electrode-electrolyte interfaces under a variety of configurations. Experimental measurements have been performed where possible and appropriate, such that comparisons and analyses can be made. The aim is to further increase fundamental understanding of behaviour and processes important to design and performance predictions of EDLCs.

On the electrolyte side we focus specifically on imidazolium RTILs (which have great potential for future use) and their mixtures with ACN, to examine if there are significant performance benefits to highly concentrated or dilute ions. As stated previously RTIL/ACN mixtures have trade-offs with different performance metrics, such as capacitance, energy-density, cost, toxicity, lifetime, etc.; however the influence of ACN over a range of concentrations is not well characterised, and often studies are limited to either very high or very low ion concentrations. Furthermore, the structure of RTIL/ACN mixtures inside nanopores has also not been studied to a great extent.

On the electrode side we model both ordered and disordered porous (and non-porous) carbon structures to track the influence of shape and confinement effects on the interfacial electrolyte

composition. To this end; planar, slit-nanopore, and carbide-derived carbons have been modelled under a variety of conditions.

With novel combinations of electrolyte and electrode systems, we can gain important insights into the rich interfacial behaviour that occurs on the molecular scale, and help lay the groundwork for experimentalists to build upon.

To summarise, the key objectives are:

- Compare and contrast the charge storage mechanisms of RTILs in sub-nanometre slit-pore and CDC electrodes, with solvent effects, such that a more comprehensive understanding can be established.
- Analyse the adsorbed structure of RTILs inside CDC pores to better understand electrostatic screening effects of electrodes.
- Determine the contact angle dependency of RTIL drops in heterogeneous solid-liquid-vapour systems on drop size, surface interaction potential, and electric potential, with solvent effects.

1.3. Thesis structure and development

This thesis has been structured into eight chapters, three of which comprise of material based on peer-reviewed publications achieved throughout my PhD candidature. The structure has been arranged into a logical sequence which is briefly outlined below:

Chapter 1 Introduction

This chapter introduces the significance of EDLCs and their applications. The common material components are given and traditional modelling approaches are explained. The aim and scope of the thesis is outlined, as well as the motivation for the methodology selection. A global structure is given on a by chapter basis.

Chapter 2 Literature Review

In this chapter a comprehensive introduction to molecular modelling of EDLCs is given, and recent and relevant articles are discussed. The limitations of the relevant studies addressed are discussed, and the motivations for the research performed in this project are further clarified as a result.

Chapter 3 Methodology

In this chapter, the principles of MD simulation are presented, and where MD sits among other modelling types is also discussed. The benefits and limitations relevant to this topic are also discussed. Details of generic simulation conditions used in our research is also provided as an

overview to help understand the configurations used in subsequent chapters. Finally, some model validation results are shown using bulk and simplified EDLC systems

Chapter 4 Structure and capacitance of ionic-liquid and acetonitrile mixtures inside slit-pore carbon electrodes

Chapter 4 examines charge storage mechanisms in slit-pore electrodes with pore diameter of less than 1 nm. Temperature, charge, ACN concentration are all studied under constant electrode charge, and capacitance and dynamics are studied under constant electrode potential. As this pore type is ordered and has strong confinement effects, it establishes a basis for comparison with electrode materials derived from realistic disordered structure used in the following chapter.

Chapter 5 Molecular structure and capacitance properties of imidazolium ionic liquid and acetonitrile mixtures inside disordered porous carbon electrodes

Chapter 5 provides a comprehensive analysis of capacitance, structure, and dynamics of RITL/ACN mixtures inside CDC electrodes at constant potential. The difference in structure at higher electric potential is also explored, as wells as a pair distribution function (PDF) study of an RTIL in uncharged pores. Results here are accompanied by experimental measurement.

Chapter 6 Influence of drop size and surface potential on the contact angle of RTIL drops

In this chapter RTIL drops are studied at a planar graphene surface with various interaction potentials. The drop size is varied and structures are discussed in terms of their solid-vapour-liquid contact angle. Non-equilibrium structures are explored over a range of conditions.

Chapter 7 Impact of applied potential on the electrowetting of carbon surfaces by highly concentrated electrolytes

Following Chapter 6, the influence of electric potential and ACN concentration was also examined for RTIL drops on a weakly interacting graphene sheet. The electric potential is varied over moderate range and compared with experimental results and recent constant charge simulations. Drop structure and electrode charge storage is analysed.

Chapter 8 Conclusions and perspectives

Chapter 8 summarises the important contributions made to the field during the period of this thesis. Future perspectives and suggestions for improved or new areas of study are also discussed.

1.4. References

1. Conway, B., *Electrochemical Supercapacitors: Scientific Fundamentals and Technological Applications*; Kluwer Academic/Plenum. New York, 1999.
2. Gogotsi, Y.; Simon, P., True Performance Metrics in Electrochemical Energy Storage. *Science Magazine* **2011**, *334*, 917-918.
3. Faggioli, E.; Rena, P.; Danel, V.; Andrieu, X.; Mallant, R.; Kahlen, H., Supercapacitors for the Energy Management of Electric Vehicles. *J. Power Sources* **1999**, *84*, 261-269.
4. Dunn, B.; Kamath, H.; Tarascon, J.-M., Electrical Energy Storage for the Grid: A Battery of Choices. *Science* **2011**, *334*, 928-935.
5. Simon, P.; Gogotsi, Y., Materials for Electrochemical Capacitors. *Nat. Mater.* **2008**, *7*, 845-854.
6. Simon, P.; Gogotsi, Y., Charge Storage Mechanism in Nanoporous Carbons and Its Consequence for Electrical Double Layer Capacitors. *Phil. Trans. R. Soc. A* **2010**, *368*, 3457-3467.
7. Kötz, R.; Carlen, M., Principles and Applications of Electrochemical Capacitors. *Electrochim. Acta* **2000**, *45*, 2483-2498.
8. Miller, J. R.; Burke, A. F., Electrochemical Capacitors: Challenges and Opportunities for Real-World Applications. *Electrochem. Soc. Interface* **2008**, *17*, 53-57.
9. Simon, P.; Burke, A., Nanostructured Carbons: Double-Layer Capacitance and More. *Electrochem. Soc. Interface* **2008**, *17*, 38-43.
10. Furubayashi, M.; Ushio, Y.; Okumura, E.; Takeda, T.; Andou, D.; Shibya, H. In *Application of High Power Super Capacitors to an Idling Stop System for City Buses*, Proceedings of the 18th International Electric, Fuel Cell and Hybrid Vehicles Symposium, 2001.
11. Bombardier Mitrac Energy Saving System. http://www.bombardier.com/content/dam/Websites/bombardiercom/supporting-documents/BT/Bombardier-Transportation-ECO4-EnerGstor-EN.pdf.
12. El-Kady, M. F.; Kaner, R. B., Scalable Fabrication of High-Power Graphene Micro-Supercapacitors for Flexible and on-Chip Energy Storage. *Nature Communications* **2013**, *4*, 1475-1483.
13. Rogers, E. I.; Sljukić, B.; Hardacre, C.; Compton, R. G., Electrochemistry in Room-Temperature Ionic Liquids: Potential Windows at Mercury Electrodes. *J. Chem. Eng. Data* **2009**, *54*, 2049-2053.
14. Largeot, C.; Portet, C.; Chmiola, J.; Taberna, P.-L.; Gogotsi, Y.; Simon, P., Relation between the Ion Size and Pore Size for an Electric Double-Layer Capacitor. *J. Am. Chem. Soc.* **2008**, *130*, 2730-2731.

15. Merlet, C.; Rotenberg, B.; Madden, P. A.; Taberna, P.-L.; Simon, P.; Gogotsi, Y.; Salanne, M., On the Molecular Origin of Supercapacitance in Nanoporous Carbon Electrodes. *Nat. Mater.* **2012**, *11*, 306-310.

16. Buzzeo, M. C.; Evans, R. G.; Compton, R. G., Non-Haloaluminate Room-Temperature Ionic Liquids in Electrochemistry—a Review. *ChemPhysChem* **2004**, *5*, 1106-1120.

17. Huddleston, J. G.; Visser, A. E.; Reichert, W. M.; Willauer, H. D.; Broker, G. A.; Rogers, R. D., Characterization and Comparison of Hydrophilic and Hydrophobic Room Temperature Ionic Liquids Incorporating the Imidazolium Cation. *Green Chem.* **2001**, *3*, 156-164.

18. Aparicio, S.; Atilhan, M.; Karadas, F., Thermophysical Properties of Pure Ionic Liquids: Review of Present Situation. *Ind. Eng. Chem. Res.* **2010**, *49*, 9580-9595.

19. de Lemos, L. R.; Santos, I. J. B.; Rodrigues, G. D.; Ferreira, G. M. D.; da Silva, L. H. M.; da Silva, M. d. C. H.; de Carvalho, R. M. M., Phase Compositions of Aqueous Two-Phase Systems Formed by L35 and Salts at Different Temperatures. *J. Chem. Eng. Data* **2009**, *55*, 1193-1199.

20. Feng, G.; Huang, J.; Sumpter, B. G.; Meunier, V.; Qiao, R., A "Counter-Charge Layer in Generalized Solvents" Framework for Electrical Double Layers in Neat and Hybrid Ionic Liquid Electrolytes. *Phys. Chem. Chem. Phys.* **2011**, *13*, 14724-14735.

21. Lin, R.; Huang, P.; Ségalini, J.; Largeot, C.; Taberna, P. L.; Chmiola, J.; Gogotsi, Y.; Simon, P., Solvent Effect on the Ion Adsorption from Ionic Liquid Electrolyte into Sub-Nanometer Carbon Pores. *Electrochim. Acta* **2009**, *54*, 7025-7032.

22. von Helmholtz, H., On the Laws of the Distribution of Electrical Currents in Material Conductors with Application to Experiments in Animal Electricity. *Ann. Phys. Paris* **1879**, *243*, 337-382.

23. Gouy, L. G., Constitution of the Electric Charge at the Surface of an Electrolyte. *Compt. rend.* **1910**, *149*, 654-660.

24. Chapman, D. L., Li. A Contribution to the Theory of Electrocapillarity. *London, Edinburgh, and Dublin Philosophical Magazine and Journal of Science* **1913**, *25*, 475-481.

25. Stern, O., The Theory of the Electrolytic Double-Layer. *Z. Elektrochem. Angew. Phys. Chem.* **1924**, *30*, 508-523.

26. Wang, H.; Pilon, L., Accurate Simulations of Electric Double Layer Capacitance of Ultramicroelectrodes. *J. Phys. Chem. C* **2011**, *115*, 16711-16719.

27. Krylov, V. S., Theory of the Electric Double Layer with a Discrete Structure of the Specifically Adsorbed Charge. *Electrochim. Acta* **1964**, *9*, 1247-1258.

28. Lauw, Y.; Horne, M. D.; Rodopoulos, T.; Nelson, A.; Leermakers, F. A. M., Electrical Double-Layer Capacitance in Room Temperature Ionic Liquids: Ion-Size and Specific Adsorption Effects. *J. Phys. Chem. B* **2010**, *114*, 11149-11154.

29. Levi, M. D.; Sigalov, S.; Salitra, G.; Aurbach, D.; Maier, J., The Effect of Specific Adsorption of Cations and Their Size on the Charge-Compensation Mechanism in Carbon Micropores: The Role of Anion Desorption. *ChemPhysChem* **2011**, *12*, 854-862.

30. Uchida, H.; Ikeda, N.; Watanabe, M., Electrochemical Quartz Crystal Microbalance Study of Copper Adatoms on Gold Electrodes Part Ii. Further Discussion on the Specific Adsorption of Anions from Solutions of Perchloric and Sulfuric Acid. *J. Electroanal. Chem.* **1997**, *424*, 5-12.

31. Chmiola, J.; Yushin, G.; Gogotsi, Y.; Portet, C.; Simon, P.; Taberna, P.-L., Anomalous Increase in Carbon Capacitance at Pore Sizes Less Than 1 Nanometer. *Science* **2006**, *313*, 1760-1763.

2. Literature Review

2.1. Modelling techniques

Molecular modelling can provide an atomistic level understanding of both equilibrium and dynamic phenomena occurring in an EDLC. The accuracy of molecular modelling depends largely on the validity of the force fields used to describe molecular interactions in the fluid phase and the geometry and force fields of the model electrode. Monte Carlo (MC) and molecular dynamics (MD) are the two most favoured molecular simulation techniques.[1-2]

MC is based on statistical mechanics and uses importance sampling to sample the phase space of a molecular system. The properties of the system are averaged over a large number of sampling steps to give ensemble averages which can be correlated to calculate thermodynamic and equilibrium structural properties. With this statistical mechanical basis, MC simulations are limited to calculating equilibrium properties.

MD simulations solve Newton's equations of motion for a many bodied molecular system over a short period of simulated time. The properties of the molecular system are averaged over this time to calculate the properties of the system. MD simulations have the advantage of also being able to predict dynamic properties, such as ionic diffusion.

In the development of molecular models, the selection of electrolyte and solvent models is a critical step that can greatly influence the accuracy and reliability of simulation results. Earlier simulations of EDLCs favoured the use of primitive models that describe ions as hard spheres and electrodes as hard walls with solvents considered only as a dielectric constant,[3-5] or with non-primitive models that consider solvent molecules as uncharged hard spheres.[6-7] The use of primitive models greatly reduces the simulation cost due to their simplicity, and may have previously been considered a necessary concession when computational resources were lower than what is generally available today. However, the accuracy simulations using primitive models is greatly hindered due to lack of a realistic structure and inability to calculate dynamic electrostatic properties, specifically molecular dipole moments, which change with electrolyte polarisation.

All-atom electrolyte models, as the name implies, include every single atom within an electrolyte molecule, and are the most realistic models of electrolytes available. All-atom electrolytes are particularly useful models for studying specific molecular interaction, orientations, and overall structure within the EDL due to their accurate structure and polarisability. However, all-atom models have significantly high computational cost which limits their use, particularly in simulating

large systems and RTILs, which require long simulation times to equilibrate, due to their high viscosities.[8]

To overcome this computational limitation, simplifications can be made, such as using united-atom models, which unite CH_2 and CH_3 groups as single atoms, or using coarse-grained models, which group several sites of atoms together to represent them as a single pseudo-atom.[8] Coarse-grained models are of particular interest for simulating RTILs, which are bulky in size and often require large simulation box sizes with many hundreds of ions to minimise the finite size effect. Coarse-grained models can implement larger simulation time steps and simplified interactions, which can result in simulation times reduced by 100 times when compared to all-atom electrolyte model simulations.[8] Figure 2-1 provides a visual comparison between all-atom and coarse-grained electrolyte models for the readers benefit.

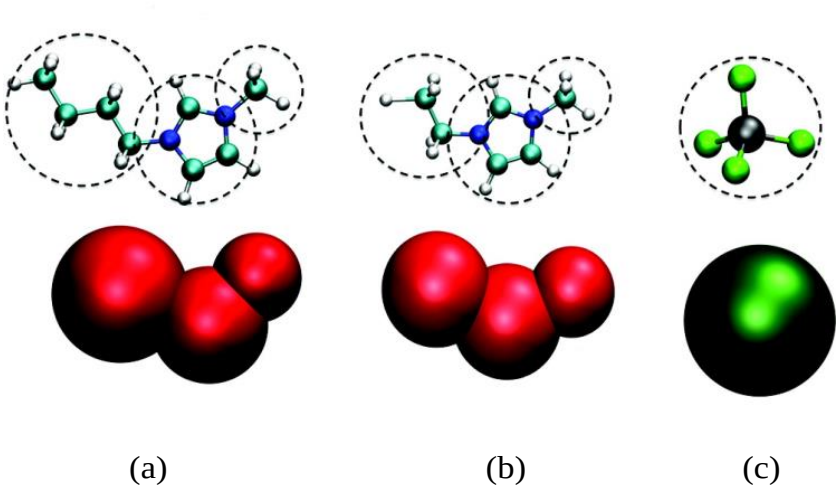

Figure 2-1. All-atom models (top) and coarse-grained equivalents (bottom) for (a) $[BMIM]^+$, (b) $[EMIM]^+$, and (c) $[BF_4]^-$. Reproduced with permission from9. Copyright 2012 American Chemical Society.

Another critical step in the accuracy of molecular simulations of EDLCs is the selection of the electrode model, namely constant and uniform surface charges or polarisable electrodes with a constant potential where partial charges on electrode atoms fluctuate throughout the simulation.[10] Many of the papers reviewed in Section 2.2 modelled electrodes with uniform surface charge to reduce the simulation times, and particularly in the earlier studies when techniques for electrode polarisability were not quite so well developed. Including electrode polarisability is important not only for the numerical difference it creates in simulation results, but also because it accurately represents a fundamental physical aspect that occurs in EDLCs which affects not only capacitance, but also dynamics.[10] Electrode polarisation enhances the surface charge in local areas via induced charges, which consequently increases the electric field strength and capacitance.[11] Omitting

polarisation of the electrode will result in artificially low capacitance when compared to experimental results.

Another simulation technique that is used is based on quantum density functional theory (q-DFT).[12] The q-DFT method solves quantum mechanical equations for a many-body system. In q-DFT, the number of particles involved in a simulation is generally far less than what is used in MC and MD simulations. These q-DFT simulations can be used as a complement to MC and MD simulations by validating force fields or other simulation results, such as the distance of the electrolyte ion from the surface of the electrode,[13-14] but cannot yet be extended to a realistic representation of a porous electrode due to the computational costs.

The closest non-atomistic technique to MC and MD simulations is classical density functional theory (c-DFT) simulation. c-DFT simulations can be applied to describe EDLCs with porous electrodes by minimising grand potential energy and obtaining local density profiles of solvent and electrolyte models, which can subsequently be used to determine EDL properties.[15-16] Simulation times for c-DFT are far shorter than those of MD or MC.[15] However, c-DFT cannot account for many important phenomena, such as surface roughness, complex electrode geometry, polarisation of the electrode surface or ionic compressibility. Often c-DFT is compared to MC simulations that make use of primitive models or non-primitive models to study various EDL structures as functions of ion size,[17-22] the valency of electrolytes,[17, 19] and pore size.[23] These simulations are often compared against modified Poisson-Boltzmann theory and can demonstrate deviation from Gouy-Chapman-Stern behaviours.[3, 17, 21] However, they are of limited use in modelling realistic EDLC systems due to their simplification of ionic structure.

Beyond c-DFT is continuum modelling, which is an efficient approach for predicting capacitance and dynamics of EDLCs. Importantly, it allows one to systematically study the influence of many influential parameters, such as ion size, electrode geometry, and electric potential more easily than by using experimental methods.[24-25]

However, continuum models cannot be used to predict capacitance in devices which employ nanoporous electrodes with pore sizes less than one nm and/or densely packed electrolyte molecules, such as in RTILs.[26-28] In these scenarios, which are becoming increasingly common in EDLCs, utilising molecular simulations are favoured for capacitance predictions due to their atomistic approach and ability to predict ion packing structure in the EDL.

2.2. Molecular simulations of the EDL

This section focuses on MD and MC simulations of EDL phenomena of various electrolytes interacting with different electrodes. First, we discuss simulations of RTILs interacting with planar,

porous, and exohedral curvature electrodes under equilibrium conditions. These simulations investigated the structure of the EDL and the influence of various parameters on the EDL. Dynamics of electrolyte transport, and non-electrostatic forces are also discussed for RTILs. Then, we discuss organic solvent based electrolytes, specifically $[TEA]^+[BF_4]^-$ electrolyte in ACN and PC solvents, as well as RTIL – ACN mixtures. Finally, aqueous electrolytes in porous electrodes are reviewed.

RTILs can be operated at higher voltages than aqueous solutions and organic solvent based electrolytes in EDLCs, thus offering opportunities for improving performance.[29-30] This means that a great deal of molecular simulations of RTIL-based EDLCs has been performed.[14, 31-35]

2.2.1. RTILs

2.2.1.1. Planar electrodes

Kornyshev[27] introduced a mean field theory (MFT) based on the Poisson-Boltzmann lattice-gas model, which takes into account the so-called 'lattice saturation effect', a constraint on maximum ionic packing density, as well as being able to describe RTILs with cations and anions of different sizes. Following this paper, Fedorov and Kornyshev[26] performed MD simulations of RTILs modelled as primitive dense Lennard-Jones spheres with symmetric ion size between charged walls in an attempt to address some of the questions raised by Kornyshev[27] about the structure of EDL in dense RTILs. Several key phenomena regarding the differential capacitance (DC) were observed as the surface charge density, q, was varied between - 48 and + 48 μC m^{-2}. The capacitance versus potential curve did not follow the U-shape characteristic of the Gouy-Chapman-Stern model, but instead had a 'bell-shape' consistent with the MFT predictions. In the wings of the capacitance versus potential curve, the capacitance was inversely proportional to the square root of potential, which was also consistent with the MFT. Most significantly, large overscreening effects were observed due to short-range ionic correlations, this feature was not seen in the MFT. The overscreening effect was especially prominent near the point of zero charge (PZC) and the maximum overscreening coincided with the maximum capacitance. Although the maximum overscreening coincided with maximum capacitance in this study, it is important to note that in general, overscreening is detrimental to capacitance. The reason for maximum capacitance and overscreening coinciding was due to the use of a symmetric primitive model for the RTIL, causing the maximum capacitance and maximum overscreening to both occur at the PZC. In addition, the overscreening effect was suppressed at high electrode polarisation following the onset of the lattice saturation effect. In a system with asymmetric electrolytes, the maximum capacitance would no

longer coincide with the PZC, which could potentially complicate the capacitance curve, as suggested by Fedorov and Kornyshev.[26]

Figure 2-2 shows an example of the overscreening effect. The charge of the first layer of adsorbed counter-ions exceeds the total charge of the electrode, and subsequent ionic layers of alternating charge form until the electrode charge is completely balanced.

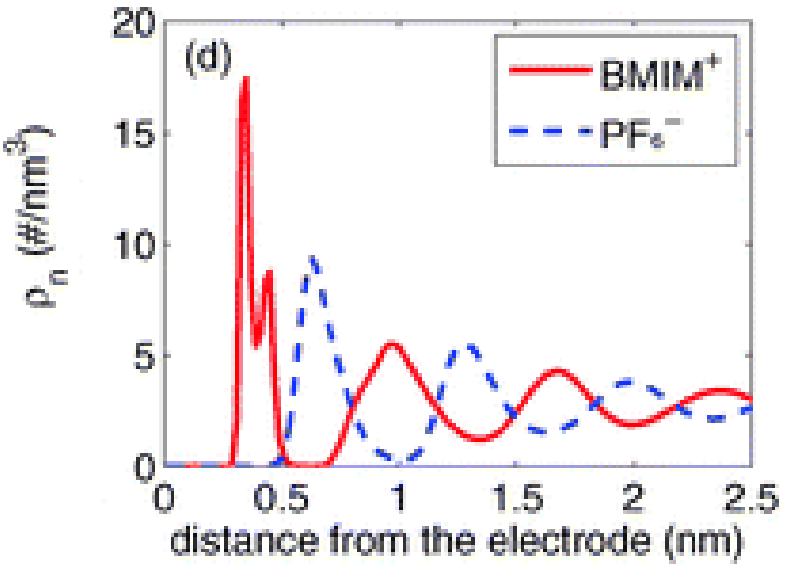

Figure 2-2. Ion density profiles of RTIL $[BMIM]^+[PF_6]^-$ exhibiting charge overscreening near a planar graphitic electrode with a surface charge density of – 0.112 C m^{-2}. Reproduced from[14] with permission from PCCP Owner Societies.

A further MD simulation study[36] was performed with surface charge densities between - 80 and + 80 μC m^{-2}, in which RTILs were again taken as primitive dense Lennard-Jones spheres between charged walls but ion size asymmetry was considered. Figure 2-3(a) shows that strong charge density waves appeared at low potentials. The first peak near the positive electrode was closer to the surface than the first peak near the negative electrode. Figure 2-3(b) demonstrates the charge overscreening effect by showing the overcompensation of potential in the adsorbed counter-ion layers. an extension to the MFT, which added in series the compact layer contributions, was employed and was able to reproduce the simulated capacitance almost quantitatively.[36] The capacitance curve generated had an asymmetric bell-shape reflecting the shift of maximum capacitance 0.3 V away from the PZC in the positive direction as a result of ion size asymmetry.

Experiments on dense RTILs, in which the length of alkyl chains on the cations varied, produced 'camel shape' capacitance as a function of voltage with two local maxima, varying in height and position.[37-39] Fedorov et al.[40] performed MC simulations[41] incorporating the excluded volume of neutral ion tails and the cation shape asymmetry to elucidate the nature of the camel-shaped capacitance curve. Three separate primitive model systems with the same anion but different cation

geometries were simulated. The three cation models were a one-bead model (1BM), a 'dumbbell' two-bead model (2BM) with one charged and one neutral bead, and a three-bead model (3BM) with one charged and two uncharged beads. The camel-shaped capacitance curve with two maxima occurred only when neutral tails were present on the cation (2BM and 3BM models).

Figure 2-4 illustrates the bell-shaped and camel-shaped capacitance curves observed in their simulations[40] as well as experimentally observed camel shaped capacitance curves.[37] The 1BM model showed only a single maximum. It was found that neutral tails on the cations, which act as latent voids, can cause a spike in capacitance at moderate electrode polarisation when ions rearrange and the space occupied by the neutral tails is replaced by charged heads. This effect was observed on both the anode and cathode, even though only one species of ion had neutral tails.

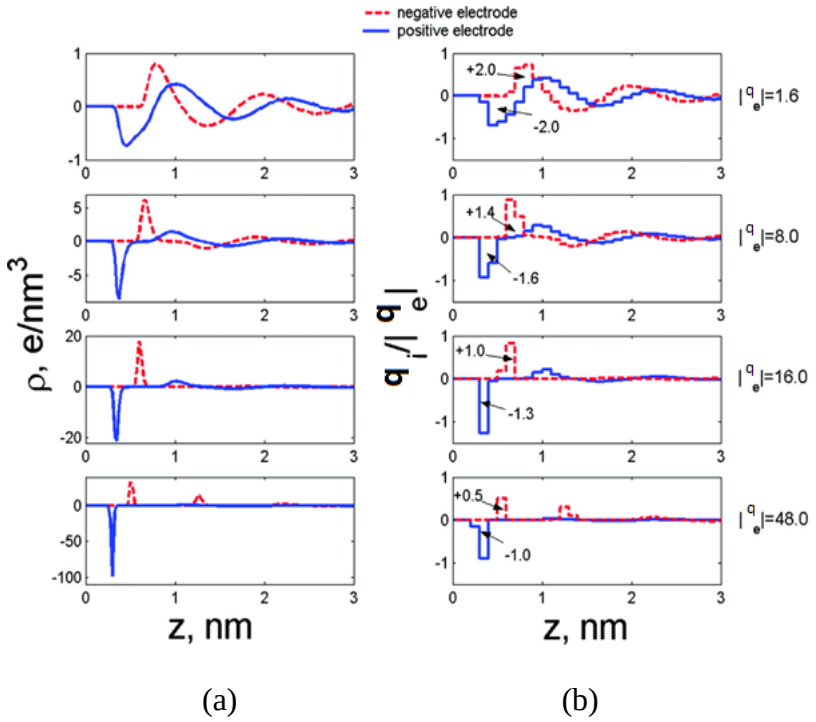

(a) (b)

Figure 2-3. (a) Volumetric charge density profiles of counter ions near both negative and positive electrodes along the *z*-direction. (b) Charge densities per unit surface area calculated for 0.1 nm thick slices along the *z*-direction. All charge densities were scaled to the corresponding absolute values of the electrode surface charge density. The arrows indicate the integrals over the first peaks and valleys at each electrode. Reproduced with permission from[36]. Copyright 2008 American Chemical Society.

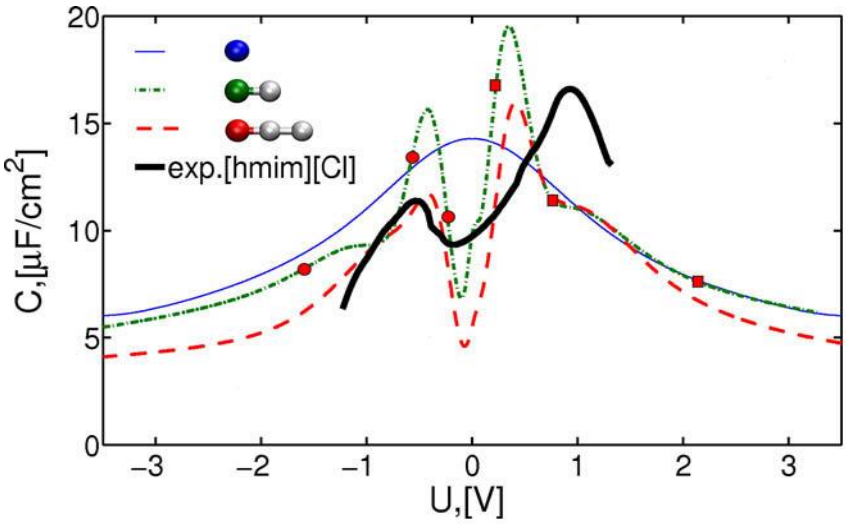

Figure 2-4. Differential capacitance obtained from simulations. The black solid curve is the experimental data for [hmim][Cl] from[37]. Reproduced with permission from[40]. Copyright Elsevier 2010.

MC simulations of anisotropic RTILs were also carried out by the same group to study electrostriction vs. lattice saturation.[42] This simulation showed that an increase in counter-ion charge density occurred due to ion rearrangements without substantial compression of the liquid and that 'lattice saturation' at high voltages was a universal effect.

The qualitative observations made from the above simulations by Fedorov et al.[26, 36, 40, 42] provided initial insight into charge overscreening and potential variations in the C-V curve with asymmetric ion sizes. However, due to the primitive models used, particularly for the electrolytes, they failed to accurately reproduce experimental results,[37-39] as can clearly been seen from

Figure 2-4. Incorporating all-atom or accurate coarse-grained electrolyte models is essential for the reproduction of experimental results or the precise study of EDL structure as they include important physical phenomenon, such as flexibility and charge rearrangement, which can't be represented with primitive models. One such simulation, aimed at precise study of EDL structure, used an all-atom model of $[BMIM]^+[NO_3]^-$ on planar electrodes[43] and showed a good agreement with that of the MFT.[27] The authors determined that capacitance is not simply a function of the approach distance of the counter-ion to an electrode, but also strongly depends on the co-ion – electrode interaction. Furthermore, cation – anion correlations and specific cationic adsorption at zero electrode charge were also shown to strongly impact the EDL capacitance. However, this study also used a simplified electrode model, which may have impeded the accuracy of the observed results.

Wang et al.[44] motivated by studying the influence of cation alkyl chain lengths on interfacial structure, performed MD simulations using all-atom models of the RTILs $[BMIM]^+[PF_6]^-$ and $[OMIM]^+[PF_6]^-$. The RTILs were simulated between uncharged planar graphite electrodes and ignored image charge effects. It was found that polar groups aggregated together to form polar

networks, and non-polar groups filled the rest of the vacancy. The imidazolium rings laid preferentially flat, parallel to the graphite surface, while the alkyl chains extended along the perpendicular direction. The surface potential drop at the interfacial region was smaller for the smaller $[BMIM]^+[PF_6]^-$ electrolyte. Although this study highlights the high level of structural rearrangement which RTILs undergo near charged electrode surfaces, ignoring image charge effects is a dubious simplification and most likely affected the accuracy of the results. Given the computational resources available to many researchers, ignoring image charge effects is no longer generally considered a necessary simplification to make.

A similar but more accurate MD study was performed by Kislenko et al.[45] using an all-atom model of $[BMIM]^+[PF_6]^-$ electrolyte near a graphite electrode. In this study, the surface charge density of the electrode was varied between positively charged, neutral, and negatively charged, however electrode partial charges were considered as constant, rather than dynamically calculated on the fly. With an uncharged electrode surface, results similar to those of Wang et al.[44] were observed, namely three dense layers formed and the imidazolium rings were orientated parallel to the electrode surface. The $[PF_6]^-$ ions did not approach the electrode surface as closely as $[BMIM]^+$ ions and two planar fluorine atom triplets formed around the phosphorous atom parallel to the graphite surface. When a charge was introduced onto the graphite surface, the angle distribution between the electrode surface and the adsorbed rings broadened and shifted the most probable tilt angle up. No anions remained adsorbed at a surface charge density of - 8.2 μC cm^{-2}, while a non-negligible number of cations remained adsorbed at a charge density of + 8.2 μC cm^{-2}. Although this study accurately modelled the electrolyte, a more accurate electrode model, in which the partial charges are not constant, would alter the capacitance results and potentially also the observed EDL structure and orientation of adsorbed ions.

A subsequent study on the same RTIL/graphite interface system focussed on the influence of temperature on the structure of ion adsorption.[46] The authors found that the magnitude of the $[PF_6]^-$ anion density peaks at the interface decreased with increasing temperature. However, anomalous behaviour for the $[BMIM]^+$ cation was observed, namely that the magnitude of the second peak increased with increasing temperature. Increasing the temperature from 300 to 400 K induced a decrease in the potential drop across the interface and a corresponding increase in the EDL capacitance. A similar study observed the effect of temperature for a united-atom $[pyr_{13}]^+$ and all-atom $[TFSI]^-$ RTIL model[47] and noted that increasing temperature was found to reduce the differential capacitance.

A comparison of the EDL structure and charging kinetics between $[pyr_{13}]^+[TFSI]^-$ and the smaller RTIL $[pyr_{13}]^+[FSI]^-$, using the same united-atom – all-atom model approach was made by MD

simulations.[48] Interestingly, the cathode differential capacitance was 30% larger for $[pyr_{13}]^+[FSI]^-$ than that for $[pyr_{13}]^+[TFSI]^-$ computed in their previous simulation.[47] $[TFSI]^-$ is a larger anion than $[FSI]^-$ therefore the increase in differential capacitance was attributed to both a closer approach of the ions to the electrode surface and increase in the rate versus potential decrease of anion desorption from the electrode surface. No significant difference in anode capacitance was observed. Refs [47] and [48] accurately modelled the electrode by iteratively calculating partial charges whilst constraining the electrostatic potential. The combination of detailed electrode and electrolyte models resulted in a more accurate and precise simulation of the structure of the EDL at a RTIL – planar surface interface compared to the studies previously discussed.

The influence of surface roughness on the shape of the C-V curve was investigated by MD simulations using an all-atom model of the RTIL $[EMIM]^+[FSI]^-$ (with a low concentration of $Li^+[FSI]^-$).**[49]** Atomically flat-surface electrodes generated camel-shaped capacitance curves while rough-surface electrodes with prismatic faces generated bell-shaped capacitance curves with a significantly higher maximum capacitance. Surface roughness was similarly investigated for RTIL $[C_nmim]^+[TFSI]^-$ (with alkyl chains of varying lengths).[50] Only a weak correlation was evident between the length of the neutral alkyl tail in $[C_nmim]^+[TFSI]^-$ ions and the reduction in differential capacitance, which further highlights the ability of RTILs to re-orientate, and rearrange charge carrying groups to maximise adsorbed counter-ion charge density. Thus, it follows that RTILs have the potential to be tailored for specific properties, for example, melting point or viscosity, by changing the neutral tail length without significantly changing the capacitance. This offers a unique advantage over aqueous solutions and organic solvent based electrolytes. The capacitances of $[C_nmim]^+[TFSI]^-$ were systematically larger at all potentials for rough surfaced electrodes,[50] whereas in their previous study, below -1 V the differential capacitance was higher for atomically flat electrodes.[49] The observed trends were attributed to faster counter-ion accumulation and ion segregation in the interfacial layer for the rough surfaces compared to the flat surfaces.

An interesting MD simulation[51] improving upon the idea of studying surface roughness used nanometre tuning to create surfaces capable of molecular separation and demonstrated that the 'refined roughness' significantly affected the differential capacitance for $[pyr_{13}]^+[FSI]^-$. Highly tuned surfaces promoted ion separation and revealed a complex relationship between capacitance and electric potential. As Figure 2-5 shows, tuning the surface so that the indentation width approaches the ion diameter results in strong ion separation, systematically larger capacitance, and a complex capacitance versus electrode potential profile with several local maxima. Furthermore, increased capacitance was maintained even at relatively large electrode potentials (> 3 V), which indicates that this electrode configuration may be capable of producing large energy densities. In a

recent MD simulation, similar qualitative observations were made for flat and rough gold electrodes.[52] Simulation of nanometre surface tuning, and possibly surface functionalization, in combination with optimal selection of RTIL electrolyte based on size, appears to be an interesting area of research for molecular modelling that is deserving of more attention and may help guide the design of novel EDLCs with greatly increased energy densities.

Simulations of RTILs at planar surfaces has provided valuable insight into the structure of the EDL and helped explain experimental variations observed in differential capacitance.[37-39] However, when considering the novel design of EDLCs which maximise energy density, the knowledge gained from these simulations is hard to put into practice as planar electrodes are unlikely to be used due to their low surface areas. Porous electrodes are more favoured for creating large surface area, but unfortunately from a simulation viewpoint, are governed by vastly different physics.

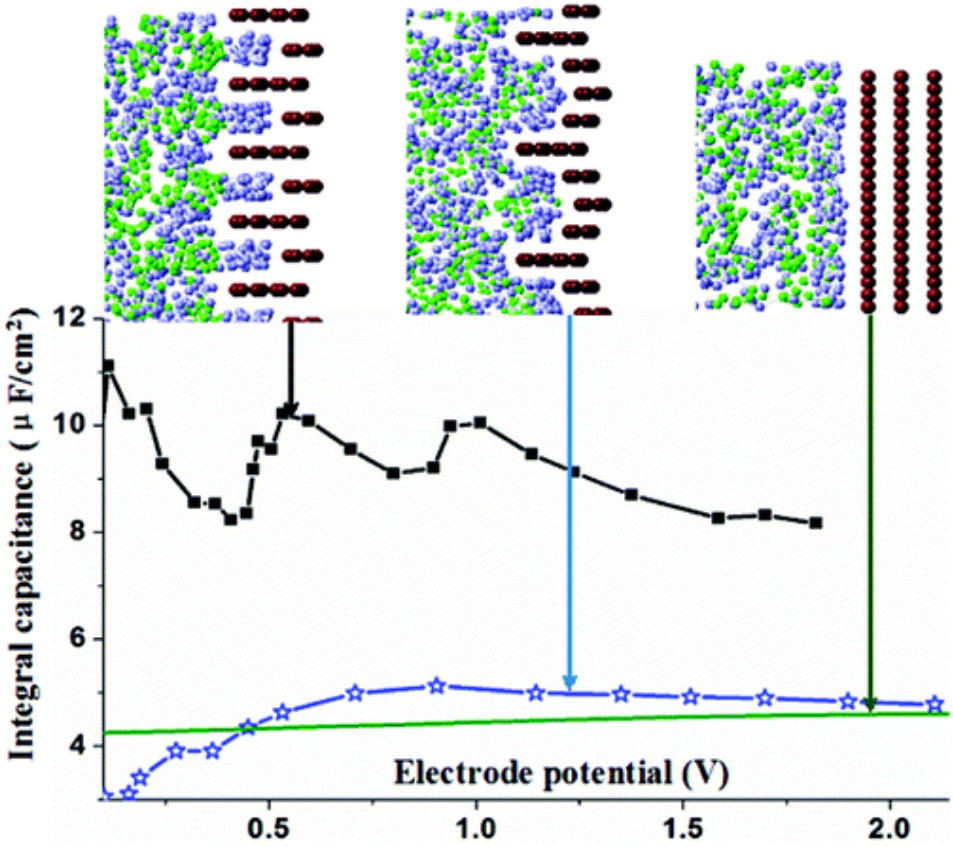

Figure 2-5. Integral capacitance as a function of electrode potential with varying precision of electrode surface tuning. Reproduced with permission from[51]. Copyright 2012 American Chemical Society.

2.2.1.2. Porous electrodes

Chmiola et al.[53] experimentally observed an anomalous increase in capacitance in pores with diameters of less than 1 nm for a 1.5 M solution of $[TEA]^+[BF_4]^-$ in ACN. A following study by Largeot et al.[29] using the RTIL $[EMIM]^+[TFSI]^-$, showed a large increase in capacitance for a pore

diameter which closely matched the ion size. It is not unsurprising that the above observations stimulated many molecular simulations of RTILs in nanoporous electrodes.[31, 33, 54-58]

Modelling a nanopore is most easily achieved by use of a slit-type model, which simply separates two like-charged planar surfaces by a small distance, creating a pore. This technique has proved to be popular among researchers and is discussed first for porous electrodes.

Kondrat and Kornyshev[59] suggested a model in which image forces exponentially screen out the ion-ion electrostatic interactions occurring in the pores. Packing of counter-ions becomes easier with a decrease in pore diameter, leaving steric interactions as the main limitation. The model suggests that a voltage-induced, first-order transition occurs in which a counter-ion-deficient phase is replaced by a counter-ion-rich phase, causing the jump in capacitance as a function of voltage, termed 'superionic' by the authors.

A MC simulation study[54] confirmed that the superionic state[59] is responsible for the anomalous increase in capacitance. The MC simulations[54] had good agreement with experimental results,[53] which lends credibility to the model,[59] however it should be noted that in the simulation a restricted primitive model was used for the RTIL electrolyte in which the ions are symmetric, hard spheres, with point charges. Such a simplification is likely to lead to significant disagreement in charge storage mechanisms when compared against more accurately modelled electrolytes

As Figure 2-6(a) shows, the capacitance as a function of voltage in narrow pores peaked sharply, followed by a drop to zero as voltage increased. The capacitance peak results from saturation of the *total* ion density, which occurs before the pore is solely filled with counter-ions. However, this prediction has not yet been verified by experiment. A MD simulations using a more accurate coarse-grained model for the RTIL $[DMIM]^+$ $[BF_4]^-$ also examined the effect of voltage on charge storage modes for a fixed pore diameter.[33] By varying the voltage, distinct ion compositions inside the pores were observed as shown in Figure 2-7. At low voltages, the charge storage was achieved by swapping co-ions inside the pore with counter-ions from the bulk. At higher voltages, a maximum capacitance occurs when co-ions are expelled from the pore. Further increasing the voltage introduces more counter-ions into the pore but lowers the capacitance due to entropic effects.[33]

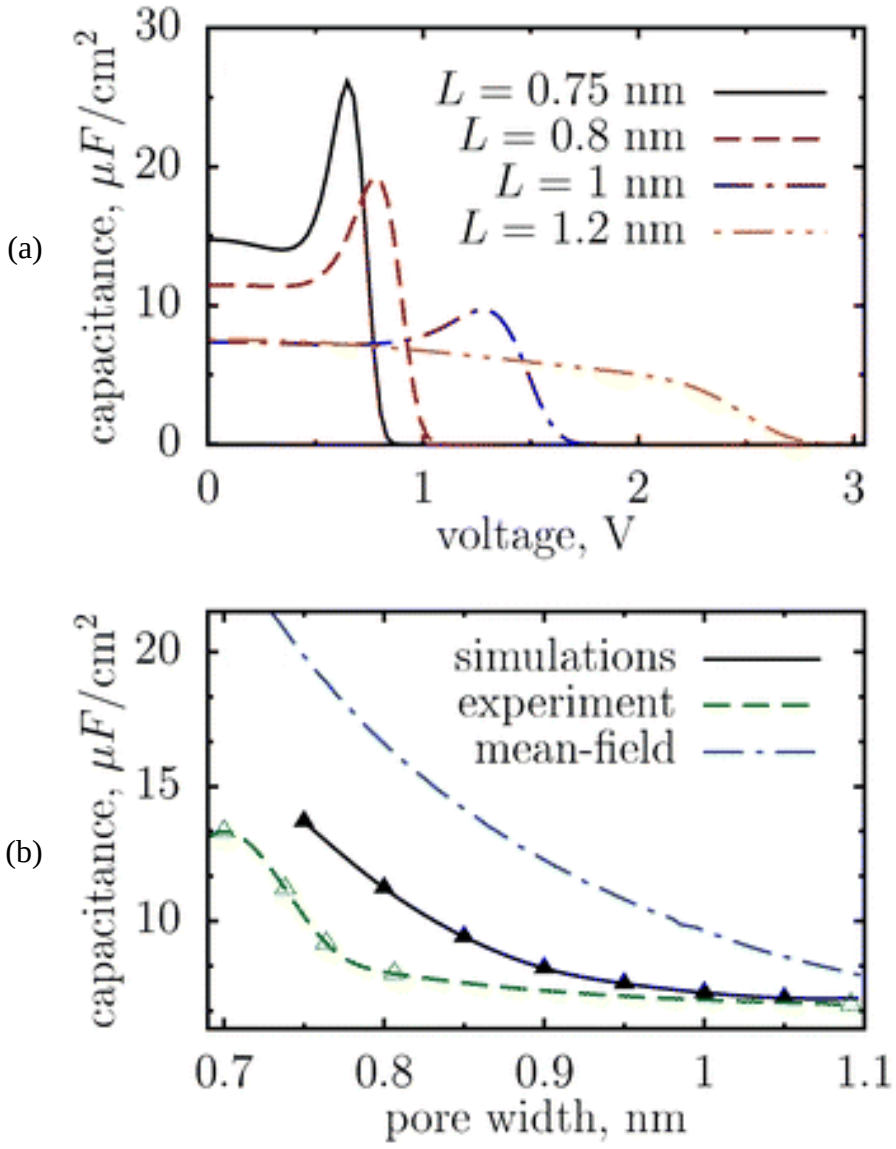

Figure 2-6. Anomalous capacitance behaviour. (a): Differential capacitance per unit surface area as a function of voltage for a few values of pore width (L). (b): Differential capacitance as a function of the pore width for zero electrode polarisation, compared with experimental data from[29] and MFT from.[44] Reproduced from[54] with permission from PCCP Owner Societies.

The differences in ion composition inside the pores at low and high voltages were due to ion size asymmetry and the dominance of ion – ion repulsion at high potentials. This implies that removal of co-ions is more effective than the insertion of counter-ions in reducing the systems energy. Capacitance increase at optimal voltage (approximately 2 V)[33] occurred when the co-ion stabilisation, which was caused by ionic charges per pore wall surface charge, became weakened due to the short ranged nature of electrostatic interactions inside sub-nanometre nanopores. These results differ from those of Kondrat et al.,[54] wherein the charge storage mechanism below optimum voltage is due to ion swapping and ion insertion, while above optimum voltage it is determined entirely by ion swapping. This difference is likely due to the asymmetric ion size used in this study compared with the symmetric ions used by Kondrat *et al.*[54] highlighting the importance of using

accurate electrolyte models when examining EDL structure and charge storage mechanisms in porous electrodes.

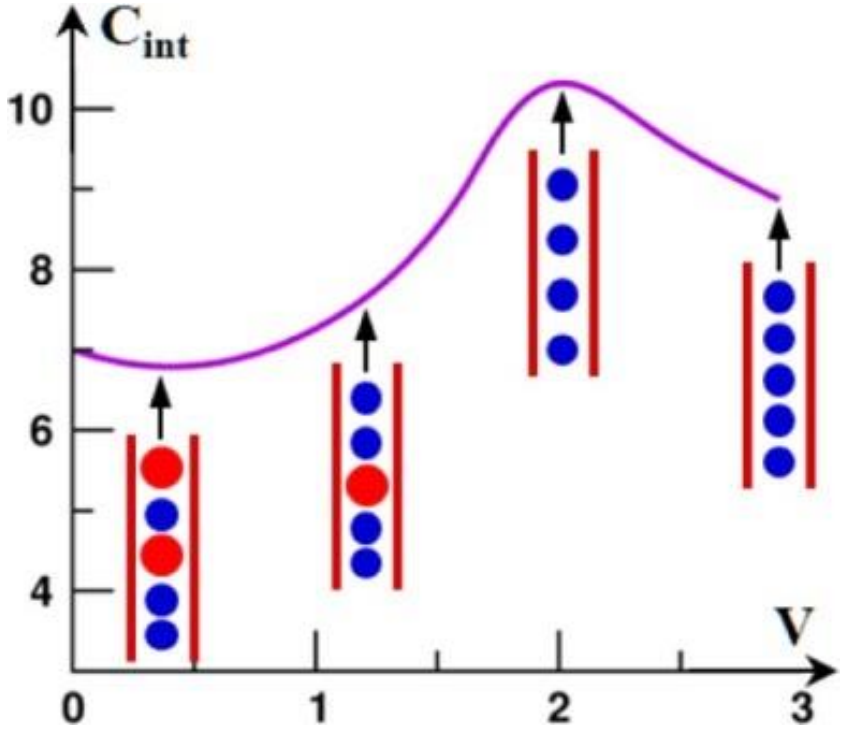

Figure 2-7. Differing ionic composition inside pores as a function of voltage and correlating integral capacitance. Blue circles depict counter-ions, and red circles depict co-ions. Reproduced with permission from[33]. Copyright 2012 American Chemical Society.

Feng and Cummings[60] used MD simulations to study $[EMIM]^+[TFSI]^-$ in nanopores of varying diameter. As the diameter of slit-type nanopores increased, the capacitance oscillated. The oscillation amplitude decreased with increasing pore diameter. The authors suggested that these results may explain the experimental observations of Centeno et al.,[61] which showed no anomalous increase in capacitance in pores of 0.7 to 15 nm. If the electrode contains pores of varying sizes with a high PSD (which is often the case for activated carbon electrode material), the weighted average pore diameter may not adequately reflect the presence of nanopores, masking their contribution to the total capacitance. Following the insight from their simulation that counter-ions form a single layer in the central plane of the pore, the authors proposed an extension to the sandwich model, which they developed previously[62] (discussed in section 2.2.1.3). The sandwich model extension describes the capacitance in nanopores as,[60]

$$C = \frac{\varepsilon_r \varepsilon_0}{\left(d_{pore} - d_{ion}\right)/2} \tag{2-1}$$

where ε_r is the relative permittivity, and ε_0 is the permittivity of vacuum (in F/m), while d_{pore} and d_{ion} are the pore diameter and effective ion-diameter perpendicular to the slit wall (in m), respectively.

A similar simulation using the RTIL $[DMIM]^+$ $[BF_4]^-$ also examined the effect of nanopore diameter[57] on the capacitance and charge storage mechanism inside nanopores. Varying the pore diameter produced two local maximum capacitances at approximate multiples of ion diameter and replicated the U-shaped capacitance versus potential curve observed experimentally[29] and in the simulation by Feng *et al.*[60] The authors, using the same reasoning as in the previous paragraph also suggested that the U-shape behaviour in the capacitance versus pore diameter provides insight into the difficulty of observing the anomalous increase experimentally, where electrodes may have a wide PSD.[61] However, neither Feng et al.[60] nor Wu *et al.*[57] explicitly simulated an electrode with multiple pore diameters to confirm their speculations of the influence of PSD on capacitance.

The authors also developed a new model framework[57] derived from thermodynamic considerations to describe capacitance inside nanopores. The framework highlights the fact that ion solvation structure, and its response to pore electrification, is a critical factor in determining the capacitance. As a pore is electrified, the change of the energy of a co-ion due to the change in its electrostatic interactions with other ions is more important than its non-electrostatic interactions with other species. The framework helps lay a theoretical basis for pore-capacitance optimisation by the manipulation of ion solvation and tailoring chemical details of ion *pairs* for a pore of a given diameter.

Capacitance enhancement of $[EMIM]^+[TFSI]^-$ was studied in sub-nanometre slit-type nanopores of varying diameters.[58] In this study, electrode polarisation was modelled using flexible Gaussian-distributed electrode charges calculated iteratively and subject to electrostatic energy minimisation. The identified optimal pore size produced an integral capacitance two times larger than that for planar electrodes. The largest contribution to increased capacitance arose from fast charge separation inside the nanopore where co-ions were removed above a certain electrode potential threshold and counter-ions remained confined in the pore. This resulted in an elevated counter-ion density and consequently increased capacitance, due to strong screening of the electrode charge by the counter-ions. Strong capacitance asymmetry was observed due to the different ion sizes. In a 0.75 nm diameter pore, the anode showed no significant increase in capacitance compared to flat electrodes whereas the cathode capacitance increased by 100%. This resulted in a 30% increase in the overall capacitance. The observed asymmetry of electrode capacitance did not result from the differences in the super-screening $[TFSI]^-$-$[TFSI]^-$ and $[EMIM]^+$-$[EMIM]^+$ interactions. It was noted that differences in chemical structure and internal charge distributions between $[TFSI]^-$ and

$[EMIM]^+$ ions resulted in confined $[TFSI]^-$ anions having significantly stronger electrostatic interactions with the charged pore walls, promoting repulsion from the cathode and increasing attraction within the anode. Furthermore, polarisation of the nanopore surface can cause bimodal and asymmetric charge distributions, generating local environments that are less repulsive for co-ions and increasing their retention.

Modelling of charge storage mechanisms in slit-type nanopores has proved useful in clarifying experimental observations involving RTILs. A recent theoretical and experimental study[55] focussing on optimal pore diameter and PSD for maximum energy density concluded that energy density is a non-monotonic function of the pore diameter and that the optimal pore diameter increases with increasing operating voltages. Due to the delicate relationship between optimal pore diameter and operating voltage, it is critical that future simulations are aware that the best electrocapacitive performance may not necessarily occur at the highest voltage available to the RTIL.

Carbon nanotubes (CNTs) as porous electrodes differ from slit-type electrodes by completely confining electrolytes in a cylindrical manner. Due to curvature effects, one could expect a closer approach of the confined counter-ions to the surface of the electrode compared to slit-type electrodes. Shim et al.[56] studied the effect of CNT nanopore diameter on the counter-ion charge density using a flexible all-atom model of the RTIL $[EMIM]^+[BF_4]^-$. The CNT diameter was varied between 0.68 – 2.03 nm, the authors concluded that capacitance normalised to pore surface area varies non-monotonically with pore diameter. For CNTs with diameters between 0.9 and 2.0 nm, the capacitance was found to increase with decreasing diameter. Below 0.8 nm the capacitance was observed to drop as the pores became too small to accommodate ions. These results qualitatively agree with experiments.[29] However, a large concern with the quality of this simulation is that the magnitude of the capacitance is consistently, and significantly, lower than that observed experimentally. The authors attributed this to the fact that the polarisability of the electrode and electrolyte was ignored in the simulations. Asymmetry between the cathode and anode was observed due to the differences in size between the $[EMIM]^+$ and $[BF_4]^-$ ions. However, due to the large disparity between the capacitances observed in this simulations and experimental results, it is questionable whether the described orientations are correct. Polarisable models for both the electrolyte and electrode would most certainly change the EDL structure.

Nevertheless, from the above observations, an extension to the EWCC model, developed by Huang et al.,[63-64] was suggested by the authors.[56] This new model was termed the 'electric multiple charge-layer capacitor' (EMLC) and was used to understand the capacitive behaviour of CNT EDLCs with RTIL electrolytes. The model assumes that there are *n* layers of concentric cylindrical charge

distributions inside the nanopore of infinite length and that there is zero electric field on the external walls of the CNTs and the innermost charge layer. This differs from CNTs of finite length in which the bulk RTIL also contributes to the capacitance by adsorption to the external surface of the CNTs. The EMLC differentiates itself from the EWCC by accounting for the charge separation of the primary counter-ion shell. This separation arises from the extended ion charge distributions in RTILs and properly reflects the multi-layered charge distributions in the compact layer. The EMLC model agreed well with both the experimental data[29] and the simulation results.

CNTs appear to be more favoured by researchers to study RTIL ion adsorption on an exohedral surface (discussed in Section 2.2.1.3) rather than internal confinement. A more promising technique for studying internal confinement of RTILs is by using accurately developed CDC electrode models which faithfully incorporate the complexities of the structure. CDCs with very narrow PSD[65] are characterised by properties close to those of metals, particularly electrical conductivity.

Merlet et al.[31] performed an insightful MD simulation with CDC electrodes and accounted for the polarisation of the electrodes due to the electrolyte. Using a coarse-grained model of the RTIL $[BMIM]^+[PF_6]^-$, the authors reported capacitance results of 87 and 125 F g^{-1} for simulations of titanium (Ti) CDC-1200 and Ti CDC-950 electrodes (the number behind each sample represents the chlorination temperature used in preparation of the sample), respectively. These simulated capacitances were in excellent agreement with experimental results.[29] Furthermore, these capacitance values were higher than the results reported by Shim et al.[56] where electrolyte and electrode polarisation was not considered, highlighting the critical nature of including electrode geometry and polarisation effects for the quantitative prediction of capacitance. Figure 2-8 shows the different environments electrolytes may experience in CDC electrodes.

The EDL structure observed at the porous Ti CDC electrodes were compared against a previous MD simulation by Merlet et al.[66] which employed a coarse-grained RTIL $[BMIM]^+[PF_6]^-$ electrolyte model between planar graphite electrodes, which generated differential capacitances of 3.9 and 4.8 μF cm^{-2} for the anode and cathode, respectively.

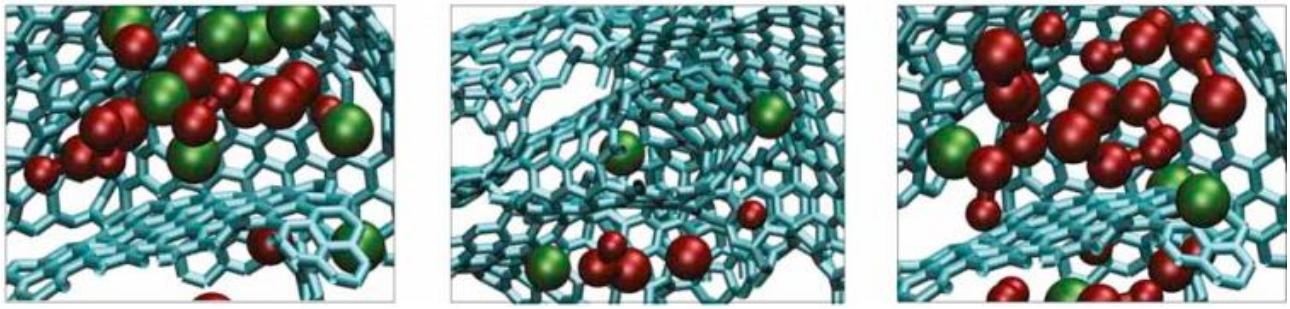

(a) (b) (c)

Figure 2-8. Simulated ion distribution of RTIL $[BMIM]^+[PF_6]^-$ inside electrified pores of a TiCDC-1200 electrode. Blue = C–C bonds, red = $[BMIM]^+$, and green = $[PF_6]^-$. a: Local ion distribution near a positive surface (+ 0.5 V), b: A single anion in a nanotube-like pore positively polarised (+ 0.5 V). c: Local structure near a negative surface (- 0.5 V). Reprinted by permission from Macmillan Publishers Ltd: Nature Materials,[31] copyright 2012.

Both cations and anions approached the surface of nanopores more closely than that of planar electrodes (by approximately 0.07 nm), which partly explains the increased capacitance observed in CDCs. However, the number of adsorbed ions per unit surface area was greater at planar graphite electrodes than in nanopores. This result is counter-intuitive as generally areal capacitance increases with the ion density adsorbed, which suggests that different charging mechanisms are involved in the anomalous regime. The simulations of nanoporous electrodes revealed that the electrodes were wetted by the RTIL at zero electric potential,[31] an effect also observed in previous simulations of slit-type nanoporous electrodes,[33, 54] which implies that the anomalous increase in capacitance does not result from a potential-driven entrance of liquid into the porous network.

The simulations at planar electrodes showed that the ions overscreened the electrode charge and formed multiple layers of adsorbed ions. In the first layer only a fraction (approximately 30% at 1 V) of the adsorbed ions were effectively used for charge storage. By contrast, in nanoporous electrodes, only one layer occurs and entirely balances the charge of the electrode, resulting in the higher efficiency. Because the attraction of ions in the single layer is not balanced by a second, oppositely-charged layer, the ions approach the surface of the electrode more closely. This unexpected new mechanism accounts for the larger charge stored inside nanoporous electrodes.[31] Interestingly, the observed capacitance of Ti CDC-950 exceeded that of Ti CDC-1200 by 43% [31], even though the PSD and average pore diameters were similar (0.93 nm and 0.95 nm).[67] This indicates that local structure can affect the capacitance, since the smaller capacitance of Ti CDC-1200 was correlated with higher occurrences of graphitic zones.

Recently, a MD simulation by the same group systematically compared accurate constant-potential electrode models to simplified electrode models with constant and uniform charge for planar graphite and nanoporous CDC electrodes interacting with a coarse-grained RTIL model of $[BMIM]^+[PF_6]^-$.[10] The simulation results indicated that simplified models with constant and uniform

charge do not provide an accurate representation of the real system. Furthermore, interesting mechanistic differences were observed. In the simplified models, the structure of adsorbed ions is partially modified. More prominently, large differences in temperature increase, due to the Joule effect associated with sudden application of electric potential, occur during the dynamics of polarisation relaxation following a sudden change in potential difference or charge.

The simulations by Merlet et al.[10, 31] have systematically shown the value of incorporating accurate electrode models that are more representative of electrodes in real EDLCs. Simulations that use accurate electrodes in combination with well-validated all-atom or coarse-grained electrolyte models is critical for future research that aims to provide further insight into the complex EDL phenomena that occurs at the confined RTIL – nanoporous electrode interface. Keeping up with material researchers who are consistently producing novel electrode materials is a challenging area for simulation researchers due to the large effort required to accurately reproduce electrode models of complex structures[67-68] and is worthy of more focus.

2.2.1.3. Exohedral curvature electrodes

Exohedral curvature is a promising class of electrode which can offer high capacitance and good dynamic performance due to the small distance from the electrode surface to the bulk,[69] and consequently has received some interest by molecular modelling. The influence of ion size, electrode potential, electrode curvature, and temperature was investigated using a combination of MD and q-DFT simulations for the EDL structure of RTILs at the surface of CNTs.[14, 70] The sizes of the counter-ions and co-ions were found to influence the EDL. The anode capacitance for $[BMIM]^+Cl^-$ was larger than that for $[BMIM]^+[PF_6]^-$ due to the closer approach of the Cl^- anions to the electrode surface. Capacitance also increased with increasing curvature (i.e. decreasing tube diameter). However, potential and temperature were found to have little influence on the capacitance.

Based on the observations of their MD simulations, Feng et al.[14] concluded that overscreening of electrode charge was a universal feature of the EDL in RTILs and suggested a new model, Multiple Ion Layers with Overscreening (MILO)[14], to account for the alternating layers of counter-ions and co-ions as well as charge overscreening. The Helmholtz[71] and EDCC[63] models assume that electrode charge is screened by a single layer, and the MFT approach[27] largely neglects ion-ion correlations. The MILO model however takes a more phenomenological approach in an attempt to capture the key feature of multiple-layered charge overscreening of the EDL structure observed in simulations. Capacitances computed from MILO agree well with those generated by their MD

simulations.[14] Unfortunately a major drawback of MILO is that some parameters need to be obtained from MD simulations, reducing the ease with which it can be applied.

Onion-like carbon (OLC), a model of which is shown in Figure 2-9, is a promising type of electrode offering high capacitance as a result of large three-dimensional exohedral curvature.[69] Simulations by Cummings et al.[72-73] revealed that the capacitance has a nearly linear response to electric potential and, similar to CNTs, the capacitance increases with increasing curvature.[72] However, unlike CNTs, the thickness of the EDL decreased and the differential capacitance increased with increasing temperature.[73] The curvature effect was ascribed to the dominance of charge overscreening, which was observed over a much wider potential range for OLCs than planar electrodes, and to the increase in ion density per unit area of electrode surface as the OLC reduced in size.

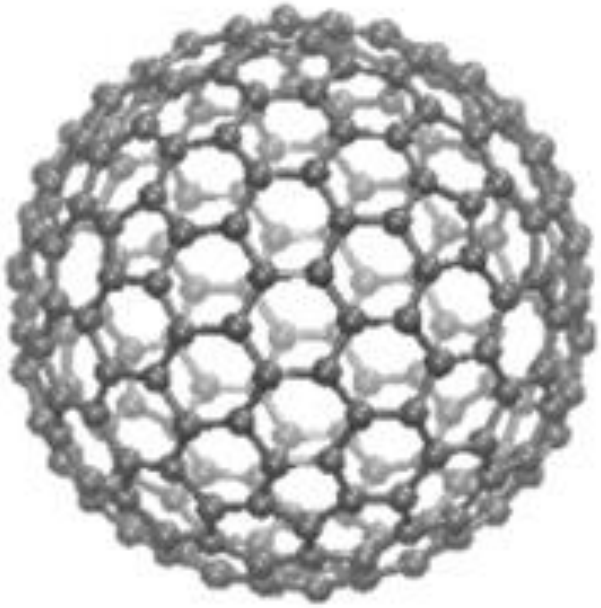

Figure 2-9. Molecular model of a spherical onion-like carbon. Reproduced with permission from[34]. Copyright 2013 American Chemical Society.

Given the relatively few number of simulations reported on exohedral curvature electrodes and their promising attributes, more simulations with diverse focuses are to be expected in future and should provide insight into design high performance ELDCs.

2.2.1.4. Dynamics

Much of the molecular modelling has focused on equilibrium conditions to observe EDL structures. Dynamic effects are arguably equally important in considering overall EDLC systems, as they influence important aspects, such as power density. A MD simulation examined the dynamic effect of RTIL polarisation relaxation,[74] whereby the electric field was removed. A united-atom model of

the RTIL $[DMIM]^+[Cl]^-$ was simulated between two planar electrodes with surface charge densities of ± 2 μC cm^{-2}. Relaxation of polarisation, in which the ions undergo structural rearrangement, was found to occur in two stages. Firstly, 80% of the decay occurs under 0.2 ps, the remaining 20% of the decay exhibited a sub-diffusive mechanism with an 8 ps time constant. The time scale for this process is too short for ionic diffusion forces to be involved. Relaxation was attributed to small anion (Cl^-) translations, with anion segregation towards the anode being the most noticeable structural change.

The effect of temperature on interface dynamics was examined by MD simulations which characterised local self-diffusion coefficients and ionic residence time.[46] Maximum local self-diffusion coefficients were found to correlate with regions of low ionic density for both anions and cations. Increasing the temperature from 300 to 400 K had no qualitative effect on the interfacial dynamics even though the self-diffusion coefficients increased by an order of magnitude. Residence times of ions in the first and second adsorbed layers were long which indicated glass-like behaviour of RTILs near electrode surfaces.[46]

Hung et al.[75-79] studied the dynamic properties of various asymmetric, imidazolium-based RTILs and their structures when confined within uncharged CNTs,[75] mesopores,[76] and slit-type graphite mesopores;[77-78] as well as between charged planar graphite electrodes.[79] For uncharged pores, regardless of their geometry, confined dynamics were found to be significantly slower than bulk dynamics. Inside pores, strong heterogeneity in dynamics was observed with dependence on the distance of the ions from the pore walls. Ions in the centre of the pores had faster dynamics and shorter relaxation times than ions near pore walls. Reduction in ion loading in the pore can create complex dynamics when regions of low and high densities form in the centre of pores. Overall, when ion loading was reduced, dynamics in pores were observed to be faster than that in the bulk.

For charged graphite electrodes, the surface charge density had a significant impact on the dynamics of confined RTILs, especially for the layers close the electrode surface. In the layer of ions near negatively charged electrode, the neutral tails of the cations clustered together to form small, non-polar domains. Raising the surface charge density reduced relaxation times and the ions exhibited strong deviations from Gaussian dynamics. The displacement of ions increased near the surface of the electrode, and in the centre of the pore, in the direction parallel to the electrode surface; and became comparable to bulk displacements.[79]

Dynamics of RTILs confined in nanopores is an area of concern in the design of EDLC due to the combination of high viscosity of the electrolytes and long diffusion paths to the bulk. More simulation research in this area with a focus, specifically on how dynamics can be

positively manipulated rather than just characterised for certain electrode – electrolyte combinations, may provide solutions to this problem.

2.2.1.5. Non-electrostatic forces

Whilst most molecular simulations have focussed on steric and electrostatic forces related to ion size asymmetry and electric potential variation, it is useful to study other forces of lesser magnitude, such as weak-intermolecular dispersion forces or specific ionic adsorption. Non-electrostatic forces can be particularly influential on EDL structure at low voltages, yet mechanisms of these forces are less well-understood than electrostatic interactions. MC simulations of dispersion forces in RTILs and their effect on the differential capacitance at planar electrodes were conducted by Trulsson *et al*.[80] Using a simple coarse-grained model based on Lennard-Jones monomers, dispersion forces were shown to play a significant role in the camel-shaped differential capacitance behaviour observed experimentally.[37-39] The mechanism was intrinsically linked to the surface tension at the electrode/electrolyte interface; at low surface charge densities, the loss of dispersion interactions near the electrode caused a reduction in ionic density, which correlated to the reduction in differential capacitance, as shown in Figure 2-10.

Specific adsorption is a phenomenon that lacks robust theory, and its effect on the performance of an EDLC is often overlooked. MD simulations were used to examine the effect of specific adsorption of the cation on the differential capacitance of $[BMIM]^+[PF_6]^-$ and $[DMIM]^+[PF_6]^-$.[81] Specific adsorption of the cation was found to affect the differential capacitance in three distinct ways. Firstly, specific adsorption caused a shift increasing the PZC. Both cations $[DMIM]^+$ and $[BMIM]^+$ are incompressible, but $[BMIM]^+$ has a butyl tail which can be thought of as a latent void that can be replaced by $[PF_6]^-$ at positive electrode polarisation. The PZC of $[DMIM]^+$ was found to locate at a local maximum and the PZC of $[BMIM]^+$ was observed to locate at a local minimum. This effect is analogous to that of the dispersion forces studied by Trulsson et al.[80]

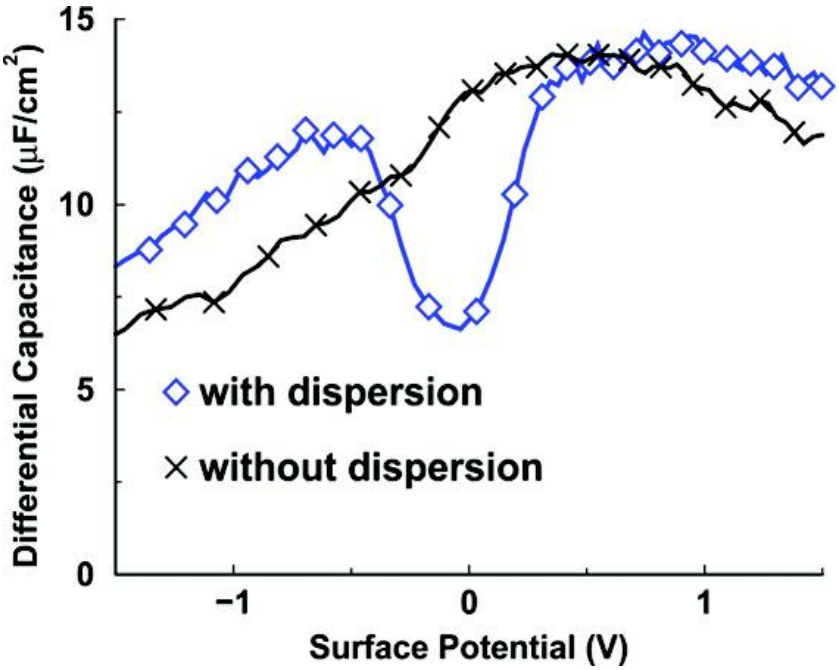

Figure 2-10. Effect of dispersion forces on differential capacitance as a function surface potential. Reproduced with permission from[80]. Copyright 2010 American Chemical Society.

Secondly, the differential capacitance was higher for positive polarisations than for negative polarisations, even though the ions were of a similar size. Specific adsorption of the cation to the anode raised the electrode potential and lowered the differential capacitance. At the cathode the specific adsorption of the cation had the opposite effect, resulting in a higher peak at the cathode than at the anode.

Thirdly, when $[DMIM]^+$ was specifically adsorbed, the variation of electrode potential near the PZC did not have a significant effect on the cation. However, the neighbouring anionic layer was altered. Consequently, the local minimum of the camel-shaped capacitance curve may be unrelated to the PZC for a system containing incompressible and specifically-adsorbed ions.

More attention on specific adsorption, and particularly how it affects the charge storage mechanisms in nanoporous electrodes, particularly at low voltages would be useful in the future for helping find high-performance electrolyte – electrode combinations.

2.2.2. Organic solvent based electrolytes

2.2.2.1. $[TEA]^+[BF_4]^-$ in ACN and PC

Organic solvent based electrolytes are the most commonly used electrolyte in commercial EDLCs. It is important for modelling to reflect contemporary research and commercial applications alongside studying innovative materials.

Reverse Monte Carlo (RMC) simulations, in which an inverse problem is solved by manipulating the model until its parameters match experimental values, was used to investigate the effect of

$[TEA]^+[BF_4]^-$ electrolytes introduced into a PC solution confined in 1 nm wide carbon nanopores.[82] Experimental data was generated by using 0.5 and 1.0 M $[TEA]^+[BF_4]^-$ - PC solutions in pitch-based activated-carbon-fibre nanopores. Synchrotron X-ray diffraction data was used in the RMC simulations to determine the probable molecular arrangements. It was found that the addition of electrolytes induced a distinct ordering of the PC molecules inside the nanopores and promoted the orientation of PC molecules along the pore walls with double peaks near the monolayer positions. PC molecules formed a double-layer-like structure including the $[TEA]^+$ and $[BF_4]^-$ ions. It was concluded that the structural modulation function of PC molecules, in which organic salts are accepted efficiently regardless of intensive space restriction, should contribute to the evolution of high-capacitance nanoporous EDLCs.

A MD simulation of $[TEA]^+[BF_4]^-$ electrolytes in a PC solution confined between CNT forests and adsorbed to the surface of a single CNT, as shown in Figure 2-11, investigated the effect of pore size on EDL capacitance.[83] A modest increase in capacitance was observed when decreasing pore size to less than 1 nm, in good agreement with the experimental observations of Chmiola et al.[53] The $[BF_4]^-$ ions were found to be more effective than $[TEA]^+$ in screening electrode charge due to their small size which allows a closer approach to the electrode surface, resulting in increased capacitance.

Feng et al.[13] also performed MD simulations of a 1.2 M solution of organic electrolyte $[TEA]^+[BF_4]^-$ solubilised in ACN between planar electrodes to study the structure and dynamics of the EDL with varying electric field strength. Their MD simulations were complimented by q-DFT calculations to determine the solvation free energy of the electrolytes. $[TEA]^+[BF_4]^-$ exhibited much weaker solvation than other inorganic ions in aqueous solutions.[84] Additionally, the ACN molecules in the solvation shell of both ions showed weak packing and orientational ordering. The EDL structure at neutral electrodes exhibited strong solvent layering and orientational ordering as well as alternating layers of counter-ions and co-ions, a feature that had not previously been observed.

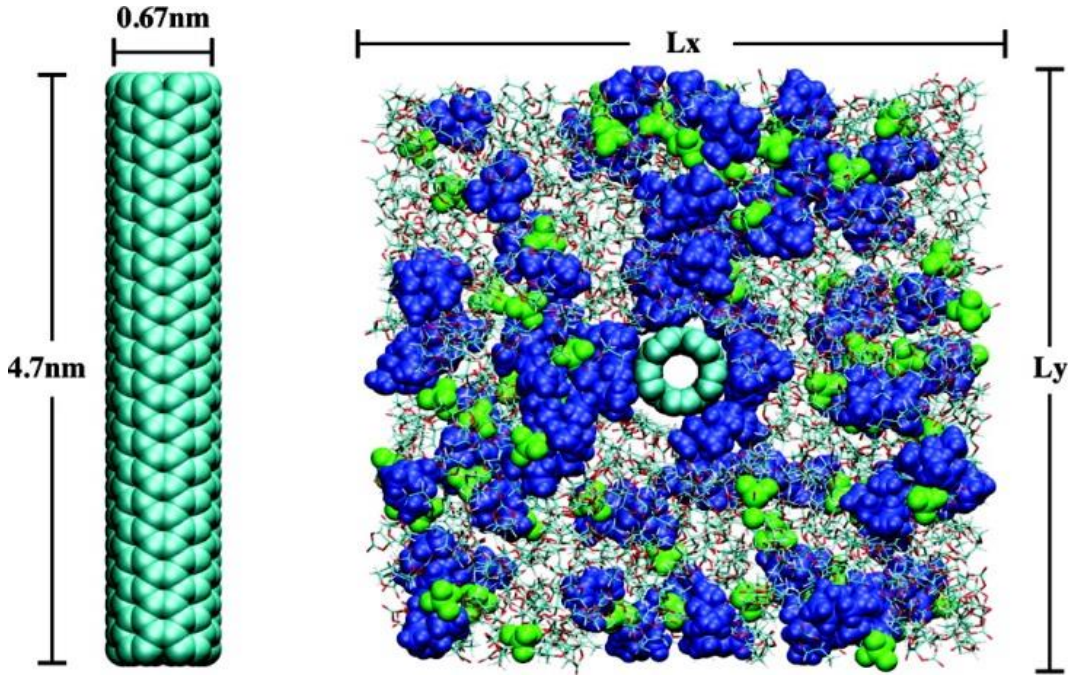

(a) (b)

Figure 2-11. Illustration of the filled nanotube forest with periodic boundary conditions. (a): The nanotube model. (b): Cross-sectional configuration perpendicular to the nanotubes, the blue balls depict the $[TEA]^+$ cations, the green balls represent the $[BF_4]^-$ anions, and the stick figures show the PC molecules. Reproduced with permission from[83]. Copyright 2009 American Chemical Society.

2.2.2.2. RTIL - ACN mixtures

Organic solvents can be used in conjunction with RTILs to introduce beneficial properties, such as increased ionic conductivity and relative permittivity. Molecular simulations of RTIL – ACN mixtures have been conducted to study the influence of the solvent and determine if RTIL – solvent mixtures have advantages over a pure RTILs in designing EDLCs.[32, 85-86]

Feng et al.[85] performed MD simulations of a pure $[BMIM]^+$ $[BF_4]^-$ RTIL and of $[BMIM]^+$ and $[BF_4]^-$ ions in ACN on the basis of their previous work.[13] Extending a previous model using MILO,[14] the authors developed a theoretical framework termed "counter-charge layer in generalised solvents" (CGS), which was used to describe the structure and capacitance of the EDL in RTILs-solvent mixtures with different mass fractions of organic solvents.

In the CGS framework[85] the EDL is treated as an N-layer entity with the zeroth layer consisting solely of counter-ions which overscreen the electrode charge. The subsequent layers contain sub-layers of counter-ions and co-ions. In the first layer, the counter-ion sub-layer is closer to the electrode surface than the co-ion sub-layer and this order alternates for all following layers. The charges of each sub-layer are equal and balance each other. As the layers increase, the effective ion accumulation oscillates in a decaying fashion between overscreening and underscreening the electrode charge until the electrode charge is exactly balanced by the adsorbed ions, as shown in

Figure 2-12. The CGS framework emphasises that the counter- and co-ions must be considered together as a pair, rather than as individual ions as done in previous frameworks. Incorporated ACN molecules have preferential orientations with respect to the electrode and the net dipole moments produced by the ACN molecules also oscillate.

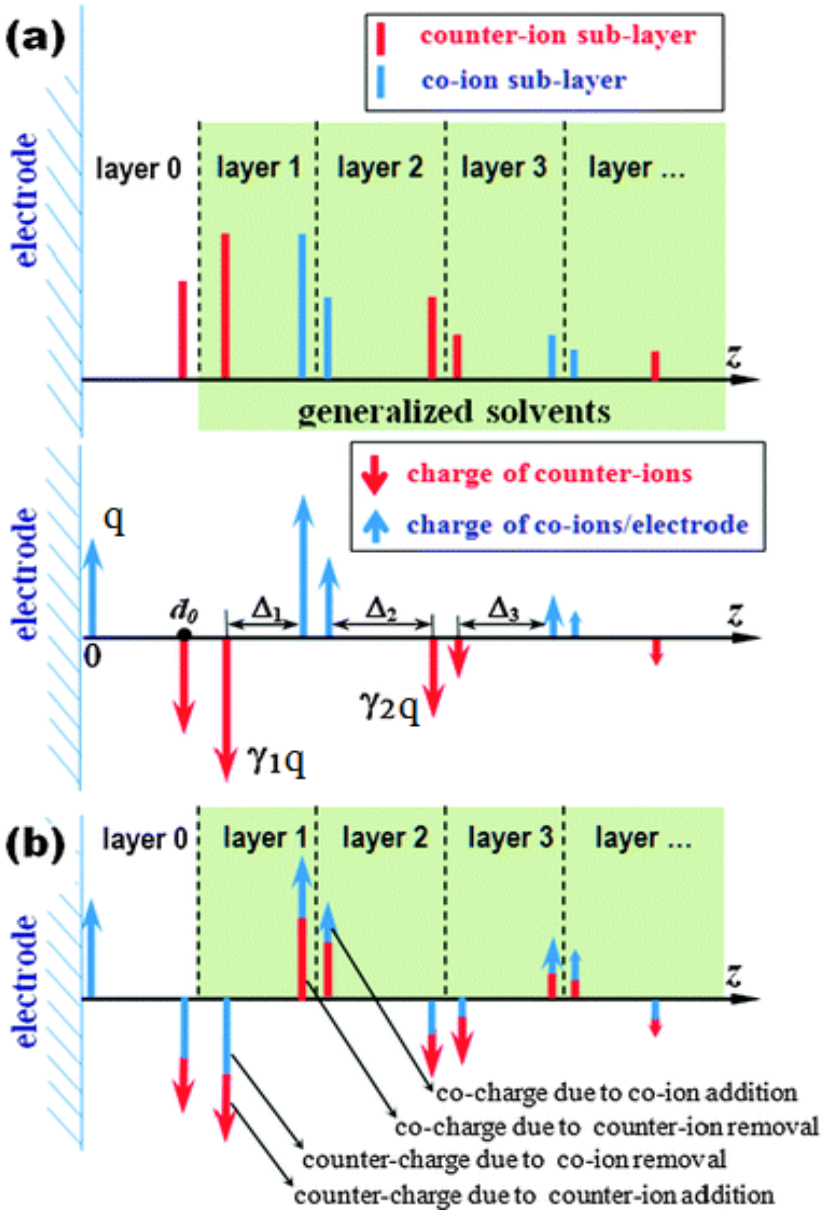

Figure 2-12. Descriptions of an EDL structure using the CGS framework. (a) Distribution of ions (top panel) and the corresponding space charges (bottom panel) inside an EDL near an electrode with a surface charge density of *q*. An EDL is divided into N layers: the zeroth layer balances the electrode charge, and all other layers consist of a counter-ion sub-layer and a co-ion sub-layer. All EDL layers except the zeroth layer carry zero net charge and are thus considered as "generalised solvents." (b) A description of the effective space charge layers inside an EDL focusing on the change of space charge as the surface charge density of the electrode changes from zero to *q*. Reproduced from[85]. with permission from PCCP Owner Societies.

The authors derived the following equation for the potential drop across the EDL by solving the Poisson equation,[85]

$$\Delta\varnothing_{EDL} = q\left[d_0 + \sum_{i-1}^{N} (-1)^i \gamma_i \Delta_i - N_{sol}\mu_{sol}\cos\theta \right] / \varepsilon_0 \qquad (2\text{-}2)$$

where q is the electrode surface charge density, d_0 is the distance between the electrode surface and the zeroth counter-ion layer, γ_i is the magnitude of the charge of counter/co-ions in the ith EDL per unit area scaled by the electrode surface charge density, Δ_i is the distance between the counter-ion sub-layer and co-ion sub-layer of the ith EDL, N_{sol} is the amount of solvent molecules inside the entire EDL per unit area scaled by the electrode surface charge density, μ_{sol} is the dipole moment of each solvent molecule, and $cos\ \theta$ is the average dipole orientation of all solvent molecules inside the EDL with respect to the normal direction of the electrode surface, and ε_0 is permittivity of vacuum.

The simulation by Feng et al.[85] modelled the electrodes as planar, graphene layers with relatively large surface charge densities of +0.1 and -0.1 C m^{-2} on the anode and cathode, respectively. The mass fraction of ACN was varied between zero and 50%. The capacitance for the pure RTIL system was found to be 6 – 8 μF cm^{-2}, which was lower than experimental measurements (approximately 12 μF cm^{-2}) on platinum, gold, and glassy carbon electrodes.[38, 87] However, at the time of publication, the predicted capacitance was consistent with previous MD simulations.[43, 45, 47]

The simulations revealed two interesting phenomena that could not be explained by previous frameworks. Firstly, the capacitance of the system increased by approximately 10% with the increase in ACN concentration from zero to 50%. This was less than expected, as the relative permittivity of ACN is higher than pure RTIL (35.8[88] compared to 12.2[89]) and the capacitance was thus expected to increase proportionally to the mass fraction of ACN.

Secondly, the capacitance near the anode with counter-ion $[BF_4]^-$ was higher than the capacitance near the cathode with counter-ion $[BMIM]^+$, even though both ions approached the electrode surfaces to effectively the same distance.

Both observations were rationalised using the CGS framework. Adding ACN molecules displaced the $[BF_4]^-$ and $[BMIM]^+$ ions in the first and second layers by approximately 60%. The ACN molecules displaced and electrostatically screened interactions between $[BF_4]^-$ and $[BMIM]^+$ ions, which reduced the correlations between the ions and in turn reduced the electrostatic overscreening and apparent capacitance. Conversely, addition of solvent molecules increased the capacitance because dielectric screening caused by the solvent was greater than that by the RTILs in the EDL.

These two effects had a competing influence on capacitance that resulted in only a small increase overall when ACN was introduced into the system, as observed previously.[85]

In addition, the counter charges in the first EDL layer near the anode were due predominately to the addition of $[BF_4]^-$ counter-ions, while the counter charges in the first EDL layer near the cathode were due predominately to the removal of $[BF_4]^-$ co-ions. It is this difference that caused the disparity of capacitance at the different electrodes. $[BMIM]^+$ ions were preferentially adsorbed to a neutral electrode, when the electrode became positively charged, the removal of larger $[BMIM]^+$ ions allowed for a significant accumulation of the smaller $[BF_4]^-$ ions. Conversely, as the electrode became negatively charged, the removal of $[BF_4]^-$ ions left little space for the adsorption of $[BMIM]^+$ ions. Additionally, the $[BMIM]^+$ ions that were already adsorbed restricted the removal of $[BF_4]^-$ ions due to electrostatic interactions.[85]

A similar MD simulation of a graphene-based EDLC with both the pure RTIL $[EMIM]^+[BF_4]^-$ and a 1.1 M solution of $[EMIM]^+[BF_4]^-$ electrolytes in ACN was performed by Shim et al.[32] The pure RTIL out-performed the ACN solution by 55-60 % in electrode-surface-normalised specific capacitance due to strong screening behaviour of the pure RTIL. Ion size asymmetry resulted in electrode capacitance disparity in both the pure RTIL and ACN solution. Interestingly, despite the higher viscosity and the lower ion diffusivity in the pure RTIL, its overall conductivity was comparable to the ACN solution due to the large number of charge carriers. This suggests that the increase in energy density for the pure RTIL does not come at the cost of a reduced power density compared to organic electrolytes at planar electrodes. It is unlikely that this observation can be extended to porous electrodes where confinement has a significant effect on the dynamics. In a following MD simulation, the authors extended the electrode model to parallel plate geometry and varied the surface charge density and the plate separation.[90]

Recently, Merlet et al.[86] used MD simulations of the pure RTILs $[BMIM]^+[BF_4]^-$ and $[BMIM]^+[PF_6]^-$ and a 1.5 M solution of the RTILs in ACN to study the capacitive properties at the surface of planar graphite electrodes. The distinct interfacial characteristics of the two pure RTILs were found to become very similar to one another upon solvation with ACN. Solvation was found to reduce the layering density near the electrode surfaces. However, this reduced the capacitance to a lesser degree than expected. Polarisation of the electrode was included by using a constant-potential model rather than a constant-charge model and found to be highly influenced by the type of electrolyte. Pure RTILs produced charge distribution functions with irregular shapes which were dependent on the specific structure and atomic composition of the ions. In contrast, charge distribution functions in solvent systems more closely matched Gaussian distributions and were independent of the anion size. Furthermore, in pure RTILs the polarisation of the electrode led to a

greater difference between positive and negative applied potentials due to the asymmetry of the ions.

The next possible steps for simulations of RTIL – organic solvent mixtures is to systematically compare the influence of PC solvent compared to ACN solvent as PC is the more favourable solvent due to its low toxicity. More importantly though, RTIL – organic solvent mixtures should be simulated with accurate nanoporous and exohedral curvature electrode models, where the charge storage mechanisms are known to be different from planar electrode surfaces, so that capacitance and ionic conductivity can be optimised for systems which can be realistically applied to EDLCs.

2.2.3. Aqueous electrolytes

Aqueous electrolytes, despite offering smaller energy density than organic solvent based electrolytes or RTILs due to their lower electric potential window, still have attractive properties such as high relative permittivity, low ESR, low toxicity, and low cost. They are preferable to other electrolyte types in certain applications. It is also important to note that exceptional performance of EDLC can be achieved with aqueous electrolytes.[91]

The extended simple point-charge model[92-93] was used to conduct equilibrium and non-equilibrium MD simulations of the transport of aqueous K^+Cl^- electrolyte in charged cylindrical nanoporous electrodes.[94] The surface of the electrode was modelled as smooth, and hydrophobic. The radius of the electrode was varied to investigate ionic confinement effects. It was found that strong confinement caused desolvation of ions, increased the influence of the external field on water molecule orientation, and decreased hydrogen bonding. Ionic conductivity was also found to decrease with decreasing pore radius.

MD simulations were used to examine ion size effects in negatively-charged nanoporous (5,5) armchair CNTs with a diameter of 0.67 nm and a length of 1.1 nm interacting with Na^+, K^+, and Cs^+ cations in an aqueous solution.[95] At zero surface potential, water molecules entered the CNTs in low concentrations and formed a single-layer wire down the centre of the CNT. At low negative surface charge densities, more water molecules were transferred into the CNTs with a preferred orientation, causing a low density area in the centre of the CNTs due to water-water molecule repulsion. At greater negative surface charge densities, it was thermodynamically favourable for cations to be partitioned into the pore. Interestingly, the medium-sized K^+ ions were found to have the least resistance to entering the pore, while the smallest Na^+ ions had the greatest partition resistance. It should be noted that no anions were included in these simulations. In fact, anions may

be present in weakly negatively-charged electrodes due to specific adsorption, which would drastically change the observed results.

Feng et al.[62] used MD simulations to study the effect of slit-type nanopore width on the distribution of K^+ ions and on the capacitance at a constant surface charge density. By examining long-range ion-ion interactions, non-electrostatic ion-electrode interactions, ion hydration, hydration water molecule – non-hydration water molecule interactions, and entropic effects, the authors were able to make several interesting observations. For pore widths between 1.0 and 1.5 nm, K^+ ions formed a well-hydrated single layer in the centre of the pores. Below 1 nm, the K^+ ions formed two separate layers near each slit wall. The transition from a single to a double layer was driven mainly by enthalpic effects between hydrated water molecules and the surrounding non-hydrated water molecules rather than by electrostatic interactions between ions. On the basis of these results, the authors suggested a 'sandwich model' describing the capacitance of single-layer ions in slit-type nanopores that is capable of predicting the anomalous increase in capacitance,[62]

$$C_{tot} = \frac{2A\varepsilon_r\varepsilon_0}{(b - a_0)} \qquad (2\text{-}3)$$

where b is the slit-pore width and a_0 is the solvated ion diameter. It is important to note that the results from this study are not valid for systems with lower surface charge densities where anions would be included inside the pore. The authors considered a simulation of an aqueous NaCl solution to examine the energy penalty associated with partial desolvation of solvated ions entering a sub-nanometre pore.[96] Low free energy penalties were observed for both Na^+ and Cl^- ions and was attributed to van der Waals attractions between ions and pore walls, image charge effects, and strengthening interactions between ions and their solvation molecules inside the pore

MD simulations of aqueous NaCl solutions in contact with uncharged slit and cylindrical porous carbon electrodes in mesoporous and nanoporous regimes were used to study interfacial confinement effects and provide an atomic-scale depiction of ion transport dynamics.[97] Their simulations indicate that ordered layers form parallel to the surface of the electrodes and facilitate focused ion motion under confined conditions. This enhances ion diffusivity in the direction of the pore or slit. However, under increased confinement where the pore or slit size is reduced, the ionic diffusivity decreases.

Similar MD simulations of aqueous NaCl electrolytes inside charged nanoporous graphene and slit-pore electrodes were performed by Kalluri *et al*.[98] Opposite sides of the pore walls were modelled as the anode and cathode. The electrolyte concentration, the surface charge densities, and the pore

diameter were all varied to study the structural properties of the aqueous electrolytes. At the highest surface charge density tested (+ 40 μC cm^{-2}) it was found that the ionic concentration inside the pores reached approximately 10 times the bulk concentration. Also at ± 40 μC cm^{-2}, it was observed that the Na^+ confined between electrodes separated by 1.2 nm approached the negatively charged graphene surface more closely than the water molecules and partly lost their hydration shells. It was also found that multiple layers of adsorbed electrolytes formed near the electrode surface. This behaviour was similar to that observed by Wander et al.[97] and was attributed not only to electrostatic interactions but also to hydration phenomena and ion-ion correlations.

Recent MD simulations considered a similar system, but included $CaCl_2$ solutions as well as NaCl solutions to investigate ion size effects alongside the effect of nanopore width.[99] A schematic of the simulation cell is shown in Figure 2-13.

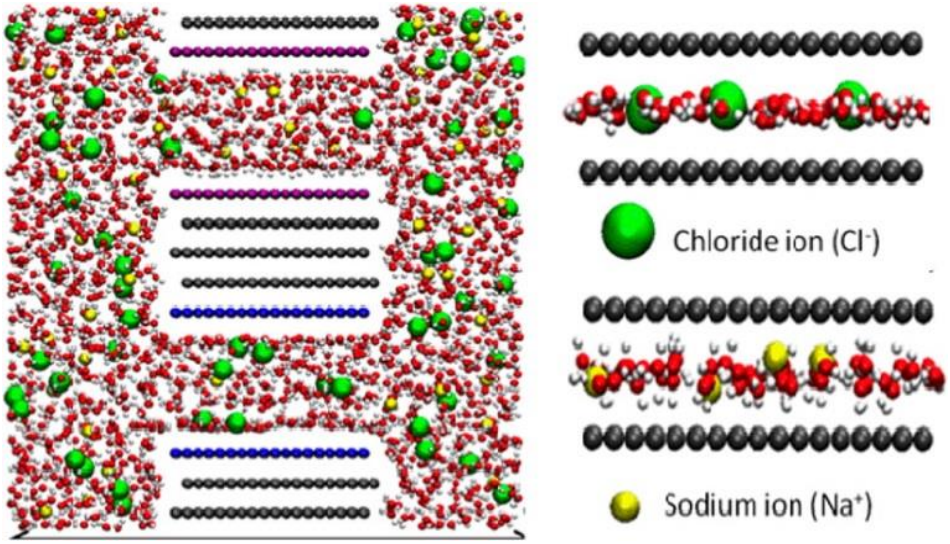

Figure 2-13. Two-dimensional schematic of simulation box with yellow Na^+ ions, green Cl^- ions, red and white water molecules, black neutral carbons, blue positively charged carbons, and purple negatively charged carbons. Reproduced with permission from[99]. Copyright 2013 American Chemical Society.

As expected, as pore size decreased, higher surface charge densities were required for ions to enter the pore. Maximum ionic densities inside the pore were dependent on the ion type and occurred at different pore widths for different ions. Analysis of the internal pore structure revealed that ion-ion correlations are only important for larger pore widths at low surface charge densities. In smaller pores especially, water-ion correlations are important for determining the correct distribution of ions. This is crucial for estimating the EDL thickness and the resulting capacitance.

Aqueous electrolytes offer exceptionally high power density for EDLCs, yet their energy densities are often lacking. To compete with high energy densities offered by RTIL electrolytes, future simulations of EDLCs with aqueous electrolytes must have a focus on optimisation of novel electrode materials, as opposed to the slit-type nanopores used in

previous simulations. Accurately incorporating pseudocapacitive behaviour into molecular simulations could also unlock a new area of simulation research relevant to aqueous electrolytes where large gains in electrocapacitive performance may be made.

2.3. Recent insights of significance

In recent years developments in molecular modelling and *in situ* techniques has led to further understanding of molecular mechanisms of charge storage mechanisms in EDLCs. Péan et al.[100] demonstrated via molecular dynamics that porous CDC electrodes exhibit fast charging dynamics when wetted with a pure RTIL. They found that the charging rate was strongly dependent on the average pore size, and that the position and magnitude of the charge stored within the electrode evolved over time as the ions migrated and rearranged. In further work that considered the influence of electrode potential, and solvation of the RTIL in ACN,[101] they showed that potential increased the charging rate yet interestingly solvation did not have an effect. The charge and discharge cycle was confirmed to be reversible in their simulation and it was concluded that counter- and co-ion rearrangement occurred on different time-scales, resulting in a two-stage, fast then slow, charging regime.

Using Gibbs MC simulations of $[EMIM]^+[BF4]^-$ inside three different porous electrodes, activated carbon fibre-15 (ACF-15), silicon derived CDC (Si-CDC), and titanium derived CDC; Varanasi et al.[102] found similar gravimetric and volumetric capacitance values for the three materials despite the large variation in their pore size distributions and local pore structures. The results were attributed to the materials with smaller accessible pore volume de-coordinating the counter-ions to a greater extent, allowing for higher induction of charge into the electrode. This study demonstrates that the constant potential method is successfully applicable to carbon electrodes of different origins, allowing for more direct simulation comparisons in future when further electrode models become available.

Development of *in situ* quartz-crystal microbalance (QCMB) and nuclear magnetic resonance (NMR) techniques have established a mechanism for experimental measurement of electrolyte structure, and charge storage mechanisms inside highly porous electrodes. This has provided molecular modelling with a pathway to compare more directly with experimental measurements, an area that was recently not available. Using QCMB measurements, Tsai et al.[103] showed that the charge storage mechanism of $[EMIM]^+[TFSI]^-$ inside CDC electrodes was potential dependent, and favoured counter-ion insertion at high potential. When the RTIL was solvated in ACN, they also quantified the cation solvation number inside the negative electrode, and showed that for smaller pores more ACN

molecules are desolvated to accommodate the ion entering. NMR measurements by Grey et al.[104-106] has been used to quantify the ion composition inside of CDC pores as a function of pore size,[105] and ion concentration in solvent and electrode potential.[106] Ion dynamics inside CDC electrodes has also been examined for different RTIL pairs, both with and without ACN solvation.[104] The insights gained have helped rationalise the rich behaviour observed in EDLCs with different electrode/electrolyte compositions and can help with future predictions of performance for new materials and combinations.

Vatamanu et al.[107] performed comprehensive MD simulations of multiple ionic liquids, and their mixtures in 1:10 mol ratio of ACN, at planar and corrugated graphitic electrodes. They noted at the planar surface (both positive and negative), the orientation of the ACN molecules switched from parallel to perpendicular with increasing electric potential, and that the capacitance systematically increased slightly with the addition of ACN. At corrugated surfaces, the mixtures with ACN did not display enhanced DC compared with the planar surface. This contrasted with the behaviour of pure ionic-liquids and was attributed to the increase in the effective solvated diameter of the ions due to the ACN solvation shell around the ions. Consequently, the thicknesses of the corrugations were no longer tuned to the ion diameter, and the ions penetrated less deeply into the corrugations. Finally, they showed that the ionic-liquid mixtures with ACN exhibited a weak temperature dependence on the DC over the range of 333 K to 493 K. This is not the case for pure RTILs where the viscosity can be greatly reduced by increased temperature.

Finally, Kondrat and Kornyshev[108] have shown by MC simulation that zero-potential non-wetting pores, termed ‘ionophobic’, can have higher energy density than conventional wettable pores, which are often activated or doped to increase their wettability. This seems counterintuitive on the surface and may open an entirely new class of pore for researchers to define. Molecular modelling will be most useful here for examining the complex energy interactions that will occur here, and the effect on kinetics and charge storage performance.

2.4. Conclusions and gaps in the literature

Contemporary molecular modelling has contributed greatly to the understanding of charge storage mechanisms and dynamics in EDLCs in response to experiments that have challenged long held views of the EDL.

Molecular modelling has largely focussed on planar electrodes to study steric and potential effects, and porous electrodes to study confinement effects, under equilibrium conditions. Molecular simulations have concluded that the EDL structure of RTILs at planar electrode

surfaces is characterised by large potential overscreening and multiple layers of adsorbed ions with alternating charge.[14] Introducing controlled surface roughness to planar electrodes can promote ion separation and increase the capacitance as the distance between extruding planes approaches the ion diameters.[51] Nanopores have greater charge storage efficiency per unit area than planar electrodes, because the total electrode charge is balanced by a single layer of ions without overscreening.[31] Optimal energy density is a non-monotonic function of pore diameter, and optimal pore diameter increases with voltage.[55] Polarisation of the electrode by the electrolyte enhances surface charge via induced charges, resulting in an increase in electric field strength and capacitance. This is a critical feature that needs to be included in molecular models that aim to quantitatively reproduce experimental results and accurately represent real systems.

Comparatively, dynamic effects have been modelled to a lesser extent and suggestions for exploiting these effects to increase EDLC performance are young. Future work in molecular modelling could expand to include a greater focus on ionic transport and charging/discharging kinetics to characterise, and improve performance of dense RTIL electrolytes in nanoporous carbons. Furthermore, simulations that predict kinetics under different charging/discharging rates will be useful for optimisation of energy and power densities, and recent studies have been performed with this in mind.

Addition of ACN organic solvent to RTILs could lead to increased electrolyte performance, however molecular modelling has shown the capacitance behaviour to be complex. The addition of an organic solvent can reduce viscosity, and ESR; as well as increase ionic conductivity, and relative permittivity. However, this is balanced by a reduction in ionic density due to solvent molecules electrostatically screening interactions and reducing ionic correlations, which in turn lowers the capacitance. Overall, minimal change in capacitance as a function of solvent concentration has been observed from simulations.[85] This contrasts with experimental results which showed large changes in capacitance as a function of ACN solvent concentration.[109] Further experimental and molecular modelling research in this area is required. A more systematic approach to understanding solvent effects inside porous electrodes would be very useful for future predictions. This is because simulations which compare only a pure RTIL and a highly solvated system lack the ability to determine if any interesting phenomena occur at intermediate concentrations. By simulating over a range of ACN concentrations, a progressive charge storage mechanism from pure RTIL to dilute in ACN would be able to be tracked. Furthermore, optimal points between capacitance and other electrolyte properties have the potential to be determined, and then predicted for a

range of various materials. This concept of systematic ACN dependence is the main focus of this thesis, and it is applied over several different solid structures. Other gaps in the literature, which are outside the scope of this thesis, are identified in the Section 8.2 of the Conclusions and Perspectives Chapter (8).

2.5. References

1. Allen, M. P.; Tildesley, D. J., *Computer Simulation of Liquids*; Oxford university press, 1989.
2. Frenkel, D.; Smit, B.; Ratner, M. A., Understanding Molecular Simulation: From Algorithms to Applications. *Phys. Today* **1997**, *50*, 66.
3. Boda, D.; Fawcett, W. R.; Henderson, D.; Sokolowski, S., Monte Carlo, Density Functional Theory, and Poisson--Boltzmann Theory Study of the Structure of an Electrolyte near an Electrode. *J. Chem. Phys.* **2002**, *116*, 7170-7.
4. Patra, C. N.; Ghosh, S. K., Structure of Electric Double Layers: A Self-Consistent Weighted-Density-Functional Approach. *J. Chem. Phys.* **2002**, *117*, 8938-6.
5. Patra, C. N., Structure of Spherical Electric Double Layers Containing Mixed Electrolytes: A Systematic Study by Monte Carlo Simulations and Density Functional Theory. *J. Phys. Chem. B* **2010**, *114*, 10550-10557.
6. Goel, T.; Patra, C. N.; Ghosh, S. K.; Mukherjee, T., Molecular Solvent Model of Cylindrical Electric Double Layers: A Systematic Study by Monte Carlo Simulations and Density Functional Theory. *J. Chem. Phys.* **2008**, *129*, 154707-10.
7. Goel, T.; Patra, C. N.; Ghosh, S. K.; Mukherjee, T., Three Component Model of Cylindrical Electric Double Layers Containing Mixed Electrolytes: A Systematic Study by Monte Carlo Simulations and Density Functional Theory. *J. Chem. Phys.* **2010**, *132*, 194706-9.
8. Wang, Y.; Jiang, W.; Yan, T.; Voth, G. A., Understanding Ionic Liquids through Atomistic and Coarse-Grained Molecular Dynamics Simulations. *Acc. Chem. Res.* **2007**, *40*, 1193-1199.
9. Merlet, C.; Salanne, M.; Rotenberg, B., New Coarse-Grained Models of Imidazolium Ionic Liquids for Bulk and Interfacial Molecular Simulations. *J. Phys. Chem. C* **2012**, *116*, 7687-7693.
10. Merlet, C.; Pean, C.; Rotenberg, B.; Madden, P. A.; Simon, P.; Salanne, M., Simulating Supercapacitors: Can We Model Electrodes as Constant Charge Surfaces? *J. Phys. Chem. Lett.* **2013**, *4*, 264-268.
11. Schmickler, W., Electronic Effects in the Electric Double Layer. *Chem. Rev.* **1996**, *96*, 3177-3200.
12. Parr, R. G.; Yang, W., *Density-Functional Theory of Atoms and Molecules*; Oxford university press, 1989; Vol. 16.

13. Feng, G.; Huang, J.; Sumpter, B. G.; Meunier, V.; Qiao, R., Structure and Dynamics of Electrical Double Layers in Organic Electrolytes. *Phys. Chem. Chem. Phys.* **2010**, *12*, 5468-5479.

14. Feng, G.; Qiao, R.; Huang, J.; Dai, S.; Sumpter, B. G.; Meunier, V., The Importance of Ion Size and Electrode Curvature on Electrical Double Layers in Ionic Liquids. *Phys. Chem. Chem. Phys.* **2011**, *13*, 1152-1161.

15. Lee, J. W.; Nilson, R. H.; Templeton, J. A.; Griffiths, S. K.; Kung, A.; Wong, B. M., Comparison of Molecular Dynamics with Classical Density Functional and Poisson–Boltzmann Theories of the Electric Double Layer in Nanochannels. *J. Chem. Theory Comput.* **2012**, *8*, 2012-2022.

16. Jiang, D.; Wu, J., Microscopic Insights into the Electrochemical Behavior of Nonaqueous Electrolytes in Electric Double-Layer Capacitors. *J. Phys. Chem. Lett.* **2013**, *4*, 1260-1267.

17. Hou, C.-H.; Taboada-Serrano, P.; Yiacoumi, S.; Tsouris, C., Monte Carlo Simulation of Electrical Double-Layer Formation from Mixtures of Electrolytes inside Nanopores. *J. Chem. Phys.* **2008**, *128*, 044705-8.

18. Kiyohara, K.; Asaka, K., Monte Carlo Simulation of Porous Electrodes in the Constant Voltage Ensemble. *J. Phys. Chem. C* **2007**, *111*, 15903-15909.

19. Kiyohara, K.; Asaka, K., Monte Carlo Simulation of Electrolytes in the Constant Voltage Ensemble. *J. Chem. Phys.* **2007**, *126*, 214704-14.

20. Lamperski, S.; Zydor, A., Monte Carlo Study of the Electrode|Solvent Primitive Model Electrolyte Interface. *Electrochim. Acta* **2007**, *52*, 2429-2436.

21. Taboada-Serrano, P.; Yiacoumi, S.; Tsouris, C., Behavior of Mixtures of Symmetric and Asymmetric Electrolytes near Discretely Charged Planar Surfaces: A Monte Carlo Study. *J. Chem. Phys.* **2005**, *123*, 054703-9.

22. Klos, J.; Lamperski, S., Electrical Double Layer Properties in Diameter Asymmetric Molten Salt Investigated by Grand Canonical Monte Carlo Method. *J. Phys. Chem. C* **2010**, *114*, 13329-13333.

23. Yang, K.-L.; Yiacoumi, S.; Tsouris, C., Monte Carlo Simulations of Electrical Double-Layer Formation in Nanopores. *J. Chem. Phys.* **2002**, *117*, 8499-9.

24. Wang, H.; Pilon, L., Accurate Simulations of Electric Double Layer Capacitance of Ultramicroelectrodes. *J. Phys. Chem. C* **2011**, *115*, 16711-16719.

25. Wang, H.; Pilon, L., Mesoscale Modeling of Electric Double Layer Capacitors with Three-Dimensional Ordered Structures. *J. Power Sources* **2013**, *221*, 252-260.

26. Fedorov, M. V.; Kornyshev, A. A., Towards Understanding the Structure and Capacitance of Electrical Double Layer in Ionic Liquids. *Electrochim. Acta* **2008**, *53*, 6835-6840.

27. Kornyshev, A. A., Double-Layer in Ionic Liquids: Paradigm Change? *J. Phys. Chem. B* **2007**, *111*, 5545-5557.

28. Wang, H.; Varghese, J.; Pilon, L., Simulation of Electric Double Layer Capacitors with Mesoporous Electrodes: Effects of Morphology and Electrolyte Permittivity. *Electrochim. Acta* **2011**, *56*, 6189-6197.

29. Largeot, C.; Portet, C.; Chmiola, J.; Taberna, P.-L.; Gogotsi, Y.; Simon, P., Relation between the Ion Size and Pore Size for an Electric Double-Layer Capacitor. *J. Am. Chem. Soc.* **2008**, *130*, 2730-2731.

30. Rogers, E. I.; Sljukić, B.; Hardacre, C.; Compton, R. G., Electrochemistry in Room-Temperature Ionic Liquids: Potential Windows at Mercury Electrodes. *J. Chem. Eng. Data* **2009**, *54*, 2049-2053.

31. Merlet, C.; Rotenberg, B.; Madden, P. A.; Taberna, P.-L.; Simon, P.; Gogotsi, Y.; Salanne, M., On the Molecular Origin of Supercapacitance in Nanoporous Carbon Electrodes. *Nat. Mater.* **2012**, *11*, 306-310.

32. Shim, Y.; Jung, Y.; Kim, H. J., Graphene-Based Supercapacitors: A Computer Simulation Study. *J. Phys. Chem. C* **2011**, *115*, 23574-23583.

33. Wu, P.; Huang, J.; Meunier, V.; Sumpter, B. G.; Qiao, R., Voltage Dependent Charge Storage Modes and Capacity in Subnanometer Pores. *J. Phys. Chem. Lett.* **2012**, *3*, 1732-1737.

34. Feng, G.; Li, S.; Presser, V.; Cummings, P. T., Molecular Insights into Carbon Supercapacitors Based on Room-Temperature Ionic Liquids. *J. Phys. Chem. Lett.* **2013**, *4*, 3367-3376.

35. Vatamanu, J.; Hu, Z.; Bedrov, D.; Perez, C.; Gogotsi, Y., Increasing Energy Storage in Electrochemical Capacitors with Ionic Liquid Electrolytes and Nanostructured Carbon Electrodes. *J. Phys. Chem. Lett.* **2013**, *4*, 2829-2837.

36. Fedorov, M. V.; Kornyshev, A. A., Ionic Liquid near a Charged Wall: Structure and Capacitance of Electrical Double Layer. *J. Phys. Chem. B* **2008**, *112*, 11868-11872.

37. Alam, M. T.; Islam, M. M.; Okajima, T.; Ohsaka, T., Measurements of Differential Capacitance at Mercury/Room-Temperature Ionic Liquids Interfaces. *J. Phys. Chem. C* **2007**, *111*, 18326-18333.

38. Alam, M. T.; Islam, M. M.; Okajima, T.; Ohsaka, T., Capacitance Measurements in a Series of Room-Temperature Ionic Liquids at Glassy Carbon and Gold Electrode Interfaces. *J. Phys. Chem. C* **2008**, *112*, 16600-16608.

39. Lockett, V.; Sedev, R.; Ralston, J.; Horne, M.; Rodopoulos, T., Differential Capacitance of the Electrical Double Layer in Imidazolium-Based Ionic Liquids: Influence of Potential, Cation Size, and Temperature. *J. Phys. Chem. C* **2008**, *112*, 7486-7495.

40. Fedorov, M. V.; Georgi, N.; Kornyshev, A. A., Double Layer in Ionic Liquids: The Nature of the Camel Shape of Capacitance. *Electrochem. Commun.* **2010**, *12*, 296-299.

41. Metropolis, N.; Rosenbluth, A. W.; Rosenbluth, M. N.; Teller, A. H.; Teller, E., Equation of State Calculations by Fast Computing Machines. *J. Chem. Phys.* **1953**, *21*, 1087-6.

42. Georgi, N.; Kornyshev, A. A.; Fedorov, M. V., The Anatomy of the Double Layer and Capacitance in Ionic Liquids with Anisotropic Ions: Electrostriction Vs. Lattice Saturation. *J. Electroanal. Chem.* **2010**, *649*, 261-267.

43. Feng, G.; Zhang, J. S.; Qiao, R., Microstructure and Capacitance of the Electrical Double Layers at the Interface of Ionic Liquids and Planar Electrodes. *J. Phys. Chem. C* **2009**, *113*, 4549-4559.

44. Wang, S.; Li, S.; Cao, Z.; Yan, T., Molecular Dynamic Simulations of Ionic Liquids at Graphite Surface. *J. Phys. Chem. C* **2009**, *114*, 990-995.

45. Kislenko, S. A.; Samoylov, I. S.; Amirov, R. H., Molecular Dynamics Simulation of the Electrochemical Interface between a Graphite Surface and the Ionic Liquid [Bmim][Pf6]. *Phys. Chem. Chem. Phys.* **2009**, *11*, 5584-5590.

46. Kislenko, S. A.; Amirov, R. H.; Samoylov, I. S., Influence of Temperature on the Structure and Dynamics of the [Bmim][Pf6] Ionic Liquid/Graphite Interface. *Phys. Chem. Chem. Phys.* **2010**, *12*, 11245-11250.

47. Vatamanu, J.; Borodin, O.; Smith, G. D., Molecular Insights into the Potential and Temperature Dependences of the Differential Capacitance of a Room-Temperature Ionic Liquid at Graphite Electrodes. *J. Am. Chem. Soc.* **2010**, *132*, 14825-14833.

48. Vatamanu, J.; Borodin, O.; Smith, G. D., Molecular Simulations of the Electric Double Layer Structure, Differential Capacitance, and Charging Kinetics for N-Methyl-N-Propylpyrrolidinium Bis(Fluorosulfonyl)Imide at Graphite Electrodes. *J. Phys. Chem. B* **2011**, *115*, 3073-3084.

49. Vatamanu, J.; Cao, L.; Borodin, O.; Bedrov, D.; Smith, G. D., On the Influence of Surface Topography on the Electric Double Layer Structure and Differential Capacitance of Graphite/Ionic Liquid Interfaces. *J. Phys. Chem. Lett.* **2011**, *2*, 2267-2272.

50. Vatamanu, J.; Borodin, O.; Bedrov, D.; Smith, G. D., Molecular Dynamics Simulation Study of the Interfacial Structure and Differential Capacitance of Alkylimidazolium

Bis(Trifluoromethanesulfonyl)Imide [Cnmim][Tfsi] Ionic Liquids at Graphite Electrodes. *J. Phys. Chem. C* **2012**, *116*, 7940-7951.

51. Xing, L.; Vatamanu, J.; Smith, G. D.; Bedrov, D., Nanopatterning of Electrode Surfaces as a Potential Route to Improve the Energy Density of Electric Double-Layer Capacitors: Insight from Molecular Simulations. *J. Phys. Chem. Lett.* **2012**, *3*, 1124-1129.

52. Hu, Z.; Vatamanu, J.; Borodin, O.; Bedrov, D., A Molecular Dynamics Simulation Study of the Electric Double Layer and Capacitance of [Bmim][Pf6] and [Bmim][Bf4] Room Temperature Ionic Liquids near Charged Surfaces. *Phys. Chem. Chem. Phys.* **2013**, *15*, 14234 - 14247.

53. Chmiola, J.; Yushin, G.; Gogotsi, Y.; Portet, C.; Simon, P.; Taberna, P.-L., Anomalous Increase in Carbon Capacitance at Pore Sizes Less Than 1 Nanometer. *Science* **2006**, *313*, 1760-1763.

54. Kondrat, S.; Georgi, N.; Fedorov, M. V.; Kornyshev, A. A., A Superionic State in Nano-Porous Double-Layer Capacitors: Insights from Monte Carlo Simulations. *Phys. Chem. Chem. Phys.* **2011**, *13*, 11359-11366.

55. Kondrat, S.; Perez, C.; Presser, V.; Gogotsi, Y.; Kornyshev, A., Effect of Pore Size and Its Dispersity on the Energy Storage in Nanoporous Supercapacitors. *Energy Environ. Sci.* **2012**, *5*, 6474-6479.

56. Shim, Y.; Kim, H. J., Nanoporous Carbon Supercapacitors in an Ionic Liquid: A Computer Simulation Study. *ACS Nano* **2010**, *4*, 2345-2355.

57. Wu, P.; Huang, J.; Meunier, V.; Sumpter, B. G.; Qiao, R., Complex Capacitance Scaling in Ionic Liquids-Filled Nanopores. *ACS Nano* **2011**, *5*, 9044-9051.

58. Xing, L.; Vatamanu, J.; Borodin, O.; Bedrov, D., On the Atomistic Nature of Capacitance Enhancement Generated by Ionic Liquid Electrolyte Confined in Subnanometer Pores. *J. Phys. Chem. Lett.* **2013**, *4*, 132-140.

59. Kondrat, S.; Kornyshev, A., Superionic State in Double-Layer Capacitors with Nanoporous Electrodes. *J. Phys.: Condens. Matter* **2010**, *23*, 022201-5.

60. Feng, G.; Cummings, P. T., Supercapacitor Capacitance Exhibits Oscillatory Behavior as a Function of Nanopore Size. *J. Phys. Chem. Lett.* **2011**, *2*, 2859-2864.

61. Centeno, T. A.; Sereda, O.; Stoeckli, F., Capacitance in Carbon Pores of 0.7 to 15 Nm: A Regular Pattern. *Phys. Chem. Chem. Phys.* **2011**, *13*, 12403-12406.

62. Feng, G.; Qiao, R.; Huang, J.; Sumpter, B. G.; Meunier, V., Ion Distribution in Electrified Micropores and Its Role in the Anomalous Enhancement of Capacitance. *ACS Nano* **2010**, *4*, 2382-2390.

63. Huang, J.; Sumpter, B. G.; Meunier, V., Theoretical Model for Nanoporous Carbon Supercapacitors. *Angew. Chem. Int. Ed.* **2008**, *47*, 520-524.

64. Huang, J.; Sumpter, B. G.; Meunier, V., A Universal Model for Nanoporous Carbon Supercapacitors Applicable to Diverse Pore Regimes, Carbon Materials, and Electrolytes. *Chem. Eur. J.* **2008**, *14*, 6614-6626.

65. Gogotsi, Y.; Nikitin, A.; Ye, H.; Zhou, W.; Fischer, J. E.; Yi, B.; Foley, H. C.; Barsoum, M. W., Nanoporous Carbide-Derived Carbon with Tunable Pore Size. *Nat. Mater.* **2003**, *2*, 591-594.

66. Merlet, C.; Salanne, M.; Rotenberg, B.; Madden, P. A., Imidazolium Ionic Liquid Interfaces with Vapor and Graphite: Interfacial Tension and Capacitance from Coarse-Grained Molecular Simulations. *J. Phys. Chem. C* **2011**, *115*, 16613-16618.

67. Palmer, J. C.; Llobet, A.; Yeon, S. H.; Fischer, J. E.; Shi, Y.; Gogotsi, Y.; Gubbins, K. E., Modeling the Structural Evolution of Carbide-Derived Carbons Using Quenched Molecular Dynamics. *Carbon* **2010**, *48*, 1116-1123.

68. Farmahini, A. H.; Opletal, G.; Bhatia, S. K., Structural Modelling of Silicon Carbide-Derived Nanoporous Carbon by Hybrid Reverse Monte Carlo Simulation. *J. Phys. Chem. C* **2013**, *117*, 14081-14094.

69. Pech, D.; Brunet, M.; Durou, H.; Huang, P.; Mochalin, V.; Gogotsi, Y.; Taberna, P.-L.; Simon, P., Ultrahigh-Power Micrometre-Sized Supercapacitors Based on Onion-Like Carbon. *Nat. Nanotechnol.* **2010**, *5*, 651-654.

70. Feng, G.; Li, S.; Atchison, J. S.; Presser, V.; Cummings, P. T., Molecular Insights into Carbon Nanotube Supercapacitors: Capacitance Independent of Voltage and Temperature. *J. Phys. Chem. C* **2013**, *117*, 9178-9186.

71. von Helmholtz, H., On the Laws of the Distribution of Electrical Currents in Material Conductors with Application to Experiments in Animal Electricity. *Ann. Phys. Paris* **1879**, *243*, 337-382.

72. Feng, G.; Jiang, D.-e.; Cummings, P. T., Curvature Effect on the Capacitance of Electric Double Layers at Ionic Liquid/Onion-Like Carbon Interfaces. *J. Chem. Theory Comput.* **2012**, *8*, 1058-1063.

73. Li, S.; Feng, G.; Fulvio, P. F.; Hillesheim, P. C.; Liao, C.; Dai, S.; Cummings, P. T., Molecular Dynamics Simulation Study of the Capacitive Performance of a Binary Mixture of Ionic Liquids near an Onion-Like Carbon Electrode. *J. Phys. Chem. Lett.* **2012**, *3*, 2465-2469.

74. Pinilla, C.; Del Pópolo, M. G.; Kohanoff, J.; Lynden-Bell, R. M., Polarization Relaxation in an Ionic Liquid Confined between Electrified Walls *J. Phys. Chem. B* **2007**, *111*, 4877-4884.

75. Singh, R.; Monk, J.; Hung, F. R., A Computational Study of the Behavior of the Ionic Liquid [Bmim+][Pf6-] Confined inside Multiwalled Carbon Nanotubes. *J. Phys. Chem. C* **2010**, *114*, 15478-15485.

76. Monk, J.; Singh, R.; Hung, F. R., Effects of Pore Size and Pore Loading on the Properties of Ionic Liquids Confined inside Nanoporous Cmk-3 Carbon Materials. *J. Phys. Chem. C* **2011**, *115*, 3034-3042.

77. Singh, R.; Monk, J.; Hung, F. R., Heterogeneity in the Dynamics of the Ionic Liquid [Bmim+][Pf6-] Confined in a Slit Nanopore. *J. Phys. Chem. C* **2011**, *115*, 16544-16554.

78. Rajput, N. N.; Monk, J.; Singh, R.; Hung, F. R., On the Influence of Pore Size and Pore Loading on Structural and Dynamical Heterogeneities of an Ionic Liquid Confined in a Slit Nanopore. *J. Phys. Chem. C* **2012**, *116*, 5169-5181.

79. Rajput, N. N.; Monk, J.; Hung, F. R., Structure and Dynamics of an Ionic Liquid Confined inside a Charged Slit Graphitic Nanopore. *J. Phys. Chem. C* **2012**, *116*, 14504-14513.

80. Trulsson, M.; Algotsson, J.; Forsman, J.; Woodward, C. E., Differential Capacitance of Room Temperature Ionic Liquids: The Role of Dispersion Forces. *J. Phys. Chem. Lett.* **2010**, *1*, 1191-1195.

81. Si, X.; Li, S.; Wang, Y.; Ye, S.; Yan, T., Effects of Specific Adsorption on the Differential Capacitance of Imidazolium-Based Ionic Liquid Electrolytes. *ChemPhysChem* **2012**, *13*, 1671-1676.

82. Tanaka, A.; Iiyama, T.; Ohba, T.; Ozeki, S.; Urita, K.; Fujimori, T.; Kanoh, H.; Kaneko, K., Effect of a Quaternary Ammonium Salt on Propylene Carbonate Structure in Slit-Shape Carbon Nanopores. *J. Am. Chem. Soc.* **2010**, *132*, 2112-2113.

83. Yang, L.; Fishbine, B. H.; Migliori, A.; Pratt, L. R., Molecular Simulation of Electric Double-Layer Capacitors Based on Carbon Nanotube Forests. *J. Am. Chem. Soc.* **2009**, *131*, 12373-12376.

84. Frese, K. W., Calculation of Gibbs Hydration Energy with the Ion-Dielectric Sphere Model. *J. Phys. Chem.* **1989**, *93*, 5911-5916.

85. Feng, G.; Huang, J.; Sumpter, B. G.; Meunier, V.; Qiao, R., A "Counter-Charge Layer in Generalized Solvents" Framework for Electrical Double Layers in Neat and Hybrid Ionic Liquid Electrolytes. *Phys. Chem. Chem. Phys.* **2011**, *13*, 14724-14735.

86. Merlet, C.; Salanne, M.; Rotenberg, B.; Madden, P. A., Influence of Solvation on the Structural and Capacitive Properties of Electrical Double Layer Capacitors. *Electrochim. Acta* **2013**, *101*, 262-271.

87. Baldelli, S., Probing Electric Fields at the Ionic Liquid−Electrode Interface Using Sum Frequency Generation Spectroscopy and Electrochemistry. *J. Phys. Chem. B* **2005**, *109*, 13049-13051.

88. Lide, D. R.; Haynes, W. M., *Crc Handbook of Chemistry and Physics* 90th ed.; CRC press: Boca Raton, FL, 2009.

89. Stoppa, A.; Hunger, J.; Buchner, R.; Hefter, G.; Thoman, A.; Helm, H., Interactions and Dynamics in Ionic Liquids. *J. Phys. Chem. B* **2008**, *112*, 4854-4858.

90. Shim, Y.; Kim, H. J.; Jung, Y., Graphene-Based Supercapacitors in the Parallel-Plate Electrode Configuration: Ionic Liquids Versus Organic Electrolytes. *Faraday Discuss.* **2012**, *154*, 249-263.

91. Lukatskaya, M. R.; Mashtalir, O.; Ren, C. E.; Dall'Agnese, Y.; Rozier, P.; Taberna, P. L.; Naguib, M.; Simon, P.; Barsoum, M. W.; Gogotsi, Y., Cation Intercalation and High Volumetric Capacitance of Two-Dimensional Titanium Carbide. *Science* **2013**, *341*, 1502-1505.

92. Berendsen, H.; Grigera, J.; Straatsma, T., The Missing Term in Effective Pair Potentials. *J. Phys. Chem.* **1987**, *91*, 6269-6271.

93. van der Spoel, D.; van Maaren, P. J.; Berendsen, H. J. C., A Systematic Study of Water Models for Molecular Simulation: Derivation of Water Models Optimized for Use with a Reaction Field. *J. Chem. Phys.* **1998**, *108*, 10220-11.

94. Tang, Y. W.; Chan, K.-Y.; Szalai, I., Structural and Transport Properties of an Spc/E Electrolyte in a Nanopore. *J. Phys. Chem. B* **2004**, *108*, 18204-18213.

95. Yang, L.; Garde, S., Modeling the Selective Partitioning of Cations into Negatively Charged Nanopores in Water. *J. Chem. Phys.* **2007**, *126*, 084706-8.

96. Feng, G.; Qiao, R.; Huang, J.; Sumpter, B. G.; Meunier, V., Atomistic Insight on the Charging Energetics in Subnanometer Pore Supercapacitors. *J. Phys. Chem. C* **2010**, *114*, 18012-18016.

97. Wander, M. C. F.; Shuford, K. L., Molecular Dynamics Study of Interfacial Confinement Effects of Aqueous Nacl Brines in Nanoporous Carbon. *J. Phys. Chem. C* **2010**, *114*, 20539-20546.

98. Kalluri, R. K.; Konatham, D.; Striolo, A., Aqueous Nacl Solutions within Charged Carbon-Slit Pores: Partition Coefficients and Density Distributions from Molecular Dynamics Simulations. *J. Phys. Chem. C* **2011**, *115*, 13786-13795.

99. Kalluri, R. K.; Ho, T. A.; Biener, J.; Biener, M. M.; Striolo, A., Partition and Structure of Aqueous Nacl and Cacl2 Electrolytes in Carbon-Slit Electrodes. *J. Phys. Chem. C* **2013**, *117*, 13609-13619.

100. Pean, C.; Merlet, C.; Rotenberg, B.; Madden, P. A.; Taberna, P.-L.; Daffos, B.; Salanne, M.; Simon, P., On the Dynamics of Charging in Nanoporous Carbon-Based Supercapacitors. *ACS Nano* **2014**, *8*, 1576-1583.

101. Pean, C.; Rotenberg, B.; Simon, P.; Salanne, M., Understanding the Different (Dis)Charging Steps of Supercapacitors: Influence of Potential and Solvation. *Electrochim. Acta* **2016**, *206*, 504-512.

102. Varanasi, S. R.; Farmahini, A. H.; Bhatia, S. K., Complementary Effects of Pore Accessibility and Decoordination on the Capacitance of Nanoporous Carbon Electrochemical Supercapacitors. *J. Phys. Chem. C* **2015**, *119*, 28809-28818.

103. Tsai, W.-Y.; Taberna, P.-L.; Simon, P., Electrochemical Quartz Crystal Microbalance (Eqcm) Study of Ion Dynamics in Nanoporous Carbons. *J. Am. Chem. Soc.* **2014**, *136*, 8722-8728.

104. Forse, A. C.; Griffin, J. M.; Merlet, C.; Bayley, P. M.; Wang, H.; Simon, P.; Grey, C. P., Nmr Study of Ion Dynamics and Charge Storage in Ionic Liquid Supercapacitors. *J. Am. Chem. Soc.* **2015**, *137*, 7231-7242.

105. Forse, A. C.; Griffin, J. M.; Wang, H.; Trease, N. M.; Presser, V.; Gogotsi, Y.; Simon, P.; Grey, C. P., Nuclear Magnetic Resonance Study of Ion Adsorption on Microporous Carbide-Derived Carbon. *Phys. Chem. Chem. Phys.* **2013**, *15*, 7722-7730.

106. Griffin, J. M.; Forse, A. C.; Tsai, W.-Y.; Taberna, P.-L.; Simon, P.; Grey, C. P., In Situ Nmr and Electrochemical Quartz Crystal Microbalance Techniques Reveal the Structure of the Electrical Double Layer in Supercapacitors. *Nat. Mater.* **2015**, *14*, 812-819.

107. Vatamanu, J.; Vatamanu, M.; Borodin, O.; Bedrov, D., A Comparative Study of Room Temperature Ionic Liquids and Their Organic Solvent Mixtures near Charged Electrodes. *J. Phys.: Condens. Matter* **2016**, *28*, 464002.

108. Kondrat, S.; Kornyshev, A. A., Pressing a Spring: What Does It Take to Maximize the Energy Storage in Nanoporous Supercapacitors? *Nanoscale Horiz.* **2016**, *1*, 45-52.

109. Frackowiak, E.; Lota, G.; Pernak, J., Room-Temperature Phosphonium Ionic Liquids for Supercapacitor Application. *Appl. Phys. Lett.* **2005**, *86*, 164104-3.

3. Methodology

In this chapter an outline of MD simulations is given, and models and parameters relevant to this thesis are discussed. The specific MD programs and models used in this thesis are detailed to give the common strategies that have been used so that the simulations within each chapter can be more easily understood and compared. Model validation for bulk and simplified EDLC systems is also presented.

3.1. Molecular dynamics principles

Molecular dynamics (MD) is a popular molecular simulation technique for many computational-chemistry applications. It is used to compute time averaged equilibrium, and dynamic properties of many bodied systems.[1] In MD simulations, atoms are treated with classical mechanics and quantum effects are ignored. Atoms and molecules are modelled individually with properties such as size, charge, and interaction potential explicitly included. With increasing complexity of molecules, when more atoms are added, a greater amount of information is required to model the molecule accurately. For two atoms, bonded energies are defined; for three atoms, angular energies; and for four atoms, torsion energies. In this way realistic molecules can be created, and they can capture nano- to meso-scale properties such as flexing or folding. Once all the particles in the many bodied system have been defined, Newton's equations of motion are solved iteratively by integration to predict the energy, velocity, trajectory, and positions of all the particles in the system. Once a sufficient number of simulation steps have been completed (which is system dependent), the system's properties will no longer change with time, and equilibrium properties can be measured over the nanosecond time scale. From this sampling, many thermodynamic and kinetic properties can be calculated.

MD simulation is an explicit nano-scale technique, and it exists in the same category as Monte Carlo (MC) simulations. The size (or number of particles) in a MD simulation is limited by the computational resources available. It is therefore not currently applicable for the study of meso- and micro-scale systems, which are modelled via continuum techniques (e.g. computational fluid dynamics). MC simulations are based on ensemble average calculations, and are therefore not as convenient as MD for calculating dynamic properties. For simulations of EDLCs, MD is the more common method of investigation.[2-5]

A step further in resolution from MD on the size scale are quantum mechanical based methods such as *ab inito* density functional theory (qDFT) simulations. Due to the high

computational cost, these are limited to a handful of particles per simulation (albeit this number is consistently increasing). qDFT simulations are able to predict interaction energies between particles, and these predictions can then be used as parameters for molecules in MD simulations.

A step back in resolution from MD on the size scale is classical density functional theory (cDFT) and continuum models, such as the Poisson-Boltzmann. This category of modelling is significantly faster than molecular modelling due to its non-discrete nature of treating bulk properties and continuum parameters. Several interesting studies on the meso to macro scale have been performed,[6-12] however they are unable to analyse the atomistic nano-scale behaviour that occurs in small pores[13] or dense electrolytes.

Due to the nano-scale behaviour inherent to EDLCs, MD simulation is an applicable technique. Unlike continuum methods, it is capable of resolution to the molecular level; and unlike qDFT, it is able to handle systems sufficiently large enough to capture interfacial behaviour with a large number of molecules. For EDLCs, the fundamental mechanism of charge storage can be reduced to a solid-liquid (electrode-electrolyte) interfacial system by ignoring the macro properties of the device, specifically current-collector and separator, as well as long time scale properties like device heating or degradation, and self-discharge.

3.2. Relevant limitations of MD

The computational requirement of MD simulations for EDLCs is very high, this is primarily due to three physical factors: (i) the addition of a porous-solid phase requires a large simulation box size, (ii) large distances between electrodes are required to reach the bulk electrolyte densities and structures between the electrodes, and (iii) the dynamics are often slow, particularly with RTILs, and many millions of simulation steps (often resulting in more than 20 ns of simulation time) are required to reach an equilibrium result. In addition to the above physical factors, the constant potential method (outlined in Section 3.3.2) also increases the computational requirement, sometimes by up to a factor of 10. These factors combined mean that the scope of study needs to be carefully considered and confined or else simulation times are excessive.

As a general rule of thumb, the time cost of a simulation is non-linearly proportional to its level of detail. This means that for complex EDLC systems, often concessions have to be made in the level of detail for the structural and charge treatment of the electrode or the electrolyte modelling. Due to current computational constraints, it is currently not feasible to

simulate systems with every particle treated to its highest level of detail. This will be covered further in Section 3.4 below.

A final, but important, limitation is the availability of accurate porous structures, as this affects the ability of modelling to compare with experimental results which come from a rich variety of materials. Realistic porous models are difficult to generate and validate. Currently there are relatively few realistic models available.[14-16] This has resulted in the widespread use of simplified electrode models such as slit-pores and carbon nano-tubes (CNTs) *in lieu* of more realistic counterparts. Furthermore, when modelling the electrodes, they are constrained (frozen) in place, which means they do not capture volumetric expansion effects observed in real devices. Defects and terminal, or active, groups are also discounted for simplicity. Similarly, but not to the same extent, the number RTIL models available is also limited compared to the wide number that have been synthesised.

3.3. Details of programs used

3.3.1. Gromacs

Gromacs is a popular open source program developed at University of Groningen, The Royal Institute of Technology, and Uppsala University.[17] It is primarily designed for the study of biomolecular systems, but is readily adaptable to other systems, including EDLCs. Electrolyte models can be generated from the supplied force-fields, or used from separate studies. The main advantage to this software is its high level of parallelisation and efficient sub-routines which results in it being one of the fastest MD programs in the world. It also contains an extensive library of post-processing scripts which enable easy extraction of simulation information. Gromacs does not contain an integrated subroutine for calculation of electric charges (which will be discussed in Section 3.3.2) 'on the fly'.[18] Due to this, Gromacs has been used only for 'constant charge' simulations in Section 4.3.1 and 'uncharged solid' simulations in Sections 5.3.3 and 7.3.1 and throughout Chapter 6.

3.3.2. Metalwalls

'Metalwalls' is an in-house MD program developed by Professor Paul Madden of Oxford University. Metalwalls was designed specifically for the study of RTILs at electrode interfaces. Its main advantage is the use of the constant potential method, or 'on the fly' electrode charge calculations. Modelling the electrode under constant potential provides greater realism which is unable to be fulfilled by constant charge electrodes, which should be limited to equilibrium studies with planar electrodes.[19] The calculation of a constant electrode potential is described in full by Merlet et al.[4] and briefly below.

Every electrode atom *j* carries a Gaussian charge distribution $\rho_j(\mathbf{r})$, and contains an integrated charge q_j with a fixed width η:

$$\rho_j(\mathbf{r}) = q_j A \exp\left(-\left|r - r_j\right|^2 \eta^2\right) \tag{3-1}$$

where $A = \eta^2\pi^{3/2}$, and is a normalisation constant. For a system with two electrodes which both extend in the *x* and *y* direction, and electrolyte in between, the coulomb energy must be calculated through two-dimensional Ewald summations[20] as a three-dimensional Ewald summations may lead to artefacts. The Coulombic energy can be expressed as:

$$U_c = \frac{1}{2}\int\int d\mathbf{r}d\mathbf{r}' \frac{\rho(\mathbf{r})\rho(\mathbf{r}')}{|\mathbf{r}' - \mathbf{r}|} \tag{3-2}$$

which can be combined with Equation (3-1) to show that the potential of any and all charges can be obtained from the partial derivate of the following expression with respect to the specific charge:

$$\Psi_j = \left[\frac{\partial U_c}{\partial q_j}\right]_{\{q_i\}i\neq j} \tag{3-3}$$

To obtain the value of each charge *j*, the sum potential experienced by *j* must equal the pre-parameterised electrode potential Ψ_x at every time step. To achieve this, and maintain the specified constant potential, a final constraint condition is added:

$$U_{constraint} = -\sum_{j=1}^{N} \Psi_x q_j \tag{3-4}$$

where N is the total number of atoms in the electrode. Simultaneous to equation (3-4) the total potential energy of the variable charges are minimised. Additional methods of maintain a constant electrode potential are discussed by Merlet et al.[4] Fundamentally, all electrode charges are allowed to fluctuate throughout the simulation. The magnitudes of the charges are induced by the location of the ions, and thus are heterogeneous across the electrode. This is a key difference to the constant charge method, where the charges are uniform across the electrode.

The main limitation of the constant potential method is that compared to constant charge, it is an order of magnitude slower, due to the additional sub-routine executed at every simulation step. Therefore, where it is prudent, constant charge simulations are employed to reduce the computational load. An example of this includes during some equilibration stages. Metalwalls was used for all constant potential simulations used throughout Chapters 4, 5, and 7.

3.4. Details of models used

3.4.1. Electrolyte

When modelling the ions and solvent in the electrolyte, there exists several options for the level of detail of structural and charge properties. Firstly for the charge modelling, as with the electrodes charge modelling discussed in Section 3.3, the atomic charges on the ions can also be modelled as polarisable,[21-22] however in this thesis (and most MD simulations of EDLCs) the atomic charges are constant due to the availability of fixed charge models and the reduction in computation time compared with polarisable models. To account implicitly for polarisation effects, which are not included in most electrolyte models in which the charges are fixed, the total molecular (sum of the partial atomic) charge, i.e. one atomic unit, can be reduced by approximately 20 percent.[23-24]

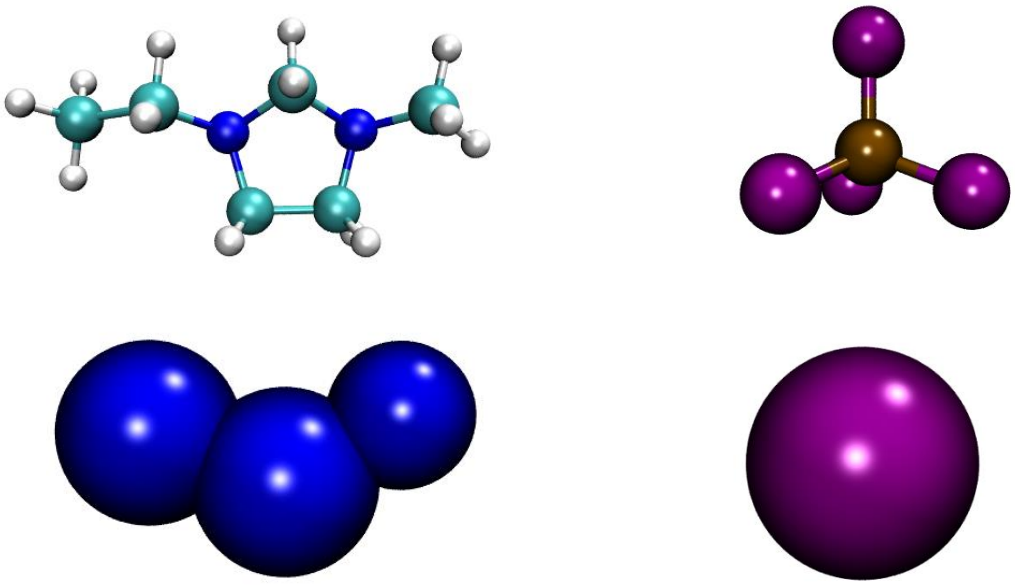

a b

Figure 3-1:All-atom and coarse-grained equivalent of $EMIM^+$ (a) and BF_4^- (b).

The structure of molecular models can explicitly account for every atom, known as all-atom, or aggregate atoms to varying degrees. Aggregated models range from united-atom with the least aggregation,[25] followed by coarse-graining,[26] and finally primitive spheres.[27-29] An example of an all atom and a course grained model of a RTIL is given in Figure 3-1. In addition to the number of atoms, the intramolecular mobility and interactions also vary between models (e.g. rigid versus flexible). The details of the intramolecular interactions vary between models. Most coarse-grained models of small molecules are rigid whereas all-atom models often define interaction parameters for bond stretching, bending, and torsion to maintain the correct structure. In this thesis several electrolyte models were utilised. For Gromacs, united-atom $BMIMBF_4$ was used from Zhong et al.,[25] coarse-grained $EMIMBF_4$ was used from Merlet et al.,[30] and all-atom EMIMTFSI was used from Köddermann et al.[31] For Metalwalls, only coarse-grained $EMIMBF_4$ was used from Merlet et al.[30] In both programs, united-atom ACN was used from Edwards et al.[32]

3.4.2. Electrode

For electrode modelling, the carbon Lennard-Jones parameters were taken from Cole *et al.*,[33] with $\sigma = 0.337$ nm and well depth (ε) = 0.23 kJ mol^{-1}, except in Chapters 6 and 7, where the well depth was modified. For non-porous flat graphene, and slit-pore electrodes, (which are idealised theoretical structures) the geometries were generated in this work maintain an atomic bond spacing of 0.142 nm and interlayer sheet spacing of 0.35 nm. Realistic carbon

electrodes with disordered and non-uniform pores were limited to CDC models from Palmer et al.[14] and Farmahini et al.,[15] for Ti-CDC 800 and Si-CDC 800 respectively (Figure 3-2).

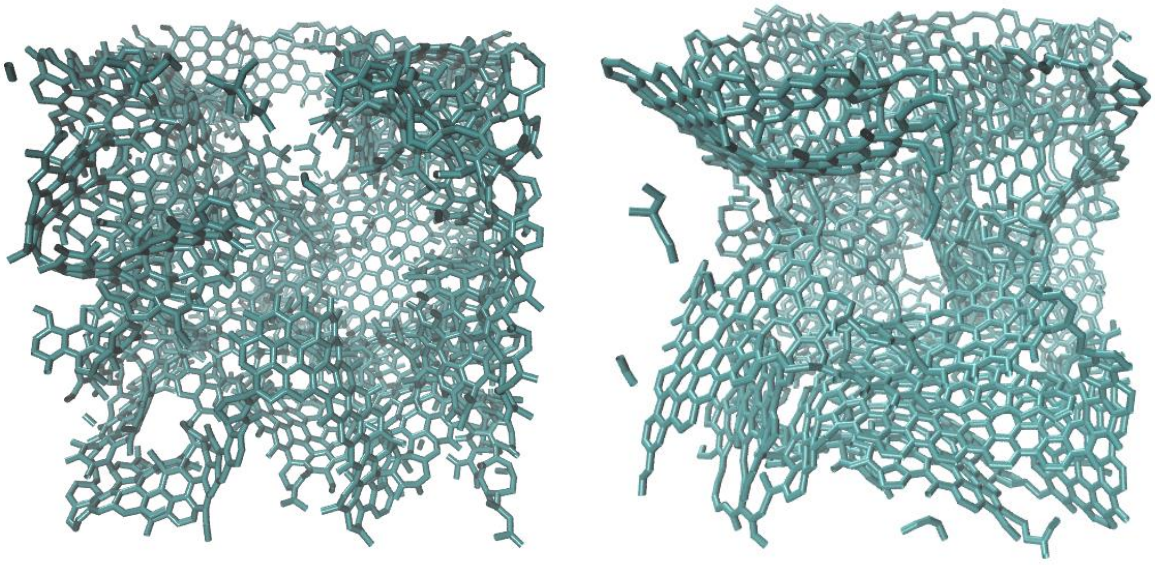

a b

Figure 3-2: Empty electrode models used for Ti-CDC 800 (a) and Si-CDC 800 (b).

3.5. Validations and simple analysis

3.5.1. Bulk simulations

In this section the coarse grained EMIMBF$_4$ model from Merlet et al.[30] is combined with united-atom/coarse grained ACN from Edwards et al.[32] to verify that the bulk RTIL and mixture with ACN behave as expected. This is an important check to make before performing interfacial studies with a solid carbon.

Simulations were performed in Gromacs,[17] with equilibration completed in three steps. Firstly, conjugate-gradient energy minimisation was run starting from a low density system. This was followed by a 200 ps NVT step at 340 K with the temperature controlled by a Nose-Hoover thermostat and 1 ps relaxation time. Finally, a NPT step was performed at 1 bar with a Parrinello-Rahman barostat and 2 ps relaxation time. This step was run for greater than 1 ns (system dependent) to ensure that equilibrium was fully reached. The number of RTIL and ACN molecules used in each bulk system studied is given in Table 3-1.

Table 3-1: Number of RTIL and ACN molecules for each bulk system studied.

	0 ACN	10 % ACN	20 % ACN	40 % ACN	67 % ACN
$EMIMBF_4$	200	198	195	196	200
ACN	0	106	235	630	1958

Production runs were performed for 5 ns using the same conditions as the NPT equilibration step. The short range electrostatic and Lennard-Jones cut-off was 1.2 nm, the long range electrostatics were controlled with three-dimensional PME summations. Energies and positions were sampled every 2 ps.

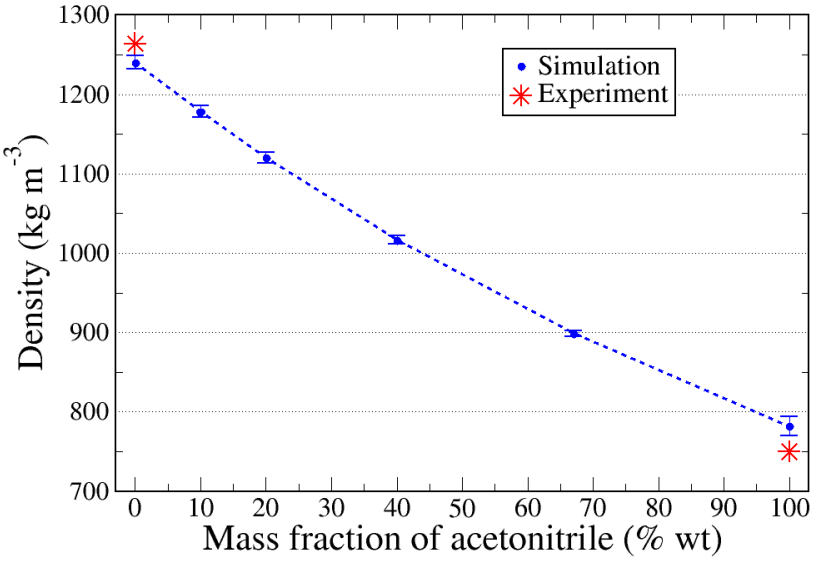

Figure 3-3: Bulk density of $EMIMBF_4$ and ACN mixtures at 340 K and 1 bar. The experimental data is at 323 K and atmospheric pressure.

As can be seen from Figure 3-3, there was a slightly non-linear reduction in density with ACN concentration. We obtained a density of 1240 kg m^{-3} for the pure $EMIMBF_4$ system, which correlates well with the simulation of Merlet et al.,[30] where they obtained a density of 1250 kg m^{-3} at 325 K. The results compare well with available experimental data. At 323 K, Wong at el.[34] obtained a density of 1246 kg m^{-3} for pure $EMIMBF_4$. Similarly for pure ACN, the experimental density at 323 K is 750 kg m^{-3}.[35]

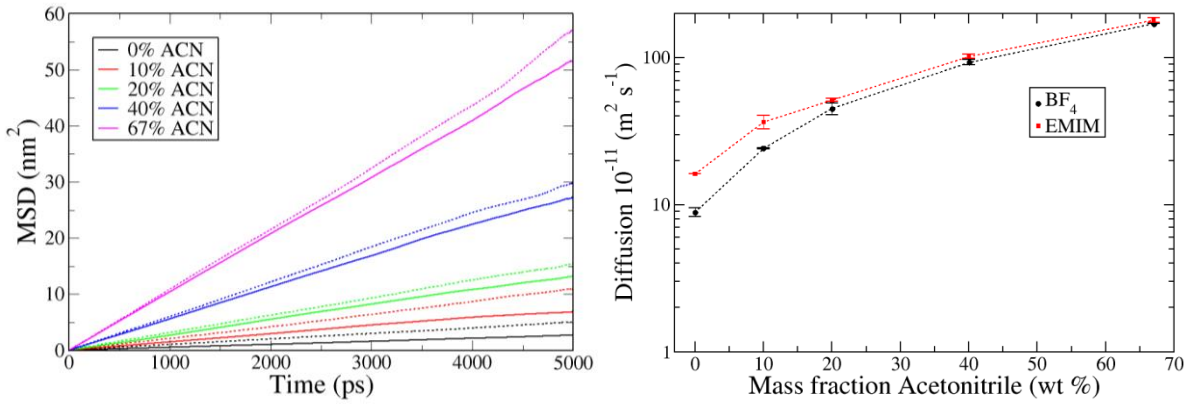

a b

Figure 3-4: a: Mean square displacements for diffusion calculations, solid lines are the BF_4^- anions dashed lines are the $EMIM^+$ cations. b: Self-diffusion coefficients for the two ionic species.

From Figure 3-4a No caging observed in mean square displacement (MSDs), but there is a clear increase in diffusion with ACN fraction in Figure 3-4b (over an order of magnitude from the highest fraction of ACN tested). A small difference between the diffusion of cations and anions; the difference minimises upon solvation with ACN.

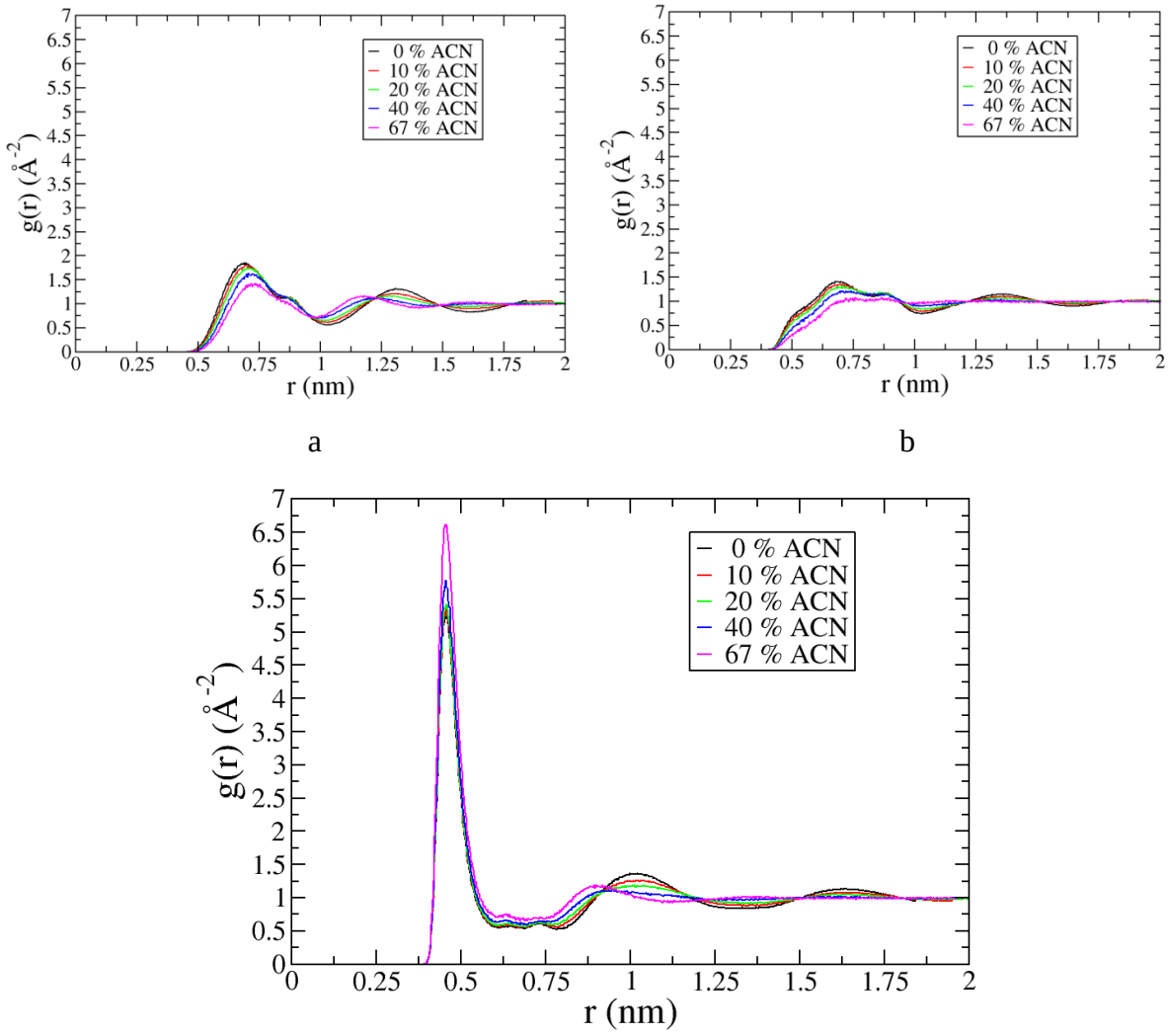

Figure 3-5:RDFs of ionic species. BF_4-BF_4 (a), EMIM-EMIM (b), BF_4-EMIM (c).

RDF data of ion-ion correlations in Figure 3-5 show that the ACN molecules do not reduce the correlations much in the bulk, and there is a strong cation-anion peak at 0.5 nm, and weak anion-anion and cation-cation peaks at approximately 0.75 nm. Weak ion-ACN peaks are also observed at 0.5 nm in Figure 3-6.

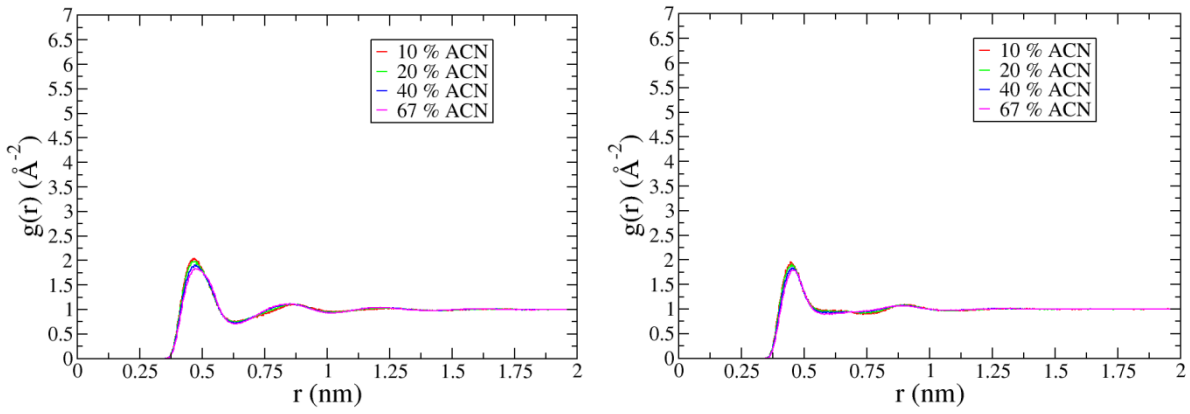

Figure 3-6:RDFs of ion-ACN. BF_4-ACN (a), EMIM-ACN (b).

Additional validation was performed by analysing conductivity and liquid-vapour surface tension of $EMIMBF_4$ and ACN mixtures at 298 K, both of which are general properties of interest to solvation thermodynamics. The methodologies and results for these analyses are given in Appendix A3.

3.5.2. Flat wall EDLC

Flat wall EDLC capacitors are the simplest geometry and most widely simulated system to date.[2] Here we perform a series of simulations with varying electrode charge densities, and the subsequent capacitance calculations to verify firstly that the united-atom $BMIMBF_4$ model from Zhong et al.[25] behaves in accordance with previous studies at solid interfaces. Secondly to verify that we can successfully compute capacitances in this type of system before moving to more advanced systems of interest.

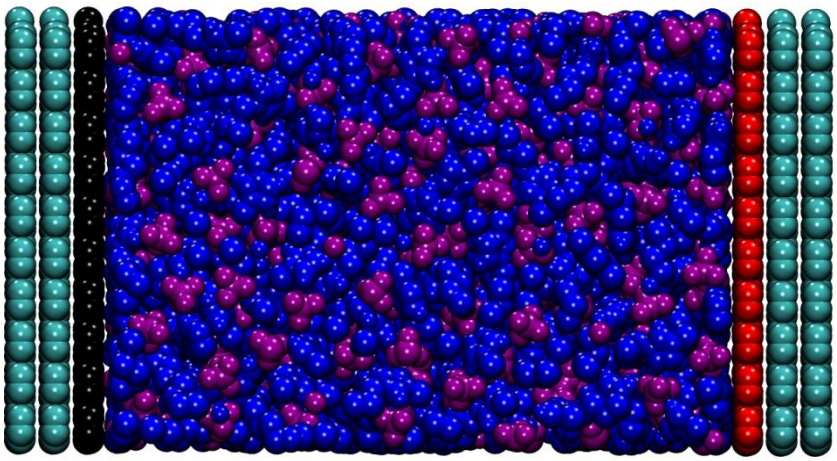

Figure 3-7: Snapshot of the planar electrode simulation, the positive and negative electrodes were set to ± 0.10 C m^{-2}. Colour scheme: purple molecules are BF_4^- anions; blue molecules are $BMIM^+$ cations; the red sheet is the positive electrode; the black sheet is the negative electrode; green sheets have neutral charge.

In this section the united-atom $BMIMBF_4$ model from Zhong et al.[25] was tested between flat, three-layer, graphene electrodes in the constant charge ensemble (Figure 3-7). Each graphene sheet consisted of 800 carbon atoms, and the sheets were spaced 0.35 nm apart with the distance between walls set to 6.6 nm (measured from centre of top layer atoms). The number of RITL pairs was 450. The number of pairs and the wall spacing combined to give the correct RTIL density between the electrodes. The electrodes were set to surface charges (σ) of ± 0, 0.02, 0.06, 0.10, and 0.14 C m^{-2}. Simulations were run in the two-dimensional NVT ensemble for 15 ns. The temperature was maintained at 353 K with a Berendsen thermostat.[36] The short range electrostatic and Lennard-Jones cut-off was 1.2 nm, the long range electrostatics were controlled with two-dimensional PME summations. After production runs were completed, the potential profile across the electrodes (ϕ_z) was calculated numerical integration of the one-dimensional Poisson Equation:

$$\nabla_z \left[\varepsilon_0 \left(\nabla_z \phi(z) \right) \right] = -\rho(z) \tag{3-5}$$

where ε_0 is the vacuum permittivity, and $-\rho(z)$ is the one-dimensional charge density profile of the RTIL between the electrodes, which can be calculated from the simulation configuration by sampling *z*-bins across the whole *x* and *y* range. Using a *z*-bin depth of 0.02 nm, the potential profiles for the electrode surface charges simulated were calculated, and shown in Figure 3-8.

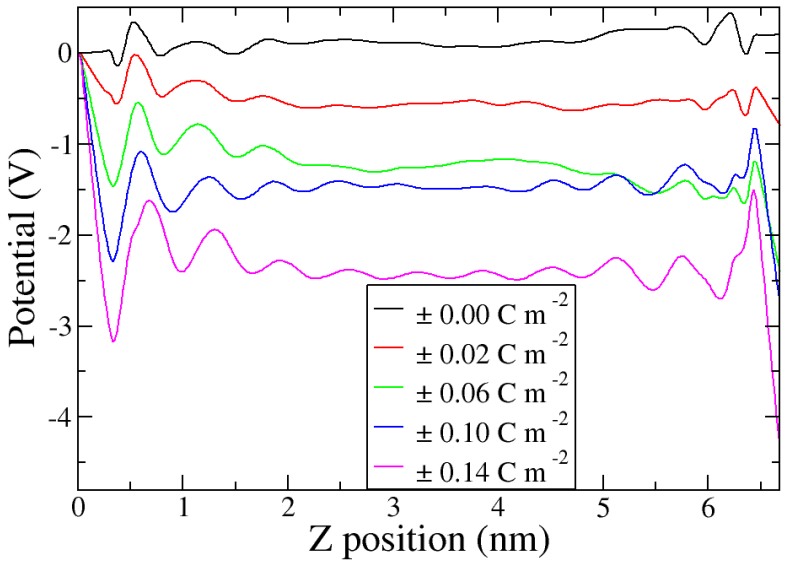

Figure 3-8: Potential profiles for varying surface charges from integration of Equation (3-5).

From Figure 3-8, it can be seen that the point of zero charge (PZC), which is the potential drop between uncharged electrodes (0.00 C m^{-2}), was - 0.2 V. The potential of the bulk can be taken from the centre point between the electrodes where the profile is flat, and from this the potential of both electrodes, and the total, can be calculated (

Table 3-2)

Table 3-2: Electrode and total potentials calculated from Equation (3-5).

$\pm\sigma$ (C m^{-2})	ϕ (neg. elec.)	ϕ (pos. elec.)	ϕ (Total)	$C_{pos.\ elec.}$ (μF cm^{-2})	$C_{neg.\ elec.}$ (μF cm^{-2})
0.02	-0.56	0.241	0.801	4.455	5.686
0.06	-1.25	1.193	2.443	4.282	5.760
0.10	-1.49	1.339	2.829	6.464	7.802
0.14	-2.476	1.752	4.228	7.140	6.174

The integral capacitance for each electrode was calaculated from the simple relation:

$$C_{\text{int}} = \frac{\sigma}{\phi - PZC} \tag{3-6}$$

It is also possible to calculate the differential capacitance (DC) from:

$$DC = \frac{d\sigma}{d(\phi - PZC)} \tag{3-7}$$

however, many data points and a small step size ($d\sigma$) are required for physically meaningful results. The electrode charge and integral capacitance are given in Figure 3-9 for the potentials calculated by integration of Equation (3-5).

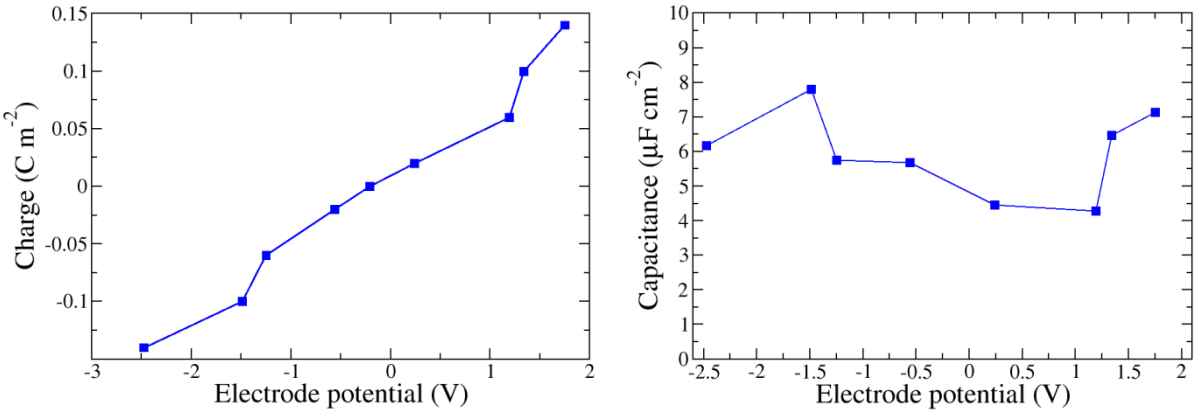

a b

Figure 3-9: Electrode charge (a) and integral capacitance (b) across the range of calculated potentials from Equation (3-5).

The C_{int} behaviour here is consistent with other literature[30, 37] and we can conclude that the models used are behaving as desired for further study in the following chapters.

Appendix A3

Ionic conductivity

To measure the ionic conductivity, a Gromacs analysis tool, *gmx current*, was utilised which provides and Einstein-Helfand fit to the current autocorrelation function *J(t)* and solves:[38]

$$\kappa = \frac{e^2}{3Vk_bT}\int_0^\infty J(t) \tag{3-8}$$

where κ is the conductivity in S m^{-1}, e is the electronc charge , V is the simulation box constant, k_b is the Boltzmann constant, and T is the simulation temperature.

To get a reasonable estimate of the autocorrelation function, high frequency sampling is required to capture the short time behaviour of the autocorrelations. Therefore, in these analyses, 30 ns production runs were performed in the NVT ensemble at 298 K, and the velocities were saved every 50 fs.

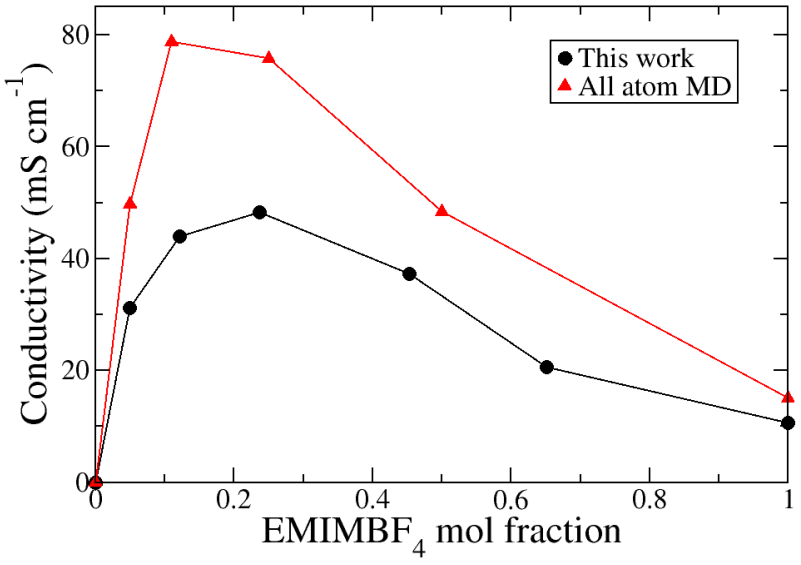

Figure 3-10: Ionic conductivity of the coarse grained $EMIMBF_4$ model used, compared with the all-atom model from ref 39.

From Figure 3-10 it can be seen that the coarse-grained model reasonably captures the trend of conductivity with ionic concentration of an all-atom simulation, but underestimates the magnitude of the conductivity peak significantly.

Liquid-vapour surface tension

Calculating surface tension requires the establishment of one or more interfaces within the simulation box. A common method was utilised here, in which a periodic *xy*-slab of equilibrated liquid is placed in the centre of the box in the *z* direction, with vapour spaces on either side of the slab, creating two interfaces in the simulation box. The surface tension was computed from the ensemble average pressure tensors using:[1]

$$\gamma_0 = \left(\langle P_{zz} \rangle - \frac{\langle P_{xx} \rangle + \langle P_{yy} \rangle}{2} \right) \frac{L_z}{N_{surfaces}} \tag{3-9}$$

where γ_0 is the surface tension without truncated tail corrections,[40] P_{zz}, P_{xx}, and P_{yy} are the ensemble average components of the pressure tensor, L_z is the length of the simulation box in the *z* direction, and $N_{surfaces}$ is the number of interfaces.

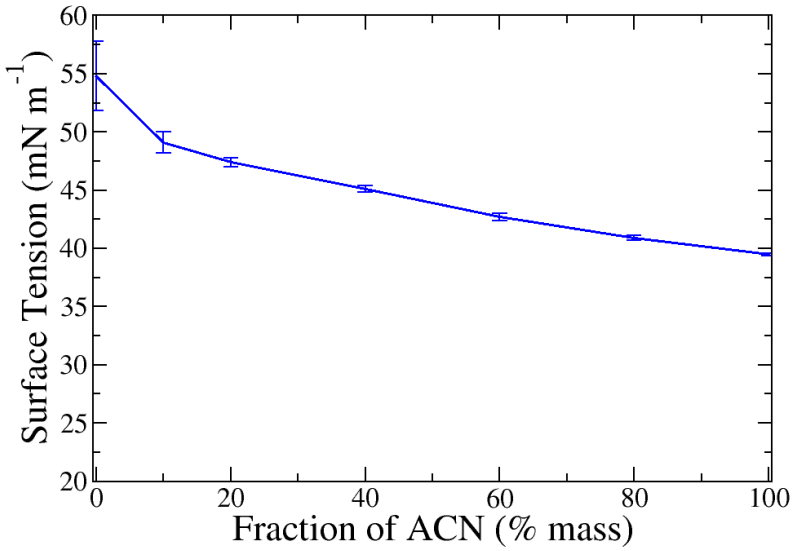

Figure 3-11: Liquid vapour surface tension at 298 K

The surface tension for $EMIMBF_4$ and ACN mixtures is given in Figure 3-11 and shows that addition of ACN smoothly decreases the surface tension in a weakly non-linear manner. Experimental values of surface tension for pure $EMIMBF_4$ and ACN are 48.13 and 28.7 mN m^{-1} respectively,[41-42] which are both significantly smaller than the values calculated for the models. To verify the calculation procedure, we simulated pure $EMIMBF_4$ at 400 K and obtained a surface tension of 43.6 ± 0.8 mN m^{-1}, which agrees with the original reported value of 44.3 mN m^{-1} from Merlet et al.[30] and 41.9 mN m^{-1} from experiments.[41]

3.6. References

1. Frenkel, D.; Smit, B.; Ratner, M. A., Understanding Molecular Simulation: From Algorithms to Applications. *Phys. Today* **1997**, *50*, 66.

2. Burt, R.; Birkett, G.; Zhao, X. S., A Review of Molecular Modelling of Electric Double Layer Capacitors. *Phys. Chem. Chem. Phys.* **2014**, *16*, 6519-6538.

3. Feng, G.; Li, S.; Presser, V.; Cummings, P. T., Molecular Insights into Carbon Supercapacitors Based on Room-Temperature Ionic Liquids. *J. Phys. Chem. Lett.* **2013**, *4*, 3367-3376.

4. Merlet, C.; Rotenberg, B.; Madden, P. A.; Salanne, M., Computer Simulations of Ionic Liquids at Electrochemical Interfaces. *Phys. Chem. Chem. Phys.* **2013**, *15*, 15781-15792.

5. Vatamanu, J.; Hu, Z.; Bedrov, D.; Perez, C.; Gogotsi, Y., Increasing Energy Storage in Electrochemical Capacitors with Ionic Liquid Electrolytes and Nanostructured Carbon Electrodes. *J. Phys. Chem. Lett.* **2013**, *4*, 2829-2837.

6. d'Entremont, A.; Pilon, L., First-Principles Thermal Modeling of Electric Double Layer Capacitors under Constant-Current Cycling. *J. Power Sources* **2014**, *246*, 887-898.

7. Wang, H.; Fang, J.; Pilon, L., Scaling Laws for Carbon-Based Electric Double Layer Capacitors. *Electrochim. Acta* **2013**, *109*, 316-321.

8. Wang, H.; Pilon, L., Accurate Simulations of Electric Double Layer Capacitance of Ultramicroelectrodes. *J. Phys. Chem. C* **2011**, *115*, 16711-16719.

9. Wang, H.; Pilon, L., Physical Interpretation of Cyclic Voltammetry for Measuring Electric Double Layer Capacitances. *Electrochim. Acta* **2012**, *64*, 130-139.

10. Wang, H.; Pilon, L., Mesoscale Modeling of Electric Double Layer Capacitors with Three-Dimensional Ordered Structures. *J. Power Sources* **2013**, *221*, 252-260.

11. Wang, H.; Thiele, A.; Pilon, L., Simulations of Cyclic Voltammetry for Electric Double Layers in Asymmetric Electrolytes: A Generalized Modified Poisson-Nernst-Planck Model. *J. Phys. Chem. C* **2013**, *117*, 18286-18297.

12. Wang, H.; Varghese, J.; Pilon, L., Simulation of Electric Double Layer Capacitors with Mesoporous Electrodes: Effects of Morphology and Electrolyte Permittivity. *Electrochim. Acta* **2011**, *56*, 6189-6197.

13. Merlet, C.; Rotenberg, B.; Madden, P. A.; Taberna, P.-L.; Simon, P.; Gogotsi, Y.; Salanne, M., On the Molecular Origin of Supercapacitance in Nanoporous Carbon Electrodes. *Nat. Mater.* **2012**, *11*, 306-310.

14. Palmer, J. C.; Llobet, A.; Yeon, S. H.; Fischer, J. E.; Shi, Y.; Gogotsi, Y.; Gubbins, K. E., Modeling the Structural Evolution of Carbide-Derived Carbons Using Quenched Molecular Dynamics. *Carbon* **2010**, *48*, 1116-1123.

15. Farmahini, A. H.; Opletal, G.; Bhatia, S. K., Structural Modelling of Silicon Carbide-Derived Nanoporous Carbon by Hybrid Reverse Monte Carlo Simulation. *J. Phys. Chem. C* **2013**, *117*, 14081-14094.

16. Rajput, N. N.; Monk, J.; Hung, F. R., Ionic Liquids Confined in a Realistic Activated Carbon Model: A Molecular Simulation Study. *J. Phys. Chem. C* **2014**, *118*, 1540-1553.

17. Hess, B.; Kutzner, C.; Van Der Spoel, D.; Lindahl, E., Gromacs 4: Algorithms for Highly Efficient, Load-Balanced, and Scalable Molecular Simulation. *J. Chem. Theory Comput.* **2008**, *4*, 435-447.

18. Reed, S. K.; Lanning, O. J.; Madden, P. A., Electrochemical Interface between an Ionic Liquid and a Model Metallic Electrode. *J. Chem. Phys.* **2007**, *126*, 084704-13.

19. Merlet, C.; Pean, C.; Rotenberg, B.; Madden, P. A.; Simon, P.; Salanne, M., Simulating Supercapacitors: Can We Model Electrodes as Constant Charge Surfaces? *J. Phys. Chem. Lett.* **2013**, *4*, 264-268.

20. Gingrich, T. R.; Wilson, M., On the Ewald Summation of Gaussian Charges for the Simulation of Metallic Surfaces. *Chem. Phys. Lett.* **2010**, *500*, 178-183.

21. Borodin, O., Polarizable Force Field Development and Molecular Dynamics Simulations of Ionic Liquids. *J. Phys. Chem. B* **2009**, *113*, 11463-11478.

22. Borodin, O.; Henderson, W. A.; Fox, E. T.; Berman, M.; Gobet, M.; Greenbaum, S., Influence of Solvent on Ion Aggregation and Transport in Py15tfsi Ionic Liquid-Aprotic Solvent Mixtures. *J. Phys. Chem. B* **2013**, *117*, 10581-10588.

23. Leontyev, I.; Stuchebrukhov, A., Accounting for Electronic Polarization in Non-Polarizable Force Fields. *Phys. Chem. Chem. Phys.* **2011**, *13*, 2613-2626.

24. Schroder, C., Comparing Reduced Partial Charge Models with Polarizable Simulations of Ionic Liquids. *Phys. Chem. Chem. Phys.* **2012**, *14*, 3089-3102.

25. Zhong, X.; Liu, Z.; Cao, D., Improved Classical United-Atom Force Field for Imidazolium-Based Ionic Liquids: Tetrafluoroborate, Hexafluorophosphate, Methylsulfate, Trifluoromethylsulfonate, Acetate, Trifluoroacetate, and Bis(Trifluoromethylsulfonyl)Amide. *J. Phys. Chem. B* **2011**, *115*, 10027-10040.

26. Wang, Y.; Jiang, W.; Yan, T.; Voth, G. A., Understanding Ionic Liquids through Atomistic and Coarse-Grained Molecular Dynamics Simulations. *Acc. Chem. Res.* **2007**, *40*, 1193-1199.

27. Kiyohara, K.; Sugino, T.; Asaka, K., Electrolytes in Porous Electrodes: Effects of the Pore Size and the Dielectric Constant of the Medium. *J. Chem. Phys.* **2010**, *132*, 144705-12.

28. Lamperski, S.; Outhwaite, C. W.; Bhuiyan, L. B., The Electric Double-Layer Differential Capacitance at and near Zero Surface Charge for a Restricted Primitive Model Electrolyte. *J. Phys. Chem. B* **2009**, *113*, 8925-8929.

29. Lamperski, S.; Zydor, A., Monte Carlo Study of the Electrode|Solvent Primitive Model Electrolyte Interface. *Electrochim. Acta* **2007**, *52*, 2429-2436.

30. Merlet, C.; Salanne, M.; Rotenberg, B., New Coarse-Grained Models of Imidazolium Ionic Liquids for Bulk and Interfacial Molecular Simulations. *J. Phys. Chem. C* **2012**, *116*, 7687-7693.

31. Köddermann, T.; Paschek, D.; Ludwig, R., Molecular Dynamic Simulations of Ionic Liquids: A Reliable Description of Structure, Thermodynamics and Dynamics. *ChemPhysChem* **2007**, *8*, 2464-2470.

32. Edwards, D. M. F.; Madden, P. A.; McDonald, I. R., A Computer Simulation Study of the Dielectric Properties of a Model of Methyl Cyanide. *Mol. Phys.* **1984**, *51*, 1141-1161.

33. Cole, M. W.; Klein, J. R., The Interaction between Noble Gases and the Basal Plane Surface of Graphite. *Surf. Sci.* **1983**, *124*, 547-554.

34. Wong, C.-L.; Soriano, A. N.; Li, M.-H., Diffusion Coefficients and Molar Conductivities in Aqueous Solutions of 1-Ethyl-3-Methylimidazolium-Based Ionic Liquids. *Fluid Phase Equilib.* **2008**, *271*, 43-52.

35. Khimenko, M.; Gritsenko, N., Determination of Polarizability and Radius of Acetonitrile and Dimethylacetamide Molecules. Mezhdunarodnaya Kinga 39 Dimitrova UL ., 113095 Moscow, Russia: 1980; Vol. 54, pp 198-199.

36. Berendsen, H. J. C.; Postma, J. P. M.; van Gunsteren, W. F.; DiNola, A.; Haak, J. R., Molecular Dynamics with Coupling to an External Bath. *J. Chem. Phys.* **1984**, *81*, 3684-7.

37. Feng, G.; Huang, J.; Sumpter, B. G.; Meunier, V.; Qiao, R., Structure and Dynamics of Electrical Double Layers in Organic Electrolytes. *Phys. Chem. Chem. Phys.* **2010**, *12*, 5468-5479.

38. Chen, T.; Smit, B.; Bell, A. T., Are Pressure Fluctuation-Based Equilibrium Methods Really Worse Than Nonequilibrium Methods for Calculating Viscosities? *J. Chem. Phys.* **2009**, *131*, 246101.

39. Vatamanu, J.; Vatamanu, M.; Borodin, O.; Bedrov, D., A Comparative Study of Room Temperature Ionic Liquids and Their Organic Solvent Mixtures near Charged Electrodes. *J. Phys.: Condens. Matter* **2016**, *28*, 464002.

40. Vrabec, J.; Kedia, G. K.; Fuchs, G.; Hasse, H., Comprehensive Study of the Vapour–Liquid Coexistence of the Truncated and Shifted Lennard–Jones Fluid Including Planar and Spherical Interface Properties. *Mol. Phys.* **2006**, *104*, 1509-1527.

41. Shamsipur, M.; Beigi, A. A. M.; Teymouri, M.; Pourmortazavi, S. M.; Irandoust, M., Physical and Electrochemical Properties of Ionic Liquids 1-Ethyl-3-Methylimidazolium Tetrafluoroborate, 1-Butyl-3-Methylimidazolium Trifluoromethanesulfonate and 1-Butyl-1-Methylpyrrolidinium Bis(Trifluoromethylsulfonyl)Imide. *J. Mol. Liq.* **2010**, *157*, 43-50.

42. Jeffery, G. H.; Vogel, A. I., 134. Physical Properties and Chemical Constitution. Part Xvii. Acetylenic Compounds and Cyanides. *J. Chem. Soc.* **1948**, 674-683.

4. Structure and capacitance of ionic-liquid and acetonitrile mixtures inside slit-pore carbon electrodes

Molecular dynamics simulations of electric double-layer capacitors with electrolytes that contain mixtures of ionic-liquid and acetonitrile have received significant attention recently due to the optimisation challenges posed with ionic liquids. However, studies have mostly been limited to systems with flat-wall electrodes. In this work, we performed molecular dynamics simulations of ionic-liquid and acetonitrile mixture electrolytes in with slit-pore electrodes. The pore size was such that only a single layer of ions could be adsorbed. We contrast the properties of pores modelled by constant charge and constant potential. This has previously been reported for flat wall and disordered porous electrodes, but not for ordered slit-pore electrodes. Charging mechanisms for slit-pore electrodes were also determined.

For all constant electrode charges tested, the influence of acetonitrile on ionic-number density diminished with increasing concentration. Temperature was tested from 280 K to 353 K, and was not found to have a significant influence on the adsorbed structure at all electrode charges and acetonitrile concentrations considered. This was despite large changes in mobility of all electrolyte species with temperature. The point at which acetonitrile concentration increase had no more influence was dependent on the constant electrode charge value, and occurred earlier for higher charges It was determined that the constant charge method for slit-pore electrodes studied was not realistic as the adsorbed layer of ions could not rearrange sufficiently to balance the electrode charge.

Constant potential simulations showed that the capacitance depended strongly on the concentration of acetonitrile, which is in agreement with recent constant potential simulations with flat-wall electrodes. The charging of the pure $EMIMBF_4$ simulation at 1 V was significantly hampered by strong structuring formation in the bulk between the electrodes. Increased capacitance with increasing acetonitrile concentration was attributed to more efficient separation of counter- and co-ions, and the charging mechanism consistently relied upon ion-exchange in both electrodes for all acetonitrile concentrations studied.

4.1. Introduction

Slit-pore electrodes occupy a unique and useful region for molecular modelling of EDLCs. Firstly, they provide an ordered porous structure that can be compared with either flat-walls or disordered porous structures, acting as a bridge to facilitate understanding differences between realistic confined and unconfined electrolyte behaviour. They simplify some phenomena and geometric effects, such as diffusion path or interactions between adjacent pores. As a result, individual effects can be more easily isolated, such as pore size and length. Variation of these properties is significantly more difficult to produce for disordered models.

Slit-pores are theoretical structures and are often modelled with ideal properties, like perfectly smooth surfaces, even spacing, parallel walls, no entrance-effects, etc. They can also be used to represent sections of a more complicated porous network, for example a single-entrance slit-pore can represent a dead-end area of a porous network, and a double-entrance slit-pore can represent a channel between two reservoir-like regions of a larger porous structure.

Naturally, for comparisons with real EDLC devices, the results with slit-pore electrodes are of more interest to devices than flat wall simulations, which lack confinement effects. However, early molecular modelling of EDLCs heavily favoured flat-wall simulations over slit-pores,[1] and current modelling is becoming more influenced by more complex electrode structures.[2-3]

The unexpected results of Chmiola et al.,[4] which reported an anomalous increase in capacitance for very small pore sizes, motivated simulations using slit-pores to investigate the effects of ion distribution,[5] pore size,[6-9] and voltage.[10-11] The most interesting observations were firstly from Kondrat et al.,[7] who described the ions inside nano-pores reaching a 'super-ionic' state due to image forces exponentially screening electrostatic interactions, allowing for an accompanying increase in the charge stored by the electrode. Feng and Cummings,[6] attributed the anomalous increase in capacitance to an overlapping of double-layers originating from both surfaces inside the pore, which helped explain the dependence of capacitance on pore size.

Jiang et al.,[12-13] used classical density functional-theory with primitive electrolyte models to predict moderate capacitive enhancement for electrolyte with solvent over a range of slit-pore sizes. Kondrat et al.[14-15] predicted that the optimal pore size for energy density increases with increasing operating voltage, and that the pore charging dynamics is dependent on the initial

composition inside the pore, with empty pores charging by a front-like manner, and filled pores having diffusive charging properties.

Recently, finite size and the ratio of the electrode to bulk thickness, which does not scale well for traditional molecular modelling setups, was address by Varansai et al.[16] using grand canonical Gibbs ensemble constant potential Monte Carlo simulations, in which mobile electrolyte molecules were able to be exchanged with an external reservoir. Their results validated previously observed capacitance dependence on pore size, and also demonstrated that asymmetric pore sizes are required to maximise capacitance for electrolytes with ion size effects. He et al.[17] observed that for slit-pores with only a single layer of ions, the rate of diffusion increased with increasing electrode charge, and at high enough charge, the diffusion was greater in the pore than the bulk.

In this work we consider the effect of ACN more accurately and comprehensively than that of Jiang et al.,[12] firstly by using MD simulation with a more accurate model of the solvent, and secondly by considering a wider range of solvent concentrations. Furthermore, temperature effects, as well as both constant charge and constant potential influences are also considered, with the aim of determining the systematic influence of ACN on electrolyte composition inside pores and capacitance.

4.2. Methodology

In this work, two different series were studied, one using a novel three-dimensional periodic setup with a vapour interface for constant charge simulations in Gromacs, and the other using a conventional two-dimensional periodic setup for constant potential simulations in Metalwalls. Splitting the simulations into two different types was necessary for various reasons outlined in Chapter 3, with the major reason being the incompatibility of three-dimensional periodic systems with the constant electrode potential method.

In both cases the pore sizes were set to sub-nanometre values to limit the scope of the studies to single-adsorbed electrolyte layers inside the electrodes.

4.2.1. Three-dimensional ensemble with constant charge electrodes

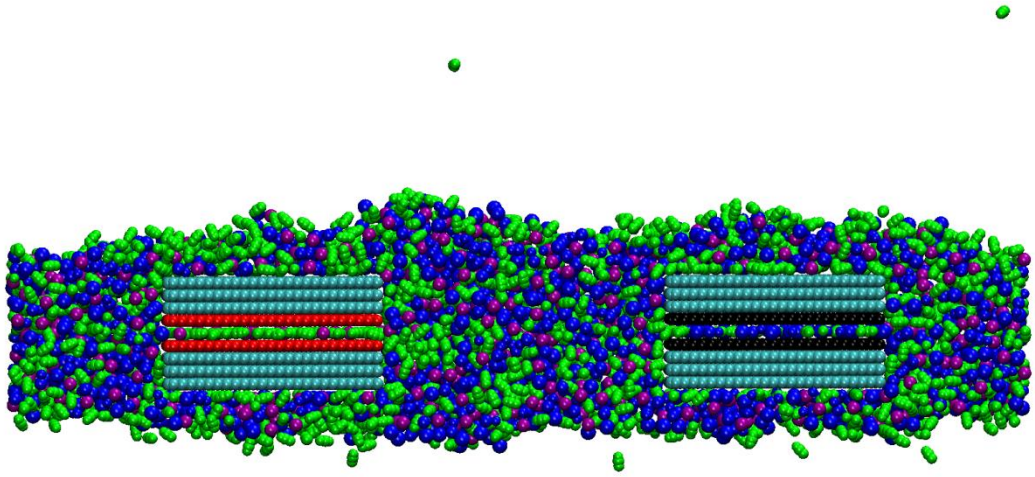

Figure 4-1: Snapshot of three-dimensional periodic system. Electrolyte is 40 % ACN, blue molecules are $BMIM^+$ cations, purple are BF_4^- anions, bright green are ACN. Red molecules are the positive electrode, black are the negative, and pale green are uncharged sheets.

An example of the simulation set up is given in Figure 4-1. The gap between the two electrodes was 8 nm. The pore size was 0.7 nm with a length and depth of 5.8 and 2.6 nm respectively, the spacing between stacked graphene-sheets was set to 0.35 nm, and the number of carbon atoms per sheet was 576. The atoms were arranged in a hexagonal structure with atomic spacing of 0.142 nm. The height of the box was set to 39 nm, creating a vapour interface and allowing the electrolyte to form a film around the pores. The main benefit of such a setup is that the density in the liquid layer is self-adjusting, simplifying the system equilibration process. However, long simulations are required.

Simulations were performed using the open source MD package Gromacs.[18] A untied-atom model of $BMIMBF_4$ was used from Zhong *et al.*[19] A United-atom model of ACN was taken from Edwards et al.,[20] and the carbon Lennard-Jones parameters were taken from Cole *et al.*,[21] with σ = 0.337 nm and ε = 0.23 kJ mol^{-1}. Lennard-Jones interaction ($\varphi(r)$) was calculated using the following equation:

$$\varphi\left(r_{ij}\right) = 4\varepsilon_{ij}\left(\left(\frac{\sigma_{ij}}{r_{ij}}\right)^{12} - \left(\frac{\sigma_{ij}}{r_{ij}}\right)^{6}\right) \tag{4-1}$$

with regular Lorentz-Berthelot mixing rules applied where:

$$\sigma_{ij} = \frac{1}{2}\left(\sigma_{ii} + \sigma_{jj}\right) \tag{4-2}$$

$$\varepsilon_{ij} = \left(\varepsilon_{ii}\varepsilon_{jj}\right)^{\frac{1}{2}} \tag{4-3}$$

Electrolyte boxes were equilibrated separately in the NVT and NPT ensembles at 298 K. These boxes were then placed above, below, and between the electrodes and allowed to relax in the NVT ensemble with zero electrode charge at four different production temperatures: 280, 298, 323, and 353 K until pore wetting was complete. The time required to complete pore filling was system dependent. Nine different electrolyte mixtures of $BMIMBF_4$ and ACN were tested, and the number of molecules in each is outlined in Table 4-1.

Table 4-1: Molecular composition of $BMIMBF_4$ and ACN mixtures.

Mass of ACN (%)	Number of $BMIBF_4$ pairs	Number of ACN molecules
0	1204	0
5	1070	310
10	981	600
15	910	884
20	814	1120
30	585	1380
40	520	1908
50	399	2196
70	232	2980

Once pore wetting was complete, constant charges on the electrode atoms were switched on, four different charges, as well as zero charge, were used as outlined in Table 4-2 with opposite signs used for the positive and negative electrodes.

Table 4-2: Constant charge values used for the electrodes.

Charge per atom (± e)	0.0	0.003	0.009	0.0151	0.0212
Electrode charge density (± C m^{-2})	0.0	0.02	0.06	0.10	0.14

Once constant charge was switched on, the systems were allowed to re-equilibrate for 5 ns, and were followed by 20 ns production runs, with a 5 ps sampling rate. The production temperatures were maintained with a Berendsen thermostat.[22] The short range electrostatic and Lennard-Jones cut-off was 1.3 nm (half the smallest system dimension), the long range electrostatics were controlled with three-dimensional PME summations.[23]

4.2.2. Two-dimensional ensemble constant potential

The setup of the two-dimensional simulations was simplified compared to the three-dimensional simulations, with the bulk being constrained between the surface adjacent to the pores, whist being periodic in the *x* and *y* dimensions, as shown in Figure 4-2. The simulation boxes were constructed in Gromacs[18] with coarse-grained models of $EMIMBF_4$ and ACN taken from Merlet *et al.*,[24] the ACN and carbon models used were the same as in Section 4.2.1 The box dimensions of the periodic *x* (depth) and *y* (height) dimensions were 2.982 and 8.56 nm respectively. The pore size was set to 0.75 nm (0.05 nm larger than in Section 4.2.1), and the pore depth was 6.0 nm (0.2 nm larger than in Section 4.2.1). In these systems the pores had a single entrance, with the opposite ends being capped by atoms. The number of atoms per pore and adjacent wall was 1376 and 864 respectively.

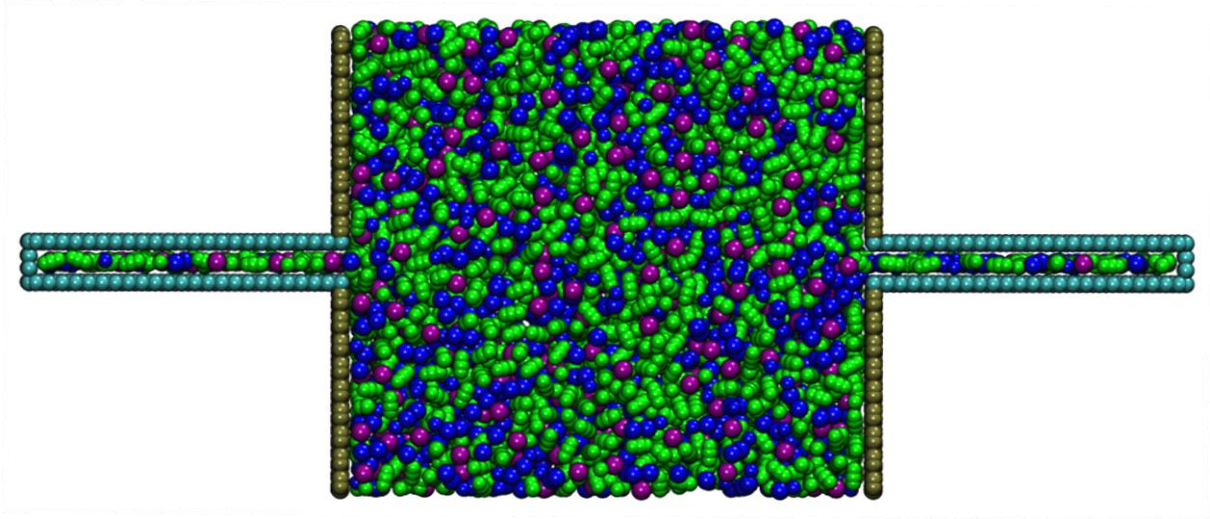

Figure 4-2: Snapshot of two-dimensional periodic system. Electrolyte is 40 % ACN, blue molecules are $EMIM^+$ cations, purple are BF_4^- anions, bright green are ACN. Pale green molecules are the uncharged electrodes with positive on the left and negative on the right. The gold molecules are uncharged wall molecules that keep the bulk electrolyte within the simulation bounds.

An initial distance between the electrodes was set to 10 nm, three mixtures of ACN and $EMIMBF_4$ were simulated, and the number of molecules required to achieve the correct bulk density was estimated from the box dimensions. The number of electrolyte molecules used is given in Table 4-3.

Table 4-3: Molecular composition of $EMIMBF_4$ and ACN mixtures.

Mass of ACN (%)	Number of $EMIBF_4$ pairs	Number of ACN molecules
0	969	0
15	774	659
40	489	1571

The electrolyte molecules were equilibrated separately in NVT and NPT ensembles at 400 K for 0.5 ns at and elevated pressure and then placed between the uncharged pores and allowed to relax. Once the pores were filled, the bulk densities of the systems were calculated and the distance between the pores was tuned until the correct densities were reached.

Second stage equilibration was performed in Metalwalls. Firstly with zero electrode charge for 0.2 ns, where the temperature was maintained at 400 K by velocity rescaling. Constant potential was then turned on to 0 V for 0.5 ns and the temperature was reduced to 340 K. The wall molecules adjacent to the pore were not included as part of the electrode. Production runs were begun by changing the system potential and turning off temperature control (NVE ensemble), two system potentials were selected for analysis: 1 V and 3 V. The short range electrostatic and Lennard-Jones cut-off was 1.5 nm (half the smallest system dimension), the long range electrostatics were controlled with two-dimensional PME summations.[23] Positions were sampled every 2 ps and the electrode potentials were evaluated at every time step.

The kinetics of the pure $EMIMBF_4$ electrolyte was examined by repeating the 1 V production run starting from and equilibrated temperature of 600 K. The influence of the wall molecules was tested by incorporating them into the charge carrying electrode and repeating the 1 V production run.

4.3. Discussion

The configurations of slit-pores are of interest because they can be used to simplify different real systems, such that they can be reduced to ordered or ideal structure so that individual phenomenon can be more easily isolated and systematically controlled. A smooth slit-pore with two entrances is a useful representation of a channel. A slit-pore with only a single entrance can represent a dead-end section of a porous network. Both configurations are studied in this chapter. Theoretically, if entrance and exit effects are removed by only sampling over a central cross-section of the pore, then the compositions between the two configurations should be reasonably comparable. However, in this work we sample from the

very entrance of the pore for convenience, but the length of the production runs were long enough to minimise this effect. Also, it is possible that during the equilibration and pore filling of the two-dimensionally periodic single-entrance simulations, which are reliant on higher than realistic bulk densities, minor artefacts were introduced. This is effect was not investigated but is most likely insignificant.

Slit-pores can serve as a bridge between understanding the different mechanisms at play for ionic liquids at flat electrodes or adsorbed inside disordered pores. Consequently, comparisons between the constant electrode-charge, and constant electrode-potential, are also very important, as these methods are thought to be realistically comparable for flat electrodes but not porous electrodes.[25]

4.3.1. Constant charge slit-pores

Firstly, we examine the constant charge simulations. The constant charge method is significantly faster to simulate, so more configurations were able to be analysed in this section. Temperature, charge, and solvent concentration effects are all considered simultaneously here to provide a comprehensive platform before further analysis.

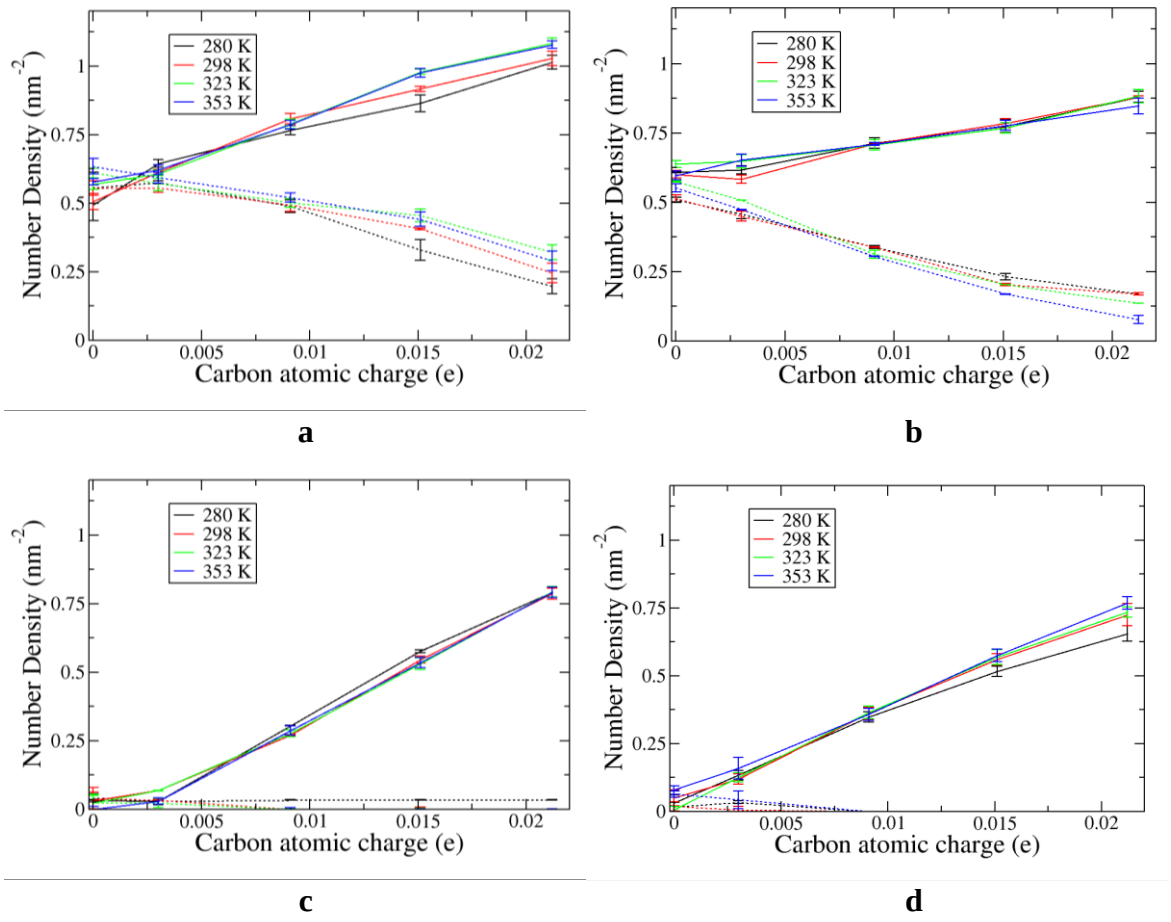

Figure 4-3: Temperature influence on electrode composition. Pure $BMIMBF_4$ is shown in the positive (a) electrode and negative electrode (b), 50 % mass ACN mixture is shown in the positive electrode (c) and negative electrode (d).

From Figure 4-3a,b it can be seen that temperature effects are minimal over the range simulated for both counter- and co-ions. The pores are still wetted even very low temperature, albeit slowly, and only at higher electrode charges does the temperature seem to have a minor influence the electrode composition. Figure 4-3c,d indicates that under moderate solvation, the effects of temperature are further reduced. Additionally, it becomes clear that for these configurations, it is possible to achieve complete co-ion removal, which would theoretically lead to a highly efficient regime, as co-ions are no longer available to detract from the induced electrode charge. The clearest observation from Figure 4-3 is that there are consistently more ions of both types in the positive electrode compared to the negative electrode. This is a result of the ion-size difference between the $BMIM^+$ and BF_4^- ions, however this effect is reduced upon moderate solvation in ACN.

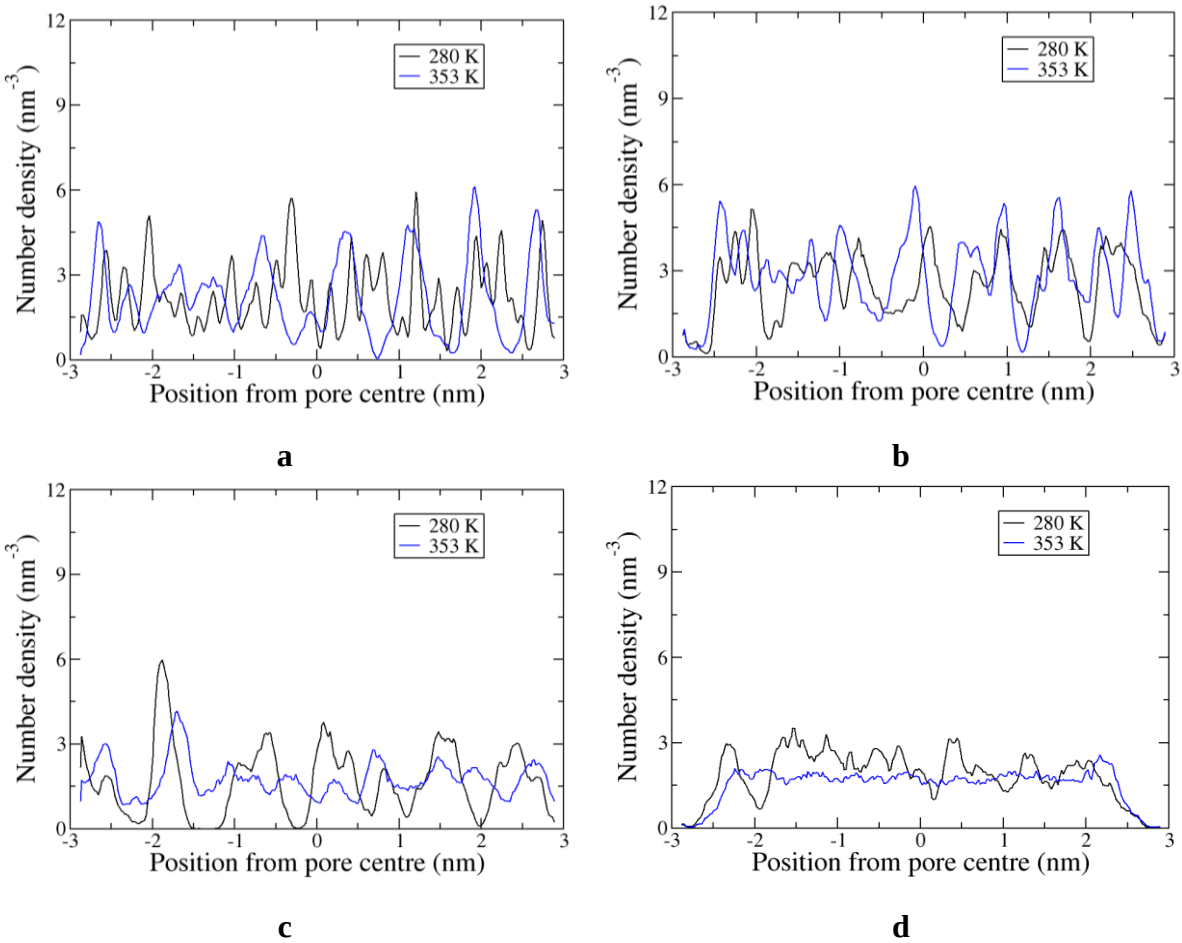

Figure 4-4: Counter-ion number density profile for Pure $BMIMBF_4$, positive electrode (a) and negative electrode (b). 40 % mass ACN mixture positive electrode (c) and negative electrode (d).

Figure 4-4 gives the number density profile along the z-dimension of the pores, with the centre point set to zero. For the pure $BMIMBF_4$ in Figure 4-4a,b neither temperature or ion-size appeared to have a significant effect on the structure, as both profiles exhibit very similar characteristics. However, upon addition of ACN in Figure 4-4c,d, the increased temperature produced a smoother more homogeneous profile, which indicates less separation between the counter-ions, and increased diffusivity inside the pore as a result of the ACN molecules screening the ion-ion interactions.

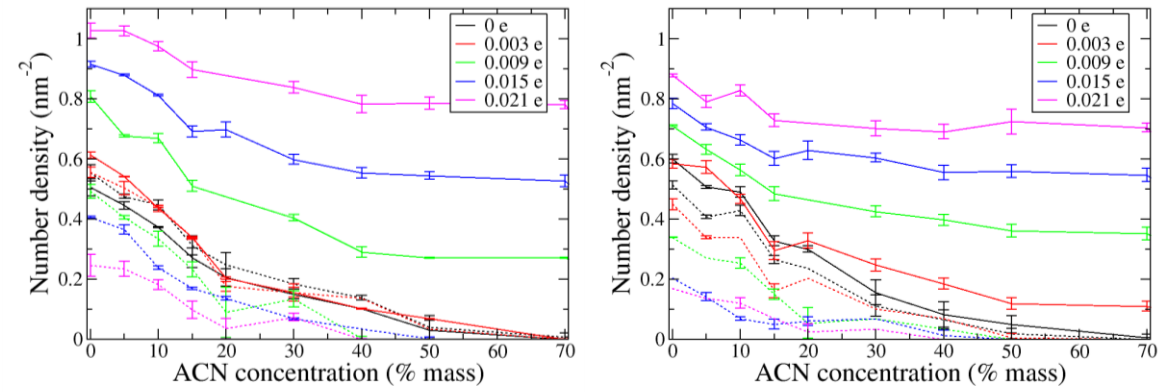

Figure 4-5: Influence of ACN on the ionic composition inside the positive electrode (a) and negative electrode (b) at 298 K for the range of carbon charges simulated. Solid lines indicate counter-ions and dashed lines indicate co-ions.

From Figure 4-5 it can be seen that across the full range of ACN concentrations tested, the carbon atomic charge has a much stronger influence on the composition of the electrodes than the ACN concentration. Beyond 15 % mass ACN, the influence of concentration was greatly diminished, except for the lowest of carbon atomic charges considered. Consequently, in Figure 4-6 we examine the influence of carbon atomic charge on electrode ionic-composition for pure $BMIMBF_4$, 15 % mass ACN, and 40 % mass ACN.

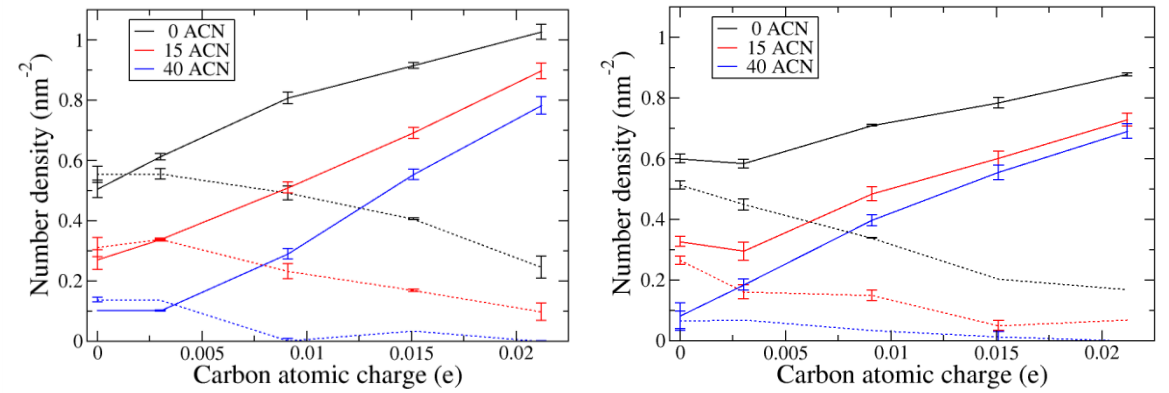

Figure 4-6: Influence of constant electrode charge on the ionic composition inside the positive electrode (a) and negative electrode (b) at 298 K. Solid lines indicate counter-ions and dashed lines indicate co-ions.

Figure 4-6 shows that that for carbon charges greater than ± 0.003 e, the counter-ion density increased linearly with charge, and the reduction in co-ion density was slightly more erratic. The net ionic-charge, which is the difference between the number of counter- and co-ions, is an indicator charge storage performance of the electrodes. In a constant potential simulation, or in a real device, if electrode-charge was plotted against net ionic-charge, then the gradient would be one (or slightly less). This because the electrode charge is induced by, and balances,

the net-ionic charge. However, in constant charge simulations, this mechanism is reversed and the net-ionic charge is a response to the constant electrode charge. As shown in Figure 4-7.

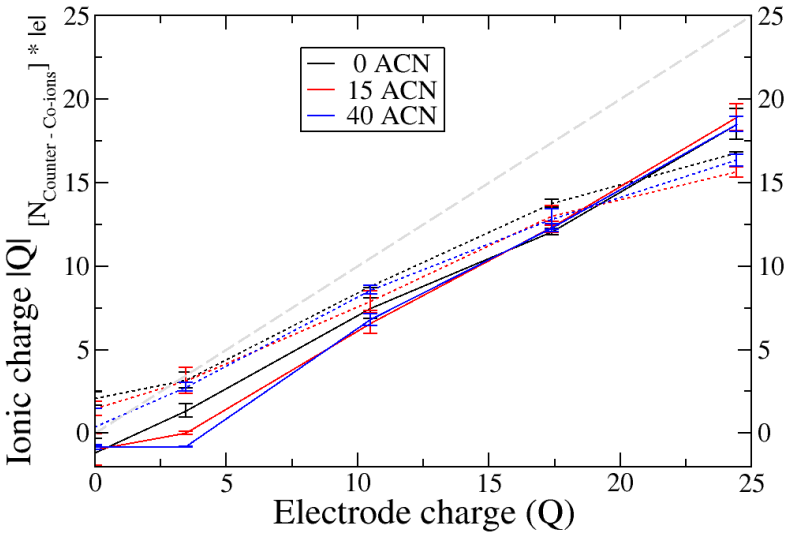

Figure 4-7: Electrode charge storage efficiency via the difference between number of counter-ions and co-ions. Solid lines indicate counter-ions and dashed lines indicate co-ions. Non-zero PZC charge as the neutral pore favours the anion slightly.

In Figure 4-7, the gradient of one is given as the dashed grey line. Below this line indicates the area where the electrode-charge was not able to be balanced fully be the net ionic-charge, and as mentioned above this behaviour is non-physical. For a real electrode, the charge dependency is reversed, so if the systems in Figure 4-7 were switched from constant charge to constant potential, the charge of the electrodes would decrease until they matched or were slightly below the net ionic-charge. I.E the charge of the electrodes would be induced by the ionic charge inside the electrodes, which are of insufficient value to maintain the original electrode charge. It is possible that ions outside of the pores could be contributing to balancing the charge of the electrodes, in which case these ions would accumulate near the pore entrances at a high density than in the bulk. However, initial two-dimensional density heat-maps, shown in Figure A4-14 of Appendix A4, do not indicate any such accumulation of ions near the pore entrances.

The significance of this observation is that the ionic composition values obtained are higher than what would be obtained in an equivalent real system. This is an important factor to keep in mind when examining constant-charge simulations of porous carbon electrodes, as the simplification of the method may lead to these artefacts. However in Figure 4-7, the extent of the discrepancy increased with increasing electrode charge, which means that constant-charge

method may be reasonably applicable when modelling small charges in porous carbon electrodes.

4.3.2. Constant potential slit-pores

In the constant potential simulations analysed in this section, the cation size was reduced by changing from $BMIM^+$ to $EMIM^+$, and the pore size was increased by 0.05 nm. Both of these factors should help in increasing the dynamics of the systems studied, which is an important computational consideration when performing constant-potential simulations. Here, the scope of the simulations was limited to considering only three different concentrations of ACN: 0, 15, and 40 % mass ACN at 323 K. These values were selected based on the results of Section 4.3.1. Additionally, only potentials of 1 and 3 V were simulated, to compare low charge, and high charge systems.

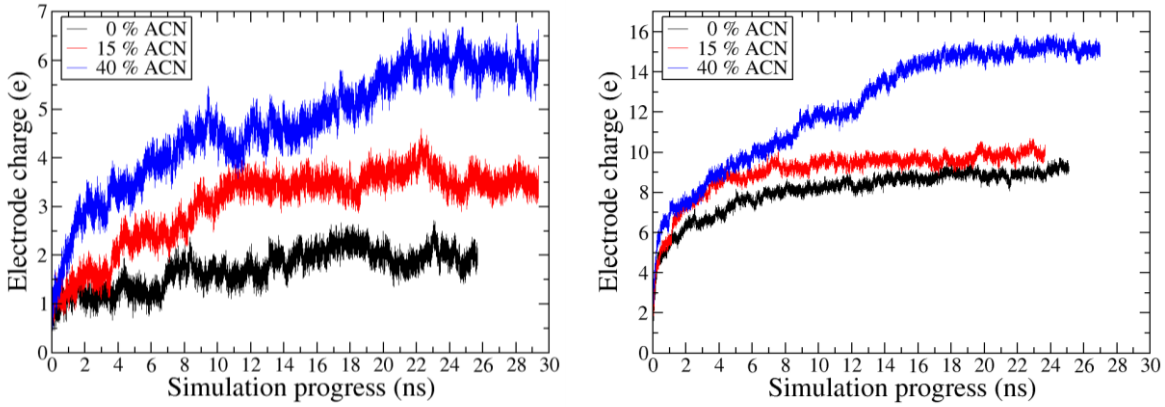

a b

Figure 4-8: Positive electrode charging curve at 1 V (a) and 3 V (b). The y-axes are shown on different scales to improve readability.

It can be seen from Figure 4-8a that the pure $EMIMBF_4$ system at 1 V exhibited slow charging with step like increases in the charge stored in the electrode. In the 15 % mass ACN systems this was also observed, but less apparent, and the 40 % mass ACN system displayed more diffusive-like charging. The slow charging of the pure $EMIMBF_4$ system can possibly be attributed to the spontaneous charge increase after a change in the ionic-composition inside the electrodes, which occurred slowly in a single-file like manner. Comparatively, the charging curves at 3 V in Figure 4-8b were much smoother, which indicates a more continual change in ionic-composition inside the electrodes. The charging behaviour observed here does not agree well with mean-field predictions by Kondrat et al.,[15] which are significantly smoother and consistent.

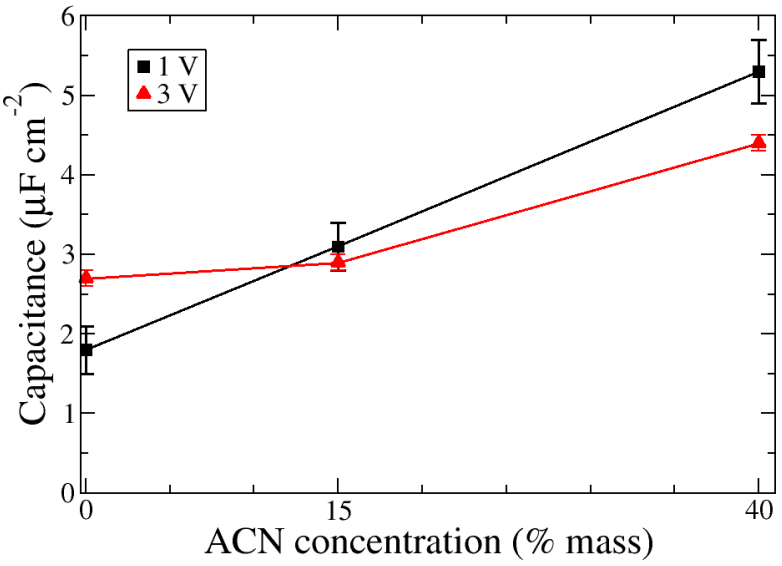

Figure 4-9: Integral areal capacitance calculated from the positive electrode charge.

In Figure 4-9 the total integral capacitance is given, as it is not possible to use to Poisson equation to determine the electrolyte potential-profile, as the slit-pore profiles can't be reduced to a single dimension in the same manner as what flat walls can. The total capacitance can be related to the individual electrode capacitances from:

$$\frac{1}{C_T} = \frac{1}{C_{P.E.}} + \frac{1}{C_{N.E.}} \tag{4-4}$$

where $C_{P.E.}$ and $C_{N.E.}$ are the capacitance of the positive and negative electrodes respectively. If it is assumed the capacitances of the individual electrodes are equal, which is reasonable in this case when considering the charge accumulation lines Figure 4-12, the individual electrode areal capacitances would be double the total capacitance, and closer to values reported elsewhere.[26]

The pure $EMIMBF_4$ simulation at 1 V exhibited low capacitance and the formation of strong layering structures at the uncharged surfaces adjacent to the pore entrances, as shown in Figure 4-10a. Seven and five layers formed at the surface of the positive and negative electrode respectively. The magnitude of the first adsorbed peak is comparable to previous results, but the number of layers is very large and contrasts strongly with characteristic IL structure between non-porous flat walls, such as Figure S2 of Merlet et al.,[24] which shows the number density profile across the bulk for the same RTIL, but with the system held at a potential 1.5 V.

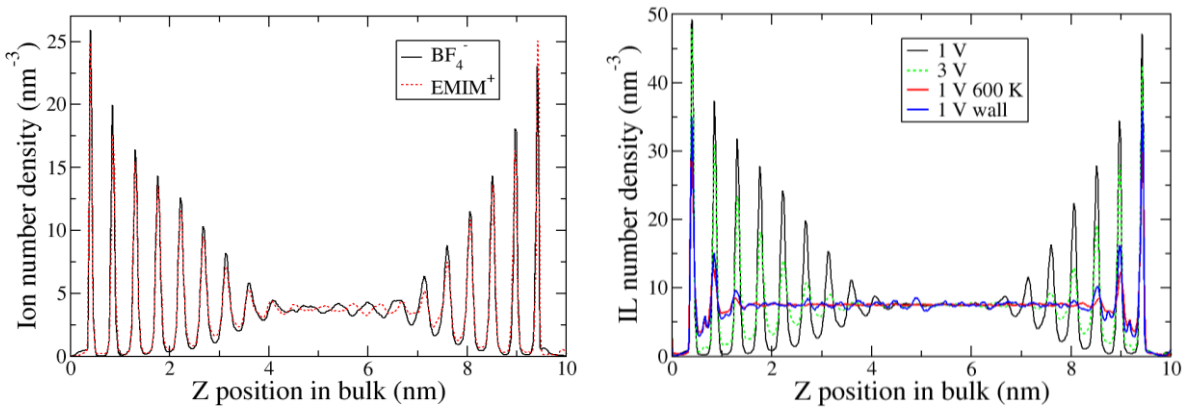

a b

Figure 4-10: (a) Ionic layering occurring in the bulk adjacent to the entrance of the electrodes, for pure $EMIMBF_4$ at 1 V potential. (b) Comparison of the $EMIMBF_4$ layering profiles in the bulk for the different systems simulated. 1 V wall refers to the simulation where the wall atoms facing the surface of the bulk were also included as electrode atoms.

As the electric field originates inside the pores only, and not at the surface of the bulk-interface, the layering observed here could be a consequence of the bulk ions balancing the electric potential due to insufficient or slow exchange of ions inside the pores, as shown in Figure 4-12a,b. To further investigate this behaviour, two additional pure $EMIMBF_4$ simulations were performed. One simply by increasing the temperature to 600 K, and the other by incorporating the previous uncharged walls into the electrode, such that the electrodes became a combination of slit-pore and flat wall. Figure 4-10b shows that when increasing the temperature, or incorporating wall atoms into the electrode, the magnitude of the first layer peak reduced and two layers formed at the surface of each electrode, more data these simulations is given in Appendix A4. The capacitance of the 600 K simulation increased significantly to 4.4 µF cm^{-2}, whereas when incorporating wall atoms the capacitance only increased to 2.5 µF cm^{-2}. The difference in capacitance observed between the 1 V simulations at 323 and 600 K appear to be a result of phase change rather than simply an increase in the charging kinetics. At 323 K, the 1 V system had significant solid-like behaviour. The more regular bulk structure which occurred from incorporating wall charges into the electrodes strongly suggest that the original 1 V solid-like behaviour was most likely an artefact of not including the wall atoms as part of the electrode, which affects the shape of the electric field. Interestingly, increasing the potential reduced the magnitude of the adsorbed peaks significantly but not their number. However, the charging of the 3 V simulation was not hampered by an insufficient rearrangement of ions inside the pore, which suggests high voltage is sufficient to charge the electrodes even if the bulk is in a solid-like phase.

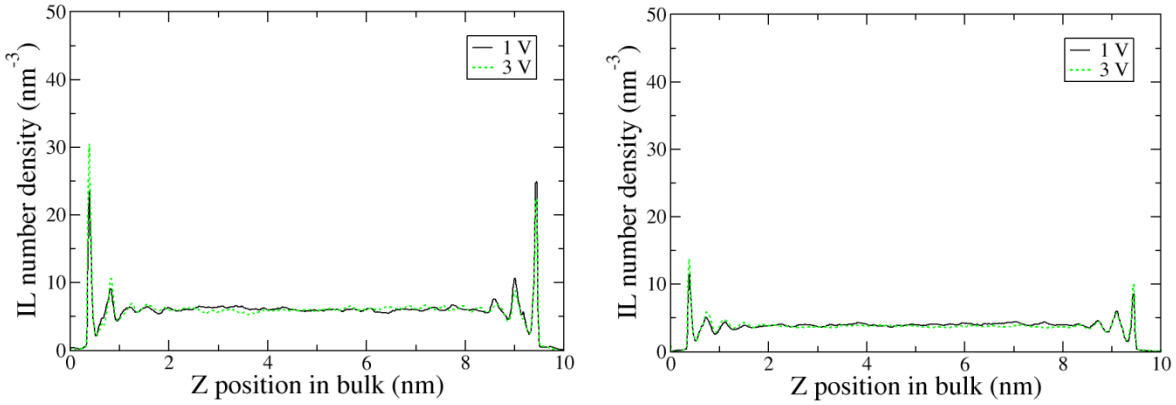

Figure 4-11: Ionic layering occurring in the bulk adjacent to the entrance of the electrodes for systems with 15 % mass ACN (a) and 40 % mass ACN (b).

The bulk profiles for the systems with ACN in Figure 4-11 show that ACN significantly reduced the number of layers formed, and their density. It is clear that the formation of strong structure in the bulk inhibits charge accumulation and capacitance in the slit-pore electrodes for these systems.

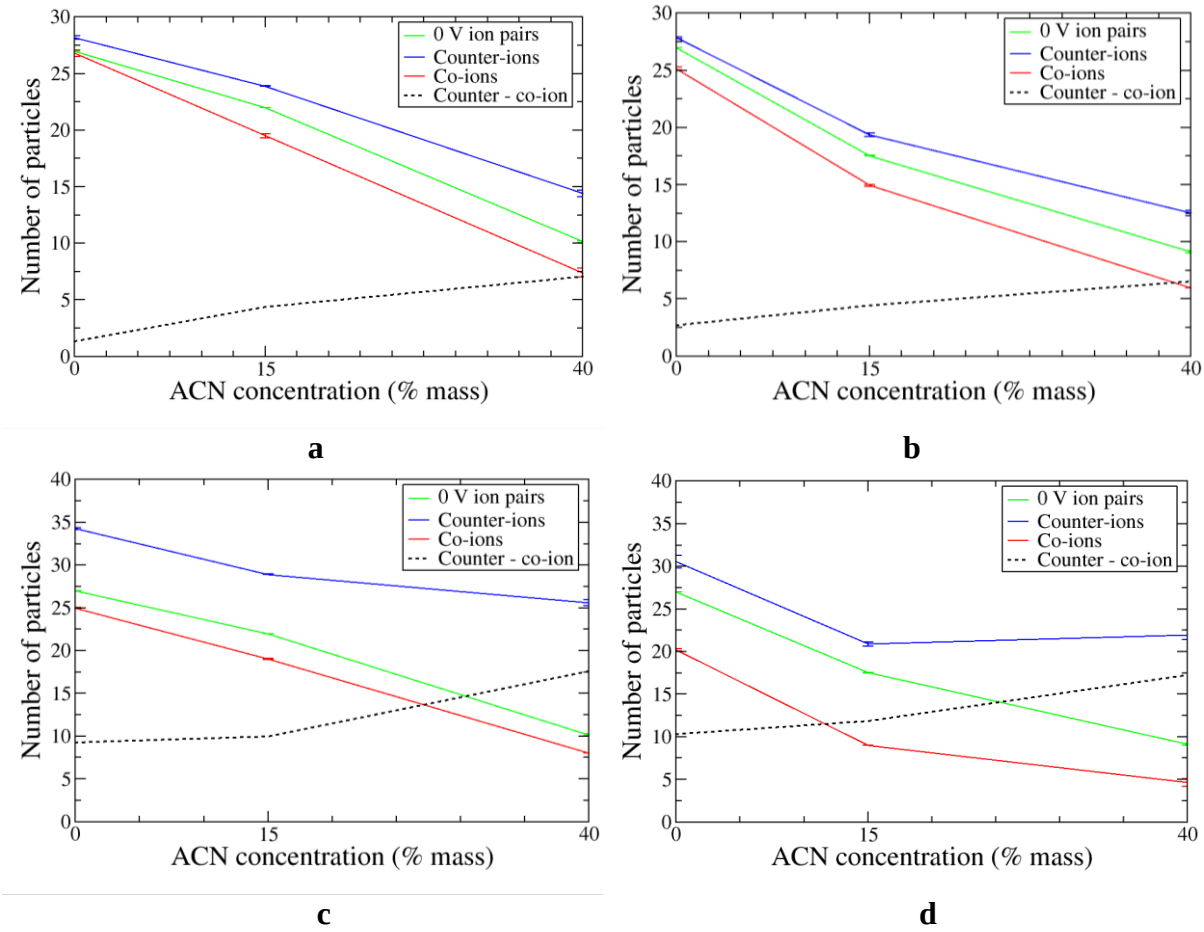

Figure 4-12: Number of ions inside the left (a) and right (b) electrode at 1 V total potential, with the equivalent 3 V total potential results given in c and d. The number of ion pairs at zero potential is given as the solid green line, and the difference between counter- and co-ions, which indicates the maximum amount of charge that can be accumulated in the electrode, is shown as the dotted black line.

From Figure 4-12 it is clear that the net ionic-charge (dashed black line) is a function of ACN in both the positive and negative electrodes, at 1 and 3 V. This can be attributed to ACN molecules screening the ion-ion Coulombic interactions, which then allows the ions to more easily enter or exit the electrodes. This behaviour is significantly different from previously results of flat-wall simulations,[26-27] but similar to recent results of Uralcan et al.[28] As with Section 4.3.1, ion size-effects are also visible here due to the larger size of the $EMIM^+$ cation. Figure 4-12d also shows a clear change in the rearrangement of ions in the negative electrode from the 15 to 40 % mass ACN systems.

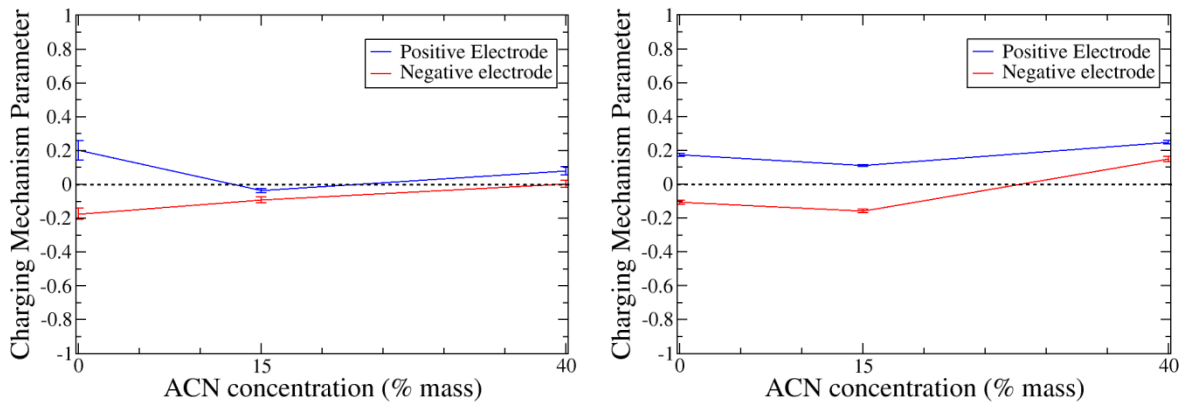

Figure 4-13: Charging mechanism parameter for 1 V (a) and 3 V (b) total system potential.

The charging mechanism parameter, shown in Figure 4-13 for both electrodes as a function of ACN concentration, was introduced recently by Forse et al.,[2] as:

$$X = \frac{N(\Psi) - N(0V)}{\left[\left|Q(\Psi)\right| - \left|Q(0V)\right|\right]/e} \tag{4-5}$$

where $N(\Psi)$ is the total number of in-pore ions at a given voltage Ψ, $Q(\Psi)$ is the corresponding electrode charge, $0V$ are the values when no electrode potential is applied, and e is the elementary charge. It can be seen that the charging mechanism parameter was dominated by ion-exchange and unresponsive to increased ACN concentration. The consistent differences between positive and negative electrodes can be attributed to ion-size difference between $EMIM^+$ and BF_4^-. However, upon solvation with ACN, the charging mechanisms appear to be converging towards counter-ion insertion, although the values remain closer to ion-exchange. Tracking the charging mechanism parameter through to more strongly diluted systems would certainly be of interest.

4.4. Conclusions

In this work, constant charge and constant potential MD simulations were performed on mixtures of ionic-liquid and ACN inside narrow slit-pores which could accommodate a single layer of ions only. The influence of electrode charge, temperature, and ACN concentration on the structural and charging properties of the narrow slit-pore were all assessed to evaluate the suitability of using slit-pore electrodes for MD simulation of EDLCs, and to provide a basis of comparison for more realistic porous-electrode models.

With constant charge electrodes, temperature had minimal effect on the ionic composition inside the electrodes, whilst ACN had a diminishing influence on electrode composition with increasing solvent concentration. The extent of ACN concentration influence was also dependent on the electrode charge. The net ionic charge inside the electrodes was consistently too low to exactly balance the constant electrode charge, and the divergence worsened with increasing electrode charge. This indicates that the constant charge method may not give realistic ionic compositions for narrow slit-pore electrodes.

For constant potential electrodes, the computational requirement for these simulations was significantly higher due to the excessively long charging times required to reach equilibrium. The capacitance of the pores was found to increase with the concentration of ACN. For the pure $EMIMBF_4$ electrolyte, maintaining the potential difference between the pores at 1 V resulted in solid-like structure forming in the bulk, this was alleviated by increasing the temperature of the system to help break the strong Coulombic couplings of the ions, and also by incorporating the wall molecules perpendicular to the pore entrance into the charge carrying electrode structure, which changed the shape of the electric field. Increasing the electric potential from 1 V to 3 V resulted in a flatter capacitance profile with ACN concentration, however no significant difference in the charging mechanism was observed, and ion-exchange dominated in all systems.

Appendix A4

a)

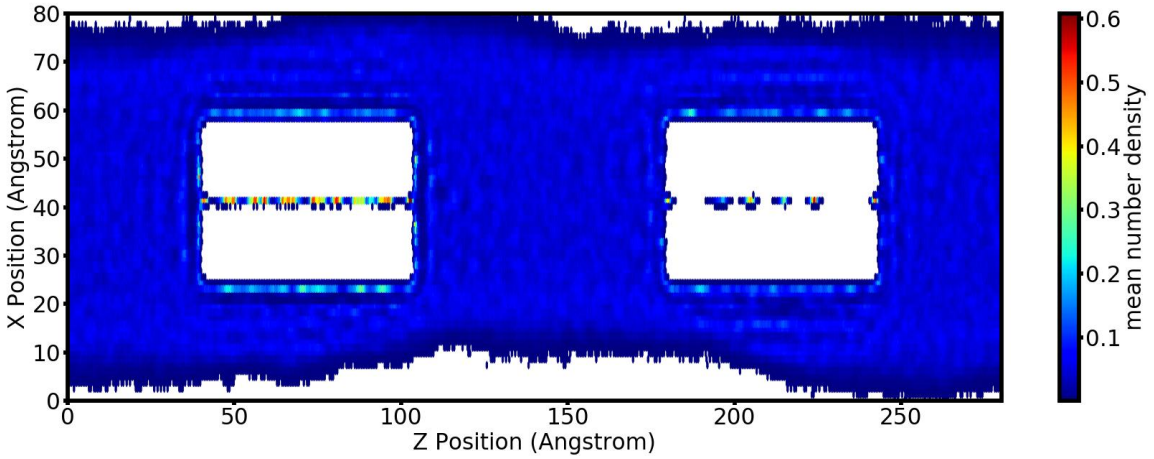

b)

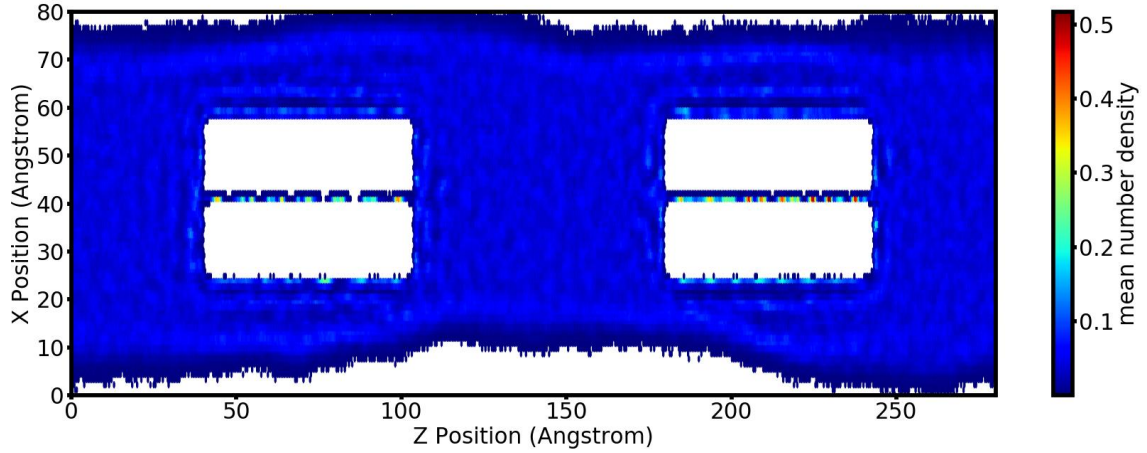

Figure A4-14: Two dimensional number density heat-maps of the centre of mass atoms for the anion (a) and cation (b). The heat maps were produced in Python 2.7.10, using the MDAnalysis toolkit.[29-30] The bin size in the x and z dimensions were set to 0.05 nm. The system shown is pure $BMIMBF_4$ at 323 K where the electrodes were held at ± 0.10 C m^{-2}.

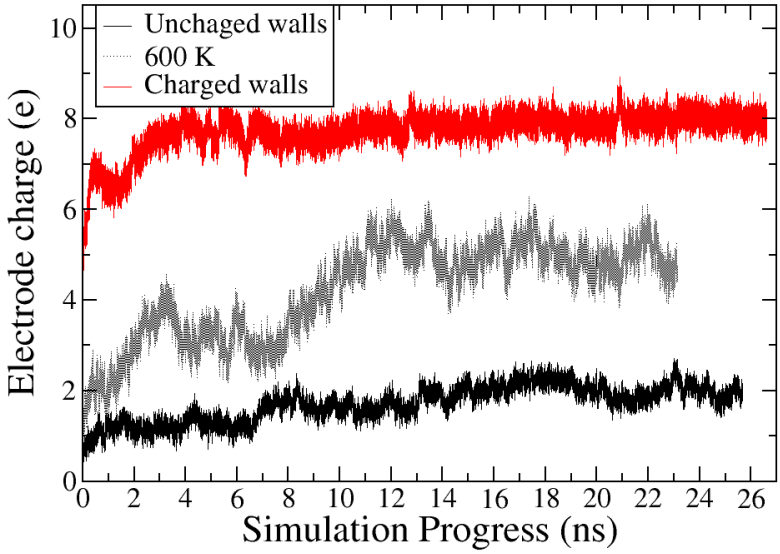

Figure A4-15: Positive electrode charging curve at 1 V for the pure $EMIMBF_4$ simulations. Uncharged walls refers to the original 323 K simulation, the 600 K simulation is also with uncharged walls, and the charged walls simulation is at 323 K.

Table A4-4: Ionic composition inside the electrodes, and the charging mechanism parameters, for the additional pure $EMIMBF_4$ 1V simulations.

	N_{EMIM} P.E.	N_{BF4} P.E.	N_{EMIM} N.E.	N_{BF4} N.E.	*X* P.E.	*X* N.E.
1 V 600 K	25.5 ± 0.1	31.1 ± 0.3	29.1 ± 0.1	23.4 ± 0.1	0.18 ± 0.03	-0.11 ± 0.02
1 V with wall	26.4 ± 0.2	29.7 ± 0.4	27.1 ± 0.3	28.0 ± 0.2	0.16 ± 0.03	0.04 ± 0.02

4.5. References

1. Burt, R.; Birkett, G.; Zhao, X. S., A Review of Molecular Modelling of Electric Double Layer Capacitors. *Phys. Chem. Chem. Phys.* **2014**, *16*, 6519-6538.

2. Forse, A. C.; Merlet, C.; Griffin, J. M.; Grey, C. P., New Perspectives on the Charging Mechanisms of Supercapacitors. *J. Am. Chem. Soc.* **2016**, *138*, 5731–5744.

3. Vatamanu, J.; Bedrov, D., Capacitive Energy Storage: Current and Future Challenges. *J. Phys. Chem. Lett.* **2015**, *6*, 3594-3609.

4. Chmiola, J.; Yushin, G.; Gogotsi, Y.; Portet, C.; Simon, P.; Taberna, P.-L., Anomalous Increase in Carbon Capacitance at Pore Sizes Less Than 1 Nanometer. *Science* **2006**, *313*, 1760-1763.

5. Feng, G.; Qiao, R.; Huang, J.; Sumpter, B. G.; Meunier, V., Ion Distribution in Electrified Micropores and Its Role in the Anomalous Enhancement of Capacitance. *ACS Nano* **2010**, *4*, 2382-2390.

6. Feng, G.; Cummings, P. T., Supercapacitor Capacitance Exhibits Oscillatory Behavior as a Function of Nanopore Size. *J. Phys. Chem. Lett.* **2011**, *2*, 2859-2864.

7. Kondrat, S.; Georgi, N.; Fedorov, M. V.; Kornyshev, A. A., A Superionic State in Nano-Porous Double-Layer Capacitors: Insights from Monte Carlo Simulations. *Phys. Chem. Chem. Phys.* **2011**, *13*, 11359-11366.

8. Wu, P.; Huang, J.; Meunier, V.; Sumpter, B. G.; Qiao, R., Complex Capacitance Scaling in Ionic Liquids-Filled Nanopores. *ACS Nano* **2011**, *5*, 9044-9051.

9. Jiang, D.; Jin, Z.; Wu, J., Oscillation of Capacitance inside Nanopores. *Nano Lett.* **2011**, *11*, 5373-5377.

10. Wu, P.; Huang, J.; Meunier, V.; Sumpter, B. G.; Qiao, R., Voltage Dependent Charge Storage Modes and Capacity in Subnanometer Pores. *J. Phys. Chem. Lett.* **2012**, *3*, 1732-1737.

11. Xing, L.; Vatamanu, J.; Borodin, O.; Bedrov, D., On the Atomistic Nature of Capacitance Enhancement Generated by Ionic Liquid Electrolyte Confined in Subnanometer Pores. *J. Phys. Chem. Lett.* **2013**, *4*, 132-140.

12. Jiang, D.-e.; Jin, Z.; Henderson, D.; Wu, J., Solvent Effect on the Pore-Size Dependence of an Organic Electrolyte Supercapacitor. *J. Phys. Chem. Lett.* **2012**, *3*, 1727-1731.

13. Jiang, D.; Wu, J., Microscopic Insights into the Electrochemical Behavior of Nonaqueous Electrolytes in Electric Double-Layer Capacitors. *J. Phys. Chem. Lett.* **2013**, *4*, 1260-1267.

14. Kondrat, S.; Perez, C.; Presser, V.; Gogotsi, Y.; Kornyshev, A., Effect of Pore Size and Its Dispersity on the Energy Storage in Nanoporous Supercapacitors. *Energy Environ. Sci.* **2012**, *5*, 6474-6479.

15. Kondrat, S.; Kornyshev, A., Charging Dynamics and Optimization of Nanoporous Supercapacitors. *J. Phys. Chem. C* **2013**, *117*, 12399-12406.

16. Varanasi, S. R.; Bhatia, S. K., Capacitance Optimization in Nanoscale Electrochemical Supercapacitors. *J. Phys. Chem. C* **2015**, *119*, 17573-17584.

17. He, Y.; Qiao, R.; Vatamanu, J.; Borodin, O.; Bedrov, D.; Huang, J.; Sumpter, B. G., The Importance of Ion Packing on the Dynamics of Ionic Liquids During Micropore Charging. *J. Phys. Chem. Lett.* **2015**, 36-42.

18. Hess, B.; Kutzner, C.; Van Der Spoel, D.; Lindahl, E., Gromacs 4: Algorithms for Highly Efficient, Load-Balanced, and Scalable Molecular Simulation. *J. Chem. Theory Comput.* **2008**, *4*, 435-447.

19. Zhong, X.; Liu, Z.; Cao, D., Improved Classical United-Atom Force Field for Imidazolium-Based Ionic Liquids: Tetrafluoroborate, Hexafluorophosphate, Methylsulfate, Trifluoromethylsulfonate, Acetate, Trifluoroacetate, and Bis(Trifluoromethylsulfonyl)Amide. *J. Phys. Chem. B* **2011**, *115*, 10027-10040.

20. Edwards, D. M. F.; Madden, P. A.; McDonald, I. R., A Computer Simulation Study of the Dielectric Properties of a Model of Methyl Cyanide. *Mol. Phys.* **1984**, *51*, 1141-1161.

21. Cole, M. W.; Klein, J. R., The Interaction between Noble Gases and the Basal Plane Surface of Graphite. *Surf. Sci.* **1983**, *124*, 547-554.

22. Berendsen, H. J. C.; Postma, J. P. M.; van Gunsteren, W. F.; DiNola, A.; Haak, J. R., Molecular Dynamics with Coupling to an External Bath. *J. Chem. Phys.* **1984**, *81*, 3684-7.

23. Ewald, P., Evaluation of Optical and Electrostatic Lattice Potentials. *Ann. Phys.* **1921**, *64*, 253-287.

24. Merlet, C.; Salanne, M.; Rotenberg, B., New Coarse-Grained Models of Imidazolium Ionic Liquids for Bulk and Interfacial Molecular Simulations. *J. Phys. Chem. C* **2012**, *116*, 7687-7693.

25. Merlet, C.; Pean, C.; Rotenberg, B.; Madden, P. A.; Simon, P.; Salanne, M., Simulating Supercapacitors: Can We Model Electrodes as Constant Charge Surfaces? *J. Phys. Chem. Lett.* **2013**, *4*, 264-268.

26. Feng, G.; Huang, J.; Sumpter, B. G.; Meunier, V.; Qiao, R., A "Counter-Charge Layer in Generalized Solvents" Framework for Electrical Double Layers in Neat and Hybrid Ionic Liquid Electrolytes. *Phys. Chem. Chem. Phys.* **2011**, *13*, 14724-14735.

27. Merlet, C.; Salanne, M.; Rotenberg, B.; Madden, P. A., Influence of Solvation on the Structural and Capacitive Properties of Electrical Double Layer Capacitors. *Electrochim. Acta* **2013**, *101*, 262-271.

28. Uralcan, B.; Aksay, I. A.; Debenedetti, P. G.; Limmer, D. T., Concentration Fluctuations and Capacitive Response in Dense Ionic Solutions. *J. Phys. Chem. Lett.* **2016**, *7*, 2333-2338.

29. Michaud-Agrawal, N.; Denning, E. J.; Woolf, T. B.; Beckstein, O., Mdanalysis: A Toolkit for the Analysis of Molecular Dynamics Simulations. *J. Comput. Chem.* **2011**, *32*, 2319-2327.

30. R. J. Gowers; M. Linke; J. Barnoud; T. J. E. Reddy; M. N. Melo; S. L. Seyler; D. L. Dotson; J. Domanski; S. Buchoux; I. M. Kenney, et al. In *Mdanalysis: A Python Package for the Rapid Analysis of Molecular Dynamics Simulations*, Proceedings of the 15th Python in Science Conference, Austin, TX, SciPy: 2016; pp 102-109.

5. Molecular structure and capacitance properties of imidazolium ionic liquid and acetonitrile mixtures inside disordered porous carbon electrodes

Room temperature ionic-liquid electrolytes have received significant attention for use in electric double-layer capacitors due to their favourable properties, such as high voltage window and low vapour pressure. In this work we performed molecular dynamics simulations, with complementary experiments, on systems of the pure room temperature ionic-liquid $EMIMBF_4$, and highly concentrated mixtures with acetonitrile, inside disordered porous carbide-derived carbon electrodes. The results help to elucidate the systematic contribution of acetonitrile and ion concentration to capacitance, and to the underlying charge storage mechanisms inside microporous electrodes.

Electrochemical measurements showed that the capacitance was not significantly affected by ion concentration when switching from pure $EMIMBF_4$ to $EMIMBF_4$ diluted in acetonitrile. Complimentary molecular dynamics simulations showed that this may be due to increased difficulty in separating un-like ions at higher concentrations where solvent molecules are not present to screen the strong Coulombic interactions of the ionic liquid species. A charging mechanism which differentiates between counter-ion adsorption, co-ion desorption, and ion-exchange showed that the charging mechanism consistently changed with ion concentration. With the most concentrated system yielding an ion-exchange mechanism and the most diluted a counter-ion adsorption mechanism. Unlike capacitance, the in pore diffusion was shown to strongly depend on ion concentration. The dynamics of highly concentrated ions was significantly slower, suggesting longer charging times for high concentrations.

Increasing the electric potential by threefold resulted in a 15 % reduction in capacitance for pure $EMIMBF_4$ electrolyte, despite the counter-ions moving closer to the internal pore surface. In this regime the pores are saturated with ions to such an extent that sufficient rearrangement of ions to induce a proportional increase in electrode charge is inhibited.

Pair-distribution function analysis of a single uncharged pore with filled with EMIMTFSI showed that confinement of ions breaks the long range structures that are formed at distances of greater than 1 nm in bulk liquid regions, suggesting that the three-dimensional nature of microporous CDCs enables stronger solid-liquid interactions.

5.1. Introduction

Electric double-layer capacitors (EDLCs) are a promising electrochemical energy storage technology that in recent years have received significant attention both commercially and by researchers. EDLCs store charge by ion adsorption and subsequent charge accumulation in the region known as the electric double layer (EDL).[1] Research and development of EDLCs is being driven by demand from emerging applications which require efficient energy storage, most prominently renewable energy[2] electric vehicles,[3] and smart-grid management.[4-5] Key to the development of EDL is understanding the complex molecular mechanisms that are part of the charging and discharging processes.[6]

Currently, commercial EDLCs have energy densities in the vicinity of 5 Wh kg^{-1}. For EDLCs to compete with batteries, which can have approximately ten times the energy density,[5] energy storage improvements must be made. Two of the most promising areas for research are high surface-area electrodes,[7] and electrolytes with high voltage windows.[8] Experiments by Chmiola et al.[9] reported an anomalous increase in capacitance in electrodes with pore diameters of less than one nm due to the desolvation of ions upon entering the pores. This was followed by experiments by Largeot et al.,[10] where it was shown that capacitance can reach a maximum when the pore diameter closely matches the ion diameter. These studies challenged the traditional beliefs held about the EDL in pores (that pores smaller than one nm did not contribute to capacitance), and stimulated much debate among researchers. What has become clear is that when designing a device, it is critical to consider both the electrode and electrolyte dimensions as a pair, so that maximum efficiency can be obtained.[11] On the electrolyte side, there is great and ongoing interest in improving the design and performance by replacing the traditional organic solutions. In this regard, room temperature ionic-liquids (RTILs) are emerging candidates due to their high voltage window,[12] thermal stability,[13] and low toxicity.[14] The cation and anion sizes are tunable in RTILs, which gives the benefit of being able to select pairs to match specific electrodes.[10] Unfortunately, pure RTILs suffer from poor conductivity and high viscosity,[15] a problem which is exacerbated in EDLCs with highly microporous carbon electrodes. A potential solution is to use "superconcentrated electrolytes", which are highly-concentrated mixtures of RTILs and organic solvents.[16]

When combining microporous electrodes with pure RTILs or superconcentrated electrolytes, it is unclear what the exact molecular mechanisms and structures are that contribute to enhanced capacitance. The fundamental difficulty of selecting an optimal electrolyte in

EDLCS is that ions are absorbed inside electrified (and often disordered) nanoporous carbon electrodes. Electrolyte structures are greatly altered by strong electric fields and confinement effects. Significant progress towards understanding the molecular mechanisms that cause enhanced capacitance has been made,[6] however the charge storage mechanisms can change across different solid-materials and liquids, and these have not been widely studied. Elucidating this knowledge by traditional experiments is problematic and expensive due to the difficulty of probing inside three dimensional porous structures of very small diameters. Complicated *in situ* techniques have to be employed.[17-19] Similarly, observing the layered liquid structure at the electrode surface is difficult when considering the density of ions in RTILs. Mean field theories and molecular modelling of RTILs on planar or porous carbon interfaces have been used to compliment experiments due to their ability to predict structures and mechanisms on an atomic scale. Many articles have been published in this area over the last several years.[20-25] These studies are able to bring unique insight into the performance and design of EDLCs, however only a limited variety of systems have been investigated so far.

Using molecular dynamics (MD) simulations of mixture of RTILs and acetonitrile (ACN) at flat non-porous graphite electrodes, Feng et al.[26] showed that the concentration of ACN only results in a small change in capacitance. Larger variations have been recently reported by Uralcan et al.[27] By using a simple analytical model, Lee and Perkin[28] showed that mixing ionic liquids with solvents is also an efficient way to avoid hysteresis effects due to phase transitions in the adsorbed layer.

Merlet et al.[29] demonstrated that the interfacial layering structures of two distinct RTILs at a flat graphene electrode can become similar upon addition of ACN due to the reduction in ion size differences of the solvated ions. Xing et al.[30] showed that integral capacitance (IC) can be increased by texturising the flat electrode surface on an atomic scale, to essentially create pores of a very short length and diameters matching that of the ions.

When considering ordered slit-pore electrodes, the structure and capacitance behaviour changes significantly from flat electrodes due to molecule realignment and confinement effects. Several MD studies[11, 31-32] have replicated the experimentally observed capacitance peak in small slit-pores.[10] The reported capacitances were consistently lower than experimental results, but this is reasonable when considering the simplicity of slit-pore electrodes and difficulty of accurately capturing confinement effects with complicated RTIL models. Further studies with slit-pores have demonstrated that capacitance has a non-linear

relationship with voltage,[33] and also that optimal operating voltage decreases with decreasing pore diameter.[34]

Merlet et al.[35] performed a novel MD study by incorporating three-dimensional carbide-derived carbon (CDC) electrodes, which had a disordered structure and pore-size distribution. Their simulations gained insight into the charge screening behaviour occurring inside realistic microporous electrodes, and established a new process for more realistic MD simulations of EDLCs. Further work by Péan et al.[36] demonstrated that the charging behaviour of RTILs in CDC electrodes is heterogeneous and dependent on pore size. Upon addition of ACN to an RTIL, Péan et al.[37] also showed that the pore-scale charging mechanism became slightly modified, but no significant global (electrode-scale) charging change was noted. They also stated that ACN addition, and increased electric potential, have similar effects on dynamics.

In this work we firstly studied the behaviour of pure 1-ethyl-3-methylimidazolium tertafluoroborate (EMIMBF_4) and mixtures with ACN, ranging from dilute to pure RTIL, in combination with nanoporous CDC electrodes. Cyclic voltammetry experiments were performed and showed negligible change in capacitance with ionic concentration. By performing MD simulations on the same systems, we quantitatively studied how ACN influenced the charge storage mechanisms inside microporous electrodes, in the dilute superconcentrated electrolyte regimes. An example of the simulation cell configuration can be seen in Figure 5-1. Simulations were performed predominantly at 1 V with a selected simulation at 3 V.

Finally, pair-distribution functions (PDFs) were calculated for 1-ethyl-3-methylimidazolium bis(trifluoromethylsulfonyl)imide (EMIMTFSI) inside uncharged titanium and silicon CDCs. Structural properties of the ionic liquid, and screening effects of the CDCs were examined to further characterise RTIL-CDC interaction properties.

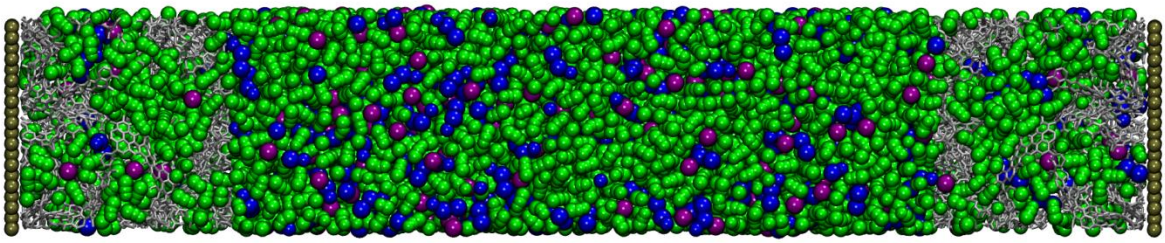

Figure 5-1: Simulation cell of an $EMIMBF_4$ and 67 % mass ACN electrolyte mixture wetting uncharged disordered porous Ti-CDC800 electrodes. Colour scheme; blue: 3-site $EMIM^+$ molecules, purple: single-site BF_4^- molecules, green: 3-site ACN molecules, silver: carbon electrode atoms. Gold molecules cap the cell in the z-dimension, as this is non-periodic.

5.2. Methodology

5.2.1. Electrochemistry experiments - $EMIMBF_4$ and ACN mixtures in CDC 800 electrodes

Electrochemistry experiments were performed by Barbara Daffos, Pierre-Louis Taberna and Patrice Simon at The University of Toulouse, France. $EMIMBF_4$ ionic liquid (Solvionic, France) and ACN (Acros organic, France) were used as purchased. They were mixed at room temperature, yielding five different ionic concentrations as listed in Table 5-1. Carbide-derived carbon (CDC) powder (Y-Carbon, USA) was prepared by chlorination of TiC powder at 800 ^oC which corresponds to a pore size of 0.77 nm, as reported elsewhere.[9-10] The pore size distribution (PSD) of the CDC powder was obtained from Ar-isotherms using NLDFT and QSDFT models (NOVAe SERIES software, QUANTACHROME, USA). The measured average pore sizes were 0.77 and 0.66 nm respectively. Active films were made by mixing 95 wt % CDC with 5 wt % polyTetraFluoroEthylene (PTFE) binder. Once calendered, 8 mm diameter electrodes were cut. The active film thickness was around 300 µm, with a weight loading of 15 mg cm^{-2}. Active films were laminated onto treated aluminium current collectors[38] and two layers of 25 µm-thick porous PTFE were used as a separator. A silver wire was used as a pseudo-reference electrode, for monitoring the negative and positive electrode potentials, separately during the cell cycling. Cell assembly was done in a glove box under an argon atmosphere (< 1 ppm of O_2 and H_2O content) in three electrode Swagelok cells. Cyclic voltammetry tests were carried out between 0 and 2.3 V, at a scan rate of 5 mV s^{-1}.

5.2.2. Molecular dynamics simulations - $EMIMBF_4$ and ACN mixtures in CDC 800 electrodes

Electrolyte compositions used can be found in Table 5-1. Coarse-grained models for ACN and $EMIMBF_4$ were obtained from Edwards et al.[39] and Merlet et al.[40] respectively. The simulation boxes consist of $EMIMBF_4$ and ACN surrounded by two symmetric carbide-derived carbon electrodes, with an average pore size of approximately 0.75 nm. The model electrodes were obtained by quenched molecular dynamics from Palmer et al.,[41] by quenching a sample of liquid carbon consisting of approximately 4000 atoms with a rate of $20 * 10^{12}$ K s^{-1}. Finally, the carbon Lennard-Jones parameters of $\sigma = 0.337$ nm and $\varepsilon = 0.23$ kJ mol^{-1} were obtained from Cole et al.[42]

Table 5-1: Electrolyte compositions

ACN Mass %	0 (pure IL)	10	20	40	67
Ion conc. (mol L^{-1} at 298.15 K)	6.40	5.28	4.58	3.01	1.51
Ion Pairs	600	601	608	326	324
ACN molecules	0	322	733	1048	3172

Initial equilibration and pore filling was performed in the open source MD package Gromacs.[43] Firstly, the liquid molecules were equilibrated separately at 340 K. The liquid boxes were then placed between the electrodes and allowed to relax in the NVT ensemble. Pore filling rate was enhanced by cycling the constant charge values of the electrode atoms between ± 0.01 e for 10 iterations. The boxes were then equilibrated at zero electrode charge for 500 ps. Second stage equilibration was performed with Metalwalls. The distance between the electrodes was tuned by position rescaling for each system, such that the bulk densities matched those of the pure $EMIMBF_4$/ACN mixtures at 1 bar and 340 K. The temperature of 340 K was chosen to increase the ion mobility and reduce the required simulation time. Once correct bulk densities were achieved, the final equilibration step was performed with velocity rescaling and electrode atoms charged to constant values of ± 0.01 e for the positive and negative electrode, this step was run for several nanoseconds so that sufficient equilibrium was achieved.

For production runs, the electrodes were switched to a constant potential, following a method developed by Reed et al.,[44] and the systems were run in the NVE ensemble with ± 0.5 V for the half-cell potentials of the positive and negative electrodes. The length of production runs

exceeded 15 ns to ensure that average electrode atom charges had reached a steady equilibrium value. 2D Ewald summations[44-45] were used for all coulombic interaction calculations, with a short range cut-off distance of 2.2 nm (half the length of the *x* and *y* cell dimensions). Lorentz-Berthelot combination mixing rules were employed for non-bonded potential interactions.

The capacitance was calculated using

$$C = \frac{Q^{\pm}}{\Psi^{\pm}} \tag{5-1}$$

where Q and Ψ are the electrode charge and voltage respectively. In the simulations, Ψ is a known and constrained parameter, and Q can be determined directly from the simulation data.

An additional simulation was run at cell potential of 3 V, using pure $EMIMBF_4$ as the electrolyte. This system was equilibrated at zero electrode potential and 340 K for 5 ns. For production, the half-cell potentials were spontaneously increased to ± 1.5 V and run in the NVE ensemble until the electrode charge equilibrated to a steady-state value. (This occurred after approximately 4 ns.)

5.2.3. PDF analysis- EMIMTFSI in uncharged Ti-CDC 800 and Si-CDC 800 pores

5.2.3.1. Experiments

The PDF experiments were performed by Dr Boris Dyatkin and colleagues at Drexel University, PA, USA. Empty and filled Si-CDC 800 (prepared as described in ref. 46), along with bulk EMIMTFSI, were loaded into Capton capillaries for X-ray total scattering reflection experiments at the 1-1D-B beamline of the Advanced Photon Source (Argonne National Laboratory). 58.65 keV (λ = 0.2114 Å) incident emission and measured scattering in the 0.01 $Å^{-1}$ < Q < 22.2 $Å^{-1}$ range was used. Measurements were calibrated using the Fit2D program and obtained S(Q) and G(r) analysis from PDFGetX2 data reduction software.[47]

5.2.3.2. MD simulations

Simulations were performed using the molecular dynamics package Gromacs.[43] The EMIM-TFSI electrolyte pore force fields was provided from Köddermann et al.[48] The Ti-CDC 800 model was obtained as previously from Palmer et al.,[41] and the Si-CDC 800 model was obtained from Farmahini et al.[49] The simulations were equilibrated in the 2D-periodic NVT ensemble. The temperature was maintained at 298 K with the Nose-Hoover thermostat.[50-51]

Electrostatic calculations used particle mesh Ewald summations, with a potential cut-off distance of 1.2 nm for electrostatic and van der Waals interactions, half the smallest cell dimension. The initial simulations placed an equilibrated box of 216 ion pairs next to the CDC pores in the non-periodic direction and were capped by a wall of immobile carbon atoms at the simulation boundary (Figure B5-14 of Appendix B5). To facilitate the filling of the pore, the wall of carbons was incrementally and periodically shifted closer towards the pore to act as a piston.

Once the pore filling was completed, the position of the carbon walls was shifted away from the pore and the system was allowed to relax for 1 ns until the correct density of ions in the pore was reached. Following this, all the excess ions outside the pore and the carbon walls were removed leaving 72 ion pairs for the Ti-CDC 800 pore and 74 ion pairs for the Si-CDC 800 pore, with concentrations of 1.6 and 2.0 mmol/g carbon inside the pore respectively (Figure B5-15 of Appendix B5). The simulations were then switched to the 3D periodic NVT ensemble and re-equilibrated for 550 ps. A 5 ns production run was performed with trajectories and energies sampled every 5 ps. From the production run data, radial distribution functions (RDFs) were calculated for all possible atom combinations and included intramolecular combinations. The RDF information was then used to calculate the PDF for the total system. The PDF was also computed for an empty Ti-CDC 800 and Si-CDC 800 pore and the pure EMIM-TFSI liquid.

5.3. Results and discussion

5.3.1. $EMIMBF_4$ and ACN mixtures inside CDC electrodes

5.3.1.1. Capacitance

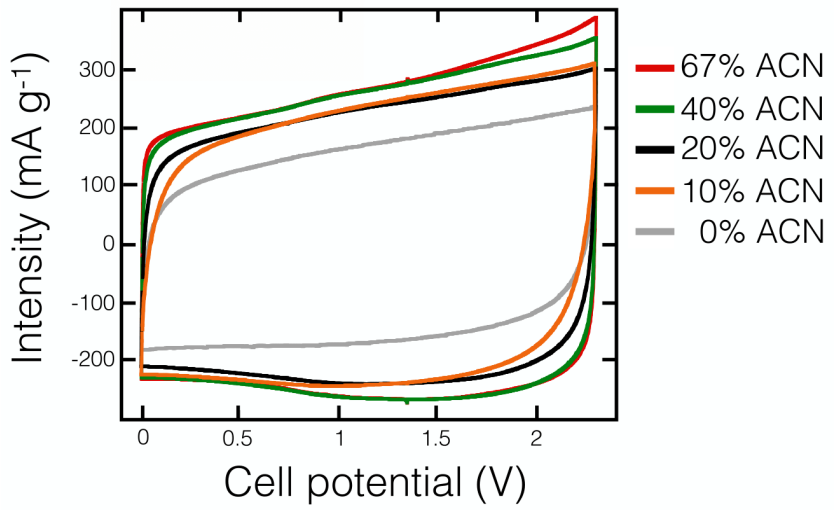

Figure 5-2: Cyclic voltammograms of supercapacitor cells assembled with two electrodes based on 0.77 nm average pore size carbide-derived carbons (CDC), in electrolytes composed of $EMIMBF_4$ mixed with ACN at several mass fractions. The potential scan rate is 5 mV s^{-1}.

Cyclic voltammetry (CV) experiments were carried out for potentials ranging between 0 and 2.3 V, at a scan rate of 5 mV s^{-1}. The recorded voltammograms are shown in Figure 5-2. The CVs look very similar across the whole range of composition, except for the pure RTIL. The corresponding specific capacitances are provided in Table 5-2.

Table 5-2: Summary of the experimental and simulated capacitances. The experimental data is obtained from CV by integration of the electric current during the discharge of the cell at a scan rate of 5 mV s^{-1}. The MD simulation data is extracted from the charge accumulated at the surface of the electrodes for an applied voltage of 1 V.

ACN mass %	0	10	20	40	67
Ion conc. (mol L^{-1} at T = 298 K)	6.40	5.28	4.58	3.01	1.51
C (F g^{-1}) / CV, T = 298 K, scan rate = 5 mV s^{-1}	70	100	100	105	105
C (F g^{-1}) / CV, T = 298 K, scan rate = 1 mV s^{-1}	80	-	-	-	-
C (F g^{-1}) / CV, T = 373 K, scan rate = 5 mV s^{-1}	150	-	-	-	-
C (F g^{-1}) / MD, T = 340 K	140	145	145	125	115

Here we attempt to interpret these experimental results by performing complimentary MD simulations on the same systems. Of prominent interest is how well the capacitances can be compared with experimental results, and the underlying molecular mechanisms that can

explain the observed capacitance phenomena. In this work the electrodes were maintained at a constant potential, as outlined in Chapter 3.

It is difficult to make accurate comparisons between simulation and experimental results, this is due to differences in experimental and simulation method. On the simulation side, the models used are not perfect representations, and acceptable concessions (such as coarse-graining or non-polarisability, ideal conduction in the electrode, etc.) have to be made to enable the simulations to be computationally feasible. Experimentally, capacitance determined by cyclic voltammetry is usually at a constant scan rate, and if electrolytes in a device have low ionic mobility, it may not reach full charge. This will result in a lower capacitance value. However, this phenomenon does not occur in simulations as the electrodes are fully charged before the capacitance sampling is performed.

Simulations were performed at 340 K and experiments at 298 K. The reason for using different simulation temperature was that the dynamics of the pure RTIL at 298 K is very slow, and would require excessively long simulation times. Temperature effects on capacitance are expected to be small,[52] unless the temperature at which the experiments are carried is too low to allow for a good diffusivity of the ions,[53] in which case the capacitance measurement is hampered by a large ohmic drop. Overall, we observe reasonable qualitative agreement between experiments and simulations; it is notable that the simulations overestimate the experimental capacitance, this is likely due to the simplifications of coarse-graining the RTIL, ignoring field penetration effects, and treating the electrode as a perfect conductor.[54] The comparison between experimental and simulation improves at higher concentration of ACN, as seen in Table 5-2.

The obvious discrepancy between experimental capacitance at 298 K and simulated capacitance at 340 K is the result for the pure RTIL, where the experimental value is significantly lowered. The comparison is improved when a slower scan rate of 1 mV s^{-1} is used for measuring the experimental capacitance (80 F g^{-1} instead of 70 F g^{-1}), which points towards a kinetic cause for this discrepancy. To test this discrepancy an additional experiment was performed at 373 K and yielded a two-fold increase in capacitance, consistent with an increase in the ionic conductivity. Therefore, it can be reasonably concluded that the difference between simulation and experiment for the pure RTIL was due to a large ohmic drop in the experiment at 298 K.

The main conclusion that can be made from Table 5-2 is that capacitance is not particularly sensitive to ACN concentration in the range studied. For experiments the increase in capacitance was approximately 5 % (if discarding the pure RTIL) and not deemed to be significant. The reduction in simulated capacitance was more pronounced at 25 %, however there is a greater than four-fold difference in ionic concentration between the two extreme cases. This result contrasts with the more dilute regime (100 mmol L^{-1} or less, i.e. not at all in the supercapacitor regime, for which large variations of the capacitance are observed, especially for low applied potentials). The significance of these observations is that it is not efficient to attempt to increase the capacitance of a device by increasing the concentrations of ions, such as by using a pure RTIL. Similar results have recently been reported by Uralcan et al.[27] on RTIL mixtures with ACN between atomically flat walls at a constant applied potential, where they also found a peak in capacitance that was between low ion concentration in ACN and a pure RTIL.

Explaining these observations is attempted below by examining the molecular composition and associated charging mechanism.

5.3.1.2. Electrolyte compositions and charging mechanism of pores

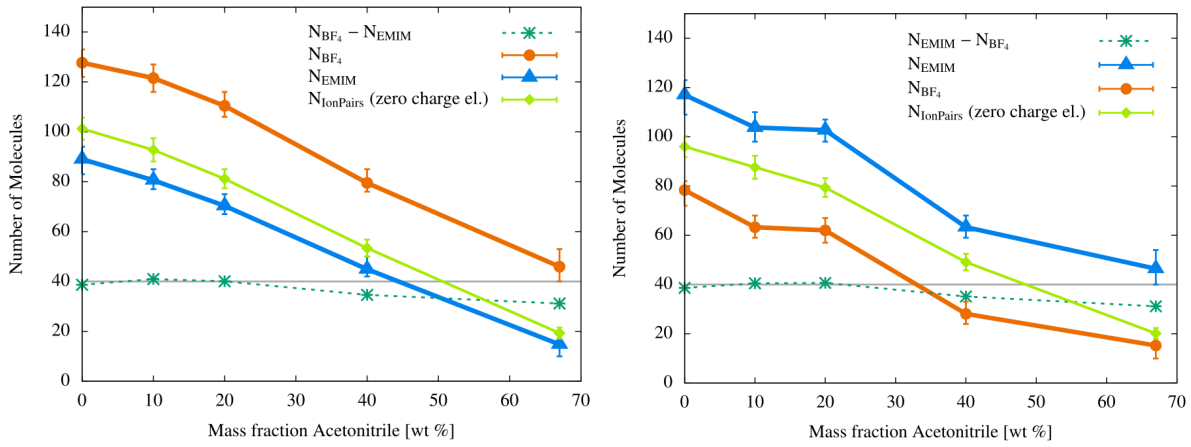

a) Positive electrode b) Negative electrode

Figure 5-3: Electrolyte composition inside the electrodes. Light green: uncharged CDC electrodes; Orange/Blue: electrodes held at a constant potential difference of 1 V. Dark green: difference between the counter-ions and the co-ions numbers for the 1 V simulation.

Examining the electrolyte composition inside the pores as a function of ACN in Figure 5-3 shows some interesting features. Firstly, in all cases, there was a large linear decrease in the population of ions in the pore proportional to the fraction of ACN in the electrolyte. This demonstrates that the pores do not become saturated with ions upon electric potential, and that the total number of ions adsorbed into the pore at zero charge is not a good indicator for

high capacitance. Instead what is clearly shown is that the net ionic-charge (dashed green line) was almost constant at 1 V, despite the large reduction in ion concentration. Results here are consistent with recent work by Péan et al.,[37] in which the larger RTIL 1-butyl-3-methylimidazloium hexafluorophosphate (BMIM-PF_6) was used as the electrolyte inside CDC electrodes of various sizes at 1V potential. Similar differences in the in-pore ion populations were observed between the positive and negative electrode, however in this work greater ion separation was achieved.

More quantitatively, the net ionic-charge at 67 % mass ACN (1.5 mol L^{-1}) was 80 % of the pure $EMIMBF_4$ value. This matches the induced electrode charge quite closely, where the induced charge reduced to approximately 82 %. Again, this was consistent with recent the publication by Péan et al.,[37] which showed that upon solvation of the BMIM-PF_6 ions to 1.5 mol L^{-1} in ACN (57 % wt ACN), the net ionic-charge also reduced to approximately 80 % of the pure RTIL case. The decrease in charge here may be caused by the reduction in ion-ion correlations lowering the driving force for co-ions to be expelled from the pore.

Further differences between electrodes can be attributed to an ion size effect between the smaller BF_4^- anion compared to the larger less symmetric $EMIM^+$ cation. There were consistently more ions in the positive electrode, and both species decreased smoothly. In contrast, the decrease was more sporadic in the negative electrode, with an almost negligible change in ion number between 10 and 20 wt% ACN. At the highest fraction of ACN used, difference in the electrolyte composition minimised, this is expected as ion size effects reduce upon solvation.[29]

In order to better understand the influence of ionic concentration on the charge storage mechanism, and the differences between the positive and negative electrodes, we use a charging mechanism parameter, *X*, recently introduced by Forse et al.,[55] which quantifies the origin of charge induction between three different mechanisms: counter-ion adsorption, ion exchange, or co-ion desorption. It is defined for each electrode as:

$$X = \frac{N(\Psi) - N(0V)}{\left[\left|Q(\Psi)\right| - \left|Q(0V)\right|\right]/e} \tag{5-2}$$

where $N(\Psi)$ is the total number of in-pore ions at a given voltage Ψ, $Q(\Psi)$ is the corresponding electrode charge, $0V$ are the values when no electrode potential is applied, and e is the elementary charge. X is plotted in Figure 5-4 as a function of the ACN mass fraction.

This parameter takes a value of 1 for counter-ion adsorption, 0 for ion exchange, and -1 for ion desorption; while intermediate values point to a combination of two such mechanisms. The large error bars in Figure 5-4 are due to the propagation of statistical errors on the values of *N* and *Q*. However, clear trends for both electrodes can be observed. In both cases, ion exchange dominated in the pure RTIL ($X \approx 0.1$ and 0.3 in the negative and positive electrodes respectively). In the positive electrode the mechanism progressively switched to counter-ion adsorption, while in the negative electrode ion exchange dominated until the most diluted ion concentration. In both cases a value of 0.7 was obtained for *X* in the 1.5 mol L^{-1} solution (67 wt % ACN). The evolution of the mechanisms gives a first hint why the RTIL capacitance is little affected by ionic concentration. Initially at 0 V, the pores are completely filled with ions already, adsorbing a counter-ion therefore requires the simultaneous desorption of a co-ion. This implies that there is a counter-force impeding charging due to the strong Coulombic attraction between ions of opposite charge, which therefore impedes efficient charging in this system (even if this interaction is screened in the nanopores, leading to a superionic state as was shown by Kondrat and Kornyshev).[56] In the highly solvated system, the ion interactions are dampened, such that this effect becomes less important.

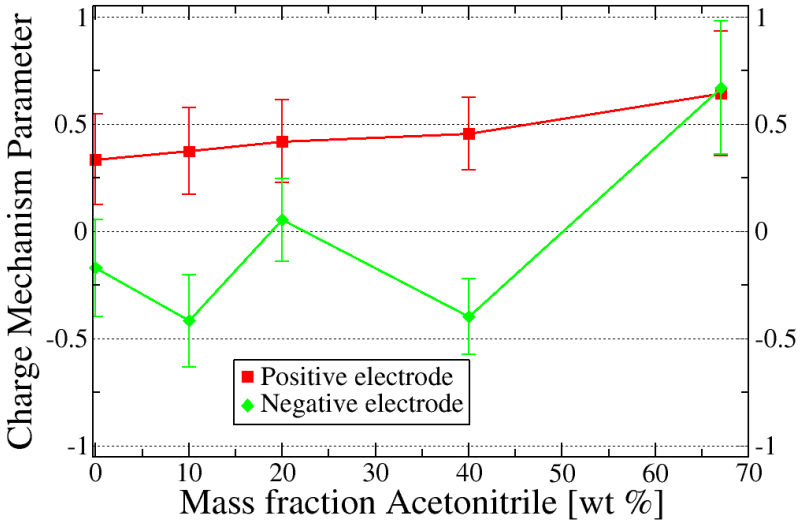

Figure 5-4: Variation of the charging mechanism parameter with the ACN mass fraction for the positive and negative electrodes.

Interesting comparisons to this analysis can be made with recent *in situ* NMR experiments by Griffin et al.,[57] which used 1.5 mol L^{-1} tetraethylphosphonium tetrafluoroborate (Pet_4-BF_4) in solvated ACN as the electrolyte, and a YP-50F activated carbon electrode. In their work, the zero-potential in-pore ion density was approximately 0.85 mmol g^{-1}, whereas in this work the equivalent ion density was 0.44 mmol g^{-1}. The difference here is most likely explained by the

electrolyte/electrode combinations used. At a full cell potential of 1 V the charge storage mechanisms have minor differences. In their work the negative electrode did not rely on co-ion removal to induce electrode charge, whereas here both electrodes showed identical ion insertion and removal trends for the range of ion concentrations. Significantly, the in-pore counter-ion densities were very similar in both studies, in the work of Griffin et al.[57] approximately densities of 0.92 and 1.05 mmol g^{-1} were recorded for the positive and negative electrode respectively, compared to 1.00 and 1.01 mmol g^{-1} in this work. The partial agreement here between MD simulation and experimental *in situ* NMR molecular analysis of the wetted porous electrode compositions is a promising step towards understanding charge storage mechanisms in nanoporous carbon electrodes. More comparisons where the experimental and simulation systems are more closely matched would be of great use.

The solvation effects discussed in this section (5.3.1.2) do not explain why the charging mechanism shifts to counter-ion adsorption in the highly solvated systems. It is possible that at zero potential, ion pairs interact more strongly inside the electrodes than in the bulk, due to partial desolvation upon entering the pores and confinement effects limiting ion mobility. At high solvation, the energy barrier for an ion entering a pore under applied potential may be lowered to a greater extent than the energy barrier of a co-ion exiting a pore, as the entering ion can replace solvent molecules, which will not interact strongly, whereas the exiting co-ion has to overcome its existing ion-ion interactions inside the pore.

5.3.1.3. Structure and mobility

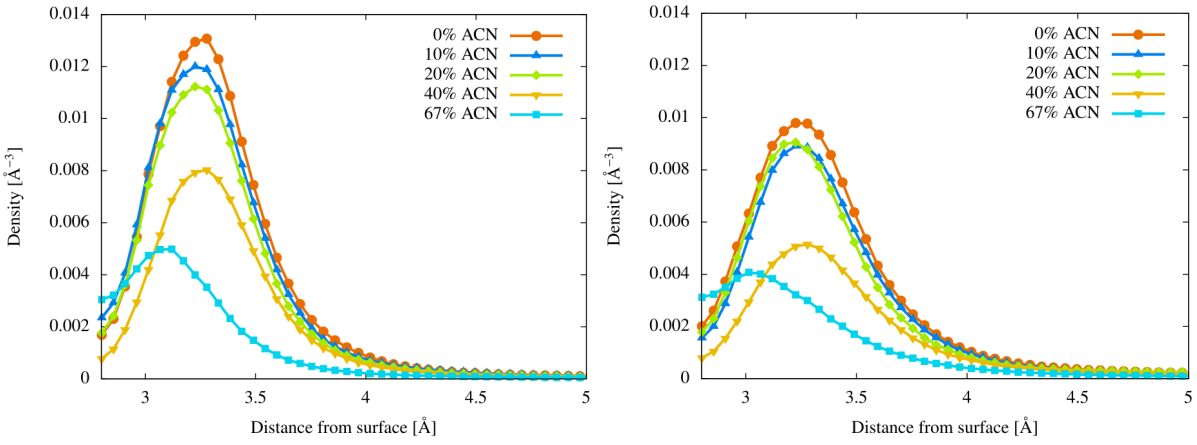

a) Positive electrode b) Negative electrode

Figure 5-5: Counter-ion distance from the internal surface of the electrodes

Figure 5-5 shows the positional distribution of counter-ions with respect to the internal surface of the positive and negative electrodes for different fractions of ACN in the

electrolyte. This analysis was first introduced by Merlet et al.,[35] and is performed firstly by probing the carbon electrode atoms outwards with an argon atom to determine which volumetric sections of the electrode are accessible to the electrolyte molecules. The distance of the molecules inside this volume to the nearest carbon atom can then be calculated, and the distribution of ion positions with respect to the surface found.

From Figure 5-5 it can be seen that there is no change in the position of the density peaks in both electrodes, except for the highest fraction of ACN, and that the magnitude of the peaks are consistent with results in Figure 5-3. As the position of the peaks was consistent with increasing fractions of ACN, the solid-counter-ion interactions were therefore not affected and consistent access to the surface was facilitated. Another interesting observation of Figure 5-5 is that the positions of the peak remained constant until the ACN fraction was increased to 67 % mass, where the peak shifts approximately 0.02 nm closer to the surface. There is no clear explanation for this phenomenon, but it is possible that with the reduced ion density, the counter-ions were able to pack more efficiently. Another possible explanation is that the solvent molecules replace ions in the more bulk-like regions of the electrode to a greater extent than the more confined regions of the electrode, leaving the remaining ions closer on average to the internal surface. As for the solvation numbers of the ions, their variation is linear, with no particular change at a given concentration.

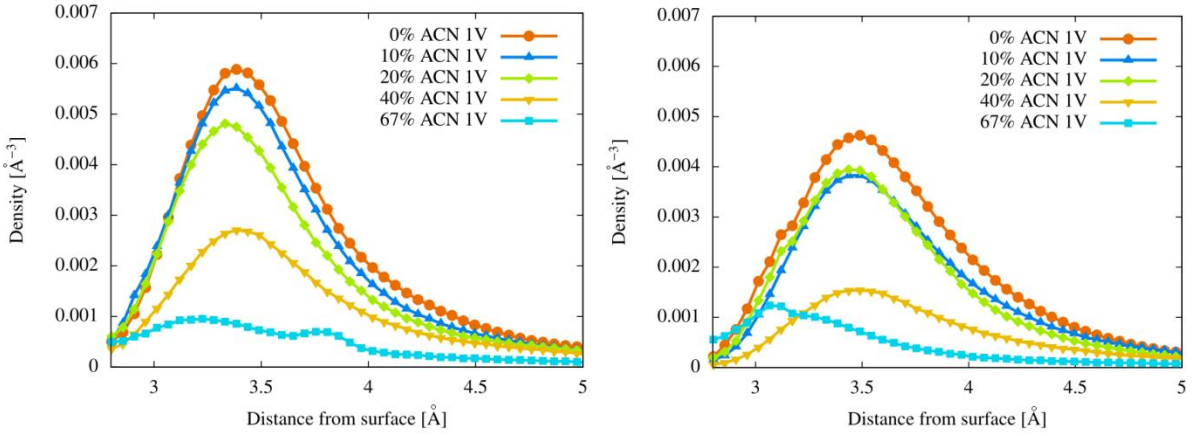

a) Positive electrode b) Negative electrode

Figure 5-6: Co-ion distance from the internal surface of the electrodes

The positions of the peaks do not have any correlation to the capacitance trend observed in Table 5-2, which indicates that the approach distance of the molecules to the internal surface of the electrode was not a significant contributor to the induced charge in this system, which is expected in nanopores where the ion size and pore size are already closely matched.

Whether this observation would hold in a system with larger nanopores is an interesting question that could be further explored. From Figure 5-6 it can be seen that the intensities of the co-ion peaks are less, and have a broader distribution. The peaks are also centred further away from the internal surface but remain consistent with ACN concentration.

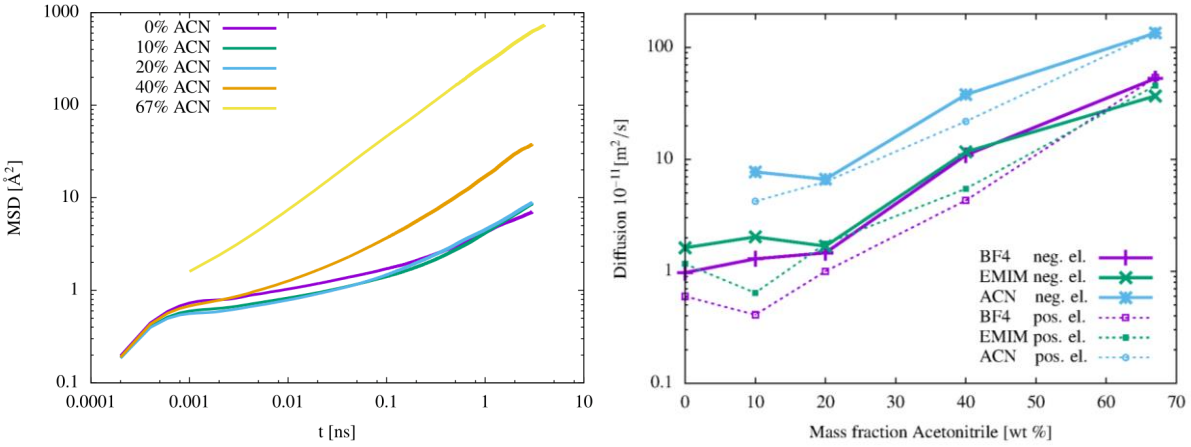

a b

Figure 5-7: Mean squared displacement of BF_4^- counter-ions inside the positive electrode (a), and diffusion coefficients of all molecular species inside both electrodes (b).

Finally, one of the benefits of adding ACN to the electrolyte is to increase the mobility of ions so that they more rapidly diffuse into and out of the pores. This increases the capacitive performance at higher current densities. However, in small pores, strong confinement and desolvation can occur, making the prediction of ion mobility difficult. Experimentally, it is also difficult to separate the contributions of individual molecular species, with measured conductivity being the single result of all species present.

The benefit of ACN can be clearly deduced from the mean squared displacements of the various species. As shown in Figure 5-7a for the BF_4 anions, a caging regime[58-59] is observed for the pure RTIL, and the diffusive regime is reached for times greater than 1 ns. When the concentration of ACN was increased, the extent of this caging regime decreased, and it completely vanished for the most diluted system. In Figure 5-7b the extracted self-diffusion coefficients of all molecular species are given for each electrode. The solvent molecules diffused around 10 times faster than the ions, and the $EMIM^+$ cations were slightly more mobile than the smaller BF_4^- anions, which is consistent with previous results,[40] (and our own bulk simulations shown in Figure 3-4b of Chapter 3). In most cases the result here correlates well with the ion populations, the negative electrode has consistently less ions except at the highest ACN fraction used, and this is reflected with slightly higher diffusion values. It can be seen that significant gains in diffusion are not reached before the ACN mass fraction is 40

% wt. Below this value, the concentration of ACN appears to be too low to decrease the ion-ion correlations enough to facilitate increased ion mobility.

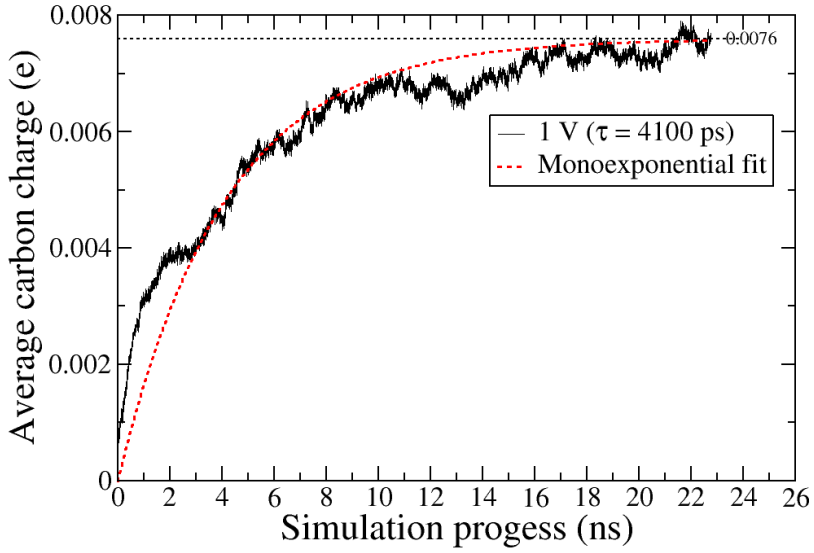

Figure 5-8: Electrode charging rate of 1.5 mol L^{-1} $EMIMBF_4$ in ACN at 1 V

The charging dynamics of the 1.5 mol L^{-1} (67 % wt ACN) system is shown in Figure 5-8. In this simulation the production run was begun by switching the potential from 0 V to 1 V, this differs from the equilibration methodology described in Section 5.2.3.2. Details for the fitting of the exponential function (and further dynamics analysis) are given in Appendix A5.

The result here showed a greater than four-fold reduction in dynamics, when compared to a similar system by Péan et al.,[37] which simulated 1.5 mol L^{-1} of $BMIMPF_6$ in ACN (57 % wt ACN) and Ti-CDC 1200 pores at 1V. The average pore sizes for the two models are 0.95 nm for CDC 1200 and 0.75 nm for CDC 800. The large increase in charging time observed here, even considering the difference in ion sizes, reinforces that pore size limits the charging rate even for highly diluted ions.

5.3.2. $EMIMBF_4$ inside CDC 800 electrodes at 3 V total potential

The above work in Section 5.3.1 was performed at 1 V as this potential is suitable to study molecular mechanisms. However, real devices with RTIL or organic electrolytes operate at higher voltages, above 3 V for the former and commonly at 2.7 V for the latter. In this work pure $EMIMBF_4$ was simulated at 3 V. Kondrat et al.[34] proposed that in nanoporous carbon electrodes, energy density is a non-monotonic function of pore size, for non-disperse electrodes (I.E. slit-pores or CNTs). They found that for CDC electrodes with a pore size distribution, the predicted maximum in capacitance as a function of voltage (observed in non-

disperse electrodes) shifted or disappeared for experimental results. A key take-away was that the optimal voltage for capacitance increases with increasing pore size. In this work, as the average pore size is very small (approximately 0.75 nm), it would be expected that the capacitance would decrease at high voltage with the onset of ion saturation inside the pores. This is indeed what occurred, as the capacitance at 3 V was found to be 120 F g^{-1}, 86 % of the capacitance at 1 V (which was 140 F g^{-1}).

To maintain a constant capacitance when increasing the voltage by a factor of three, the net ionic-charge would also need to increase by the same amount, if we assume perfect balancing of ionic chare by the electrode. However, the net ionic charge at 3 V potential only reached 76 % of the required value to maintain a constant capacitance. Interestingly, the charging parameter (previously defined in Equation (4-5)) did not change with the increase in potential. This implies that there was no change in the relative difficulties of counter-ion insertion or co-ion desorption, even though total number ions in both electrodes increased compared to at 1 V.

Table 5-3: Electrolyte composition inside the pores and charge storage properties

	Cations P.E.	Anions P.E.	Cations N.E.	Anions N.E.
1 V	89	128	117	78
3 V	78	167	151	62
	Net ionic-charge P.E	Net ionic-charge N.E.	*X* P.E.	*X* N.E.
1 V	30	30	0.4	0.1
3 V	69	70	0.41	0.11

What is noticeable is that whilst the net ionic-charge fell to 76 % of the required value, the induced electrode charge (and capacitance) only fell to 86 % of the required value. A possible explanation for this observation is given in Figure 5-9 below, which was calculated using the same method as detailed in Section 5.3.1.3.

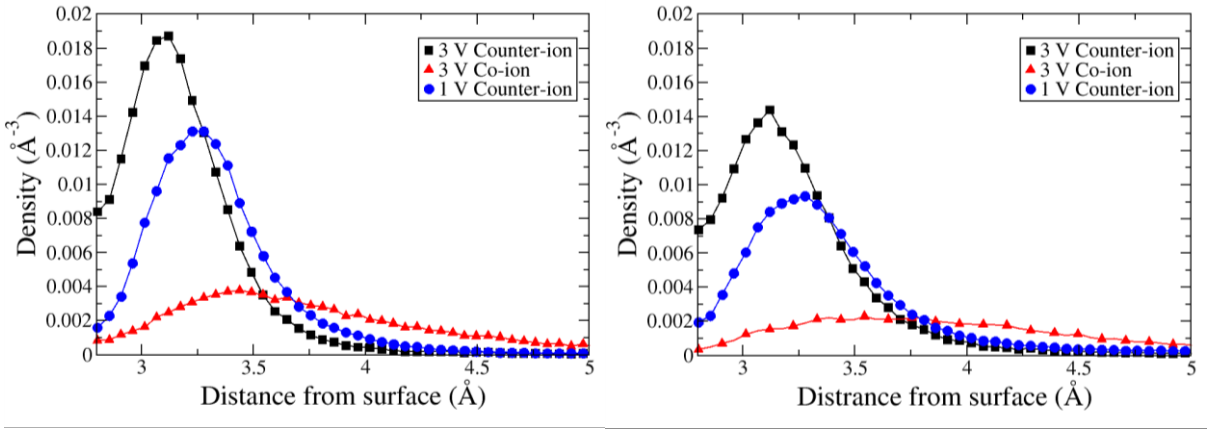

a) Positive electrode b) Negative electrode

Figure 5-9: Distance from the internal surface of the electrodes for counter- and co-ions, 1 V counter-ion result also included

From Figure 5-9 there are two interesting observations that can be made. Firstly, at 3 V the counter-ions are more closely adsorbed to the internal surface of both electrodes compared to 1 V. The second is that the co-ion peak nearly disappears completely at 3 V in both electrodes, reducing the negative impact of co-ion adsorption of charge accumulation in the electrode. These two observations show that the ions are likely being stored more efficiently at the higher voltage, even though there is an insufficient net ionic-charge to reach the same capacitance value as at 1 V.

An analysis of the dynamics of this system is given in Appendix A5.

5.3.3. EMIMTFSI structure in disordered pores by PDF analysis

One of the largest difficulties that molecular modelling of EDLCs faces is how to improve the quality of the models used, particularly for disordered porous carbons, which require substantial effort to generate. Additionally, the methods which are used to analyse the quality of the models is also important, especially when on the experimental side there is disagreement among the best method to measure surface area (BET vs DFT).[60] Calculating the PDF for systems is an accurate method that allows for precise analysis of short- and long-range interactions that are not apparent in other thermodynamic measurements.

PDF (G(r)) calculated by MD simulation requires firstly computing the partial RDF (g(r)) for all possible atomic pair combinations, whilst aggregating like atom types across all molecule types:

$$g(r) = \frac{1}{\rho_{Blocal}} \frac{1}{N_A} \sum_{i \in A}^{N_A} \sum_{j \in B}^{N_B} \frac{\delta(r_{ij} - r)}{4\pi r^2} \tag{5-3}$$

where N is the number of particles, ρ_{Blocal} is the particle density of B around all spheres of A, and $\delta(r_{ij} - r)$ is the Dirac delta function. The PDF is obtained by first calculating the partial structure factors (S(Q)) via Fourier transform, and the summing the partial S(Q) using Q-dependent atomic form factors to calculate the PDF:[61]

$$G(r) = \left(\frac{2}{\pi}\right) \int_0^\infty S(Q) \sin(Qr) dQ \tag{5-4}$$

where ρ_0 is the average density. Analysing the PDF of the models separately, and combined together allows for the tracking of inaccuracies in one or both models. The PDF experiments were performed by Dr Boris Dyatkin and colleagues at Drexel University, PA, USA as part of a collaborative experiment and simulation research project that is currently unpublished. Dr Dyatkin kindly agreed to share limited experimental data with us for use in this thesis to analyse the structural accuracy of the CDC models. The PDF experimental data is incorporated solely into Figure 5-10 and Figure 5-11.

The PDF of pure EMIMTFSI is given in Figure 5-10a. It can be seen that there is not much structure beyond 5 Å, and overall the model captures the experimental structure well, with the least accurate region being between 1.9 – 2.4 Å where there is one less peak in the model, and the existing peak and trough have less intensity. This region corresponds to the intramolecular distances between atoms on the EMIM imidazolium ring (N – N, C – C, and C – N) and F – F atom distances at the extreme ends of the TFSI molecule.[62]

a

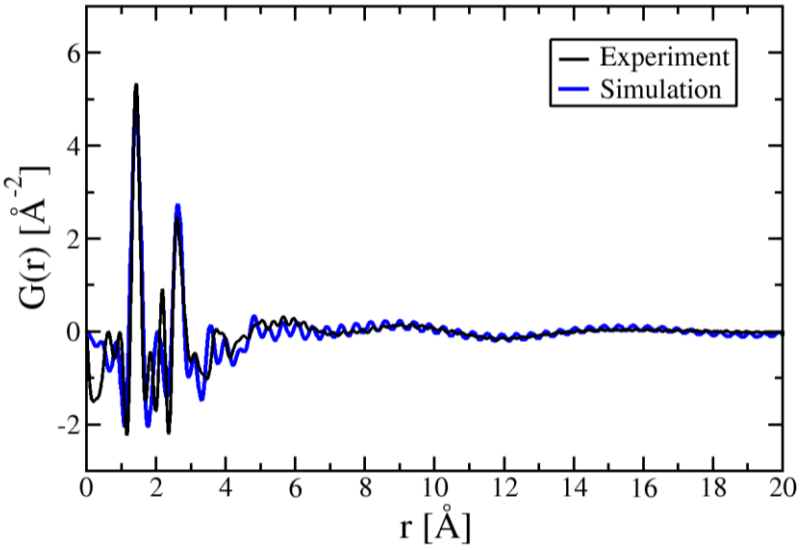

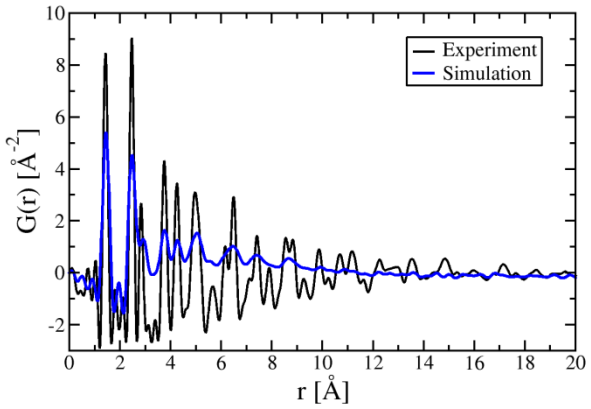

b

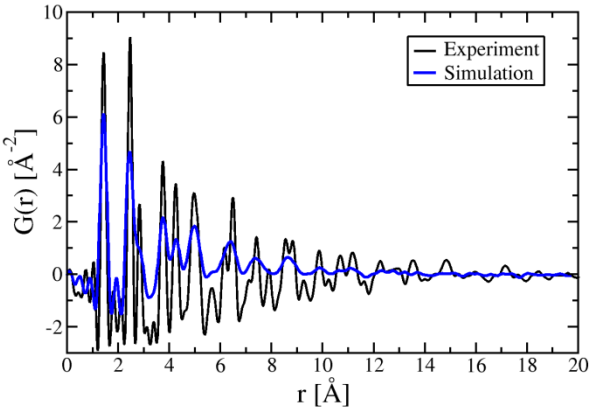

c

Figure 5-10: (a): PDF of bulk EMIMTFSI at room temperature from experiment and MD simulation. (b): PDF of empty Si-CDC 800 from experiment and empty Ti-CDC 800 from simulation. (c): PDF of empty Si-CDC 800 from experiment and empty Si-CDC 800 from simulation.

The experimental and simulations comparisons for empty CDC 800s are given in Figure 5-10b for Ti-CDC, and Figure 5-10c for Si-CDC. In both cases it is clear that the CDC models match the location of the peaks very closely, however they suffer from a consistent lack of intensity, which becomes more apparent in the medium range beyond 4 Å. This is most likely indicative of under graphitisation of the pores during their development, compared to the experimental structure.

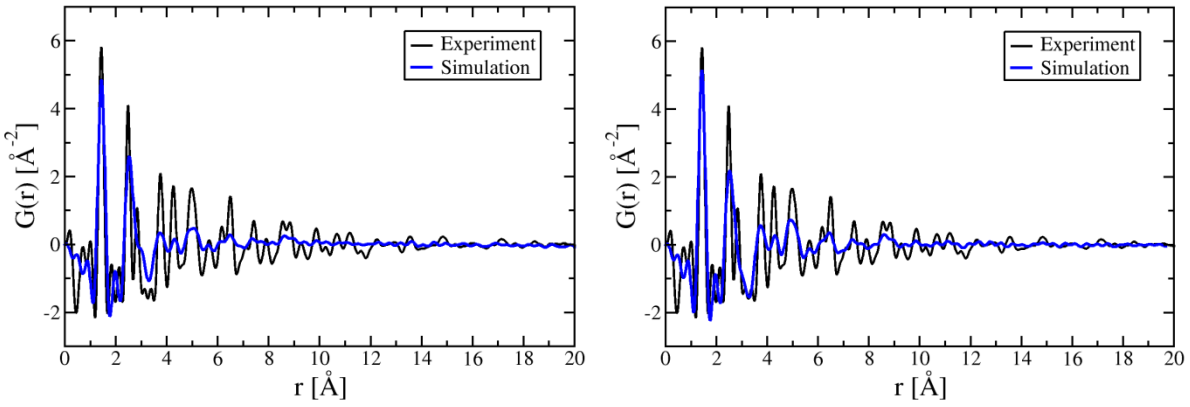

a b

Figure 5-11: (a): PDF of EMIMTFSI inside Si-CDC 800 from experiment and Ti-CDC 800 from simulation. (b): PDF of EMIMTFSI inside Si-CDC 800 from experiment and Si-CDC 800 from simulation.

As can be seen in Figure 5-11, the simulated pore artefacts carry over to the analysis where the pores are filled with EMIMTFSI, however the effect is dampened moderately by the presence of the ions. Perhaps when generating the CDC models, PDF data could be of more use than RDF for energy minimisation steps, as it appears to be the most sensitive to graphitisation.

An analysis of the EMIMTFSI structure inside the pores is given in Appendix B5.

5.4. Conclusions

In conclusion, in this work constant potential CV experiments and MD simulations were performed to determine the influence of ACN fraction in an RTIL based electrolyte on capacitance and ionic structure inside nanoporous CDC electrodes. Qualitative agreement between experiment and simulation was found. However, a small overestimation of the capacitance by simulations was present due to the absence of some phenomena because of several necessary simplifications introduced in the models (as described in Chapter 3). Analysis of the PDF indicates that the electrode models used may be under-graphitised, when compared to experimental PDFs, and that the PDF may be a useful parameter in the simulation technique for developing disordered porous models. Both experiment and simulation showed a small fluctuation of the capacitance despite the drastic variation of ionic concentration (with a factor of four between the most dilute and the most concentrated systems analysed).

The simulations showed noticeable charging mechanism dependence on the ACN concentration. The pure RTIL was characterised by a large ionic density close to the carbon surface. Adding a counter-ion upon application of a voltage can thus be achieved by

exchanging a co-ion only, which requires breaking of cation-anion associations which are favoured by the strong Coulombic interactions (albeit the latter are screened by the electrostatic potential due to the metallic walls). In an ACN-based system, it is not necessary to remove co-ions for adsorbing additional counter-ions, resulting in a mechanism dominated by counter-ion adsorption. The transition from one mechanism to another was smoother in the positive electrode than in the negative electrode. In parallel, the dynamics of the ions increased by one order of magnitude when switching from the pure RTIL to the diluted electrolyte, however even the most dilute system had slow dynamics when compared to systems with large average pore size.

When increasing the potential to 3 V for the pure RTIL system, the capacitance dropped to 86 % of the original value at 1 V, 140 to 120 F g^{-1}. This occurred despite the counter-ions being adsorbed marginally closer to the internal surface, and without any change of the charging mechanism parameter in both electrodes. The most likely explanation for these observations is that it becomes increasingly difficult for the electrodes to maintain the same ratio of ion-exchange with increasing electric potential, and steric limitations may also occur if the electrodes become saturated with counter-ions.

Since the ionic concentration does not affect the capacitance much in disordered nanoporous electrodes, the choice of electrolyte for efficient supercapacitors should therefore be made by comparing the ionic conductivity, which determines the internal resistance of the device, and the operating voltage it allows. However, these two quantities vary in opposite ways in concentrated electrolytes,[63] so that the optimum will necessarily be a trade-off between these quantities.[64-65] Other limitations such as the operating temperature or the long-term stability may also be taken into account. It is worth noting that several ionic liquids may be combined,[66] which increases further the number of potential electrolytes. Computational screening approaches have therefore recently been proposed to tackle this difficult problem.[67]

Interestingly, the capacitance dependence observed here contrasts quite strongly with the results in Chapter 4, which showed strong capacitance dependence on the concentration of ACN. The origin of the difference observed could occur from either, or a combination of, fundamental differences in the electrode structures, or inaccuracies of the CDC model in capturing real behaviour. The charging mechanism parameters appear to be similar across both slit-pore and CDC over the concentration range tested, which seems to indicate that the different models do not suffer from fundamentally incompatible behaviour. It is therefore reasonable to conclude, when simultaneously considering the PDF analysis in this chapter,

that the current CDC models suffer moderately from under-graphitisation. Furthermore, real behaviour might better be described by a combination of CDC pores, and slit-pores for the most highly confined regions, as slit pores display lower gravimetric capacitance than CDCs. This could potentially result in bringing capacitance predictions closer to what is currently observed in experiments, however this would need to be extensively tested.

Appendix A5

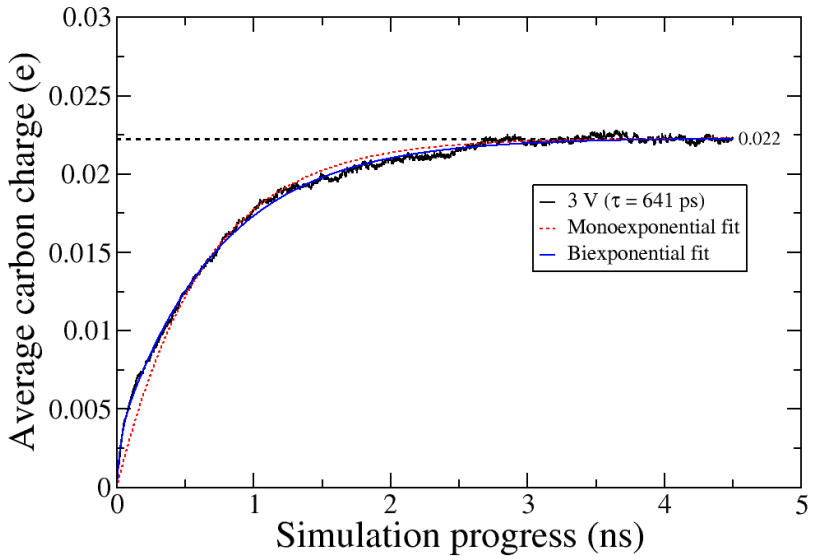

Figure A5-12: Electrode charging rate at 3 V. Here two fitting functions have been provided, a mono- and bi-exponential fit.

As this system was equilibrated at zero potential and productions runs were initiated by instantaneously switching to 3 V, charging rate characteristics can be extracted. As demonstrated by Péan et al.,[37] because the charging curve follows the general form of $y = 1 - e^{-x}$, it can be fitted with a mono-exponential function of Equation (5-5):

$$Q(t) = Q_{\max}\left(1 - e^{\frac{-t}{\tau}}\right) \tag{5-5}$$

where τ is the characteristic time constant. This is a useful and relatively simple method for comparing the charging dynamics of different systems. As can be seen from Figure A5-12, charging the pure RITL at a potential of 3 V gave a time constant of approximately 640 ps. There appears to be a change of charging regimes from fast to slow at approximately 1.5 ns, evidenced by the improved fit of a bi-exponential function, which is consistent with previous simulation and mean field theory,[36, 68] which showed diffusive charging as counter-ions migrated deeper into the pores. The mono-exponential function does not capture this

precisely and as a result underestimates the beginning of the fast regime and overestimates the beginning of the slow regime. The bi-exponential function provides a better fit to both regimes and gives characteristics time constants of approximately 30 and 740 ps for the fast and slow regimes respectively, however when comparing different systems the mono-exponential function is sufficient. Using CDC 1200 and the pure RTIL BMIMPF$_6$, Péan et al. obtained characteristic time constants of 275, 619, and 967 ps for electric potentials of 4, 2, and 1 V respectively.[37] Compared with the values obtained here, it appears that larger pore size has a greater influence on increasing dynamics than high potential, as our result here at 3 V was slightly slower than the result of Péan et al.[37] at 2 V.

As discussed by Merlet et al.,[69] upon sudden application of a high electric potential, the temperature of the system increases due to the Joule effect. Here we obtain a heating rate of 2.6 K ps^{-1}at 3 V, which is good agreement with Merlet et al. who obtained 2.5 K ps^{-1} at 5 V.[69] The greater sensitivity to heating in our system is very likely of the smaller pore size used here, which increases the resistance of the system.

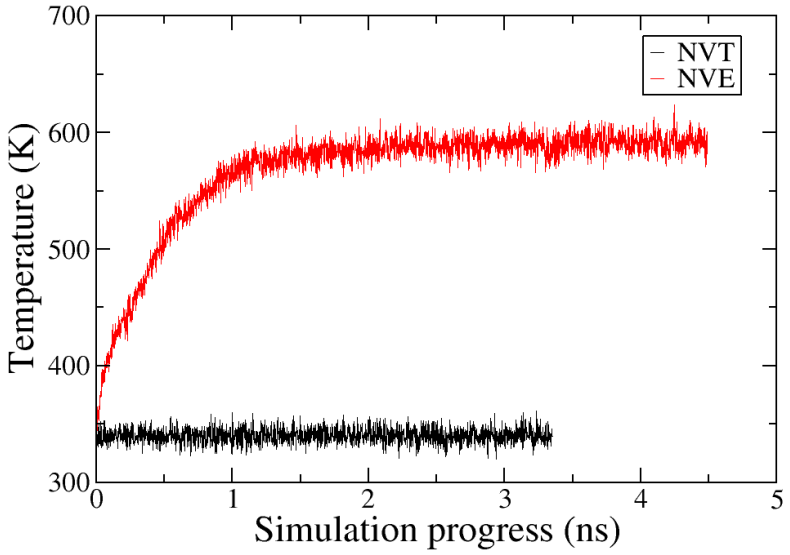

Figure A5-13: Temperature rise due to the Joule effect at application of 3 V total potential.

Overall, the dynamics of the systems studied emphasise that although operating at a low potential can offer high capacitance, there is a trade off in other important properties which should also be considered.

Appendix B5

Equilibration for simulation of EMIMTFSI inside CDC800 pores

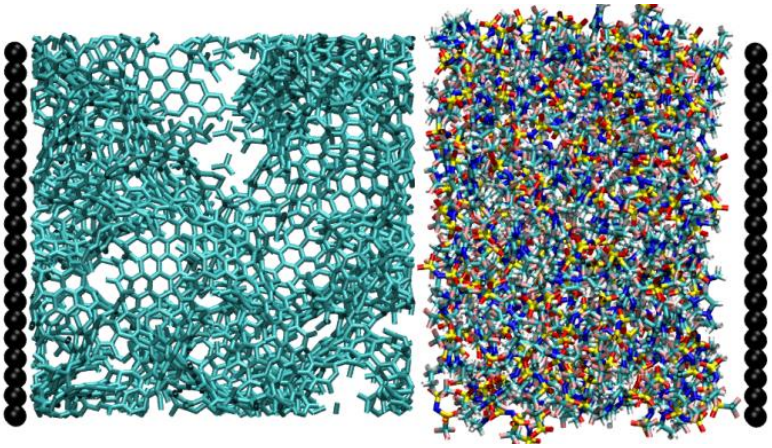

Figure B5-14: Simulation snapshot during equilibration before pore filling. Empty CDC is displayed on the left, and pressurised EMIM-TFSI on the right. The simulation was capped by immobile wall atoms in the non-periodic dimension.

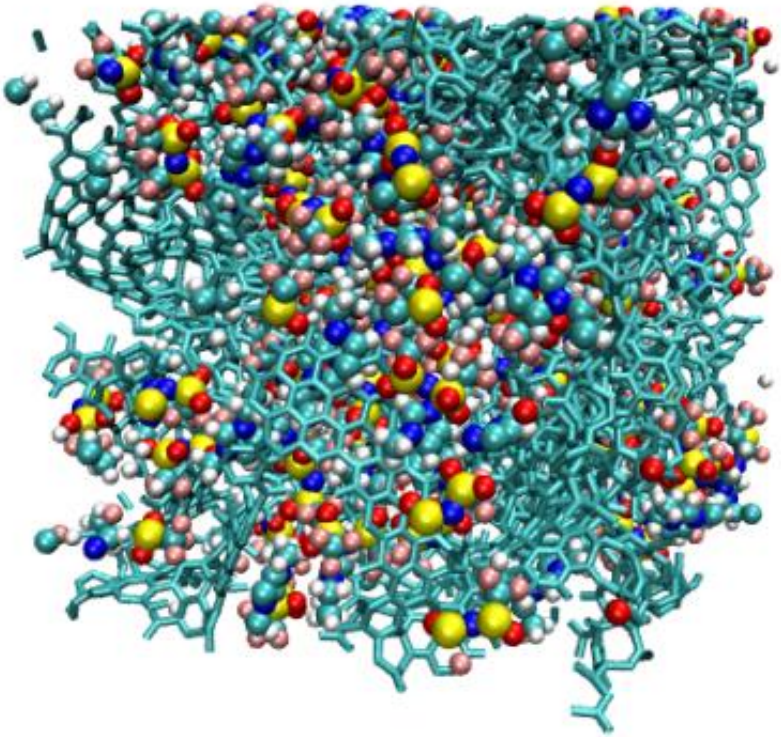

Figure B5-15 3D periodic filled CDC pore used for MD production runs.

Liquid structure of EMIMTFSI inside the CDC pores by PDF and partial RDF analysis

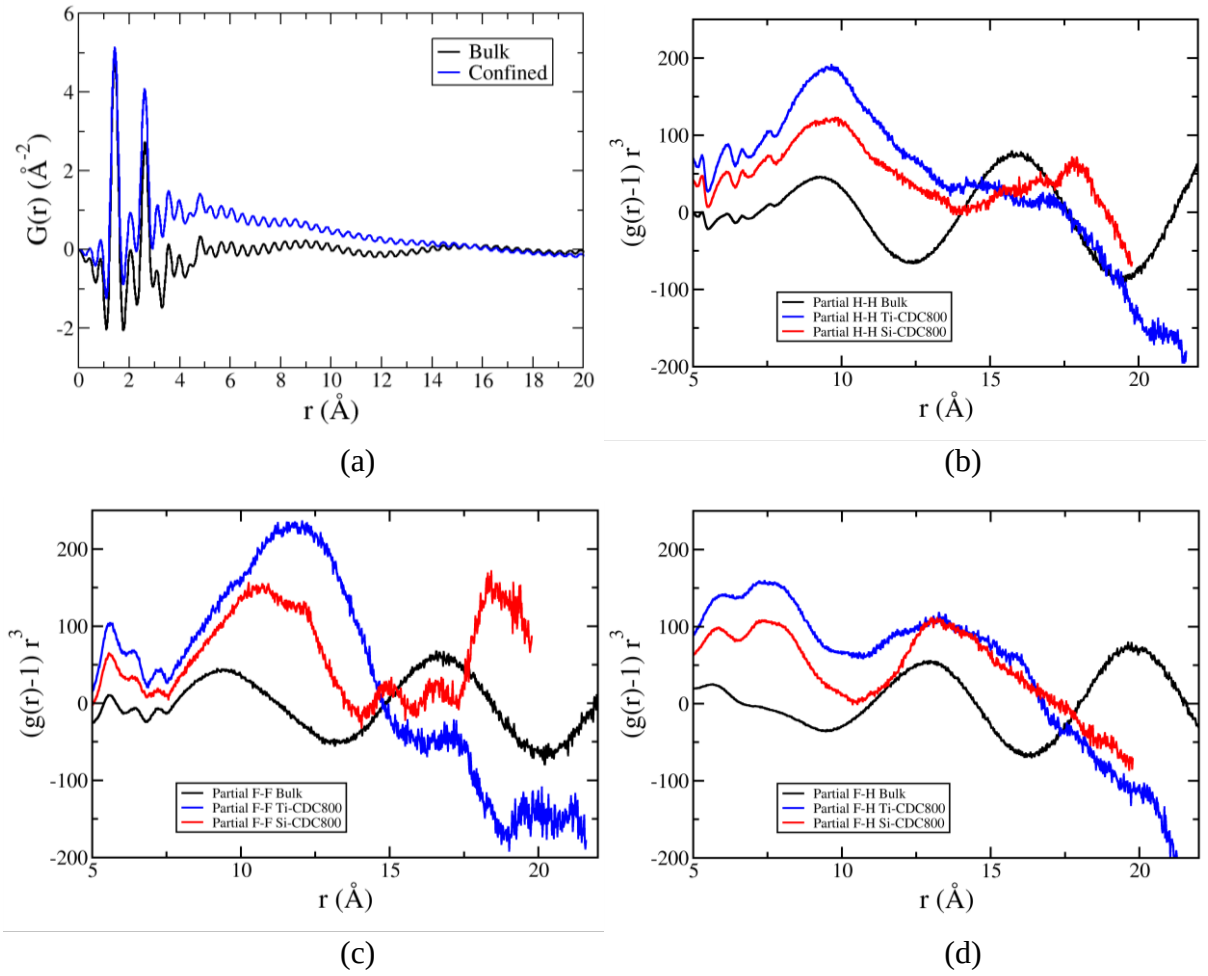

Figure B5-16: (a): Isolated PDF for the pure IL in bulk and Ti-CDC 800 confined-simulations. (b-d): Partial RDFs from MD simulation (multiplied by r^3) for atomic pairs in bulk RTIL, Ti-CDC 800 pores, and Si-CDC 800 pores. (b) H-H pairs for cation-cation interaction. (c) F-F pairs for anion-anion interaction. (d) F-H pairs for anion-cation interaction.

Figure B5-16a is a simulation only result that has isolated the PDF of the EMIMTFSI ions inside a Ti-CDC pore, and in its regular bulk solution. This was achieved by explicitly excluding the contributions of the CDC atoms. What can be seen is that the short range structure, which is dominated by intra-molecular and first-neighbour contributions, is not greatly affected by confinement in the CDC. Changes to the medium range structure (3 – 12 Å) can most likely be attributed to the excluded volume which causes normalisation differences between the two series.

A more striking analysis can be seen by comparing partial g(r) for atomic pairs, which are given in Figure B5-16b-d where (b) corresponds to cation-cation, (c) to anion-anion, and (d) to anion-cation interactions. The partial g(r) data has been multiplied by r^3 to better observe the most important differences which occurred at medium and long range. In the bulk liquid,

characteristic long range ordering was shown for all atomic-pair interactions, with second neighbours occurring at approximately 16 Å. This long range ordering was completely lost inside the CDC pores at approximately 14 Å. Overall from section 5.3.3, it can be concluded that confinement inside CDC nanopores does not significantly affect the short range RTIL structure, but the medium to long range interactions are broken by the inherent disordered structure of the CDC, resulting in no observed coordination beyond first neighbour RTIL pairs.

5.5. References

1. Frackowiak, E.; Abbas, Q.; Béguin, F., Carbon/Carbon Supercapacitors. *J. Energy Chem.* **2013**, *22*, 226-240.
2. Gogotsi, Y.; Simon, P., True Performance Metrics in Electrochemical Energy Storage. *Science Magazine* **2011**, *334*, 917-918.
3. Faggioli, E.; Rena, P.; Danel, V.; Andrieu, X.; Mallant, R.; Kahlen, H., Supercapacitors for the Energy Management of Electric Vehicles. *J. Power Sources* **1999**, *84*, 261-269.
4. Dunn, B.; Kamath, H.; Tarascon, J.-M., Electrical Energy Storage for the Grid: A Battery of Choices. *Science* **2011**, *334*, 928-935.
5. Simon, P.; Gogotsi, Y., Materials for Electrochemical Capacitors. *Nat. Mater.* **2008**, *7*, 845-854.
6. Salanne, M.; Rotenberg, B.; Naoi, K.; Kaneko, K.; Taberna, P. L.; Grey, C. P.; Dunn, B.; Simon, P., Efficient Storage Mechanisms for Building Better Supercapacitors. *Nat. Energy* **2016**, *1*, 16070-10.
7. Zhang, L. L.; Gu, Y.; Zhao, X. S., Advanced Porous Carbon Electrodes for Electrochemical Capacitors. *J. Mater. Chem. A* **2013**, *1*, 9395-9408.
8. Brandt, A.; Pohlmann, S.; Varzi, A.; Balducci, A.; Passerini, S., Ionic Liquids in Supercapacitors. *MRS Bull.* **2013**, *38*, 554-559.
9. Chmiola, J.; Yushin, G.; Gogotsi, Y.; Portet, C.; Simon, P.; Taberna, P.-L., Anomalous Increase in Carbon Capacitance at Pore Sizes Less Than 1 Nanometer. *Science* **2006**, *313*, 1760-1763.
10. Largeot, C.; Portet, C.; Chmiola, J.; Taberna, P.-L.; Gogotsi, Y.; Simon, P., Relation between the Ion Size and Pore Size for an Electric Double-Layer Capacitor. *J. Am. Chem. Soc.* **2008**, *130*, 2730-2731.

11. Feng, G.; Cummings, P. T., Supercapacitor Capacitance Exhibits Oscillatory Behavior as a Function of Nanopore Size. *J. Phys. Chem. Lett.* **2011**, *2*, 2859-2864.

12. Rogers, E. I.; Sljukić, B.; Hardacre, C.; Compton, R. G., Electrochemistry in Room-Temperature Ionic Liquids: Potential Windows at Mercury Electrodes. *J. Chem. Eng. Data* **2009**, *54*, 2049-2053.

13. Huddleston, J. G.; Visser, A. E.; Reichert, W. M.; Willauer, H. D.; Broker, G. A.; Rogers, R. D., Characterization and Comparison of Hydrophilic and Hydrophobic Room Temperature Ionic Liquids Incorporating the Imidazolium Cation. *Green Chem.* **2001**, *3*, 156-164.

14. Buzzeo, M. C.; Evans, R. G.; Compton, R. G., Non-Haloaluminate Room-Temperature Ionic Liquids in Electrochemistry—a Review. *ChemPhysChem* **2004**, *5*, 1106-1120.

15. Guerfi, A.; Dontigny, M.; Charest, P.; Petitclerc, M.; Lagacé, M.; Vijh, A.; Zaghib, K., Improved Electrolytes for Li-Ion Batteries: Mixtures of Ionic Liquid and Organic Electrolyte with Enhanced Safety and Electrochemical Performance. *J. Power Sources* **2010**, *195*, 845-852.

16. Yamada, Y.; Yamada, A., Review—Superconcentrated Electrolytes for Lithium Batteries. *J. Electrochem. Soc.* **2015**, *162*, A2406-A2423.

17. Forse, A. C.; Griffin, J. M.; Merlet, C.; Bayley, P. M.; Wang, H.; Simon, P.; Grey, C. P., Nmr Study of Ion Dynamics and Charge Storage in Ionic Liquid Supercapacitors. *J. Am. Chem. Soc.* **2015**, *137*, 7231-7242.

18. Richey, F. W.; Elabd, Y. A., In Situ Molecular Level Measurements of Ion Dynamics in an Electrochemical Capacitor. *J. Phys. Chem. Lett.* **2012**, *3*, 3297-3301.

19. Banuelos, J. L.; Feng, G.; Fulvio, P. F.; Li, S.; Rother, G.; Dai, S.; Cummings, P. T.; Wesolowski, D. J., Densification of Ionic Liquid Molecules within a Hierarchical Nanoporous Carbon Structure Revealed by Small-Angle Scattering and Molecular Dynamics Simulation. *Chem. Mater.* **2013**, *26*, 1144-1153.

20. Burt, R.; Birkett, G.; Zhao, X. S., A Review of Molecular Modelling of Electric Double Layer Capacitors. *Phys. Chem. Chem. Phys.* **2014**, *16*, 6519-6538.

21. Feng, G.; Li, S.; Presser, V.; Cummings, P. T., Molecular Insights into Carbon Supercapacitors Based on Room-Temperature Ionic Liquids. *J. Phys. Chem. Lett.* **2013**, *4*, 3367-3376.

22. Merlet, C.; Rotenberg, B.; Madden, P. A.; Salanne, M., Computer Simulations of Ionic Liquids at Electrochemical Interfaces. *Phys. Chem. Chem. Phys.* **2013**, *15*, 15781-15792.

23. Vatamanu, J.; Hu, Z.; Bedrov, D.; Perez, C.; Gogotsi, Y., Increasing Energy Storage in Electrochemical Capacitors with Ionic Liquid Electrolytes and Nanostructured Carbon Electrodes. *J. Phys. Chem. Lett.* **2013**, *4*, 2829-2837.

24. Fedorov, M. V.; Kornyshev, A. A., Ionic Liquids at Electrified Interfaces. *Chem. Rev.* **2014**, *114*, 2978-3036.

25. He, Y.; Huang, J.; Sumpter, B. G.; Kornyshev, A. A.; Qiao, R., Dynamic Charge Storage in Ionic Liquids-Filled Nanopores: Insight from a Computational Cyclic Voltammetry Study. *J. Phys. Chem. Lett.* **2015**, *6*, 22-30.

26. Feng, G.; Huang, J.; Sumpter, B. G.; Meunier, V.; Qiao, R., A "Counter-Charge Layer in Generalized Solvents" Framework for Electrical Double Layers in Neat and Hybrid Ionic Liquid Electrolytes. *Phys. Chem. Chem. Phys.* **2011**, *13*, 14724-14735.

27. Uralcan, B.; Aksay, I. A.; Debenedetti, P. G.; Limmer, D. T., Concentration Fluctuations and Capacitive Response in Dense Ionic Solutions. *J. Phys. Chem. Lett.* **2016**, *7*, 2333-2338.

28. Lee, A. A.; Perkin, S., Ion–Image Interactions and Phase Transition at Electrolyte–Metal Interfaces. *J. Phys. Chem. Lett.* **2016**, *7*, 2753-2757.

29. Merlet, C.; Salanne, M.; Rotenberg, B.; Madden, P. A., Influence of Solvation on the Structural and Capacitive Properties of Electrical Double Layer Capacitors. *Electrochim. Acta* **2013**, *101*, 262-271.

30. Xing, L.; Vatamanu, J.; Smith, G. D.; Bedrov, D., Nanopatterning of Electrode Surfaces as a Potential Route to Improve the Energy Density of Electric Double-Layer Capacitors: Insight from Molecular Simulations. *J. Phys. Chem. Lett.* **2012**, *3*, 1124-1129.

31. Wu, P.; Huang, J.; Meunier, V.; Sumpter, B. G.; Qiao, R., Complex Capacitance Scaling in Ionic Liquids-Filled Nanopores. *ACS Nano* **2011**, *5*, 9044-9051.

32. Xing, L.; Vatamanu, J.; Borodin, O.; Bedrov, D., On the Atomistic Nature of Capacitance Enhancement Generated by Ionic Liquid Electrolyte Confined in Subnanometer Pores. *J. Phys. Chem. Lett.* **2013**, *4*, 132-140.

33. Wu, P.; Huang, J.; Meunier, V.; Sumpter, B. G.; Qiao, R., Voltage Dependent Charge Storage Modes and Capacity in Subnanometer Pores. *J. Phys. Chem. Lett.* **2012**, *3*, 1732-1737.

34. Kondrat, S.; Perez, C.; Presser, V.; Gogotsi, Y.; Kornyshev, A., Effect of Pore Size and Its Dispersity on the Energy Storage in Nanoporous Supercapacitors. *Energy Environ. Sci.* **2012**, *5*, 6474-6479.

35. Merlet, C.; Rotenberg, B.; Madden, P. A.; Taberna, P.-L.; Simon, P.; Gogotsi, Y.; Salanne, M., On the Molecular Origin of Supercapacitance in Nanoporous Carbon Electrodes. *Nat. Mater.* **2012**, *11*, 306-310.

36. Pean, C.; Merlet, C.; Rotenberg, B.; Madden, P. A.; Taberna, P.-L.; Daffos, B.; Salanne, M.; Simon, P., On the Dynamics of Charging in Nanoporous Carbon-Based Supercapacitors. *ACS Nano* **2014**, *8*, 1576-1583.

37. Pean, C.; Rotenberg, B.; Simon, P.; Salanne, M., Understanding the Different (Dis)Charging Steps of Supercapacitors: Influence of Potential and Solvation. *Electrochim. Acta* **2016**, *206*, 504-512.

38. Portet, C.; Taberna, P. L.; Simon, P.; Flahaut, E.; Laberty-Robert, C., High Power Density Electrodes for Carbon Supercapacitor Applications. *Electrochim. Acta* **2005**, *50*, 4174-4181.

39. Edwards, D. M. F.; Madden, P. A.; McDonald, I. R., A Computer Simulation Study of the Dielectric Properties of a Model of Methyl Cyanide. *Mol. Phys.* **1984**, *51*, 1141-1161.

40. Merlet, C.; Salanne, M.; Rotenberg, B., New Coarse-Grained Models of Imidazolium Ionic Liquids for Bulk and Interfacial Molecular Simulations. *J. Phys. Chem. C* **2012**, *116*, 7687-7693.

41. Palmer, J. C.; Llobet, A.; Yeon, S. H.; Fischer, J. E.; Shi, Y.; Gogotsi, Y.; Gubbins, K. E., Modeling the Structural Evolution of Carbide-Derived Carbons Using Quenched Molecular Dynamics. *Carbon* **2010**, *48*, 1116-1123.

42. Cole, M. W.; Klein, J. R., The Interaction between Noble Gases and the Basal Plane Surface of Graphite. *Surf. Sci.* **1983**, *124*, 547-554.

43. Hess, B.; Kutzner, C.; Van Der Spoel, D.; Lindahl, E., Gromacs 4: Algorithms for Highly Efficient, Load-Balanced, and Scalable Molecular Simulation. *J. Chem. Theory Comput.* **2008**, *4*, 435-447.

44. Reed, S. K.; Lanning, O. J.; Madden, P. A., Electrochemical Interface between an Ionic Liquid and a Model Metallic Electrode. *J. Chem. Phys.* **2007**, *126*, 084704-13.

45. Gingrich, T. R.; Wilson, M., On the Ewald Summation of Gaussian Charges for the Simulation of Metallic Surfaces. *Chem. Phys. Lett.* **2010**, *500*, 178-183.

46. Dyatkin, B.; Zhang, Y.; Mamontov, E.; Kolesnikov, A. I.; Cheng, Y.; Meyer, H. M.; Cummings, P. T.; Gogotsi, Y., Influence of Surface Oxidation on Ion Dynamics and

Capacitance in Porous and Nonporous Carbon Electrodes. *J. Phys. Chem. C* **2016**, *120*, 8730-8741.

47. Chatterjee, S.; Jones, E. B.; Clingenpeel, A. C.; McKenna, A. M.; Rios, O.; McNutt, N. W.; Keffer, D. J.; Johs, A., Conversion of Lignin Precursors to Carbon Fibers with Nanoscale Graphitic Domains. *ACS Sus. Chem. & Eng.* **2014**, *2*, 2002-2010.

48. Köddermann, T.; Paschek, D.; Ludwig, R., Molecular Dynamic Simulations of Ionic Liquids: A Reliable Description of Structure, Thermodynamics and Dynamics. *ChemPhysChem* **2007**, *8*, 2464-2470.

49. Farmahini, A. H.; Opletal, G.; Bhatia, S. K., Structural Modelling of Silicon Carbide-Derived Nanoporous Carbon by Hybrid Reverse Monte Carlo Simulation. *J. Phys. Chem. C* **2013**, *117*, 14081-14094.

50. Nosé, S., A Unified Formulation of the Constant Temperature Molecular Dynamics Methods. *J. Chem. Phys.* **1984**, *81*, 511-9.

51. Hoover, W. G., Canonical Dynamics: Equilibrium Phase-Space Distributions. *Phys. Rev. A* **1985**, *31*, 1695-1697.

52. Vatamanu, J.; Xing, L.; Li, W.; Bedrov, D., Influence of Temperature on the Capacitance of Ionic Liquid Electrolytes on Charged Surfaces. *Phys. Chem. Chem. Phys.* **2014**, *16*, 5174-5182.

53. Feng, G.; Li, S.; Atchison, J. S.; Presser, V.; Cummings, P. T., Molecular Insights into Carbon Nanotube Supercapacitors: Capacitance Independent of Voltage and Temperature. *J. Phys. Chem. C* **2013**, *117*, 9178-9186.

54. Kornyshev, A. A.; Luque, N. B.; Schmickler, W., Differential Capacitance of Ionic Liquid Interface with Graphite: The Story of Two Double Layers. *J. Solid State Electrochem.* **2014**, *18*, 1345-1349.

55. Forse, A. C.; Merlet, C.; Griffin, J. M.; Grey, C. P., New Perspectives on the Charging Mechanisms of Supercapacitors. *J. Am. Chem. Soc.* **2016**, *138*, 5731–5744.

56. Kondrat, S.; Georgi, N.; Fedorov, M. V.; Kornyshev, A. A., A Superionic State in Nano-Porous Double-Layer Capacitors: Insights from Monte Carlo Simulations. *Phys. Chem. Chem. Phys.* **2011**, *13*, 11359-11366.

57. Griffin, J. M.; Forse, A. C.; Tsai, W.-Y.; Taberna, P.-L.; Simon, P.; Grey, C. P., In Situ Nmr and Electrochemical Quartz Crystal Microbalance Techniques Reveal the Structure of the Electrical Double Layer in Supercapacitors. *Nat. Mater.* **2015**, *14*, 812-819.

58. Magde, D.; Elson, E.; Webb, W. W., Thermodynamic Fluctuations in a Reacting System - Measurement by Fluorescence Correlation Spectroscopy. *Phys. Rev. Lett.* **1972**, *29*, 705-708.

59. Yeung, C.; Shtrahman, M.; Wu, X.-l., Stick-and-Diffuse and Caged Diffusion: A Comparison of Two Models of Synaptic Vesicle Dynamics. *Biophys. J.* **2007**, *92*, 2271-2280.

60. Centeno, T. A.; Sereda, O.; Stoeckli, F., Capacitance in Carbon Pores of 0.7 to 15 Nm: A Regular Pattern. *Phys. Chem. Chem. Phys.* **2011**, *13*, 12403-12406.

61. Farrow, C. L.; Billinge, S. J. L., Relationship between the Atomic Pair Distribution Function and Small-Angle Scattering: Implications for Modeling of Nanoparticles. *Acta Crystallogr., Sect. A: Found. Crystallogr.* **2009**, *65*, 232-239.

62. Fujii, K.; Soejima, Y.; Kyoshoin, Y.; Fukuda, S.; Kanzaki, R.; Umebayashi, Y.; Yamaguchi, T.; Ishiguro, S.-i.; Takamuku, T., Liquid Structure of Room-Temperature Ionic Liquid, 1-Ethyl-3-Methylimidazolium Bis-(Trifluoromethanesulfonyl) Imide. *J. Phys. Chem. B* **2008**, *112*, 4329-4336.

63. Béguin, F.; Presser, V.; Balducci, A.; Frackowiak, E., Carbons and Electrolytes for Advanced Supercapacitors. *Adv. Mater.* **2014**, *26*, 2219-2251.

64. Krause, A.; Balducci, A., High Voltage Electrochemical Double Layer Capacitor Containing Mixtures of Ionic Liquids and Organic Carbonate as Electrolytes. *Electrochem. Commun.* **2011**, *13*, 814-817.

65. Pohlmann, S.; Olyschläger, T.; Goodrich, P.; Vicente, J. A.; Jacquemin, J.; Balducci, A., Mixtures of Azepanium Based Ionic Liquids and Propylene Carbonate as High Voltage Electrolytes for Supercapacitors. *Electrochim. Acta* **2015**, *153*, 426-432.

66. Lin, R.; Taberna, P.-L.; Fantini, S.; Presser, V.; Pérez, C. R.; Malbosc, F.; Rupesinghe, N. L.; Teo, K. B. K.; Gogotsi, Y.; Simon, P., Capacitive Energy Storage from −50 to 100 °C Using an Ionic Liquid Electrolyte. *J. Phys. Chem. Lett.* **2011**, *2*, 2396-2401.

67. Schütter, C.; Husch, T.; Korth, M.; Balducci, A., Toward New Solvents for Edlcs: From Computational Screening to Electrochemical Validation. *J. Phys. Chem. C* **2015**, *119*, 13413-13424.

68. Kondrat, S.; Kornyshev, A., Charging Dynamics and Optimization of Nanoporous Supercapacitors. *J. Phys. Chem. C* **2013**, *117*, 12399-12406.

69. Merlet, C.; Pean, C.; Rotenberg, B.; Madden, P. A.; Simon, P.; Salanne, M., Simulating Supercapacitors: Can We Model Electrodes as Constant Charge Surfaces? *J. Phys. Chem. Lett.* **2013**, *4*, 264-268.

6. Influence of Drop Size and Surface Potential on the Contact Angle of Ionic-Liquid Drops

In this chapter we have performed molecular dynamics simulations of the room temperature ionic-liquid 1-ethyl-3-methylimidazolium tetrafluoroborate on a surface with graphene structured sheets. Contact angles were calculated via polynomial-fitting of two dimensional atomic density contours. Drop size and surface interaction were varied to assess their influences on the contact angle. At low graphene interaction potential no change in contact angle with drop size was found. When increasing the surface interaction potential towards actual graphene, the drops deviated to fully wetting, but the spreading rate and extent became dependent on drop size. The smallest drop formed a single adsorbed layer due to its initial size and the large ratio of ions in the adsorbed layer. Larger drops wetted and formed non-uniform metastable drops upon several layers of spread liquid. These were not true equilibrium structures as when starting from a single adsorbed layer film at room temperature, the metastable layers were not reformed. An increase in temperature resulted in the drop forming a single layer film, which implied that the behaviour here can be considered a form of contact hysteresis, enabled by a kinetic barrier between the metastable and film layers. At low surface potential, a single layer reverted to a drop and had the same contact angle as when starting from a drop, which showed that the hysteresis is potential dependent and that low surface potentials more readily form equilibrium structures.

6.1. Introduction

The experimental and theoretical contact angle for liquids on solid substrates is a useful measurement to quantify interfacial energy between solid, liquid, and vapour phases.[1-2] The determination of these energies is useful in various applications of modern materials. On the substrate side, pure graphene and graphene-substrate coating, have received attention for uses in photocatalytic,[3] optical,[4] medical,[5] and substrate protection[6] applications. This is due to graphene's well known properties of excellent thermal conductivity, optical transmittance, and mechanical strength.

Experimental[7-8] and theoretical[9] studies have been conducted to characterise graphene's wettability. Water in particular has been widely studied.[9-19] Among non-aqueous media, interest in ionic-liquids (ILs) is emerging due to their favourable conductive, and vapour pressure properties.[20] Graphene-IL interfacial properties have been mostly studied in the context of electric double-layer capacitors (EDLCs).[21-26] Significantly increased understanding, particularly of the charge over-screening behaviour of ILs,[27-28] has been gained in recent years. In the context of advanced EDLCs, Kondrat and Kornyshev have proposed to use 'ionophobic' nanopores for accelerated charging and high energy-storage.[29-30] Non-graphene substrates with ILs are also of interest for wetting studies with similar applications to that of graphene.[31-37]

There have been few explicit reports of the contact angle between ionic liquids and graphene. Herrara et al.[38] performed recent molecular dynamics (MD) simulations of the amino-acid IL 1-ethyl-3-methylimidazolium glycine (EMIM-GLY) and reported 40 degree variation in contact angle with the size of the nano-drops (from 100 to 500 IL pairs) on highly attractive graphene sheets. Taherian et al.[39] used MD simulations for an electrowetting study of 1-butyl-3-methylimidazolium tetrafluoroborate (BMIM-BF_4) ions bridging between graphene surfaces of opposing and fixed coulombic charges. In their simulations, ions were bonding with each other in one of the two dimensions parallel to the sheets, such that the IL was continuous in this direction and formed a pillar-like bridge between electrodes. This enabled curvature effects such as line tension to be removed from the contact angle calculation. Asymmetry was found in the contact angle between surfaces, and attributed firstly to the ion size asymmetry, and secondly to differences in cation orientation in the second adsorbed layer at the oppositely charged surfaces. Higher IL spreading was observed at the most negatively charged surface, with a contact angle of 54.3 degrees, compared to 61.6 degrees at the most positively charged surface.

Baldelli et al.[40-41] used sum frequency generation (SFG) to study the orientation of 1-butyl-3-methylimidazolium methane sulfate (BMIM-MS) on single layer graphene, and found that the methyl of the MS anion orientated greater than 40 degrees from the normal of the surface, whilst the BMIM cation aligned in a weakly parallel arrangement. They also reported a contact angle of 58 degrees for this system. Xu et al.[42] also used SFG in their work to investigate 1-butyl-3-methylimidazolium dicyanamide (BMIM-DCA) with bare, and graphene coated, barium fluoride (BaF_2) substrates. They found that upon coating with graphene, the BaF_2 transitioned from only DCA anions to both ion species being detected in the first layer of the solid-liquid interface. This was accompanied by an increase in contact angle from 57 to 69 degrees with a single layer of graphene added. Further layers of graphene were found to slightly decrease the measured contact angle. Electrowetting on dielectric (EWOD) experiments by Ralston et al.[35] showed that ILs can be used for electrowetting applications and that they behave in a manner analogous to aqueous electrolyte solutions but with some important differences due to the ion-size asymmetry in the ILs used.

In this chapter we report on MD simulations of the IL 1-ethyl-3-methylimidazolium tetrafluoroborate (EMIM-BF_4) on graphene sheets. As with the work by Herrara et al.,[38] here the IL drop size was also varied. Also changed were the graphene sheet properties, to examine the influence of interaction potential on contact angle. To obtain accurate results, a method used in previous work was employed,[43] where two-dimensional number density contours are converted into atomic density contours. This gives a smoother fit of the drops contour and more closely matches experimental contact angle measurement. An example of atomic density contours used for the contact angle measurement is given in Figure 6-1. In this figure, a height of zero corresponds to the plane through the centre of the carbon atoms in the top layer of graphene. The horizontal line at $z_\theta^* = 1$ is the distance at which the tangent of the isochor ($\rho^* = 0.35$) is taken to determine the contact angle (θ). In this chapter the contact angles are reported at $z_\theta^* = 0$ except where otherwise stated.

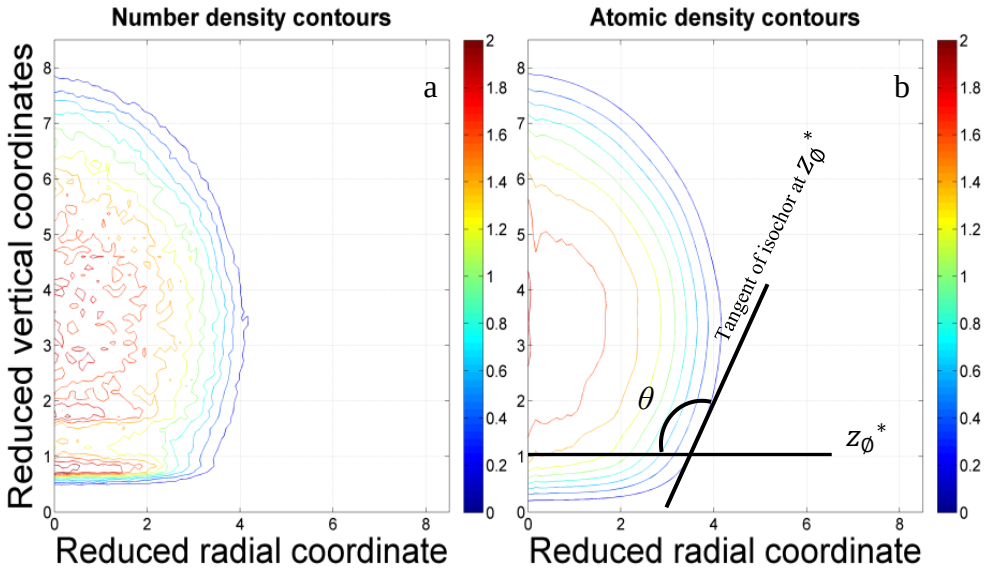

Figure 6-1: Two dimensional number (a) and atomic (b) density contours of a drop consisting of 100 EMIM-BF_4 pairs on a surface with low a low interaction potential. The outer layer is fitted with a polynomial, to calculate the contact angle at z_θ^* = 1. Here the coordinates are reduced by 0.34 nm.

6.2. Methodology

Simulations were performed using the open source MD package Gromacs.[44] A coarse-grained model of $EMIMBF_4$ was used from Merlet *et al.*, [45] and the carbon Lennard-Jones parameters were taken from Cole *et al.*,[46] with σ = 0.337 nm and well depth (ε) varied between 0.01, 0.05, 0.10, 0.15, and 0.23 kJ mol^{-1} depending on the simulation. Lennard-Jones interaction ($\varphi(r)$) was calculated using the following equation:

$$\varphi\left(r_{ij}\right) = 4\varepsilon_{ij}\left(\left(\frac{\sigma_{ij}}{r_{ij}}\right)^{12} - \left(\frac{\sigma_{ij}}{r_{ij}}\right)^{6}\right) \tag{6-1}$$

with regular Lorentz-Berthelot mixing rules applied where:

$$\sigma_{ij} = \frac{1}{2}\left(\sigma_{ii} + \sigma_{jj}\right) \tag{6-2}$$

$$\varepsilon_{ij} = \left(\varepsilon_{ii}\varepsilon_{jj}\right)^{\frac{1}{2}} \tag{6-3}$$

Boxes of $EMIMBF_4$ were equilibrated separately in the NVT and NPT ensembles at 298 K. These boxes were then placed above three layers of immobile graphene sheets and equilibrated for 500 ps in the 3D-periodic NVT ensemble to allow the formation of a drop. The temperature was maintained by a Nose-Hoover[47-48] thermostat with long range particle

mesh Ewald (PME) summations[49] performed for electrostatics. A short range cut-off distance of 1.2 nm was used for Lennard-Jones and electrostatic calculations. Production runs were then run in 5 ns blocks, sampling positions every 2 ps. For systems with higher interaction potentials, longer simulation times were required to reach the equilibrium wetting state.

For variation in drop size, 100, 200, 300, and 500 ion pairs were used. Various sheet sizes were used throughout depending on the combination of drop size and surface strength. The sheets were checked to be sufficiently large enough such that no finite size effects, or bridging through the periodic simulation box was realised. The sheet sizes used in all simulations are listed in Table A6-2 of Appendix A6, and finite size effects relevant to contact angle calculation are shown in Figure A6-10 of Appendix A6. Sheets were arranged in a hexagonal structure with atomic spacing of 0.142 nm and sheet spacing of 0.35 nm. For variation of interaction potential, ε values of 0.01, 0.05, 0.10, 0.15, and 0.23 kJ mol^{-1} were used in conjunction of drop sizes consisting of 100, 200 and 500 ion pairs.

Time averaged r-z number density profiles were then computed with a bin size of 0.05 nm. Then using a method consistent with our previous publication,[43] number density profiles were converted into atomic density contours, reducing the diameters by 3.4 Å and accounting for the correct collision diameter of each atom type. The atomic density contours were fitted with polynomial functions with the lower bound cut-off distance set to $z_\theta^* = 2$, to compute contact angle for several heights, beginning with the origin at the VdW surface of the graphene sheet.

6.3. Results and Discussion

MD simulations of water nanodrops on graphene have shown that there is a strong dependence on drop size for the contact angle.[50] A similar dependence for an imidazolium IL on graphene has been reported by Herrara et al.[38] In this chapter, a similar IL is used on graphene and pseudo-graphene sheets with various carbon-atom interaction potentials to further test the size-dependent result of the IL contact angle on graphene. The potentials ranged from the real potential of 0.23 kJ mol^{-1} (strongly interacting) to a minimum of 0.01 kJ mol^{-1} (weakly interacting). The ionic liquid is represented by a coarse-grained model which has been shown to well approximate bulk (density, diffusion coefficients) and interfacial (surface tension) properties.[45]

6.3.1. Ionic liquid drop size on low-potential graphene sheet

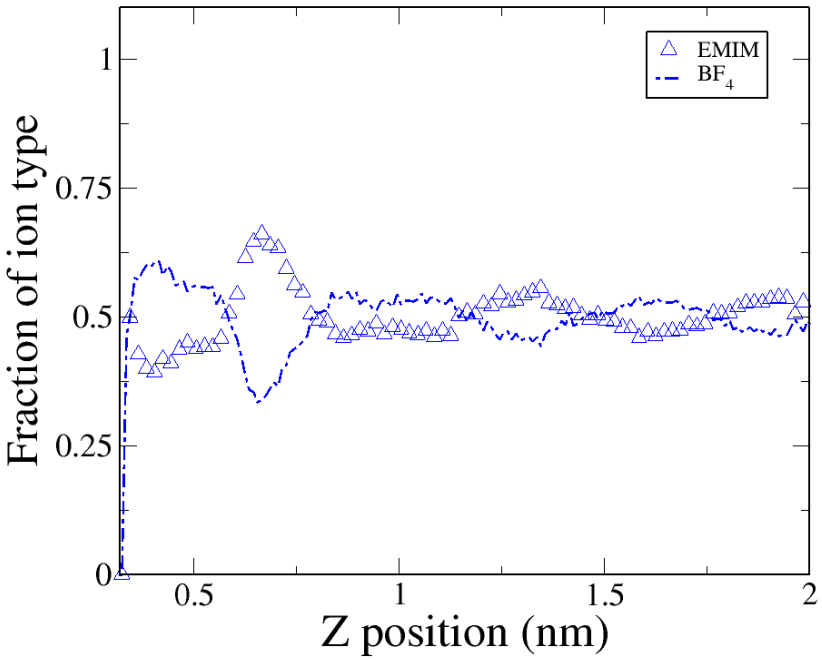

Figure 6-2: Fractional number density profiles for drop size of 500 IL pairs. Symbols correspond to EMIM cations, and lines to BF_4 anions. A bin depth 0.01 nm was used in the z dimension.

Firstly, the IL drop size dependence was studied on a weakly interacting sheet with an interaction potential (ε) of 0.01 kJ mol^{-1}, which should correspond to the ionophobic surface introduced by Kondrat and Kornyshev.[29-30] For clarity, in Figure 6-2, the first two bins with ions detected, corresponding to the very bottom of the first adsorbed layer, were omitted due to the small number of ions in these bins causing poor statistical sampling. Only the drop size of 500 IL pairs is shown here. However, a full plot including the drops sizes of 100, 200, and 300 IL pairs is given in Figure A6-8 of Appendix A6. Most significantly, the structure of the drops did not change with size, and there was clear ordering in all cases with a higher density of BF_4 anions in the first layer, and EMIM cations in the second layer. This multilayer structure is consistent with previous experiments which have been performed to characterise the (bulk) liquid-solid interfaces of ionic liquids, using surface force apparatus,[51] atomic force microscopy,[52] or X-ray reflectivity.[53] At the sheet surface, the average contact angle after 4 ns production runs was found to be 146 ± 4 degrees, and it can be concluded that IL contact angle is independent of the size of the drop for a weakly interacting sheet. More contact angles are reported in Table 6-1, where it can be seen that seen that the 100, 300, and 500 IL pair contact angles converged with a relatively low uncertainty. The 200 IL pair system likely encountered an unfavourable configuration during the simulation, which shifted the mean and

increased the uncertainty. It is believed that this system would regress to a contact angle value and uncertainty in line with the other systems, if a longer simulation was performed.

Table 6-1: Contact angle as function of drop size at the sheet surface ($z_\theta^* = 0$) and a height above the sheet of ($z_\theta^* = 1$). Uncertainties are from splitting the 5 ns simulation into 1 ns blocks.

	100 IL Pairs	**200 IL Pairs**	**300 IL Pairs**	**500 IL Pairs**
$z_\theta^* = 0$	147 ± 3	153 ± 12	140 ± 5	146 ± 3
$z_\theta^* = 1$	125 ± 2	133 ± 7	127 ± 3	133 ± 2

6.3.2. Higher sheet interaction potentials

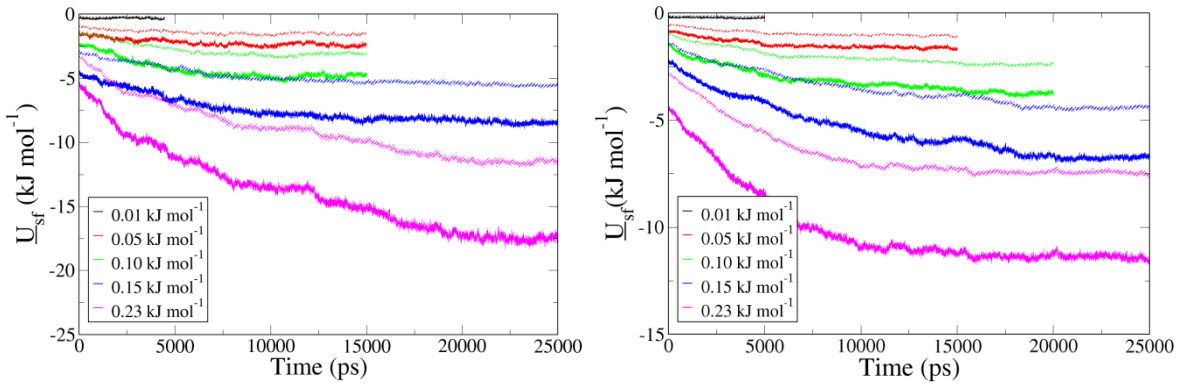

Figure 6-3: Solid-fluid interaction energy per IL pair to show the time required to reach equilibrium for increasing carbon interaction potential with drops of 200 pairs (a) and 500 pairs (b). Solid lines depict EMIM cations and broken lines BF_4 anions.

When using higher interaction potentials, the simulation time required to reach equilibrium increased due to the greater solid-fluid interaction and collective rearrangement of ions. The greater interaction caused the drops to spread and, as the viscosity of the IL is large and ion mobility is low, the speed of this process was slow. To test how the sheet interaction potential affects the contact angle, we selected a range of potentials for IL drop sizes of 100, 200, and 500 pairs. The sheet size to drop size ratios were carefully checked to ensure that the sheets were large enough such that no finite size effects, or bridging through the periodic image, occurred. Details of this validation are given at the end of the Section 6.2.

From Figure 6-3 it is obvious that required simulation time before equilibrium is reached is dependent strongly on interaction potential and weakly on drop size. As the size increases the proportion of ions in the first adsorbed layer decreases (since the adsorbed layer thickness does not change), and therefore the solid-fluid interaction energy per ion pair also decreases

as most of the interaction with the solid occurs in the first adsorbed layer. The difference is seen between the energy values in Figure 6-3. For the interaction potential of 0.23 kJ mol^{-1}, simulation times in excess of 20 ns were required to reach equilibrium, this is a large increase over that reported by Herrara et al.,[38] where less than 5 ns were required with a simulation temperature of 403 K. The differences in time required could be partly explained by the temperature used in this work, 298 K, and the differences in the liquid-liquid interactions between the two IL pairs used may also have played a role.

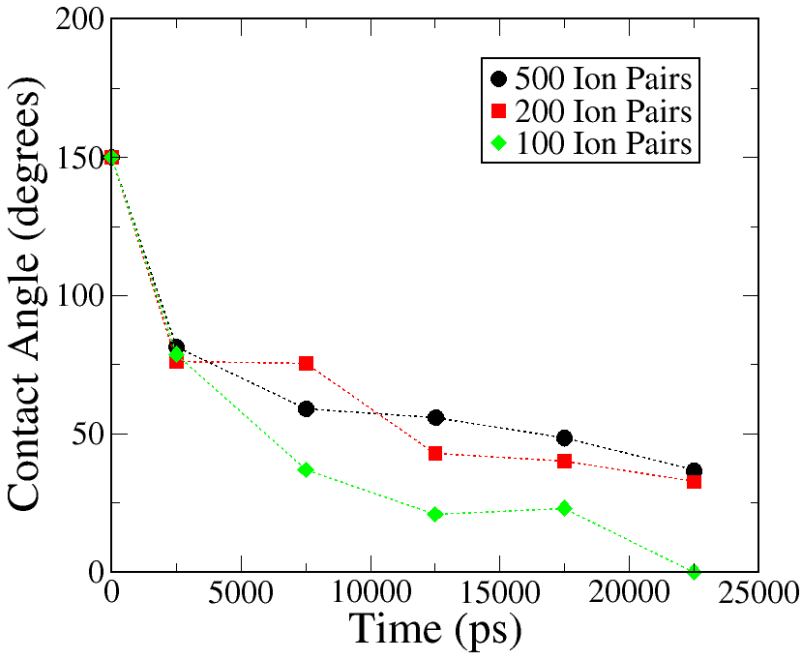

Figure 6-4: Contact angle as a function of time at a sheet interaction potential of 0.15 kJ mol^{-1}.

Figure 6-4 shows the variation of contact angle as a function of time. It can be seen that the drop of 100 IL pairs spread on the graphene surface faster than that of the 200 and 500 IL pairs, which is expected due to its smaller size creating shorter diffusion paths for the ions. The drop in contact angle from 25 to zero degrees for the 100 IL pairs is due to the instability (or sensitivity) of polynomial fit at such low angles. The actual structure of the drop did not change significantly between these two reported values and both can be considered as wetting. It can also be seen that 200 and 500 IL pairs yielded similar results. It was only when the interaction potential was increased to 0.23 kJ mol^{-1} that large differences in the drop spreading rate became apparent, this is shown in Figure A6-9 of Appendix A6. The time scale for equilibrium contact angle observed here is much greater than that of simulations with water,[54] highlighting how the strong ion-ion interactions in ILs limit their mobility and ability to transition into adjacent interfacial layers.

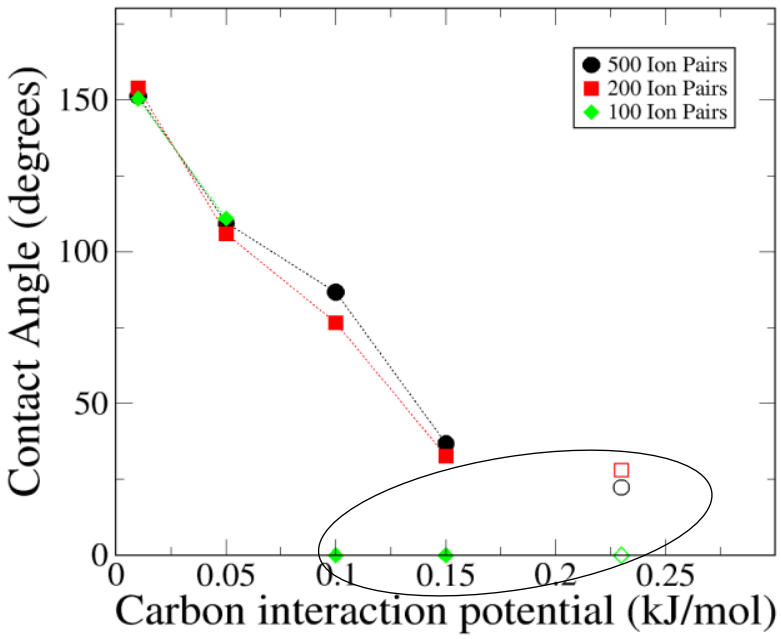

Figure 6-5: Contact angle at various interaction potentials for drops of 100, 200, and 500 IL pairs. The circled systems were considered to be fully wetting, with the filled symbols representing uniform adsorbed structures and unfilled symbols representing non-uniform adsorbed structures.

The contact angle varied almost linearly with the surface interaction potential until full wetting was obtained, as shown in Figure 6-5. This supports the choice of a simple energetic parameter to describe the ionophobicity of the surface.[29-30] Systems were considered fully wetting when the shape of the adsorbed liquid deviated significantly from that of a typical round drop. These are shown in the circled region of Figure 6-5. Two distinct wetting states were observed. The first wetting state was a uniformly adsorbed structure (filled symbols in the circled region of Figure 6-5), with a characteristic square shape, and thickness of 2-3 molecules depending on the interaction energy. 100 IL pair ε = 0.10 and 0.15 kJ mol^{-1} systems fell into this category and a simulation snapshot of this wetting structure is shown in Figure 6-6a.

The second wetting state was a non-uniform adsorbed structure (unfilled symbols in the circled region of Figure 6-5), with two distinct meta-stable layers. The first layer was one molecule thick, non-circular, and had straight edges. The second layer was adsorbed on top of the first layer, and was more drop-like in shape. The thickness and radius of this layer was dependent on the size of the drop. The proportion of ions in the second drop also increased with drop size. All of the ε = 0.23 kJ mol^{-1} systems (100, 200, and 500 IL pairs) fell into this category and a simulation snapshot of this wetting structure is shown Figure 6-6b. If given a significantly long enough time, to account for the low ion mobility and energy barrier for an

ion to shift layers, it is likely that this "metastable-solid" would transition into a more uniform, layered wetting structure. This concept is further explored below with a simulation at increased temperature.

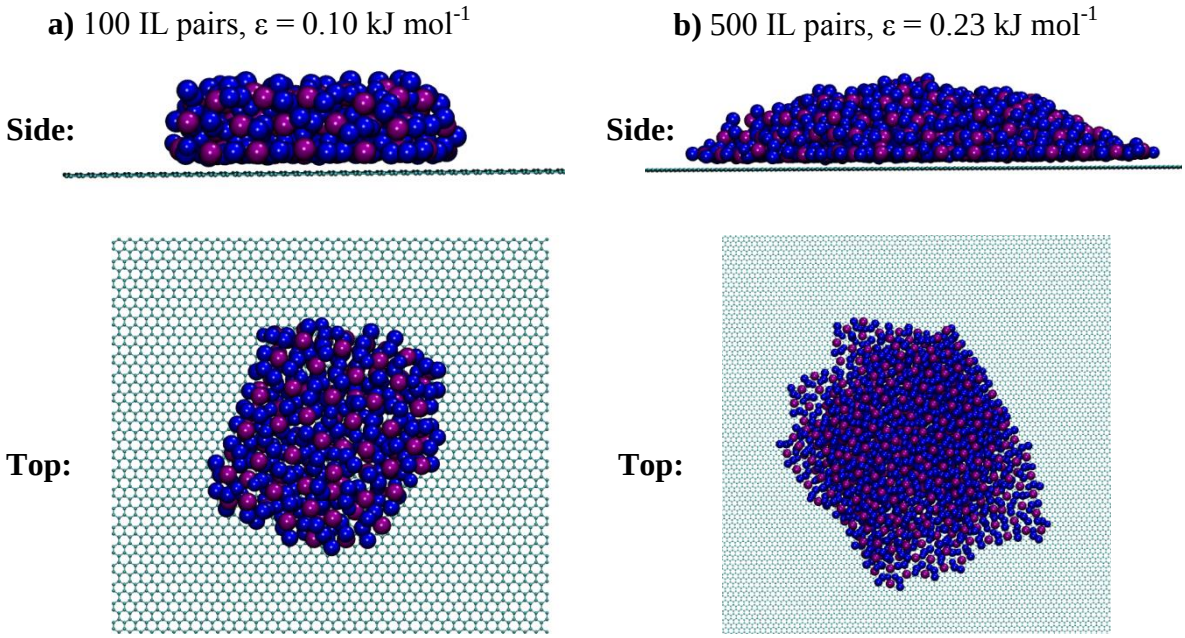

Figure 6-6: a: side view of uniform wetting state for the 100 IL pair simulation with an interaction energy of ε = 0.10 kJ mol^{-1}. b: top view of non-uniform wetting state for the 500 IL pair simulation with an interaction energy of ε = 0.23 kJ mol^{-1}. EMIM cations are represented as the blue beads, and BF_4 anions as the purple beads.

The structures observed for the systems in Figure 6-5, and their contact angles, are likely a result of the ratio of ions in the first adsorbed layer to ions in the subsequent layers. This ratio is not constant and decreases with increasing drop size, since the surface layer has a fixed thickness. When the surface interaction potential is increased, the drop spreads and the proportion of ions in the first adsorbed layer increases. When a critical ratio of ions in the first adsorbed layer is reached, it becomes more favourable to form a film rather than a drop, and this was reached at a weaker interaction strength for the 100 IL pair drop as its initial first adsorbed layer ratio was the highest. For the larger drops at the highest surface interaction potential, the ratio of ions in the first adsorbed layer did not reach this critical point and instead formed non-uniform metastable layers.

It can be concluded that for $EMIMBF_4$, the critical solid interaction energy, above which wetting will occur and drop behaviour cannot be studied, is 0.05 kJ mol^{-1} for small drops, and 0.15 kJ mol^{-1} for larger drops (Figure 6-5). The results here contrast with the ones obtained by Herrara et al.[38] Firstly, in this chapter, no consistent drop size dependence on the contact angle was found. Most significantly however, is that the results here show wetting behaviour

that significantly deviates from a regular drop at a sheet interaction potential of 0.23 kJ mol^{-1}, whilst Herrara et al.[38] reported contact angles of 48 and 80 degrees for drop sizes of 200 and 500 IL pairs respectively whilst using an even more strongly interacting sheet of $\varepsilon = 0.2929$ kJ mol^{-1}.

This difference cannot be explained by temperature, as when the temperature of the 200 IL pair simulation, with a sheet interaction potential of 0.23 kJ mol^{-1}, was increased from 298 K to 400 K (114 K above the melting temperature of 286 K) , the sheet was fully wetted (Figure 6-7b). The contrasting results are very likely due to the different structure of the anions, which results in different adsorption profiles. Although we observe that the first adsorbed layer is enriched with anions, in the case of EMIM-GLY no such effect was observed (on the contrary, cations seem to approach slightly closer to the surface).[38] The size and shape of the ions therefore play an important role on the contact angle, and results obtained for a specific ionic liquid cannot easily be transferred to other systems.

To further investigate the causes of the second wetting state observed (Figure 6-6b), a new starting structure of a single adsorbed ion layer, centred on a large sheet, was created. This simulation had 200 IL pairs and was tested under three conditions, high surface strength and normal temperature, high surface strength and high temperature, and low surface strength and normal temperature (Figure 6-7, d-f). These are compared with their counterparts starting from a drop configuration (Figure 6-7, a-c).

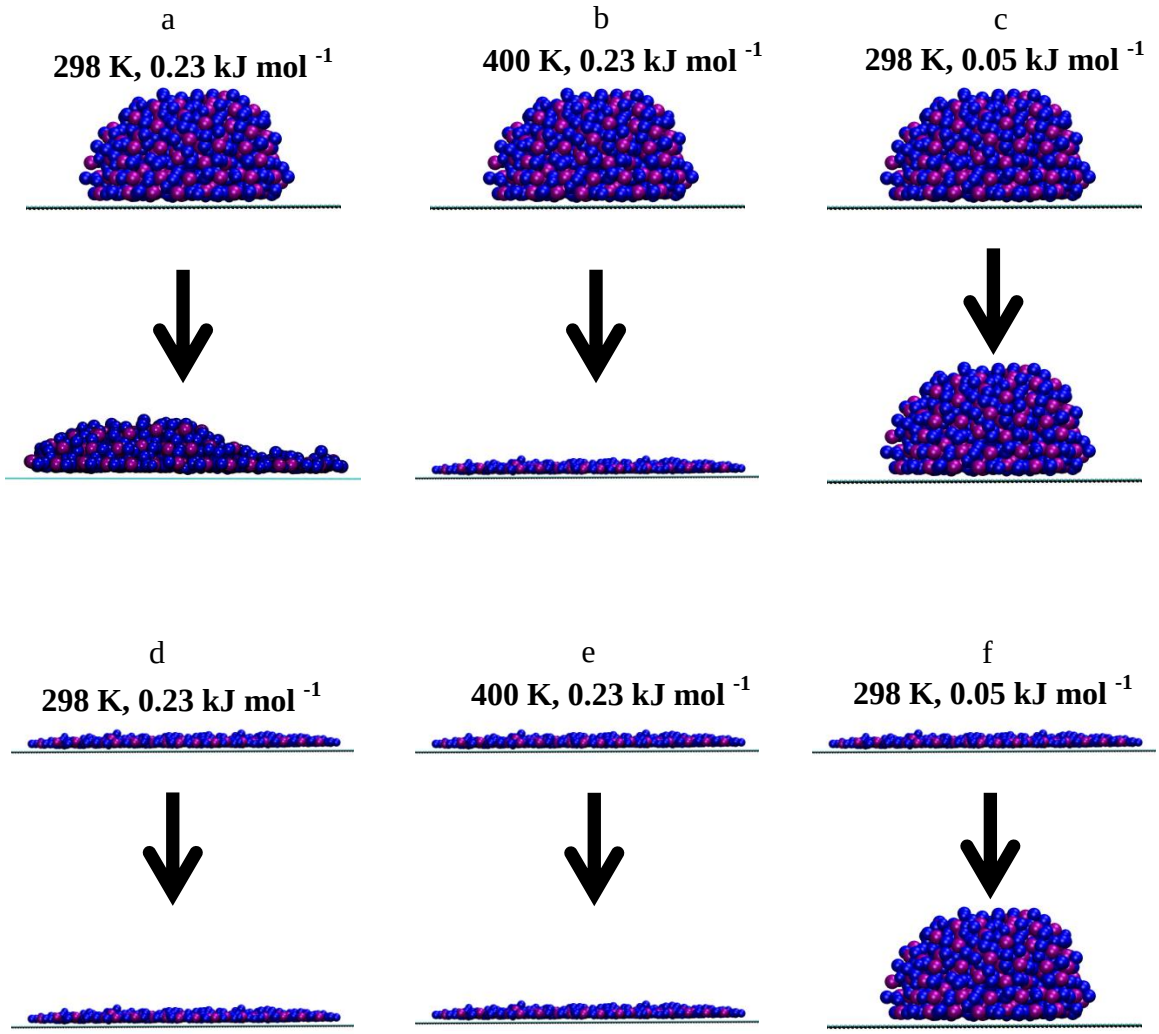

Figure 6-7: a: 200 IL pairs simulated at 400 K on a sheet with ε = 0.23 kJ mol^{-1}. b and c: Single adsorbed layer film of 200 IL pairs on a large sheet with ε = 0.23 (b) and 0.05 kJ mol^{-1} (c). Top panes show the initial simulation configurations and bottom the final.

Figure 6-7 (a and b) showed that the metastable second wetting state was not a true equilibrium state as upon temperature increase the final configuration was a single layer film. Most significantly however is that when starting from a film rather than a drop, the weakly interacting system (Figure 6-7f) formed a drop with a contact angle of 109 degrees (identical to the contact angle of Figure 6-7c), whereas the film on the high-potential surface (Figure 6-7d) did not revert back to its metastable ”drop”. As the 400 K simulation (Figure 6-7b) formed a single layer film, and did not get “trapped” at the metastable state, the behaviour here is likely kinetic. This indicates that at an interaction potential of 0.23 kJ mol^{-1}, all drop sizes used in this study would form films if given sufficient time.

Finally, to investigate whether this metastable state is observable in other ILs, we simulated a 216 IL pair drop with an all-atom model of 1-ethyl-3-methylimidazolium bis(trifluoromethyl-

sulfonyl)imide (EMIM-TFSI) from Köddermann et al.[55] At a low surface potential (0.05 kJ mol^{-1}) a drop formed with a contact angle of 103 ± 3 degrees, and at a high surface potential (0.23 kJ mol^{-1}), a metastable structure was formed and was persistent for more than 25 ns. The transition from equilibrium to metastable wetting formation with surface potential may be a generic feature of many ILs and has implications of the applicability of continuum theories on nano-scale IL drops.

6.4. Conclusions

In this chapter the wetting behaviour of $EMIMBF_4$ ionic liquid drops on graphene sheets of various interaction potentials was studied using molecular dynamics simulations. The results showed that there was no difference in contact angle for drops of different sizes, from 100 to 500 IL pairs, on a low-potential graphene surface. The contact angle of the weakest surface studied (ε = 0.01 kJ mol^{-1}) was found to be 146 ± 4 degrees at $z_\theta^* = 0$. Increasing the surface interaction potential caused a strong reduction in the contact angle with progressively longer simulation times required to reach equilibrium. For a drop size of 100 IL pairs, the surface was wetted at an interaction potential of 0.10 kJ mol^{-1}, and formed a uniform and square shaped structure three molecules thick. Larger drops at this surface potential, or stronger, did not fully wet the surface but gave drops that had a solid-like surface structure with a liquid drop on top. These drops appear to be non-equilibrium and metastable, as drops that start from a layer configuration stay in a layer configuration. At 400 K, the drops could fully wet the surface from an initial drop configuration. This temperature is 114 K above the melting point of $EMIMBF_4$, and the metastable structures at the surface seen at 298 K do not occur here. When starting with a single-layer film, the ions on high potential sheet did not revert back to the metastable structures observed when starting from a drop configuration, which shows that these metastable drops were not at equilibrium and that there is a kinetic barrier between metastable and film states. The formation of (metastable) ordered structures at the surface of ionic liquids seems to be a rather generic feature which has been observed in other contexts,[56-57] and understanding their impact on the wetting properties would certainly be of great interest in the future.

Appendix A6

Table A6-2: Number of ion pairs, sheet dimensions and number of carbon atoms for all simulation systems.

Drop size at 0.01 kJ mol $^{-1}$ interaction potential			
Series	x sheet length (nm)	y sheet length (nm)	Carbon atoms
100 ion pairs	9.840	8.946	10080
200 ion pairs	9.840	8.946	10080
300 ion pairs	9.840	8.946	10080
500 ion pairs	9.840	8.946	10080
Sheet size at 0.01 kJ mol $^{-1}$ interaction potential and 100 pairs			
Series	x sheet length (nm)	y sheet length (nm)	Carbon atoms
Standard	6.396	5.964	4368
4x	12.792	11.928	17472
16x	25.584	23.856	69888
0.83x	5.904	5.538	3744
0.73x	5.412	5.112	3168
0.60x	4.920	4.686	2640
0.50x	4.428	4.260	2160
100 pairs and variable carbon interaction potential			
Series	x sheet length (nm)	y sheet length (nm)	Carbon atoms
0.01 kJ mol $^{-1}$	9.840	8.946	10080
0.05 kJ mol $^{-1}$	9.840	8.946	10080
0.10 kJ mol $^{-1}$	9.840	8.946	10080
0.15 kJ mol $^{-1}$	9.840	8.946	10080
0.23 kJ mol $^{-1}$	12.792	11.928	17472
200 pairs and variable carbon interaction potential			
Series	x sheet length (nm)	y sheet length (nm)	Carbon atoms
0.01 kJ mol $^{-1}$	9.840	8.946	10080
0.05 kJ mol $^{-1}$	9.840	8.946	10080
0.10 kJ mol $^{-1}$	9.840	8.946	10080
0.15 kJ mol $^{-1}$	12.792	11.928	17472
0.23 kJ mol $^{-1}$	12.792	11.928	17472
500 pairs and variable carbon interaction potential			

Series	x sheet length (nm)	y sheet length (nm)	Carbon atoms
0.01 kJ mol $^{-1}$	12.792	11.928	17472
0.05 kJ mol $^{-1}$	12.792	11.928	17472
0.10 kJ mol $^{-1}$	12.792	11.928	17472
0.15 kJ mol $^{-1}$	12.792	11.928	17472
0.23 kJ mol $^{-1}$	25.584	23.856	69888
200 pairs at higher temperatures on a sheet with a 0.23 kJ mol^{-1} interaction potential			
Series	x sheet length (nm)	y sheet length (nm)	Carbon atoms
400 K	12.792	11.928	17472
500 K	12.792	11.928	17472
200 pairs starting from a single adsorbed layer film			
Series	x sheet length (nm)	y sheet length (nm)	Carbon atoms
0.23 kJ mol $^{-1}$	25.584	23.856	69888
0.05 kJ mol $^{-1}$	25.584	23.856	69888

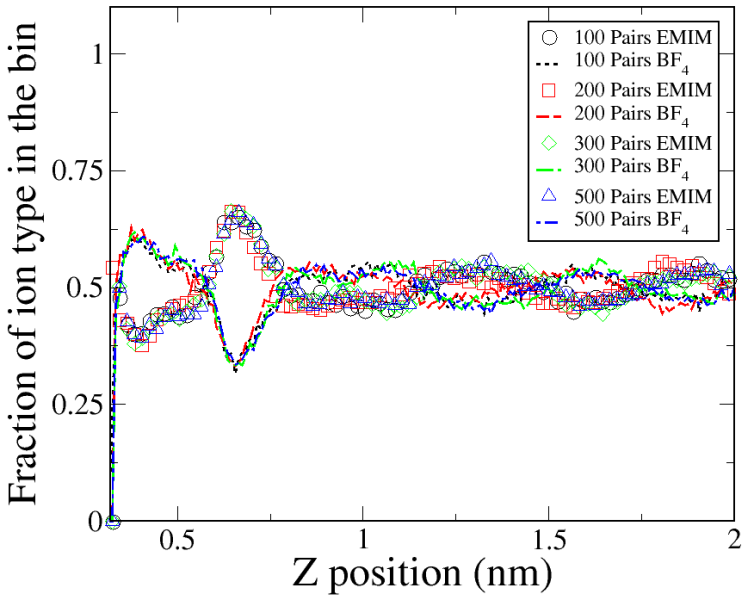

Figure A6-8: Fractional number density profiles for drops of increasing sizes. Symbols correspond to $EMIM^+$ cations, and lines to BF_4^- anions.

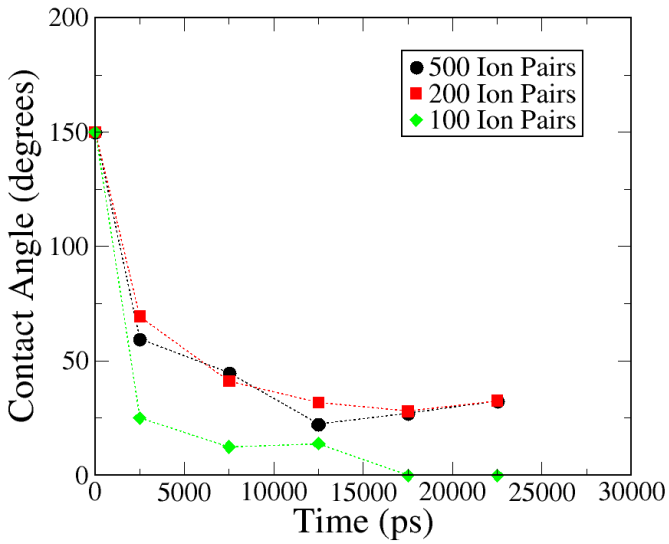

Figure A6-9: Contact angle as a function of time at a sheet interaction potential of 0.23 kJ mol^{-1}.

Accounting for the shape of the drops

Unfortunately, when calculating atomic contours from r-z density profiles, and fitting circles for contact angle measurement, it is possible to generate erroneous results due to the averaging from the centre of mass in a radial direction. An example of this phenomenon is given in Figure A6-10 where the contact angle was calculated to be 144 degrees at the sheet surface. It is critical to visualise the simulation trajectories as a means to check for correct drop shape, and not rely on the solid-fluid interaction energies, and density contours for validation.

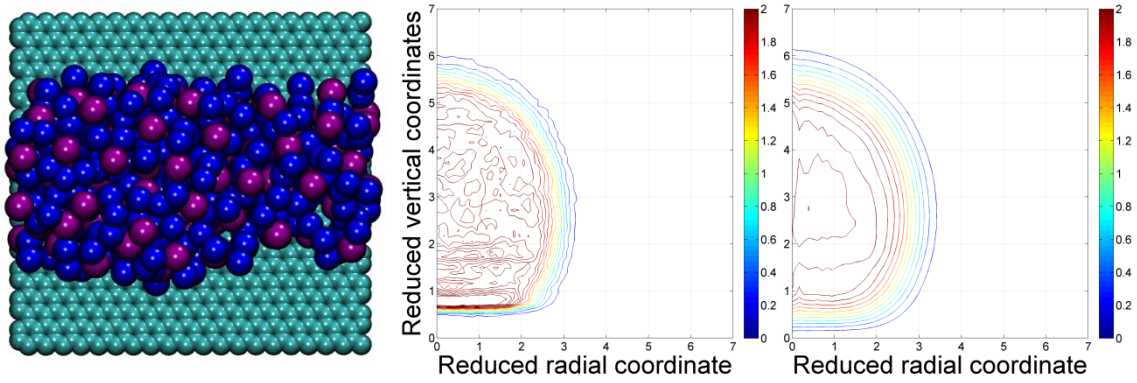

Figure A6-10: Left: top view snapshot of the 0.60x standard simulation, blue = EMIM cations, purple = BF_4 anions. Centre: corresponding number density contours. Right: corresponding atomic density contours.

6.5. References

1. Good, R. J., Contact Angle, Wetting, and Adhesion: A Critical Review. *J. Adhes. Sci. Technol.* **1992**, *6*, 1269-1302.

2. Kwok, D. Y.; Neumann, A. W., Contact Angle Measurement and Contact Angle Interpretation. *Adv. Colloid Interface Sci.* **1999**, *81*, 167-249.

3. Kamegawa, T.; Yamahana, D.; Yamashita, H., Graphene Coating of Tio2 Nanoparticles Loaded on Mesoporous Silica for Enhancement of Photocatalytic Activity. *J. Phys. Chem. C* **2010**, *114*, 15049-15053.

4. He, P.; Li, L.; Yu, J.; Huang, W.; Yen, Y.-C.; Lee, L. J.; Yi, A. Y., Graphene-Coated Si Mold for Precision Glass Optics Molding. *Opt. Lett.* **2013**, *38*, 2625-2628.

5. Podila, R.; Moore, T.; Alexis, F.; Rao, A. M., Graphene Coatings for Enhanced Hemo-Compatibility of Nitinol Stents. *RSC Advances* **2013**, *3*, 1660-1665.

6. Singh Raman, R. K.; Chakraborty Banerjee, P.; Lobo, D. E.; Gullapalli, H.; Sumandasa, M.; Kumar, A.; Choudhary, L.; Tkacz, R.; Ajayan, P. M.; Majumder, M., Protecting Copper from Electrochemical Degradation by Graphene Coating. *Carbon* **2012**, *50*, 4040-4045.

7. Wang, S.; Zhang, Y.; Abidi, N.; Cabrales, L., Wettability and Surface Free Energy of Graphene Films. *Langmuir* **2009**, *25*, 11078-11081.

8. Yin, J.; Li, X.; Yu, J.; Zhang, Z.; Zhou, J.; Guo, W., Generating Electricity by Moving a Droplet of Ionic Liquid Along Graphene. *Nat. Nanotechnol.* **2014**, *9*, 378-383.

9. Kim, H.-Y.; dos Santos, M. C.; Cole, M. W., Wetting Transitions of Water on Graphite and Graphene. *J. Phys. Chem. A* **2014**, *118*, 8237-8241.

10. Li, H.; Zeng, X. C., Wetting and Interfacial Properties of Water Nanodroplets in Contact with Graphene and Monolayer Boron–Nitride Sheets. *ACS Nano* **2012**, *6*, 2401-2409.

11. Li, Z.; Wang, Y.; Kozbial, A.; Shenoy, G.; Zhou, F.; McGinley, R.; Ireland, P.; Morganstein, B.; Kunkel, A.; Surwade, S. P., et al., Effect of Airborne Contaminants on the Wettability of Supported Graphene and Graphite. *Nat. Mater.* **2013**, *12*, 925-931.

12. Ma, M.; Tocci, G.; Michaelides, A.; Aeppli, G., Fast Diffusion of Water Nanodroplets on Graphene. *Nat. Mater.* **2016**, *15*, 66-71.

13. Rafiee, J.; Mi, X.; Gullapalli, H.; Thomas, A. V.; Yavari, F.; Shi, Y.; Ajayan, P. M.; Koratkar, N. A., Wetting Transparency of Graphene. *Nat. Mater.* **2012**, *11*, 217-222.

14. Raj, R.; Maroo, S. C.; Wang, E. N., Wettability of Graphene. *Nano Lett.* **2013**, *13*, 1509-1515.

15. Sergi, D.; Scocchi, G.; Ortona, A., Molecular Dynamics Simulations of the Contact Angle between Water Droplets and Graphite Surfaces. *Fluid Phase Equilib.* **2012**, *332*, 173-177.

16. Shih, C.-J.; Strano, M. S.; Blankschtein, D., Wetting Translucency of Graphene. *Nat. Mater.* **2013**, *12*, 866-869.

17. Taherian, F.; Marcon, V.; van der Vegt, N. F. A.; Leroy, F., What Is the Contact Angle of Water on Graphene? *Langmuir* **2013**, *29*, 1457-1465.

18. Xu, K.; Heath, J. R., Wetting: Contact with What? *Nat. Mater.* **2013**, *12*, 872-873.

19. Werder, T.; Walther, J. H.; Jaffe, R. L.; Halicioglu, T.; Koumoutsakos, P., On the Water−Carbon Interaction for Use in Molecular Dynamics Simulations of Graphite and Carbon Nanotubes. *J. Phys. Chem. B* **2003**, *107*, 1345-1352.

20. Aparicio, S.; Atilhan, M.; Karadas, F., Thermophysical Properties of Pure Ionic Liquids: Review of Present Situation. *Ind. Eng. Chem. Res.* **2010**, *49*, 9580-9595.

21. Burt, R.; Birkett, G.; Zhao, X. S., A Review of Molecular Modelling of Electric Double Layer Capacitors. *Phys. Chem. Chem. Phys.* **2014**, *16*, 6519-6538.

22. Uesugi, E.; Goto, H.; Eguchi, R.; Fujiwara, A.; Kubozono, Y., Electric Double-Layer Capacitance between an Ionic Liquid and Few-Layer Graphene. *Sci. Rep.* **2013**, *3*, 1595.

23. Tamilarasan, P.; Ramaprabhu, S., Graphene Based All-Solid-State Supercapacitors with Ionic Liquid Incorporated Polyacrylonitrile Electrolyte. *Energy* **2013**, *51*, 374-381.

24. Lei, Z.; Liu, Z.; Wang, H.; Sun, X.; Lu, L.; Zhao, X. S., A High-Energy-Density Supercapacitor with Graphene-Cmk-5 as the Electrode and Ionic Liquid as the Electrolyte. *J. Mater. Chem. A* **2013**, *1*, 2313-2321.

25. Feng, G.; Li, S.; Presser, V.; Cummings, P. T., Molecular Insights into Carbon Supercapacitors Based on Room-Temperature Ionic Liquids. *J. Phys. Chem. Lett.* **2013**, *4*, 3367-3376.

26. Salanne, M.; Rotenberg, B.; Naoi, K.; Kaneko, K.; Taberna, P. L.; Grey, C. P.; Dunn, B.; Simon, P., Efficient Storage Mechanisms for Building Better Supercapacitors. *Nat. Energy* **2016**, *1*, 16070-10.

27. Fedorov, M. V.; Kornyshev, A. A., Ionic Liquid near a Charged Wall: Structure and Capacitance of Electrical Double Layer. *J. Phys. Chem. B* **2008**, *112*, 11868-11872.

28. Fedorov, M. V.; Kornyshev, A. A., Towards Understanding the Structure and Capacitance of Electrical Double Layer in Ionic Liquids. *Electrochim. Acta* **2008**, *53*, 6835-6840.

29. Kondrat, S.; Kornyshev, A. A., Pressing a Spring: What Does It Take to Maximize the Energy Storage in Nanoporous Supercapacitors? *Nanoscale Horiz.* **2016**, *1*, 45-52.

30. Kondrat, S.; Wu, P.; Qiao, R.; Kornyshev, A. A., Accelerating Charging Dynamics in Subnanometre Pores. *Nat. Mater.* **2014**, *13*, 387-393.

31. Batchelor, T.; Cunder, J.; Fadeev, A. Y., Wetting Study of Imidazolium Ionic Liquids. *J. Colloid Interface Sci.* **2009**, *330*, 415-420.

32. Dubois, P.; Marchand, G.; Fouillet, Y.; Berthier, J.; Douki, T.; Hassine, F.; Gmouh, S.; Vaultier, M., Ionic Liquid Droplet as E-Microreactor. *Anal. Chem.* **2006**, *78*, 4909-4917.

33. Krumpfer, J. W.; Bian, P.; Zheng, P.; Gao, L.; McCarthy, T. J., Contact Angle Hysteresis on Superhydrophobic Surfaces: An Ionic Liquid Probe Fluid Offers Mechanistic Insight. *Langmuir* **2011**, *27*, 2166-2169.

34. Liu, Y.; Zhang, Y.; Wu, G.; Hu, J., Coexistence of Liquid and Solid Phases of Bmim-Pf6 Ionic Liquid on Mica Surfaces at Room Temperature. *J. Am. Chem. Soc.* **2006**, *128*, 7456-7457.

35. Millefiorini, S.; Tkaczyk, A. H.; Sedev, R.; Efthimiadis, J.; Ralston, J., Electrowetting of Ionic Liquids. *J. Am. Chem. Soc.* **2006**, *128*, 3098-3101.

36. Nanayakkara, Y. S.; Moon, H.; Payagala, T.; Wijeratne, A. B.; Crank, J. A.; Sharma, P. S.; Armstrong, D. W., A Fundamental Study on Electrowetting by Traditional and Multifunctional Ionic Liquids: Possible Use in Electrowetting on Dielectric-Based Microfluidic Applications. *Anal. Chem.* **2008**, *80*, 7690-7698.

37. Paneru, M.; Priest, C.; Sedev, R.; Ralston, J., Static and Dynamic Electrowetting of an Ionic Liquid in a Solid/Liquid/Liquid System. *J. Am. Chem. Soc.* **2010**, *132*, 8301-8308.

38. Herrera, C.; García, G.; Atilhan, M.; Aparicio, S., Nanowetting of Graphene by Ionic Liquid Droplets. *J. Phys. Chem. C* **2015**.

39. Taherian, F.; Leroy, F.; Heim, L.-O.; Bonaccurso, E.; van der Vegt, N. F. A., Mechanism for Asymmetric Nanoscale Electrowetting of an Ionic Liquid on Graphene. *Langmuir* **2016**, *32*, 140-150.

40. Baldelli, S.; Bao, J.; Wu, W.; Pei, S.-s., Sum Frequency Generation Study on the Orientation of Room-Temperature Ionic Liquid at the Graphene–Ionic Liquid Interface. *Chem. Phys. Lett.* **2011**, *516*, 171-173.

41. Baldelli, S., Interfacial Structure of Room-Temperature Ionic Liquids at the Solid–Liquid Interface as Probed by Sum Frequency Generation Spectroscopy. *J. Phys. Chem. Lett.* **2012**, *4*, 244-252.

42. Xu, S.; Xing, S.; Pei, S.-S.; Baldelli, S., Sum Frequency Generation Spectroscopy Study of an Ionic Liquid at a Graphene-Baf2 (111) Interface. *J. Phys. Chem. B* **2014**, *118*, 5203-5210.

43. Peng, H.; Nguyen, A. V.; Birkett, G. R., Determination of Contact Angle by Molecular Simulation Using Number and Atomic Density Contours. *Mol. Simul.* **2012**, *38*, 945-952.

44. Hess, B.; Kutzner, C.; Van Der Spoel, D.; Lindahl, E., Gromacs 4: Algorithms for Highly Efficient, Load-Balanced, and Scalable Molecular Simulation. *J. Chem. Theory Comput.* **2008**, *4*, 435-447.

45. Merlet, C.; Salanne, M.; Rotenberg, B., New Coarse-Grained Models of Imidazolium Ionic Liquids for Bulk and Interfacial Molecular Simulations. *J. Phys. Chem. C* **2012**, *116*, 7687-7693.

46. Cole, M. W.; Klein, J. R., The Interaction between Noble Gases and the Basal Plane Surface of Graphite. *Surf. Sci.* **1983**, *124*, 547-554.

47. Nosé, S., A Unified Formulation of the Constant Temperature Molecular Dynamics Methods. *J. Chem. Phys.* **1984**, *81*, 511-9.

48. Hoover, W. G., Canonical Dynamics: Equilibrium Phase-Space Distributions. *Phys. Rev. A* **1985**, *31*, 1695-1697.

49. Ewald, P., Evaluation of Optical and Electrostatic Lattice Potentials. *Ann. Phys.* **1921**, *64*, 253-287.

50. Santiso, E.; Herdes, C.; Müller, E., On the Calculation of Solid-Fluid Contact Angles from Molecular Dynamics. *Entropy* **2013**, *15*, 3734.

51. Smith, A. M.; Lovelock, K. R. J.; Gosvami, N. N.; Licence, P.; Dolan, A.; Welton, T.; Perkin, S., Monolayer to Bilayer Structural Transition in Confined Pyrrolidinium-Based Ionic Liquids. *J. Phys. Chem. Lett.* **2013**, *4*, 378-382.

52. Elbourne, A.; McDonald, S.; Voïchovsky, K.; Endres, F.; Warr, G. G.; Atkin, R., Nanostructure of the Ionic Liquid–Graphite Stern Layer. *ACS Nano* **2015**, *9*, 7608-7620.

53. Mezger, M.; Roth, R.; Schröder, H.; Reichert, P.; Pontoni, D.; Reichert, H., Solid-Liquid Interfaces of Ionic Liquid Solutions—Interfacial Layering and Bulk Correlations. *J. Chem. Phys.* **2015**, *142*, 164707-8.

54. Blake, T. D.; Clarke, A.; De Coninck, J.; de Ruijter, M. J., Contact Angle Relaxation During Droplet Spreading: Comparison between Molecular Kinetic Theory and Molecular Dynamics. *Langmuir* **1997**, *13*, 2164-2166.

55. Köddermann, T.; Paschek, D.; Ludwig, R., Molecular Dynamic Simulations of Ionic Liquids: A Reliable Description of Structure, Thermodynamics and Dynamics. *ChemPhysChem* **2007**, *8*, 2464-2470.

56. Hayes, R.; Warr, G. G.; Atkin, R., Structure and Nanostructure in Ionic Liquids. *Chem. Rev.* **2015**, *115*, 6357-6426.

57. Rotenberg, B.; Salanne, M., Structural Transitions at Ionic Liquids Interfaces. *J. Phys. Chem. Lett.* **2015**, *6*, 4978-4985.

7. Impact of applied potential on the electrowetting of carbon surfaces by highly concentrated electrolytes

In this chapter we have performed molecular dynamics simulations of the electrowetting behaviour of drops containing mixtures of the room temperature ionic-liquid 1-ethyl-3-methylimidazolium tetrafluoroborate and acetonitrile on a carbon surface with varying applied potentials. On an uncharged surface, the increase of acetonitrile concentration continuously reduces the contact angle as the solvent screens the ion-ion interactions. The pure ionic-liquid drop displays a negligible response to electrowetting over the simulated potential range of –5 to +5 V. This lack of contact angle sensitivity is attributed to the number of charged carbon atoms in the electrode remaining almost constant with increasing potential. Due to ion-size effects, the ionic liquid at the negative electrode is less structured and does not form the same well-defined layers as the ones observed at the positive electrode, possibly indicating the cause of contact angle asymmetry observed in experiments. In the presence of acetonitrile, no variation in contact angle was observed at 4 V over the range of concentrations simulated, despite changes in the charge-density profiles of the drops.

7.1. Introduction

Electrowetting involves decreasing the contact angle of a liquid by applying an electric potential to a solid substrate. Electrowetting can temporarily increase the wettability of a phobic surface whilst maintaining its chemical properties. The voltage applied is limited to the electrochemical window of the liquid.[1] For electrowetting on a dielectric surface (EWOD), greatly increased electric potential is needed compared to a conductive surface.[1] The EWOD contact angle can be derived from combining Young's equation and Lippmann's equation (YLE), equation (7-1):[2-3]

$$\cos\theta = \cos\theta_0 + \frac{U^2}{2\gamma_{lv}}\frac{dC}{dA_{sl}} \tag{7-1}$$

where θ and θ_0 are the contact angle at the applied voltage and zero-voltage, respectively, γ is liquid-vapour tension, U is applied voltage, and C is the total capacitance for the solid-liquid contact area, A_{sl}. As described by Choudhuri et al.,[2] C is usually proportional to the A_{sl} for conducting liquids, but the differential form is more appropriate for nanodrops in which some electrical charge is stored in the liquid phase. In the case of electrowetting directly on a conductive surface, no such predictive relation exists.

Aqueous solutions are commonly used as electrowetting agents, however these electrolytes can be problematic due to solvent evaporation, low thermal stability, and low voltage window.[4] Ionic liquids (ILs) have a wider electrochemical window,[5] they also have other favourable properties such as low vapour pressure[6] and low toxicity.[7] They are emerging electrowetting candidates due to the aforementioned thermodynamic properties as well as having good reversibility.[4, 8] ILs may be suitable for traditional electrowetting applications such as displays,[9] fluid-lens systems,[10] and for controlling fluid-flow in multiple phase channel configurations.[11]

Understanding the nanostructure and wetting behaviour of ILs is critical for further developing their use in electrowetting applications. MD simulations have shown that for a graphite/bulk IL interface, dense IL layers form, and the imidazolium rings on the cation lay preferentially flat on an uncharged graphite surface.[12] When an electrode charge is introduced the density of co-ions in the first layer are greatly reduced.[13-14] Addition of acetonitrile (ACN) solvent to the IL has been shown to homogenise differences in ion size and asymmetry effects, and produce similar adsorption profiles.[15]

EWOD experiments of ILs have shown that the contact angle profile is asymmetric with electrode potential, and that the contact angle-voltage saturation point is dependent on the ions size and specific IL structure.[4, 8] When an immiscible IL is diluted with water, the EWOD contact angle has also been shown to have no dependence on water concentration, despite the alteration of thermodynamic properites.[4, 16] Interestingly, when immersing the IL 1-butyl-3-methylimidazolium tetrafluoroborate (BMIM-BF_4) in non-polar *n*-hexadecane, Paneru et al.[17] showed that the EWOD is greatly enhanced with applied potential. This was attributed to the reduction in the surface tension when replacing the IL/air layer with an IL/liquid layer.

Liu et al.[18] showed via MD simulations that the YLE applies to EWOD of linear Lennard-Jones molecules at low voltages. Saturation occurred at higher charge density and molecules were expelled from the drop. Taherian et al.[19] used MD simulation of BMIM-BF_4 bridged between conductive graphene surfaces with uniform and constant partial charges. Their simulations were repeating (infinite) in one of the two dimensions parallel to the surfaces, eliminating line tension and allowing 2D contact angles to be calculated. Their simulations showed asymmetric electrowetting contact angle which could not be explained by the solid-liquid interfacial free energy or the YLE. The asymmetry was explained by structural and packing effects of the ions at the charged surfaces.

In general, many of the above EWOD studies display characteristic similarities with three distinct regions for the variation of contact angle with applied potential: unresponsive, responsive, and saturated. Firstly, an unresponsive/unchanging contact angle centred at 0 V which extends approximately to 20 V in both the positive and negative directions. Beyond 20 V, a spontaneous reduction in the contact angle occurs in the responsive region. The extent in contact angle reduction is between 10 – 15 degrees before the saturation point is reached at high voltage (± 50 V or beyond) and normal contact angle behaviour no longer applies. Explaining the molecular origin of the heterogeneity characteristically displayed in EWOD curves is difficult to achieve with experimental methods. MD simulations are suitable to provide additional insight, however there are finite size effects that limit the directness of comparisons that can be made. The recent simulations by Taherian et al.[19] offer interesting molecular mechanisms for asymmetric wetting behaviour, however their use of constant partial charges on the electrode atoms may lead to significant deviations with respect to real electrodes.[20] Here we attempt to investigate the suitability of the constant potential method for electrowetting simulations over the constant charge method. The main aspect of these

simulations is to allow the electrode atoms charges to fluctuate in response to the adsorbed electrolyte.

In this chapter we present molecular dynamics simulations of drops of the IL 1-ethyl-3-methylimidazolium tetrafluoroborate (EMIM-BF_4), and super-concentrated mixtures with ACN, on a weakly interacting carbon surface with no charge, constant charges, and at applied constant electric potentials, where the surface partial charges fluctuate and are calculated at each simulation time step. An example of the electrowetting set up is given in Figure 7-1.

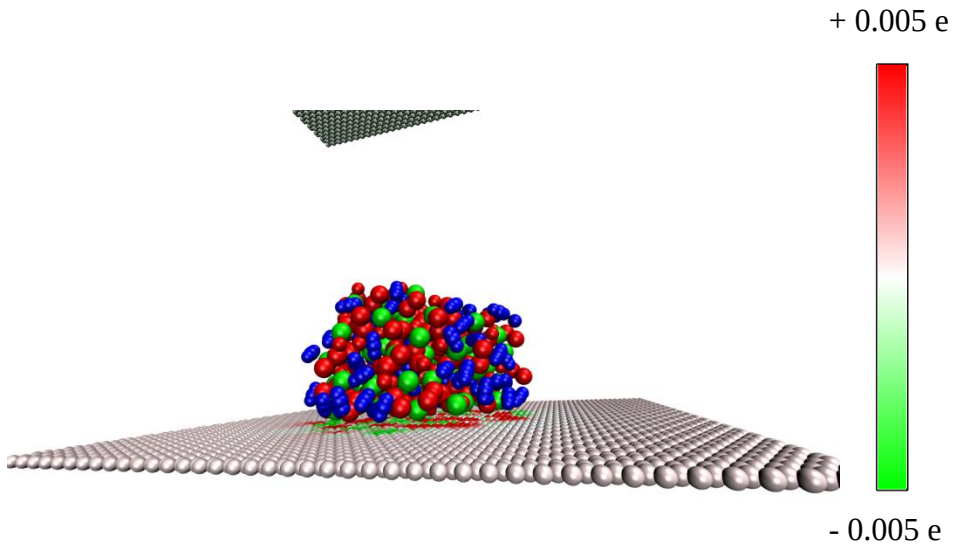

Figure 7-1: Simulation snapshot of an EMIM-BF_4 and ACN drop (20 % mass ACN) on the surface of the positive electrode. Green molecules are BF_4^- anions, red molecules are $EMIM^+$ cations, and blue molecules are ACN solvent. The IL and electrode atoms are shown with a colour scale (right) where positive charges are red and negative charges are green. It can be seen that the electrode accumulates charge directly beneath the drop, and the remaining atoms have close to neutral charges. A section of the negative electrode is also shown for perspective.

7.2. Methodology

Simulations containing uncharged carbon sheets were performed using the MD package Gromacs.[21] Coarse-grained molecular models for $EMIMBF_4$ and ACN were used from Merlet et al.[22] and Edwards et al.[23] respectively. For the carbon Lennard-Jones parameters, σ was maintained at the regular value of 0.337 nm,[24] but the well depth (ε) was reduced to 0.05 kJ mol^{-1} so the solid-liquid interaction was weakened. Lennard-Jones interaction ($\varphi(r)$) was calculated from equation (7-2), and Lorentz-Berthelot mixing rules from equations (7-3) and (7-4):

$$\varphi\left(r_{ij}\right)=4\varepsilon_{ij}\left(\left(\frac{\sigma_{ij}}{r_{ij}}\right)^{12}-\left(\frac{\sigma_{ij}}{r_{ij}}\right)^{6}\right) \tag{7-2}$$

$$\sigma_{ij}=\frac{1}{2}\left(\sigma_{ii}+\sigma_{jj}\right) \tag{7-3}$$

$$\varepsilon_{ij}=\left(\varepsilon_{ii}\varepsilon_{jj}\right)^{\frac{1}{2}} \tag{7-4}$$

Four different drop compositions were considered, with the number of molecules for the different drops given in Table 7-1. For the surface, a carbon sheet was used with *x* and *y* dimensions of 9.84 and 8.96 nm respectively, where atoms were arranged in a hexagonal structure with atomic spacing of 0.142 nm.

Table 7-1. Number of IL pairs and solvent molecules, with the IL concentration

ACN fraction (% mass)	IL conc. (mol L^{-1})	IL molecules	ACN molecules
0	6.40	100	0
10	5.28	71	38
20	4.58	73	88
40	3.01	70	225

Boxes of electrolyte were equilibrated separately in the NPT ensemble at 298 K. The boxes were then placed above the surface and equilibrated for 0.5 ns in the 3D periodic NVT ensemble. The temperature was maintained by a Nose-Hoover[25-26] thermostat with long range particle mesh Ewald (PME) summations[27] being performed for electrostatics. A short range cut-off distance of 1.2 nm was used for Lennard-Jones and electrostatic calculations. Production runs were then run for 15 ns, sampling positions every 2 ps. A pure ACN drop simulation was also conducted under the same conditions for reference.

Electrowetting simulations were performed using an in-house MD program so that a constant electric potential could be maintained between two electrodes using Metalwalls,[28-29] with configurations from the uncharged-surface production runs used as the inputs. For the pure IL drop, 11 voltages were considered: 0V, ± 2 V, ± 3 V, ± 4 V, ± 5 V and ± 6.5 V. In each case the drops were simulated separately on the surface of the positive electrode and negative electrode, except for the 0 V which was only simulated on the single electrode. Three

constant charge simulations were performed with constant atomic charges applied to the carbon electrodes, 0, ± 0.00833, and ± 0.00131 e.

Drops with 10, 20 and, 40 % mass ACN were also simulated at 4 V on the surface of the positive electrode, and the temperature was maintained by velocity rescaling for equilibration before production runs which were run in the NVE ensemble at 298 K. The distance between the electrodes was set to 10 nm for all systems. Production runs were performed for at least 10 ns, with some systems run for longer to improve the statistical sampling. The contact angle was averaged in 1 ns blocks. A snapshot of the electrowetting setup is shown in Figure 7-1.

7.3. Discussion

7.3.1. Drops with ACN solvent on an uncharged surface

ACN is a commonly used solvent for dissolving organic ions.[30-31] There are many studies of solid-liquid interfaces involving mixtures of ILs and ACN,[15, 32-33] but comparatively the influence of ACN concentration in the electrolyte at solid-liquid-vapour interfaces have been far less reported. Its effect on the contact angle of IL drops at uncharged and charged surface remains relatively unknown, therefore this chapter firstly addresses ACN concentration at an uncharged weakly-interacting carbon surface.

The contact angle was averaged in 5 ns blocks, and calculated using a method consistent with our previous publication where polynomials are fitted to isochors of two-dimensional r-z atomic density contour profiles.[34] This enables the contact angle to be calculated at multiple heights of the drop (z_θ^*). In this chapter, data below z_θ^* = 1 was excluded from the polynomial fitting, and the contact angles were reported at z_θ^* = 1 to reduce the influence of statistical fluctuations and get a clearer indication of the contact angle trends.

Increasing the fraction of ACN in the IL drop results in a non-linear decrease in the contact angle, as seen in Figure 7-2. When extended to a drop of pure ACN, the rate of contact angle decrease remains relatively constant, and total difference in contact angle between drops of pure $EMIMBF_4$ and ACN is only 25 ± 3 degrees.

Figure A7-7 and A7-8 of Appendix A7 show that the layering structure of the drops becomes more homogeneous with ACN concentration. However, ion-size effects are still retained in the first two adsorbed layers. Interestingly, the contact angle of drops with IL/solvent mixtures decreases more than expected by mass weighted averages of the pure IL and ACN

systems, and the deviation is greater at the sheet surface, as can be seen in Figure A7-9 of Appendix A7.

This non-linear dependence indicates that even at low fractions, ACN can reduce the ion-ion correlations significantly in the interfacial region of the drop. ACN has a weak interaction with the surface, compared with the IL, and most likely it more significantly affects the liquid-vapour interface. However correlating this phenomenon to surface tension is difficult, due to the lack of mixture data for this specific combination of IL and solvent. Pure $EMIMBF_4$ has a liquid-vapour surface tension of approximately 44 – 54 mN m^{-1} at 298 K,[35-40] and pure ACN 28.4 mN m^{-1}.[41]

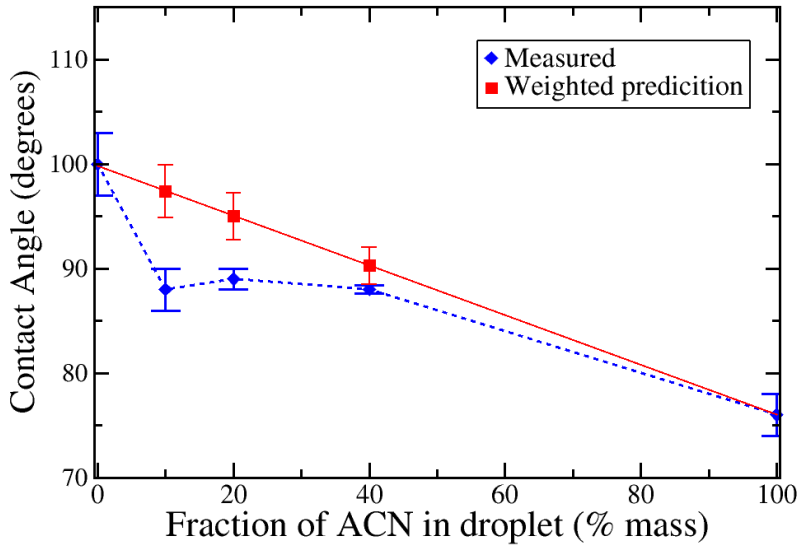

Figure 7-2: Contact angle with increasing ACN fraction in the drops. Zero percent refers to pure $EMIMBF_4$. The Blue diamonds are the contact angles as measured at $z_\theta^* = 1$, where the coordinates are reduced by 0.34 nm. The red squares are the predicted contact angles for the mixtures by mass weighted averages of the pure systems' contact angles. Uncertainties are one standard deviation of the mean, this is repeated in the subsequent figures.

Unfortunately there is no direct experimental data to compare to, but a reasonable comparison can be made from Rilo et al.,[38] who reported the surface tension of mixtures of $EMIMBF_4$ and ethanol. Over an IL mol fraction of 1 – 0.5 (0 – 20 % mass ethanol for comparison here), they found a linear reduction in the surface tension from 53 to 28 nM m^{-1}, which does not correlate to the contact angle response observed here over the same solvent concentration range. One explanation is that as ACN is a polar aprotic solvent, whereas as ethanol is polar protic, the solvation behaviour will be different due to the lack of hydrogen bonding of solvent to anion, resulting in equal dissociation of both ion species in ACN. Of course, correlating the contact angle trend to solely the liquid-vapour surface tension is not sufficient as the solvent molecules will also affect the solid-liquid surface tension. Nevertheless, it is

difficult to find a satisfactory explanation for the non-linearity observed. Certainly, further investigation of the vapour-liquid interface with highly concentrated solutions of ILs in ACN would be of interest in the future.

7.3.2. Electrowetting of pure IL

The electrowetting properties of ILs are of great interest as outlined in the introduction above, yet whether the continuum behaviour of IL drops can be applied for nanoscale drops is not comprehensively studied, and explaining the observations of experimental EWOD studies remains difficult. Here this is examined within the limitations of MD simulations, at a range of potentials with the IL drop adsorbed directly onto the surface of the positive and negative electrodes, and the resulting contact angles are shown in Figure 7-3.

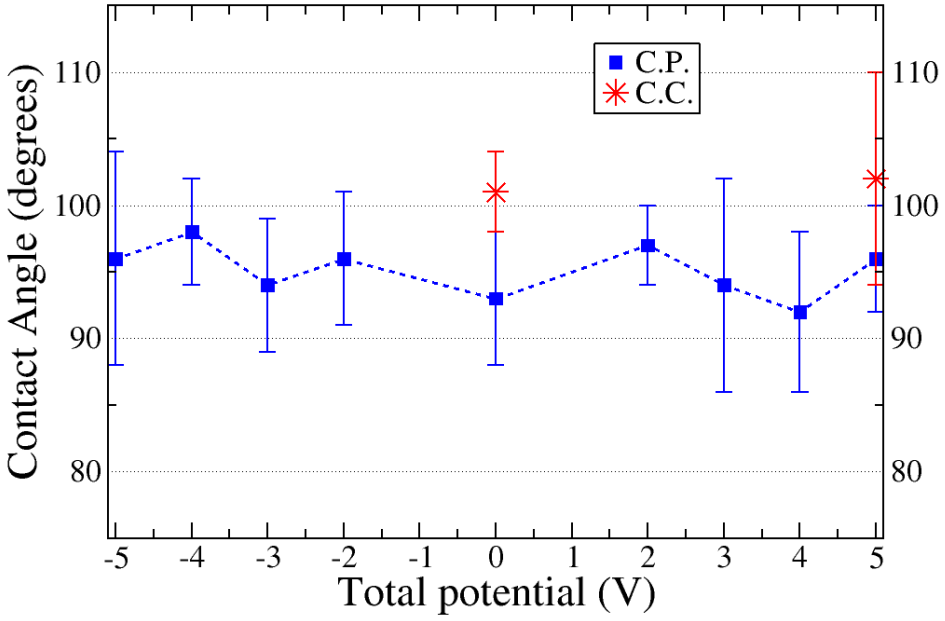

Figure 7-3: Electrowetting contact angle of pure IL drop measured at z_θ^* = 1. The potential on the x-axis refers to total cell voltage, for positive (negative) values the drop is adsorbed to the surface of the positive (negative) electrode. The blue squares indicate simulations performed under constant electrode potential, and the red stars are the result for equivalent constant-charge simulations at that voltage.

More contact angles at different drop heights are given in Figure A7-10 of Appendix A7. Due to the finite size of simulations, it is not possible to directly replicate EWOD experiments. In particular the thickness of the dielectric would be prohibitively large, and application of a Pt-wire like electrode could also be problematic. For this reason a smaller voltage window was used here. We found 6.5 V (which corresponds to 0.065 V $Å^{-1}$ electric field strength) to be above the maximum applicable voltage before finite size effects, and contact angle saturation occurred, as shown in Figure A7-11 of Appendix A7. Therefore our maximum was limited to

± 5 V (0.05 V $Å^{-1}$). Direct comparison of the electric field strengths between our simulations and previous EWOD experiments is difficult as the latter do not publish the distance between their electrodes.

Contact angle values obtained from the simpler constant charge approach are also shown in Figure 7-3. They appear to overestimate this quantity compared to the constant potential method. Below, we attempt to explain this, and the weak reduction in contact angle over the region of simulated voltages, with electrode atom charge histograms and consideration of the position and number of charge carrying carbons relative to the drop (shown in Figure 7-1).

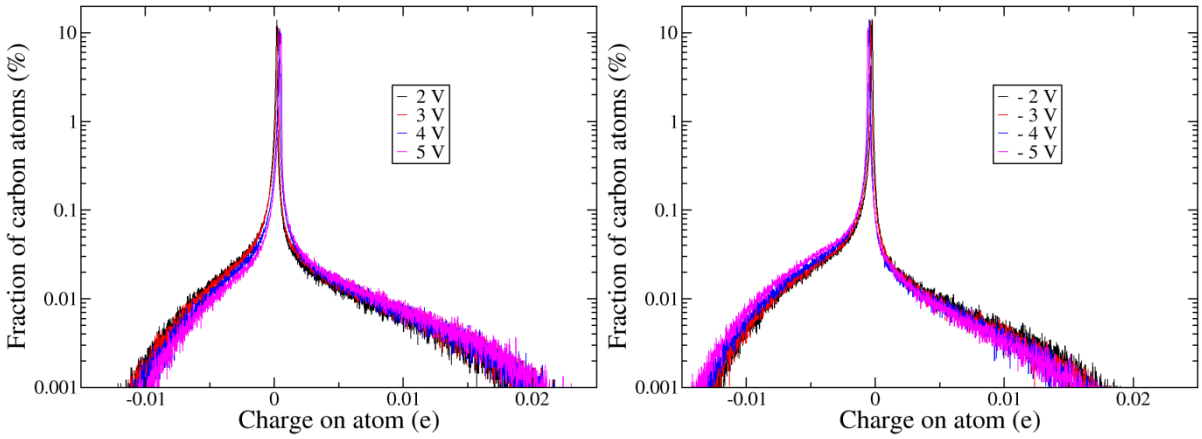

a b

Figure 7-4: Electrode charge histogram of the final nanosecond of simulation for drops adsorbed onto the positive electrode (a) and negative electrode (b). The histograms have been plotted on a log scale, in this way the number of carbons contributing to balancing the drop charge can be more easily seen. The electrode atom charges were sampled every 2 ps.

Figure 7-4 reveals the cause of the small variation in contact angle with applied potential. Despite the large change in potential, there was very little shift in the median charge of the electrodes. The positive electrode consistently has a greater proportion of highly charged atoms than the negative electrode. However, in both cases the increase in the number of highly charged atoms, and decrease in number of lowly charged atoms, with increasing potential, (i.e. a right shift at the positive electrode and left shift at the negative electrode) was too small to affect the contact angle significantly. Instead of the number of charge carrying carbons increasing significantly (which would mostly cause the drops to spread), the existing charge carrying atoms increase (or decrease) the magnitude of the charge that they carry. This means the electrode charge increases with potential but the area of charged atoms remains the same.

The total charge on the electrodes is given in Figure A7-12 of Appendix A7. The large difference observed between median charge and average charge indicates that modelling the

electrode by constant charges for electrowetting, such as that performed recently by Taherian et al.,[19] may result in incorrect behaviour. Under constant potential, the majority of electrode atoms do not contribute to balancing the charge of the IL drop. This can clearly be seen in the supporting information video 7-1. This is further supported by the larger contact angles observed for the constant charge simulations show in Figure 7-3, where the constant value at 5 V was 0.000833 e per atom for the positive electrode (Figure A7-12 of Appendix A7), which the drop was adsorbed onto. The balancing negative electrode charge was - 0.000833 e per atom to maintain electric neutrality. Using a value of 0.0131 e per atom (which is equivalent to the highest surface charge density simulated by Taherian et al.,[19] 8 μF cm^{-2}), we obtained a contact angle of 90 ± 5 degrees at z_{θ}^{*} = 1, which is a significant decrease from the contact angle at 0.000833 e but still within the range of constant-potential contact angles observed in Figure 7-3. In this regime co-ions were expelled from the drop and pulled to the negative electrode, indicating that contact angle saturation was reached, this behaviour is consistent with previous constant charge simulations.[18-19] As previously stated, simulations performed at a constant potential of ± 6.5 V, displayed finite size effects (and contact angle saturation). These potentials were approximately equivalent to surface charge densities of 8 μF cm^{-2} (Figure A7-12 of Appendix A7), which indicates that the constant potential method can capture contact angle saturation in a similar manner to the constant charge method, but better captures the electrode behaviour corresponding to the unresponsive contact angle regime observed in some EWOD experiments.[4, 8]

Direct differences between histograms of the drops adsorbed onto positive and negative sheets are given in Figure A7-13 of Appendix A7. It is clearly seen that the median values did not change significantly, but the differences in the number of high charge carrying, and low charge carrying atoms, were consistent. To investigate this difference further, fractional density profiles were calculated to examine the layering structure of the ions in the drop, and can be seen in Figure 7-5.

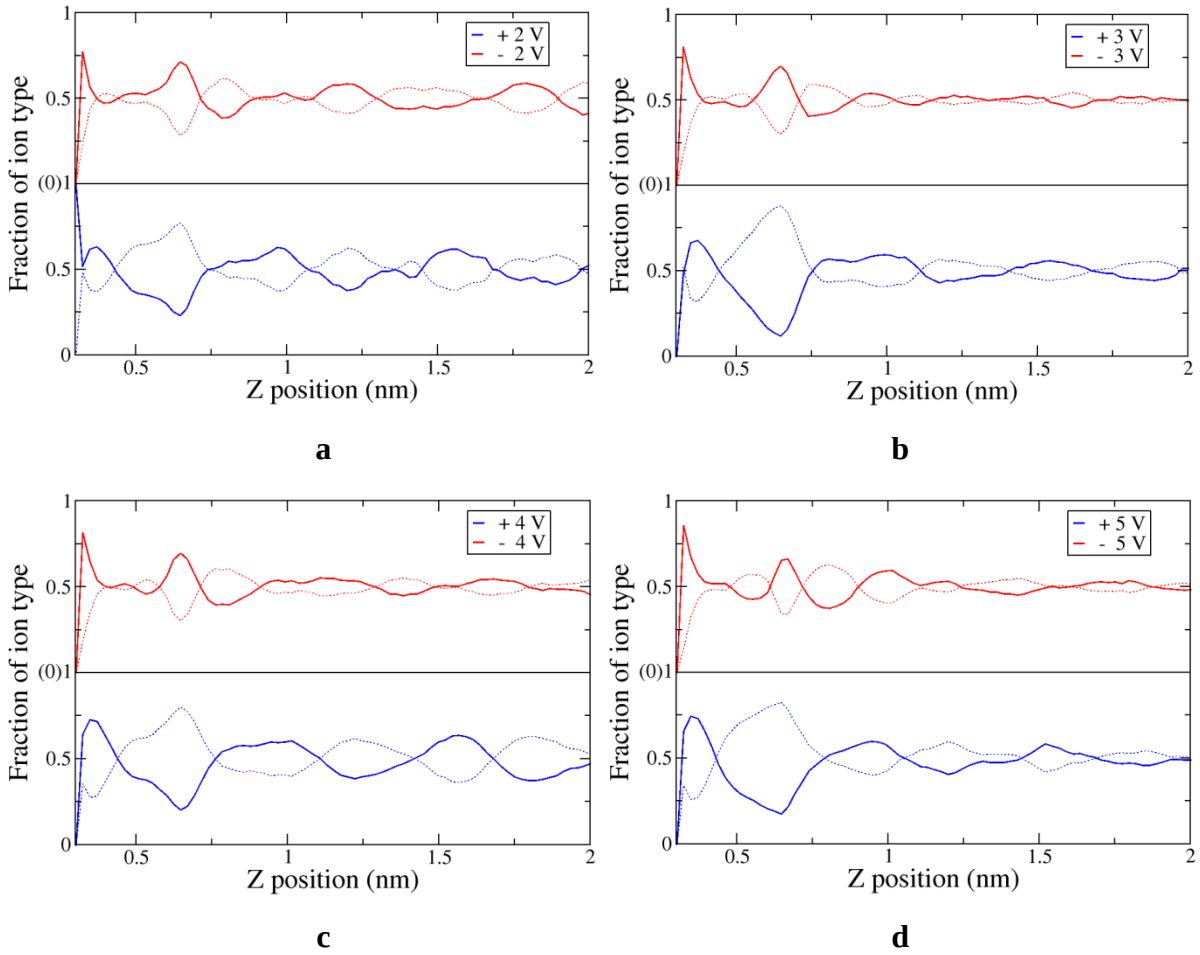

Figure 7-5: Fractional number density profiles for a pure IL drop adsorbed onto the positive (blue) and negative (red) electrode. (a) ± 2 V, (b) ± 3 V, (c) ± 4 V, (d) ± 5 V. Solid lines depict the counter-ions, and dotted lines the co-ions. Densities were calculated from the final nanosecond of production runs using the centre of mass of the ions and a bin depth of 0.023 nm.

Figure 7-5 shows that the drops display significantly different structures in all voltages tested. At the positive electrode, two distinct compositional-layers form within the first 0.75 nm, with the second layer being the largest. However, over the same region in the negative electrode, the layering is much smaller and more compact. Beyond the first two layers, the drops at the positive electrodes maintain more ordered profiles with oscillating ion-compositions, and this is less strongly observed for drops at the negative electrode. These observations are in agreement with Taherian et al.,[19] and the results here may also serve as a possible explanation for the asymmetry of contact angle saturation observed on the macroscale at high voltages,[8] as the ability (and extent) of the ions to rearrange in the drop in response to electric-potential may depend on the layering structure and corresponding strength of Coulombic interactions within the layers.

7.3.3. Electrowetting of IL/ACN mixtures

Finally, we combined electrowetting (at a total potential of 4 V) with ACN concentration in the drop to examine if the behaviour of IL/ACN drops changes under an applied electrowetting potential. As ACN is a non-polar molecule, it should not have strong Coulombic interactions with the electrode, however ACN will screen ion-ion correlations in the drop, and whether this will facilitate greater rearrangement of drop structure and contact angle reduction in response to the electrode potential is an interesting question. The electrowetting contact angles are displayed in Figure 7-6a.

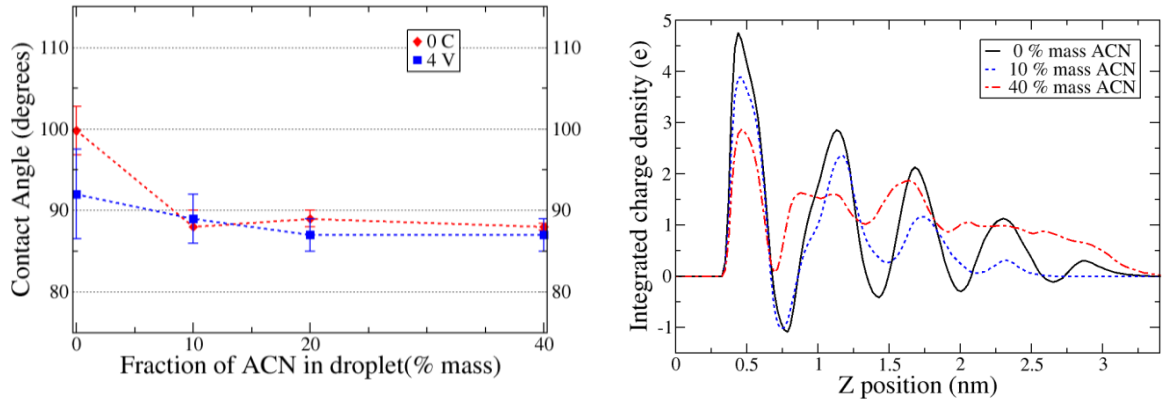

a b

Figure 7-6: (a) Electrowetting contact angle on the positive electrode (total potential is 4 V, zero charge contact angles from Figure 7-2 are given as the red diamonds for reference). Zero percent refers to pure $EMIMBF_4$. The blue squares are the contact angles measured at z_θ^* = 1. (b) Charge density profile of 4 V drops, 20 % mass ACN omitted for brevity.

From Figure 7-6a it can be seen that at the applied potential of 4 V, addition of ACN does not enable any change in the contact angle, even though the reduction in viscosity and ion-ion correlations should allow for greater rearrangements of ions in the drop. More contact angles at different heights are given in Figure A7-14 of Appendix A7.

Figure 7-6b shows the charge density profile of the drop with increasing fraction of ACN. In the first adsorbed layer, the peak in charge density reduced by 2 e from the pure IL to the 40 % mass ACN drop, this is equivalent to swapping approximately 1.3 ions, which is not enough to change the global structure of the drop. More interesting changes occur in the subsequent layers, the 10 % mass ACN drop closely matches the pure IL charges for the first three layers, then the charge oscillations dampen quickly in the remaining layers. In contrast the 40 % mass ACN drop displays a consistently positive charge profile with shallow troughs, and the positions of the peaks shift approximately 0.05 nm closer to the electrode surface, indicating that the layers are marginally more compact. To affect a change in the

contact angle, the first adsorbed layer mostly likely needs to change composition by several ion pairs, although ACN reduces the density of ions in the drop, it also increases their mobility by screening the strong ion-ion interactions, and allows the drop charges to restructure in a manner that results in equivalent contact angles.

7.4. Conclusions

In this chapter the electrowetting behaviour of $EMIMBF_4$ ionic liquid drops, and mixtures with ACN solvent, was studied on a weakly interacting carbon surface with positive, negative, and neutral electrode charges via molecular dynamics simulations. At a neutral surface, the results showed a continuous but non-linear reduction in contact angle with solvent concentration. However, the total difference in contact angle between pure IL and pure ACN was only 25 ± 3 degrees. For a pure IL drop, the electrowetting response was minor. At the z_θ^* = 1 the contact remained relatively constant around approximately 95 ± 5 degrees over the values tested between –5 V to +5 V. The unresponsiveness in contact angle with electrowetting was attributed to the number of carbon atoms in the electrode contributing to balancing the drop charge not increasing significantly with increased surface potential. Instead the magnitude of the charges carried by the carbon atoms increased. This result highlights the necessity of using fluctuating electrode charges when studying electrowetting response, as constant charge simulations do not capture the phenomenon that the majority of electrode atoms do not change their charge. Structural differences in the compositional-layering of the ions in the drops was observed at the positive and negative electrodes, which could provide a possible explanation for electrowetting asymmetry observed in IL drops on the macroscale.[8] Finally adding ACN into the drop when the electrowetting potential was 4 V resulted in no change in contact angle at the positive electrode, contrasting with the behaviour at the uncharged surface. This phenomenon warrants further investigation.

Appendix A7

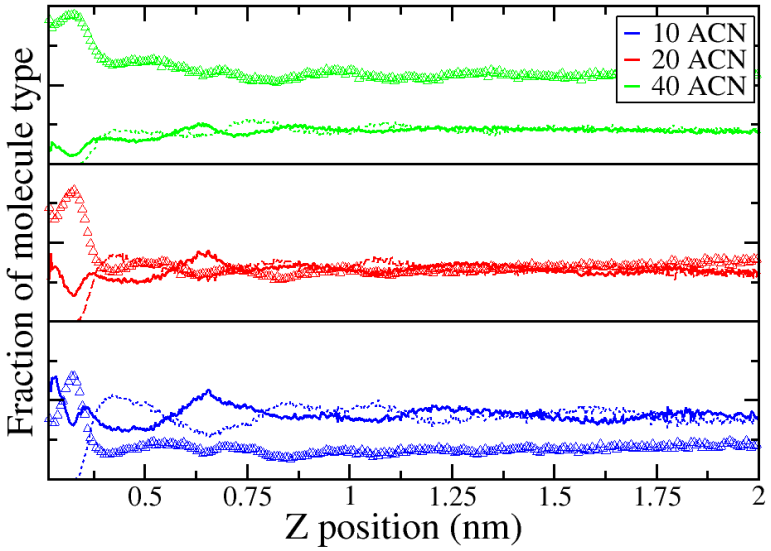

Figure A7-7: Fractional number density profiles of the molecule type in the drop. Solid lines are $EMIM^+$ cations, dotted lines are BF_4^- anions, and triangles are ACN molecules.

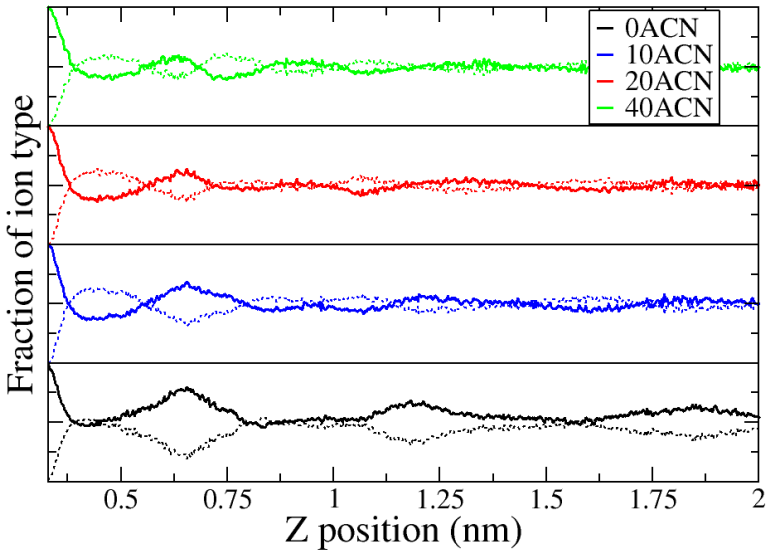

Figure A7-8: Fractional number density profiles of the ion type in the drop, with ACN excluded. Solid lines are $EMIM^+$ cations, dotted lines are BF_4^- anions.

Figures A7-7 and A7-8 show the incremental loss of layering with ACN concentration, the drop becomes more homogeneous.

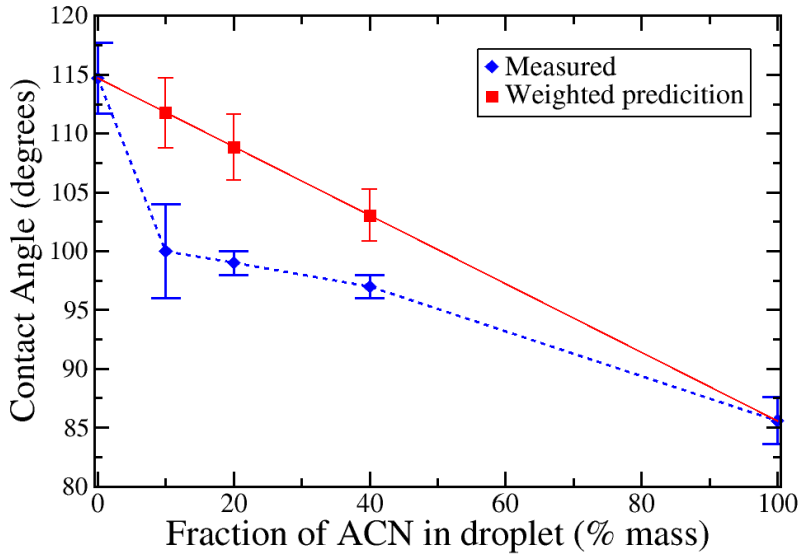

Figure A7-9: Contact angle with increasing ACN fraction in the drops. Zero percent refers to pure EMIMBF$_4$. The Blue diamonds are the contact angles as measured at the sheet surface. The red squares are the predicted contact angles for the mixtures by mass weighted averages of the pure systems' contact angles.

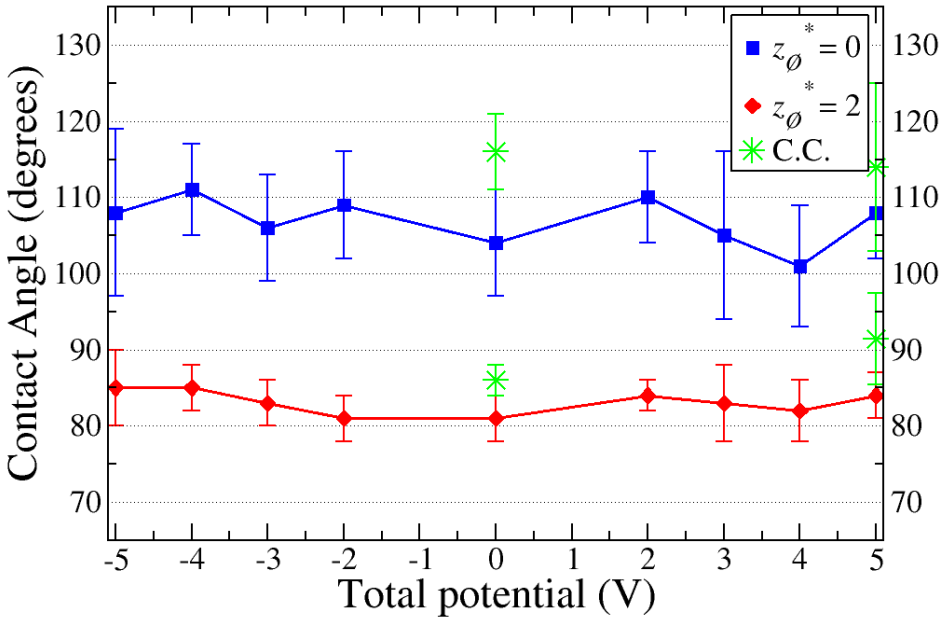

Figure A7-10: Electrowetting contact angle of pure IL drop. The blue squares are the contact angles measured at the sheet surface, and the red diamonds are at $z_{\theta}^{*} = 2$.

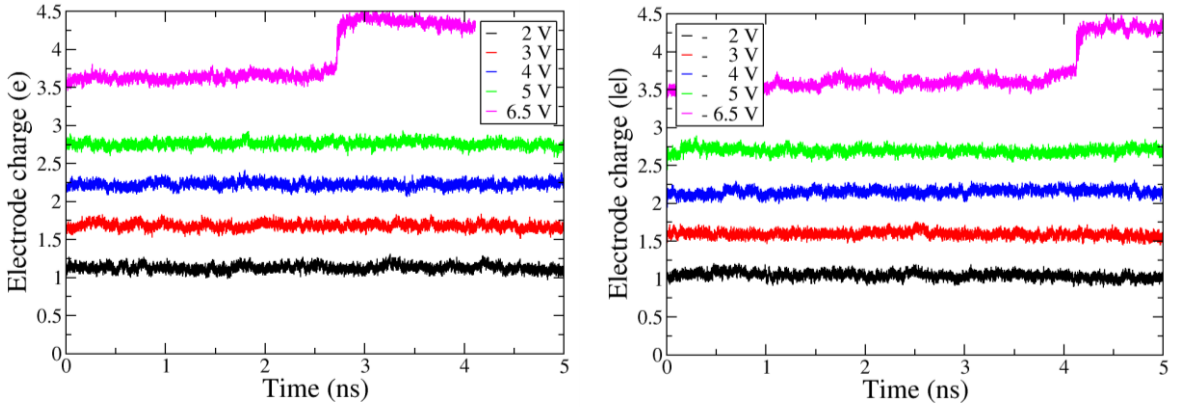

a **b**

Figure A7-11: Finite size of simulation indicates the maximum applied potential (or electric field strength) which can be used in our systems. The charge on each electrode is shown, (a) positive and (b) negative.

From Figure A7-11 it can be seen that at 6.5 V (purple line) where the electric field strength was 0.065 V $Å^{-1}$, the electrode charge spontaneously increased in both electrodes by approximately 1 e. This was a result of single co-ions being expelled from the drop. This is non-physical behaviour, and indicative of contact angle saturation in simulation. It shows the limit of potential which can be studied for our system. Therefore we limited the maximum voltage to be ± 5 V (or 0.05 V $Å^{-1}$ electric field).

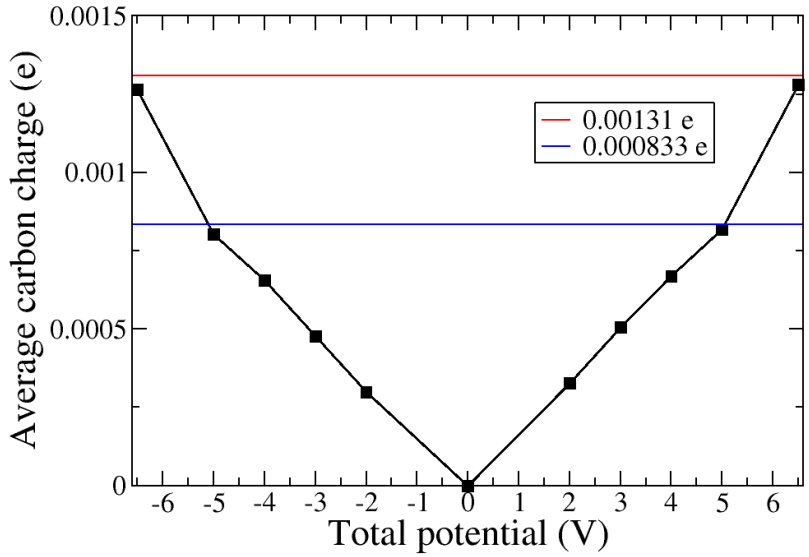

Figure A7-12: Electrode charge curve. The black line gives the average charge of the electrode atoms over the voltage range simulated. Constant charge values simulated are also included to indicate the equivalent constant potential voltage.

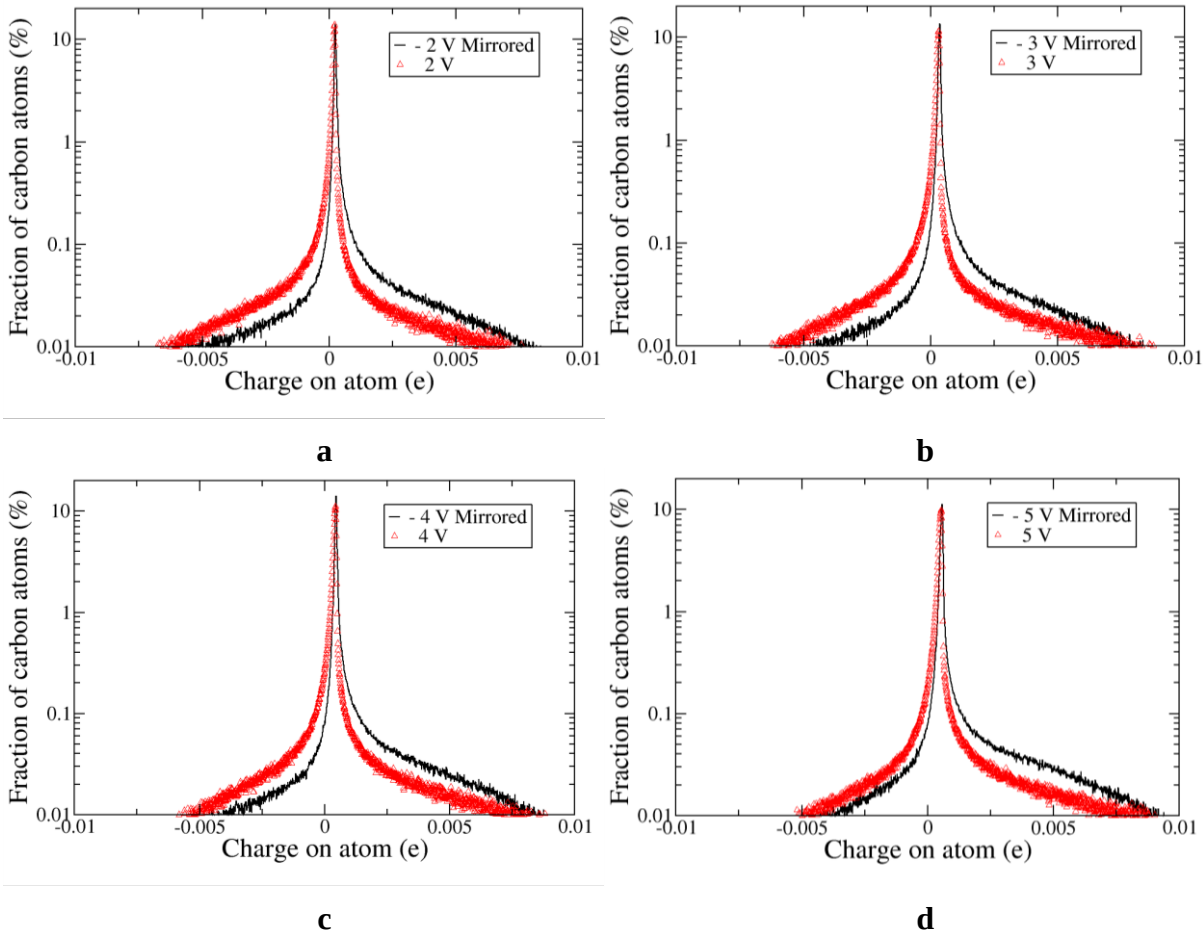

Figure A7-13: Electrode charge histogram of the final ns for the ± 2 V total simulations (a), ± 3 V total simulations (b), ± 4 V total simulations (c), and ± 5 V total simulations (d), with the pure IL drop adsorbed onto the positive and negative electrode. The simulations with the drops adsorbed onto the negative electrodes have been mirrored on the x-axis so that the charges can be compared.

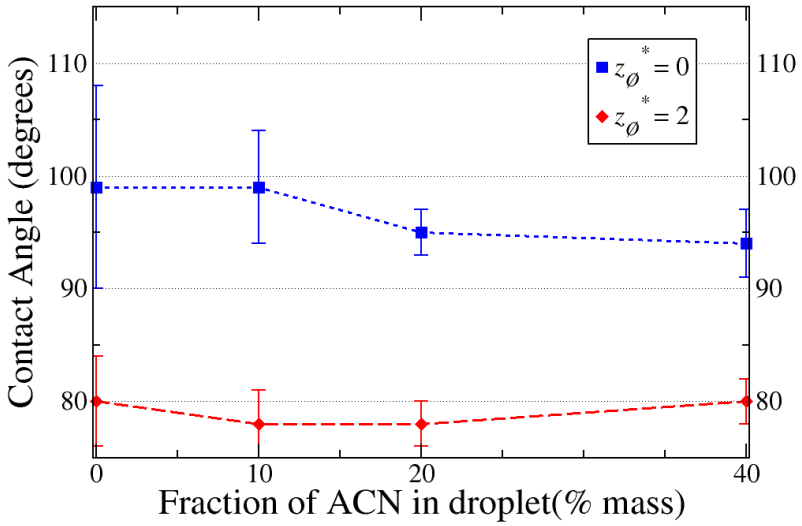

Figure A7-14: Electrowetting contact angle on the positive electrode (total potential is 4 V). Zero percent refers to pure $EMIMBF_4$. The blue squares are the contact angles measured at the sheet surface, and the red diamonds at $z_{\theta}^{*} = 2$.

7.5. References

1. Moon, H.; Cho, S. K.; Garrell, R. L.; Kim, C.-J. C., Low Voltage Electrowetting-on-Dielectric. *J. Appl. Phys.* **2002**, *92*, 4080-4087.

2. Choudhuri, J. R.; Vanzo, D.; Madden, P. A.; Salanne, M.; Bratko, D.; Luzar, A., Dynamic Response in Nanoelectrowetting on a Dielectric. *ACS Nano* **2016**, *10*, 8536-8544.

3. Shapiro, B.; Moon, H.; Garrell, R. L.; Kim, C.-J. C., Equilibrium Behavior of Sessile Drops under Surface Tension, Applied External Fields, and Material Variations. *J. Appl. Phys.* **2003**, *93*, 5794-5811.

4. Nanayakkara, Y. S.; Moon, H.; Payagala, T.; Wijeratne, A. B.; Crank, J. A.; Sharma, P. S.; Armstrong, D. W., A Fundamental Study on Electrowetting by Traditional and Multifunctional Ionic Liquids: Possible Use in Electrowetting on Dielectric-Based Microfluidic Applications. *Anal. Chem.* **2008**, *80*, 7690-7698.

5. Rogers, E. I.; Sljukić, B.; Hardacre, C.; Compton, R. G., Electrochemistry in Room-Temperature Ionic Liquids: Potential Windows at Mercury Electrodes. *J. Chem. Eng. Data* **2009**, *54*, 2049-2053.

6. Aparicio, S.; Atilhan, M.; Karadas, F., Thermophysical Properties of Pure Ionic Liquids: Review of Present Situation. *Ind. Eng. Chem. Res.* **2010**, *49*, 9580-9595.

7. Buzzeo, M. C.; Evans, R. G.; Compton, R. G., Non-Haloaluminate Room-Temperature Ionic Liquids in Electrochemistry—a Review. *ChemPhysChem* **2004**, *5*, 1106-1120.

8. Millefiorini, S.; Tkaczyk, A. H.; Sedev, R.; Efthimiadis, J.; Ralston, J., Electrowetting of Ionic Liquids. *J. Am. Chem. Soc.* **2006**, *128*, 3098-3101.

9. Hayes, R. A.; Feenstra, B. J., Video-Speed Electronic Paper Based on Electrowetting. *Nature* **2003**, *425*, 383-385.

10. Berge, B.; Peseux, J., Variable Focal Lens Controlled by an External Voltage: An Application of Electrowetting. *Eur. Phys. J. E* **2000**, *3*, 159-163.

11. Huh, D.; Tkaczyk, A. H.; Bahng, J. H.; Chang, Y.; Wei, H.-H.; Grotberg, J. B.; Kim, C.-J.; Kurabayashi, K.; Takayama, S., Reversible Switching of High-Speed Air−Liquid Two-Phase Flows Using Electrowetting-Assisted Flow-Pattern Change. *J. Am. Chem. Soc.* **2003**, *125*, 14678-14679.

12. Wang, S.; Li, S.; Cao, Z.; Yan, T., Molecular Dynamic Simulations of Ionic Liquids at Graphite Surface. *J. Phys. Chem. C* **2009**, *114*, 990-995.

13. Kislenko, S. A.; Samoylov, I. S.; Amirov, R. H., Molecular Dynamics Simulation of the Electrochemical Interface between a Graphite Surface and the Ionic Liquid [Bmim][Pf6]. *Phys. Chem. Chem. Phys.* **2009**, *11*, 5584-5590.

14. Merlet, C.; Salanne, M.; Rotenberg, B.; Madden, P. A., Imidazolium Ionic Liquid Interfaces with Vapor and Graphite: Interfacial Tension and Capacitance from Coarse-Grained Molecular Simulations. *J. Phys. Chem. C* **2011**, *115*, 16613-16618.

15. Merlet, C.; Salanne, M.; Rotenberg, B.; Madden, P. A., Influence of Solvation on the Structural and Capacitive Properties of Electrical Double Layer Capacitors. *Electrochim. Acta* **2013**, *101*, 262-271.

16. Paneru, M.; Priest, C.; Sedev, R.; Ralston, J., Electrowetting of Aqueous Solutions of Ionic Liquid in Solid−Liquid−Liquid Systems. *J. Phys. Chem. C* **2010**, *114*, 8383-8388.

17. Paneru, M.; Priest, C.; Sedev, R.; Ralston, J., Static and Dynamic Electrowetting of an Ionic Liquid in a Solid/Liquid/Liquid System. *J. Am. Chem. Soc.* **2010**, *132*, 8301-8308.

18. Liu, J.; Wang, M.; Chen, S.; Robbins, M. O., Uncovering Molecular Mechanisms of Electrowetting and Saturation with Simulations. *Phys. Rev. Lett.* **2012**, *108*, 216101.

19. Taherian, F.; Leroy, F.; Heim, L.-O.; Bonaccurso, E.; van der Vegt, N. F. A., Mechanism for Asymmetric Nanoscale Electrowetting of an Ionic Liquid on Graphene. *Langmuir* **2016**, *32*, 140-150.

20. Merlet, C.; Pean, C.; Rotenberg, B.; Madden, P. A.; Simon, P.; Salanne, M., Simulating Supercapacitors: Can We Model Electrodes as Constant Charge Surfaces? *J. Phys. Chem. Lett.* **2013**, *4*, 264-268.

21. Hess, B.; Kutzner, C.; Van Der Spoel, D.; Lindahl, E., Gromacs 4: Algorithms for Highly Efficient, Load-Balanced, and Scalable Molecular Simulation. *J. Chem. Theory Comput.* **2008**, *4*, 435-447.

22. Merlet, C.; Salanne, M.; Rotenberg, B., New Coarse-Grained Models of Imidazolium Ionic Liquids for Bulk and Interfacial Molecular Simulations. *J. Phys. Chem. C* **2012**, *116*, 7687-7693.

23. Edwards, D. M. F.; Madden, P. A.; McDonald, I. R., A Computer Simulation Study of the Dielectric Properties of a Model of Methyl Cyanide. *Mol. Phys.* **1984**, *51*, 1141-1161.

24. Cole, M. W.; Klein, J. R., The Interaction between Noble Gases and the Basal Plane Surface of Graphite. *Surf. Sci.* **1983**, *124*, 547-554.

25. Nosé, S., A Unified Formulation of the Constant Temperature Molecular Dynamics Methods. *J. Chem. Phys.* **1984**, *81*, 511-9.

26. Hoover, W. G., Canonical Dynamics: Equilibrium Phase-Space Distributions. *Phys. Rev. A* **1985**, *31*, 1695-1697.

27. Ewald, P., Evaluation of Optical and Electrostatic Lattice Potentials. *Ann. Phys.* **1921**, *64*, 253-287.

28. Pounds, M.; Tazi, S.; Salanne, M.; Madden, P. A., Ion Adsorption at a Metallic Electrode: An Ab Initio Based Simulation Study. *J. Phys.: Condens. Matter* **2009**, *21*, 424109-11.

29. Reed, S. K.; Lanning, O. J.; Madden, P. A., Electrochemical Interface between an Ionic Liquid and a Model Metallic Electrode. *J. Chem. Phys.* **2007**, *126*, 084704-13.

30. Chaban, V. V.; Voroshylova, I. V.; Kalugin, O. N.; Prezhdo, O. V., Acetonitrile Boosts Conductivity of Imidazolium Ionic Liquids. *J. Phys. Chem. B* **2012**, *116*, 7719-7727.

31. Wang, J.; Tian, Y.; Zhao, Y.; Zhuo, K., A Volumetric and Viscosity Study for the Mixtures of 1-N-Butyl-3-Methylimidazolium Tetrafluoroborate Ionic Liquid with Acetonitrile, Dichloromethane, 2-Butanone and N, N - Dimethylformamide. *Green Chem.* **2003**, *5*, 618-622.

32. Feng, G.; Huang, J.; Sumpter, B. G.; Meunier, V.; Qiao, R., A "Counter-Charge Layer in Generalized Solvents" Framework for Electrical Double Layers in Neat and Hybrid Ionic Liquid Electrolytes. *Phys. Chem. Chem. Phys.* **2011**, *13*, 14724-14735.

33. Feng, G.; Huang, J.; Sumpter, B. G.; Meunier, V.; Qiao, R., Structure and Dynamics of Electrical Double Layers in Organic Electrolytes. *Phys. Chem. Chem. Phys.* **2010**, *12*, 5468-5479.

34. Peng, H.; Nguyen, A. V.; Birkett, G. R., Determination of Contact Angle by Molecular Simulation Using Number and Atomic Density Contours. *Mol. Simul.* **2012**, *38*, 945-952.

35. Fletcher, S. I.; Sillars, F. B.; Hudson, N. E.; Hall, P. J., Physical Properties of Selected Ionic Liquids for Use as Electrolytes and Other Industrial Applications. *Journal of Chemical & Engineering Data* **2010**, *55*, 778-782.

36. Kolbeck, C.; Lehmann, J.; Lovelock, K. R. J.; Cremer, T.; Paape, N.; Wasserscheid, P.; Fröba, A. P.; Maier, F.; Steinrück, H. P., Density and Surface Tension of Ionic Liquids. *J. Phys. Chem. B* **2010**, *114*, 17025-17036.

37. Martino, W.; de la Mora, J. F.; Yoshida, Y.; Saito, G.; Wilkes, J., Surface Tension Measurements of Highly Conducting Ionic Liquids. *Green Chem.* **2006**, *8*, 390-397.

38. Rilo, E.; Pico, J.; García-Garabal, S.; Varela, L. M.; Cabeza, O., Density and Surface Tension in Binary Mixtures of Cnmim-Bf4 Ionic Liquids with Water and Ethanol. *Fluid Phase Equilib.* **2009**, *285*, 83-89.

39. Shamsipur, M.; Beigi, A. A. M.; Teymouri, M.; Pourmortazavi, S. M.; Irandoust, M., Physical and Electrochemical Properties of Ionic Liquids 1-Ethyl-3-Methylimidazolium Tetrafluoroborate, 1-Butyl-3-Methylimidazolium Trifluoromethanesulfonate and 1-Butyl-1-Methylpyrrolidinium Bis(Trifluoromethylsulfonyl)Imide. *J. Mol. Liq.* **2010**, *157*, 43-50.

40. Zhou, Z.-B.; Matsumoto, H.; Tatsumi, K., Structure and Properties of New Ionic Liquids Based on Alkyl- and Alkenyltrifluoroborates. *ChemPhysChem* **2005**, *6*, 1324-1332.

41. Jeffery, G. H.; Vogel, A. I., 134. Physical Properties and Chemical Constitution. Part Xvii. Acetylenic Compounds and Cyanides. *J. Chem. Soc.* **1948**, 674-683.

8. Conclusions and Perspectives

This thesis is a fundamental study of ionic-liquid and acetonitrile (ACN) electrolyte mixtures at carbon interfaces using molecular dynamics simulations. Two primary areas were studied. Firstly, molecular mechanisms of charge storage for electric double-layer capacitors with ordered slit-pore, and disordered CDC electrodes, where the pore size was less than 1 nm. Secondly, the contact-angle and electrowetting properties of ionic-liquid and acetonitrile mixture drops on modified graphene sheets with interaction potentials of varying strength.

8.1. Conclusions

The first aim of this thesis was to compare and contrast the charge storage behaviour of EDLCs with varying solvent concentrations between graphitic slit-pore electrodes and disordered-porous electrodes. This was achieved in Chapters 4 and 5, where the pore size was less than 1 nm, and in which only a single layer of adsorbed charge-balancing ions could be accommodated inside the pores. It was shown in slit-pore electrodes the capacitance increased significantly with the concentration of ACN, yet in carbide derived carbon (CDC) electrodes no such increase was observed. The origin of the different phenomena is due to changes in confinement behaviour between two-dimensional and three-dimensional pores.

Realistic disordered porous electrode models are of greater interest to researchers than graphitic slit-pores because they give more realistic capacitance results. However, current CDC models overestimate capacitance.[1] Further development of the highly confining sites in CDC models may be able to reduce this discrepancy. This becomes evident when considering the pair distribution function (PDF) analysis in Chapter 5, which showed that the CDC models appear to be under-graphitised, and may lack detail in the highly confining regions.

Previously, the systematic influence of ACN concentration had been limited to considerations at flat-wall electrodes,[2] whilst simulations inside slit-pores contained only studied pure ionic-liquids or a single dilute concentration in ACN. Chapter 4 also addressed the suitability of the constant-charge and constant-potential electrode methods for accurately capturing realistic charge-storage behaviour. Previously, the two methods had only been compared for flat-wall, and disordered porous electrodes.[3] It was found that the constant-charge method did not provide accurate electrolyte compositions inside the pores and the net-ionic charges inside the pores were not great enough to balance to constant electrode charge.

The second aim of this thesis was to analyse the adsorbed structure of RTILs inside CDC pores to better understand electrostatic screening effects of electrodes. This was achieved in Chapter 5 and it was shown that increasing the concentration of ACN in the electrolyte, resulted in a decrease in density of the adsorbed ions inside the electrodes. The average distance of the ions to the surface of the electrode, and the ionic diffusivities, did not change much at low to moderate concentrations of ACN. However, a large change in charging mechanism from ion-exchange to counter-ion adsorption was observed with increasing concentration of ACN, which indicates that as the density of both ion species decreases, it becomes comparatively more difficult to remove co-ions from the electrode. As the most dilute ionic concentration resulted in the lowest capacitance, the optimal ratio of ions to solvent for capacitance is likely above the dilute electrolyte regime where ion-exchange can dominate the charging mechanism.

The final aim was to determine the contact angle dependency of ionic liquid drops on: drop size, surface interaction potential, and electric potential, and solvent concentration. This was achieved in Chapters 6 and 7 and it was found that the surface interaction potential dominated the structure and contact angle of the ionic liquid drops. Comparatively, electrowetting and ACN concentration had little effect. This indicates that surface properties and the solid-liquid surface tension needs to be carefully considered when studying the contact angle ionic-liquid nano-drops. At high surface interaction-potential, non-equilibrium meta-stable structures formed in drops, the shape and number of heterogeneous layers was dependent on the drop size, but these structures were kinetically limited and transitioned into fully wetting layers at higher temperature. The formation of the metastable ordered structures at the solid-liquid interface needs to be better understood before ionic-liquids can be fully utilised in non-wetting nano-scale applications. The contact angle saturation point at high electrowetting voltage needs more study, as its molecular origin remains unclear. Constant-charge simulations were shown to be inappropriate for analysing these electrowetting systems. They did not capture fundamental molecular behaviour in the electrodes, where the charge was stored almost exclusively in a concentrated region underneath the drop. Finally, electrowetting asymmetry that has been observed experimentally may be attributable to ion-size effects, as more compact and less ordered layering occurred at the surface of the negative electrode.

8.2. Perspectives

8.2.1. Potential continuations

Within the scope of the research presented in this thesis, there exists potential for further studies and refinement of simulation methodology. In Chapter 4, strong layering occurred in the bulk at low electric potential when the walls adjacent to the bulk were uncharged. The structure formed was solid-like which disappeared at high temperature, but more examination of the kinetic properties and phase transitions of these layers would be useful. Additionally, the ratio of bulk volume to pore volume may play a role here and is worthy of more consideration. The degree of entrance confinement may also have a significant effect on the charging dynamics, and this could be more thoroughly investigated by softening or tapering the entrance to the slit-pores. Comparisons with realistic three-dimensional electrodes may improve here as often their entrances are more open than common slit-pore models used. Interactions between adjacent pores could also be studied, and the number of charged layers between pores would be of interest.

The simulations of Chapter 5 were mostly limited to 1 V potential due limited computational resources, in future more studies at higher voltage for systems containing acetonitrile would be welcome to track any potential changes in the charge storage mechanism. Contact angle of ionic liquids studied in Chapters 6 and 7 have large promise for continued work, and could be expanded to consider more families of ionic liquids. Incorporation of surface effects into the models may also be of interest. The uncertainty of the contact angle measurement in Chapter 7 was moderately high, this could potentially be alleviated by the use of larger drops, and is a worthwhile investigation as clear explanations for electrowetting behaviour of ionic liquids remain elusive.

8.2.2. Future perspectives

Outside of conventional EDLCs, pseudocapacitors and battery-EDLC hybrids are both areas of research that are receiving significant attention experimentally. However, accurate models for these systems are currently limited to a few MD simulations[4-5] and *ab initio* calculations.[6-10] Developing effective models capable of capturing the faradic process that occur may be crucial for efficiently identifying conditions and materials that can lead to gains in pseudocapacitor performance.

Simulations of more complex electrode structures, such as three-dimensional hierarchical porous networks, activated carbons, as well as other 2D and 3D graphitic materials, are noticeably lacking. Their inclusion in molecular models would provide a higher degree of realism and may offer new avenues to further improve EDLC performance. Currently the number of CDC models available to use for simulations is quite limited. A greater variety of solids or larger solids that can include more features may move simulations closer to experimental data. Similarly, ionophobic pores are a new configuration to explore.[11] Incorporation of other effects like flexibility, expansion, defects, and chemical activation also could lead to further progress in advancing the realism of molecular simulations of EDLCs. Finally, an important consideration is non-symmetric electrodes,[12-13] as many ionic-liquids are asymmetric in shape and size, the optimal pore size can different for the positive and negative electrodes.

On the electrolyte side, better development of models would also offer many advantages to the field. Coarse-graining of more families of ionic-liquids would improve the scope and output of constant potential simulations. Development of more fully polarisable force fields, such as the APPLE&P,[14-15] will also lead to more nuanced simulations. Expanding the considerations of ionic liquids to new families,[16] or eutectic mixtures of ionic liquids which are dicationic,[17-18] may result in further improvements in performance or material cost, but further molecular analysis will be required for analysing these systems.

In the future when supercomputing power is sufficiently increased, comprehensive molecular simulations that can encapsulate all of the most advanced (and computationally demanding) properties, and can be applied to large systems (in excess of 50,000 atoms) would open up possibilities for researchers to move towards more direct comparisons with experimental systems.

Of course when considering the huge number of possible configurations when combining any number of individual, or combined ionic liquids, neat or dissolved in a solvent, and evaluating their properties at an ever increasing number of electrode materials, it becomes obvious that efficient and effective screening techniques will be required to sieve for valuable information. Towards this end, multi-scale modelling approaches may provide the best outcomes, on the condition that the most important benefits of each individual scale are encapsulated effectively.

8.3. References

1. Merlet, C.; Rotenberg, B.; Madden, P. A.; Taberna, P.-L.; Simon, P.; Gogotsi, Y.; Salanne, M., On the Molecular Origin of Supercapacitance in Nanoporous Carbon Electrodes. *Nat. Mater.* **2012**, *11*, 306-310.

2. Feng, G.; Huang, J.; Sumpter, B. G.; Meunier, V.; Qiao, R., A "Counter-Charge Layer in Generalized Solvents" Framework for Electrical Double Layers in Neat and Hybrid Ionic Liquid Electrolytes. *Phys. Chem. Chem. Phys.* **2011**, *13*, 14724-14735.

3. Merlet, C.; Pean, C.; Rotenberg, B.; Madden, P. A.; Simon, P.; Salanne, M., Simulating Supercapacitors: Can We Model Electrodes as Constant Charge Surfaces? *J. Phys. Chem. Lett.* **2013**, *4*, 264-268.

4. Vatamanu, J.; Borodin, O.; Smith, G. D., Molecular Dynamics Simulation Studies of the Structure of a Mixed Carbonate/Lipf6 Electrolyte near Graphite Surface as a Function of Electrode Potential. *J. Phys. Chem. C* **2011**, *116*, 1114-1121.

5. Xing, L.; Vatamanu, J.; Borodin, O.; Smith, G. D.; Bedrov, D., Electrode/Electrolyte Interface in Sulfolane-Based Electrolytes for Li Ion Batteries: A Molecular Dynamics Simulation Study. *J. Phys. Chem. C* **2012**, *116*, 23871-23881.

6. Ozoliņs, V.; Zhou, F.; Asta, M., Ruthenia-Based Electrochemical Supercapacitors: Insights from First-Principles Calculations. *Acc. Chem. Res.* **2013**, *46*, 1084-1093.

7. Liu, Y.; Zhou, F.; Ozolins, V., Ab Initio Study of the Charge-Storage Mechanisms in Ruo2-Based Electrochemical Ultracapacitors. *J. Phys. Chem. C* **2011**, *116*, 1450-1457.

8. Tompsett, D. A.; Parker, S. C.; Bruce, P. G.; Islam, M. S., Nanostructuring of B-Mno2: The Important Role of Surface to Bulk Ion Migration. *Chem. Mater.* **2013**, *25*, 536-541.

9. Cormier, Z. R.; Andreas, H. A.; Zhang, P., Temperature-Dependent Structure and Electrochemical Behavior of Ruo2/Carbon Nanocomposites. *J. Phys. Chem. C* **2011**, *115*, 19117-19128.

10. Kang, J.; Wei, S.-H.; Zhu, K.; Kim, Y.-H., First-Principles Theory of Electrochemical Capacitance of Nanostructured Materials: Dipole-Assisted Subsurface Intercalation of Lithium in Pseudocapacitive Tio2 Anatase Nanosheets. *J. Phys. Chem. C* **2011**, *115*, 4909-4915.

11. Kondrat, S.; Kornyshev, A. A., Pressing a Spring: What Does It Take to Maximize the Energy Storage in Nanoporous Supercapacitors? *Nanoscale Horiz.* **2016**, *1*, 45-52.

12. Varanasi, S. R.; Bhatia, S. K., Optimal Electrode Mass Ratio in Nanoporous Carbon Electrochemical Supercapacitors. *J. Phys. Chem. C* **2016**.

13. Xing, L.; Vatamanu, J.; Borodin, O.; Bedrov, D., On the Atomistic Nature of Capacitance Enhancement Generated by Ionic Liquid Electrolyte Confined in Subnanometer Pores. *J. Phys. Chem. Lett.* **2013**, *4*, 132-140.

14. Borodin, O., Polarizable Force Field Development and Molecular Dynamics Simulations of Ionic Liquids. *J. Phys. Chem. B* **2009**, *113*, 11463-11478.

15. Bedrov, D.; Borodin, O.; Li, Z.; Smith, G. D., Influence of Polarization on Structural, Thermodynamic, and Dynamic Properties of Ionic Liquids Obtained from Molecular Dynamics Simulations. *J. Phys. Chem. B* **2010**, *114*, 4984-4997.

16. Aparicio, S.; Atilhan, M., Choline-Based Ionic Liquids on Graphite Surfaces and Carbon Nanotubes Solvation: A Molecular Dynamics Study. *J. Phys. Chem. C* **2012**, *116*, 12055-12065.

17. Li, S.; Guang, F.; Peter, T. C., Interfaces of Dicationic Ionic Liquids And graphene: A Molecular Dynamics Simulation Study. *J. Phys.: Condens. Matter* **2014**, *26*, 284106.

18. Lin, R.; Taberna, P.-L.; Fantini, S.; Presser, V.; Pérez, C. R.; Malbosc, F.; Rupesinghe, N. L.; Teo, K. B. K.; Gogotsi, Y.; Simon, P., Capacitive Energy Storage from −50 to 100 °C Using an Ionic Liquid Electrolyte. *J. Phys. Chem. Lett.* **2011**, *2*, 2396-2401.